

**ACOUSTIC EMISSION TECHNIQUES APPLIED
TO CONVENTIONALLY REINFORCED
CONCRETE BRIDGE GIRDERS**

FINAL REPORT

SPR 633

**ACOUSTIC EMISSION TECHNIQUES APPLIED TO
CONVENTIONALLY REINFORCED CONCRETE BRIDGE GIRDERS**

Final Report

SPR 633

by

Thomas Schumacher
Oregon State University
220 Owen Hall
Corvallis, OR 97331-3212

for

Oregon Department of Transportation
Research Unit
200 Hawthorne Ave. SE, Suite B-240
Salem OR 97301-5192

and

Federal Highway Administration
400 Seventh Street, SW
Washington, DC 20590-0003

September 2008

1. Report No. FHWA-OR-RD-09-04		2. Government Accession No.		3. Recipient's Catalog No.	
4. Title and Subtitle Acoustic Emission Techniques Applied to Conventionally Reinforced Concrete Bridge Girders				5. Report Date September 2008	
				6. Performing Organization Code	
7. Author(s) Thomas Schumacher				8. Performing Organization Report No.	
9. Performing Organization Name and Address Oregon State University 220 Owen Hall Corvallis, OR 97331-3212				10. Work Unit No. (TRAIS)	
				11. Contract or Grant No. SPR 633	
12. Sponsoring Agency Name and Address Oregon Department of Transportation Research Unit and Federal Highway Administration 200 Hawthorne Ave. SE, Suite B-240 400 Seventh Street, SW Salem, OR 97301-5192 Washington, DC 20590-0003				13. Type of Report and Period Covered Final Report	
				14. Sponsoring Agency Code	
15. Supplementary Notes					
16. Abstract Reinforced concrete (RC) bridges generally operate at service-level loads except during discrete overload events that can reduce the integrity of the structure by initiating concrete cracks, widening or extending of existing concrete cracks, as well as reinforcing steel slip or yielding. Identification of previous damage and predicting the possible impact on future performance has increasingly become of interest to load rating engineers. The ultimate goal of this project was to determine if the Acoustic Emission (AE) Technique can assist in:					
<ul style="list-style-type: none"> • Assessing and identifying previous damage • Monitoring existing bridges for real-time detection of occurring damage • Predicting critical conditions or failure of bridge members <p>The term <i>damage</i> in this context shall be defined as a <i>change in the current state or condition of a structural element that reduces its capacity</i>. Damage is not a well-defined term for reinforced concrete since cracking alone does not necessarily reduce the capacity of a member. However, crack formation and crack width growth are of importance since they may expose steel reinforcement to the environment which can lead to rebar corrosion, etc. In the present study, the term <i>deterioration</i> is therefore used rather than <i>damage</i>.</p> <p>Four conventionally reinforced concrete (CRC) girders were designed to fail in shear-compression mode and constructed with different reinforcement details to investigate the AE response due to increasing loads up to capacity, cyclic loading representing ambient service-level trucks, and simulated test trucks also at the service level.</p>					
17. Key Words Acoustic testing, reinforced concrete, bridge design, structural element, damage			18. Distribution Statement Copies available from NTIS, and online at http://www.oregon.gov/ODOT/TD/TP_RES/		
19. Security Classification (of this report) Unclassified		20. Security Classification (of this page) Unclassified		21. No. of Pages 197	22. Price

SI* (MODERN METRIC) CONVERSION FACTORS

APPROXIMATE CONVERSIONS TO SI UNITS					APPROXIMATE CONVERSIONS FROM SI UNITS				
Symbol	When You Know	Multiply By	To Find	Symbol	Symbol	When You Know	Multiply By	To Find	Symbol
<u>LENGTH</u>					<u>LENGTH</u>				
in	inches	25.4	millimeters	mm	mm	millimeters	0.039	inches	in
ft	feet	0.305	meters	m	m	meters	3.28	feet	ft
yd	yards	0.914	meters	m	m	meters	1.09	yards	yd
mi	miles	1.61	kilometers	km	km	kilometers	0.621	miles	mi
<u>AREA</u>					<u>AREA</u>				
in ²	square inches	645.2	millimeters squared	mm ²	mm ²	millimeters squared	0.0016	square inches	in ²
ft ²	square feet	0.093	meters squared	m ²	m ²	meters squared	10.764	square feet	ft ²
yd ²	square yards	0.836	meters squared	m ²	m ²	meters squared	1.196	square yards	yd ²
ac	acres	0.405	hectares	ha	ha	hectares	2.47	acres	ac
mi ²	square miles	2.59	kilometers squared	km ²	km ²	kilometers squared	0.386	square miles	mi ²
<u>VOLUME</u>					<u>VOLUME</u>				
fl oz	fluid ounces	29.57	milliliters	ml	ml	milliliters	0.034	fluid ounces	fl oz
gal	gallons	3.785	liters	L	L	liters	0.264	gallons	gal
ft ³	cubic feet	0.028	meters cubed	m ³	m ³	meters cubed	35.315	cubic feet	ft ³
yd ³	cubic yards	0.765	meters cubed	m ³	m ³	meters cubed	1.308	cubic yards	yd ³
NOTE: Volumes greater than 1000 L shall be shown in m ³ .									
<u>MASS</u>					<u>MASS</u>				
oz	ounces	28.35	grams	g	g	grams	0.035	ounces	oz
lb	pounds	0.454	kilograms	kg	kg	kilograms	2.205	pounds	lb
T	short tons (2000 lb)	0.907	megagrams	Mg	Mg	megagrams	1.102	short tons (2000 lb)	T
<u>TEMPERATURE (exact)</u>					<u>TEMPERATURE (exact)</u>				
°F	Fahrenheit	(F-32)/1.8	Celsius	°C	°C	Celsius	1.8C+32	Fahrenheit	°F

*SI is the symbol for the International System of Measurement

ACKNOWLEDGEMENTS

Support for this research by Oregon Department of Transportation and Federal Highway Administration is gratefully acknowledged. The author wishes to especially thank Dr. Steven C. Lovejoy for the introduction to the field of Acoustic Emission Testing and Dr. Christopher C. Higgins for the unquestioning support and the advising during experiment as well as analysis. The author would also like to thank Ms. MaryAnn I. Brooks, Ms. Michelle Chavez, Mr. Jason D. Boise and Ms. Angela Rogge for their assistance in experimental testing.

Dr. Christian U. Grosse, Dr. Steven D. Glaser, and Dr. Richard A. Nordstrom were always willing to respond to questions and their great knowledge in the field of AE was of invaluable help. The numerous discussions with Mr. Gregory McLaskey were very inspiring and helpful for further understanding the many complex aspects of AE.

DISCLAIMER

This document is disseminated under the sponsorship of the Oregon Department of Transportation and the United States Department of Transportation in the interest of information exchange. The State of Oregon and the United States Government assume no liability of its contents or use thereof.

The contents of this report reflect the view of the authors who are solely responsible for the facts and accuracy of the material presented. The contents do not necessarily reflect the official views of the Oregon Department of Transportation or the United States Department of Transportation.

The State of Oregon and the United States Government do not endorse products of manufacturers. Trademarks or manufacturers' names appear herein only because they are considered essential to the object of this document.

This report does not constitute a standard, specification, or regulation.

TABLE OF CONTENTS

1.0	INTRODUCTION.....	1
2.0	INTRODUCTION TO ACOUSTIC EMISSION.....	3
2.1	WAVE PROPAGATION IN HOMOGENEOUS ISOTROPIC ELASTIC MEDIA	3
2.1.1	<i>Damping</i>	6
2.1.2	<i>Reflections of p-Waves on Free Surfaces</i>	7
3.0	LITERATURE REVIEW	10
3.1	EARLY WORK	10
3.2	LABORATORY WORK	10
3.2.1	<i>Reinforced Concrete</i>	10
3.2.2	<i>Field Applications</i>	16
3.2.3	<i>Summary and Limitations</i>	17
4.0	ACOUSTIC EMISSION DATA ACQUISITION AND ANALYSIS	18
4.1	DATA PROCESS CHAIN	18
4.1.1	<i>Principle</i>	18
4.1.2	<i>AE Sensors</i>	19
4.1.3	<i>Pre-amplifiers</i>	22
4.1.4	<i>Data Acquisition System</i>	23
4.1.5	<i>Final Remarks</i>	24
4.2	DATA ACQUISITION	25
4.2.1	<i>Sources</i>	25
4.2.2	<i>Data Acquisition Parameters</i>	28
4.2.3	<i>Wave Form Examples and Filtering</i>	31
4.3	QUALITATIVE ANALYSIS	34
4.3.1	<i>Rate Process Analysis</i>	36
4.3.2	<i>Historic-Severity Analysis</i>	36
4.3.3	<i>Kaiser Effect and Felicity Ratio</i>	37
4.3.4	<i>Wave Form Analysis</i>	39
4.3.5	<i>b-Value Analysis</i>	39
4.4	QUANTITATIVE ANALYSIS	42
4.5	AE SOURCE LOCATION	43
4.5.1	<i>Components of AE Source Location</i>	43
4.5.2	<i>Used Location Algorithms</i>	49
4.5.3	<i>Determination of p-Wave Velocities</i>	50
4.5.4	<i>Evaluation of Location Uncertainties</i>	51
4.5.5	<i>Moment Tensor Inversion</i>	59
5.0	PRE-EXPERIMENTAL STUDIES.....	62
5.1	AMPLITUDE ATTENUATION DUE TO MATERIAL DAMPING	62
5.2	INFLUENCE OF INCIDENT ANGLES ON MEASURED SIGNAL AMPLITUDES	69
5.3	WHAT AE SENSORS MEASURE	71
6.0	MAIN TESTS OF FULL-SIZE REINFORCED CONCRETE GIRDERS.....	74
6.1	SPECIMEN FABRICATION AND MATERIALS	74
6.2	EXPERIMENTAL SETUP	75

6.3	INSTRUMENTATION	77
6.4	TEST SPECIMENS	77
6.4.1	<i>Cross Section</i>	77
6.4.2	<i>AE Specimen #1</i>	78
6.4.3	<i>AE Specimen #2</i>	78
6.4.4	<i>AE Specimen #3</i>	78
6.4.5	<i>AE Specimen #4</i>	79
6.4.6	<i>Comment</i>	79
6.5	ACOUSTIC EMISSION (AE) SENSOR ARRAYS	79
6.5.1	<i>Sensor Array A</i>	79
6.5.2	<i>Sensor Array B</i>	80
6.5.3	<i>Comments</i>	80
6.6	LOADING PROTOCOL	81
6.6.1	<i>Introduction</i>	81
6.6.2	<i>Unloading effect on indeterminate multi-span bridges</i>	81
6.6.3	<i>Force effects</i>	82
6.6.4	<i>Loading Procedure</i>	84
6.7	SPECIMEN RESPONSE	87
6.7.1	<i>AE Specimen #1</i>	87
6.7.2	<i>AE Specimen #2</i>	91
7.0	SENSOR ARRAY A	96
7.1	AE HIT RATES	96
7.1.1	<i>AE Specimen #1</i>	96
7.2	KAISER EFFECT AND FELICITY RATIO	100
7.3	MINIMUM <i>B</i> -VALUE ANALYSIS	101
7.3.1	<i>AE Specimen #1</i>	106
7.3.2	<i>AE Specimen #2</i>	122
7.3.3	<i>Summary and Comments</i>	139
8.0	SENSOR ARRAY B	140
8.1	AE HITS AND HIT RATES	140
8.2	KAISER EFFECT AND FELICITY RATIO	141
8.3	<i>B</i> -VALUE ANALYSIS	142
8.4	ESTIMATION OF LINEAR AE SOURCE LOCATIONS	142
9.0	SUMMARY AND CONCLUSIONS	144
10.0	REFERENCES.....	148

APPENDICIES

Appendix A: Materials and Settings

Appendix B: AE Settings

Appendix C: Data Sensor Array A

TABLE OF TABLES

Table 2.1: Theoretical p -wave amplitude ratios $A_p/A_{p,i}$	8
Table 4.1: Commercially available AE sensors with generic calibration sheets	20
Table 4.2: Elements of the Vallen AE data acquisition system and settings used for experiments	24
Table 4.3: Overview of possible AE sources in reinforced concrete	25
Table 4.4: Overview of data acquisition parameters and recommended values	28
Table 4.5: Summary of recommended values for dynamic threshold settings	30
Table 4.6: Commonly used AE parameters for qualitative AE analysis	34
Table 4.7: Model parameters and associated uncertainties	51
Table 5.1: Attenuation coefficients $\alpha_{initial}$ with correlation coefficients R	65
Table 6.1: Concrete compressive strength, f_c'	75
Table 6.2: Reinforcement steel properties	75
Table 6.3: Log File Summary AE Specimen #1 (DL = dead load, OL = overload, TT = test truck)	85
Table 6.4: Log File Summary AE Specimen #2 (DL = dead load, OL = overload, TT = test truck)	87
Table 7.1: Summary of located AE events (DL = dead load, OL = overload, TT = test truck)	106
Table 7.2: Summary of located AE events (DL = dead load, OL = overload, TT = test truck)	122
Table B1.1: Sensor Array A1 (Session 1)	B-1
Table B1.2: Sensor Array A2 (Session 2 & 3)	B-1
Table B1.3: Sensor Array A3 (Session 6 & 7)	B-2
Table B1.4: Sensor Array A4 (Session 8)	B-2
Table B1.5: Sensor Array A5 (Session 13, 14, & 18)	B-2
Table B1.6: Sensor Array B (Session 3c, 7b, 9, & 15)	B-3
Table B2.1: Sensor Array A1 (Session 1, 2, 2b, & 2c)	B-4
Table B2.2: Sensor Array A2 (Session 3, 7, 8, & 12)	B-4
Table B2.3: Sensor Array A3 (Session 13)	B-4
Table B2.4: Sensor Array A4 (Session 17, 18, & 19)	B-5
Table B2.5: Sensor Array B (Session 4, 9, & 14)	B-5
Table B3.1: Data acquisition settings used for AE Specimen #1	B-6
Table B3.2: Data acquisition settings used for AE Specimen #2	B-7

TABLE OF FIGURES

Figure 2.1: Normalized Wave Phase Velocities versus Poisson's Ratio	5
Figure 2.2: Reflections of p -waves on free surfaces.	7
Figure 2.3: Reflection coefficients for different Poisson's Ratios	8
Figure 4.1: AE process chain (for clarity only one channel shown).	18
Figure 4.2: AE Sensor (KRNi060) with fixture	21
Figure 4.3: AE data acquisition setup	23
Figure 4.4: Displacement pattern due to harmonic point source (<i>Sansalone 1997</i>)	26
Figure 4.5: Examples of artificial AE sources, A: \emptyset 0.12 mm capillary break, C: 0.5 mm pencil lead break, B: \emptyset 1.6 mm ball bearing drop, D: AE sensor pulse (<i>Breckenridge 1990</i>).	27
Figure 4.6: Example signal representation with different sampling rates.	29
Figure 4.7: Dynamic thresholds for first-hit sensors during an overload event	30
Figure 4.8: Example wave forms likely caused by primary AE sources	31
Figure 4.9: Example wave form likely caused by a secondary AE source	32
Figure 4.10: Example wave form likely caused by the electrical circuit	32
Figure 4.11: Example of filtering with the proposed filter: (a) unfiltered data, (b) filtered data	33
Figure 4.12: Example of an AE signal wave form with parameters	35
Figure 4.13: Example for evaluation of NDIS-2421 procedure	38

Figure 4.14: Example of Load and Calm Ratios for different threshold settings	39
Figure 4.15: Examples of two discrete b -value for 100 consecutive AE hit amplitudes: Likely no on-going damage, (b) likely on-going damage	40
Figure 4.16: Example of continuous b -value monitoring for one AE sensor	41
Figure 4.17: Example for evaluation of the proposed <i>minimum b-value method</i>	42
Figure 4.18: Examples of p -wave arrival estimates for two picking methods for signals with high (a) and low (b) signal-to-noise ratio	45
Figure 4.19: Example of a source location result (own scheme)	48
Figure 4.20: p -wave speed vs. concrete strength	50
Figure 4.21: Parameter uncertainties with assumed distribution functions	52
Figure 4.22: Example of the PDF solution of one AE source location	52
Figure 4.23: East face of AE Specimen #2 with installed sensors.	53
Figure 4.24: Simulation of parameter 1 (sensor locations) at the center line ($z = 0$)	54
Figure 4.25: Simulation of parameter 2 (wave speed) at the center line ($z = 0$)	55
Figure 4.26: Simulation of parameter 3 (time arrivals) at the center line ($z = 0$)	56
Figure 4.27: Simulation of all parameters simultaneously at the center line ($z = 0$)	57
Figure 4.28: Comparison of VisualAE results with MCS for pencil lead breaks	58
Figure 4.29: Classification of different fracture mechanisms (<i>Grosse 2001</i>)	60
Figure 5.1: Test cylinders (a) and block specimen (b)	63
Figure 5.2: Amplitude attenuation curves for the Vallen SE150-M sensor	64
Figure 5.3: Amplitude attenuation curves for the KRNi060 sensor	64
Figure 5.4: Amplitude attenuation curves for the Deci SE1000-H sensor	65
Figure 5.5: Example of normalized frequency responses for one PLB	66
Figure 5.6: Criteria for estimation of highest frequency component	67
Figure 5.7: Highest detected frequency (5 %) as a function of the signal travel distance	68
Figure 5.8: Semi-circular specimen, experimental setup	69
Figure 5.9: Measured p -wave amplitudes vs. incident angles	70
Figure 5.10: Results of data-fitting for the Vallen SE150-M sensor	70
Figure 5.11: Results of data-fitting for the Glaser-NIST Sensor	71
Figure 5.12: FD surface displacement from ball bearing drop (a) with frequency spectrum (b)	72
Figure 5.13: Results for ball bearing drop: (a) time history, (b) frequency spectra	73
Figure 5.14: Close-up view of p -wave arrival	73
Figure 6.1: Test configuration with typical specimen, dimensions in mm (in.)	76
Figure 6.2: Test frame with specimen, photo taken from N-E	76
Figure 6.3: Typical instrumentation (conventional sensors) on specimen	77
Figure 6.4: Specimen cross-section, dimensions in mm (in.)	78
Figure 6.5: AE Specimen #1 with sensor array A, dimension in mm (in.)	79
Figure 6.6: AE Specimen #1 with sensor array B, dimension in mm (in.)	80
Figure 6.7: Example of rebar strain response at crack location measured at actual in service bridge in Cottage Grove, OR	81
Figure 6.8: Force effects on a three span prototype bridge	82
Figure 6.9: Generalized loading protocol with used sensor arrays (designated A to D)	84
Figure 6.10: Actual loading protocol for AE Specimen #1	85
Figure 6.11: Actual loading protocol for AE Specimen #2	86
Figure 6.12: Mid-span displacement for AE Specimen #1	88
Figure 6.13: Existing cracks for each phase before test trucks were applied for AE Specimen #1 (only cracks on east face shown for clarity)	90
Figure 6.14: Crack pattern at failure for AE Specimen #1 (East face only)	90
Figure 6.15: Mid-span displacement for AE Specimen #2	91
Figure 6.16: Existing cracks for each phase before test trucks were applied for AE Specimen #2 (only cracks on east face shown for clarity)	93
Figure 6.17: Crack pattern at failure for AE Specimen #2 (East face only)	94
Figure 7.1: Cumulative AE hit rates (from all eight sensors) for AE Specimen #1: left column: overloads; right column: simulated service level test trucks	97

Figure 7.2: Cumulative AE hit rates (from all eight sensors) for AE Specimen #2: left column: overloads; right column: simulated service level test trucks.....	98
Figure 7.3: Cumulative AE hits during holding phase	99
Figure 7.4: Evaluation of AE Specimen #1 (a) and #2 (b) according to the NDIS-2421 procedure.....	100
Figure 7.5: Average <i>Calm</i> and <i>Load Ratios</i> for each phase for AE Specimen #1.....	101
Figure 7.6: Average <i>Calm</i> and <i>Load Ratios</i> for each phase for AE Specimen #2.....	101
Figure 7.7: Minimum estimated <i>b</i> -values from overloads for both specimens	102
Figure 7.8: Minimum averaged <i>b</i> -values from applied test trucks for AE Specimen #1	103
Figure 7.9: Minimum averaged <i>b</i> -values from applied test trucks for AE Specimen #2	104
Figure 7.10: Minimum averaged <i>b</i> -values for the 140 kip test truck for AE Specimen #1 (left) and #2 (right) Estimation of 3-D AE Source Locations.....	105
Figure 7.11: Estimated Source Locations, Session 1 (DL).....	107
Figure 7.12: Estimated Source Locations, Session 1 (1 st OL).....	108
Figure 7.13: Estimated Source Locations, Session 1 (4 x 500 cycles).....	109
Figure 7.14: Estimated Source Locations, Session 1 (4 x 1000 cycles).....	110
Figure 7.15: Estimated Source Locations, Session 3 (3 TT).....	111
Figure 7.16: Estimated Source Locations, Session 6 (2 nd OL).....	112
Figure 7.17: Estimated Source Locations, Session 3 (2 x 1000 cycles).....	113
Figure 7.18: Estimated Source Locations, Session 7 (3 TT).....	114
Figure 7.19: Estimated Source Locations, Session 8 (3 rd OL).....	115
Figure 7.20: Estimated Source Locations, Session 8 (1000 + 500 cycles).....	116
Figure 7.21: Estimated Source Locations, Session 8 (9 TT).....	117
Figure 7.22: Estimated Source Locations, Session 13 (4 th OL).....	118
Figure 7.23: Estimated Source Locations, Session 13 (500 + 250 cycles).....	119
Figure 7.24: Estimated Source Locations, Session 14 (16 TT).....	120
Figure 7.25: Estimated Source Locations, Session 18 (5 th overload, failure).....	121
Figure 7.26: Estimated Source Locations, Session 1 (DL).....	123
Figure 7.27: Estimated Source Locations, Session 2 (1 st OL).....	124
Figure 7.28: Estimated Source Locations, Session 2 (2 x 1000 cycles).....	125
Figure 7.29: Estimated Source Locations, Session 2b (2 x 1000 cycles).....	126
Figure 7.30: Estimated Source Locations, Session 2c (1000 cycles).....	127
Figure 7.31: Estimated Source Locations, Session 3 (3 TT).....	128
Figure 7.32: Estimated Source Locations, Session 7 (3 rd OL).....	129
Figure 7.33: Estimated Source Locations, Session 7 (2 x 1000 cycles).....	130
Figure 7.34: Estimated Source Locations, Session 8 (9 TT).....	131
Figure 7.35: Estimated Source Locations, Session 12 (3 rd OL).....	132
Figure 7.36: Estimated Source Locations, Session 12 (2 x 500 cycles).....	133
Figure 7.37: Estimated Source Locations, Session 13 (17 TT).....	134
Figure 7.38: Estimated Source Locations, Session 17 (4 th OL).....	135
Figure 7.39: Estimated Source Locations, Session 17 (250 cycles).....	136
Figure 7.40: Estimated Source Locations, Session 18 (12 TT).....	137
Figure 7.41: Estimated Source Locations, Session 19 (5 th OL, failure).....	138
Figure 7.42: Elevation view of AE Specimen #1	139
Figure 8.1: Total AE hit rates (left column) and total AE hits (right column) for AE Specimen #1.....	140
Figure 8.2: Total AE hit rates (left column) and total AE hits (right column) for AE Specimen #2.....	141
Figure 8.3: AE Events (left column) and AE event locations (right column) for AE Specimen #1.....	142
Figure 8.4: AE Events (left column) and AE event locations (right column) for AE Specimen #2.....	143
Figure A1: AE Specimen #1, concrete cylinders at test end day.....	A-3
Figure A2: AE Specimen #2, concrete cylinders at test end day.....	A-3
Figure C1.1: Basic AE data and physical measurements, Session 1	C-1
Figure C1.2: Basic AE data and physical measurements, Session 2	C-2
Figure C1.3: Basic AE data and physical measurements, Session 3	C-3
Figure C1.4: Basic AE data and physical measurements, Session 6	C-4
Figure C1.5: Basic AE data and physical measurements, Session 7	C-5
Figure C1.6: Basic AE data and physical measurements, Session 8	C-6

Figure C1.7: Basic AE data and physical measurements, Session 13	C-7
Figure C1.8: Basic AE data and physical measurements, Session 14	C-8
Figure C1.9: Basic AE data and physical measurements, Session 18	C-9
Figure C2.1: Basic AE data and physical measurements, Session 1	C-10
Figure C3.1: AE hit rates for all applied load cycles for AE Specimen #1 (left) and #2 (right)	C-11
Figure C4.1: <i>Load</i> and <i>Calm Ratios</i> for simulated test truck groups for AE Specimen #1	C-12
Figure C4.2: <i>Load</i> and <i>Calm Ratios</i> for simulated test truck groups for AE Specimen #2	C-12

1.0 INTRODUCTION

Reinforced concrete (RC) bridges generally operate at service-level loads except during discrete overload events that can reduce the integrity of the structure by initiating concrete cracks, widening or extending of existing concrete cracks, as well as reinforcing steel slip or yielding. Identification of previous damage and predicting the possible impact on future performance has increasingly become of interest to load rating engineers. The ultimate goal of this project was to determine if the Acoustic Emission (AE) Technique can assist in:

- Assessing and identifying previous damage
- Monitoring existing bridges for real-time detection of occurring damage
- Predicting critical conditions or failure of bridge members

The term *damage* in this context shall be defined as a *change in the current state or condition of a structural element that reduces its capacity*. Damage is not a well-defined term for reinforced concrete since cracking alone does not necessarily reduce the capacity of a member (*Potisuk 2004*). However, crack formation and crack width growth are of importance since they may expose steel reinforcement to the environment which can lead to rebar corrosion, etc. In the present study, the term *deterioration* is therefore used rather than *damage*.

Four conventionally reinforced concrete (CRC) girders were designed to fail in shear-compression mode and constructed with different reinforcement details to investigate the AE response due to increasing loads up to capacity, cyclic loading representing ambient service-level trucks, and simulated test trucks also at the service level.

Two different sensor arrays were deployed on the specimens for evaluation. Existing standards were used when appropriate (*ASTM 2002, and 2004*).

2.0 INTRODUCTION TO ACOUSTIC EMISSION

Acoustic Emissions (AE) are the result of a sudden, spontaneous strain release within a solid body, i.e. the formation of a crack. A stress wave is generated, traveling from the source origin away to the surface of the body where it can be recorded by sensors. This process is irreversible and therefore not repeatable. Other names for AE include stress wave emission or micro-seismic activity. Formally defined, AE is the *term used for transient elastic waves generated by the release of energy within a material or by a process (EN 2000)*. Within the family of non-destructive testing methods, AE has its own special place because it is a passive technique. Rather than scanning a structural element, i.e. with the ultrasonic technique (UT), the AE technique records the emitted stress waves produced by a change of the internal integrity.

2.1 WAVE PROPAGATION IN HOMOGENEOUS ISOTROPIC ELASTIC MEDIA

Stress waves are generated by a sudden strain release within the solid body. The simplest case is the one of an infinite media. In air or water, only one type, often referred to as mode, of wave exists. This wave is called compression or dilatation (*p*-) wave where the particles move in the direction of the wave. The propagation of stress waves in solids like concrete is more complex because solids can resist shear forces. An additional wave mode exists that is independent of the *p*-wave which is called distortion, or shear (*s*-) wave with particle motion perpendicular to the direction of wave travel.

With the introduction of boundaries and interfaces like free surfaces or cracks, a third type of wave may exist. It is called surface or Rayleigh (*R*-) wave and has an out-of-plane particle motion component. This motion is elliptical in nature and retrograde with respect to the direction of propagation. The vertical component of the displacement is greater than the horizontal component at the surface. The motion decreases exponentially in amplitude away from the surface (*Graff 1991*). Surface waves are typically large in amplitude compared to the *p*-wave or *s*-wave from the same source and therefore easier to detect but their travel path can be complicated.

The governing differential equations to describe wave motions in solids and some practical solutions such as the wave phase velocities are presented next. Complete derivations can be found in (*Graff 1991*).

The elasticity equations (also known as Navier's Equations) for a homogeneous isotropic elastic infinite media are:

$$(\lambda + \mu)u_{j,ji} + \mu u_{i,jj} + \rho f_i = \rho \ddot{u}_i \quad (2.1)$$

In terms of rectangular scalar notation, equation (2.1) represents the three following equations:

$$\begin{aligned} (\lambda + \mu) \left(\frac{\partial^2 u}{\partial x^2} + \frac{\partial^2 v}{\partial x \partial y} + \frac{\partial^2 w}{\partial x \partial z} \right) + \mu \left(\frac{\partial^2 u}{\partial x^2} + \frac{\partial^2 u}{\partial y^2} + \frac{\partial^2 u}{\partial z^2} \right) + \rho f_x &= \rho \left(\frac{\partial^2 u}{\partial t^2} \right) \\ (\lambda + \mu) \left(\frac{\partial^2 u}{\partial y \partial x} + \frac{\partial^2 v}{\partial y^2} + \frac{\partial^2 w}{\partial y \partial z} \right) + \mu \left(\frac{\partial^2 v}{\partial x^2} + \frac{\partial^2 v}{\partial y^2} + \frac{\partial^2 v}{\partial z^2} \right) + \rho f_y &= \rho \left(\frac{\partial^2 v}{\partial t^2} \right) \\ (\lambda + \mu) \left(\frac{\partial^2 u}{\partial z \partial x} + \frac{\partial^2 v}{\partial z \partial y} + \frac{\partial^2 w}{\partial z^2} \right) + \mu \left(\frac{\partial^2 w}{\partial x^2} + \frac{\partial^2 w}{\partial y^2} + \frac{\partial^2 w}{\partial z^2} \right) + \rho f_z &= \rho \left(\frac{\partial^2 w}{\partial t^2} \right) \end{aligned} \quad (2.2)$$

Where u , v , and w are the particle displacements in the x , y , and z direction. The mass density per unit volume is ρ and f_i are the body forces per unit mass of material.

λ and μ (called Lamé's Constant) in terms of E (Modulus of Elasticity) and ν (Poisson's Ratio) are:

$$\lambda = \frac{E\nu}{(1+\nu)(1-2\nu)}, \quad \mu = \frac{E}{2(1+\nu)} \quad (2.3), (2.4)$$

In the absence of body forces ($f = 0$) the propagation velocities c_p and c_s can be determined as:

$$c_p = \sqrt{\frac{E}{\rho} \sqrt{\frac{1-\nu}{(1+\nu)(1-2\nu)}}} = \sqrt{\frac{\lambda + 2\mu}{\rho}} \quad (2.5)$$

$$c_s = \sqrt{\frac{E}{\rho} \sqrt{\frac{1}{2(1+\nu)}}} = \sqrt{\frac{\mu}{\rho}} \quad (2.6)$$

The ratio κ of these two velocities is only dependant on Poisson's Ratio ν as:

$$\kappa = \frac{c_p}{c_s} = \sqrt{\frac{\lambda + 2\mu}{\mu}} = \sqrt{\frac{2-2\nu}{1-2\nu}} \quad (2.7)$$

The exact relationship between p -wave, s -wave, and R -wave velocity is described as:

$$\frac{c_R^2}{c_s^2} = 2 - 4 \sqrt{1 - \frac{c_R^2}{c_s^2}} \sqrt{1 - \frac{c_R^2}{c_p^2}} \quad (2.8)$$

An approximate expression also called Bergmann Formula for the Rayleigh wave velocity is given in (*Graff 1991*) as:

$$c_R = c_s \left(\frac{0.87 + 1.12\nu}{1 + \nu} \right) \quad (2.9)$$

From Equations 2.7-2.9 we also find that the following condition is always true:

$$c_p > c_s > c_R \quad (2.10)$$

All three velocities depend only on the material properties E , ν , and ρ but not on frequency which means that they are not dispersive. Figure 2.1 shows the relationship for different values of Poisson's Ratio ν . A vertical line is plotted at $\nu = 0.30$ which was found to be a representative value for the concrete used for experiments performed at OSU (*Lovejoy 2006*). For $\nu = 0.30$, s -wave and R -wave velocities are approximately 53% and 50%, respectively, of the p -wave velocity normalized to 100%.

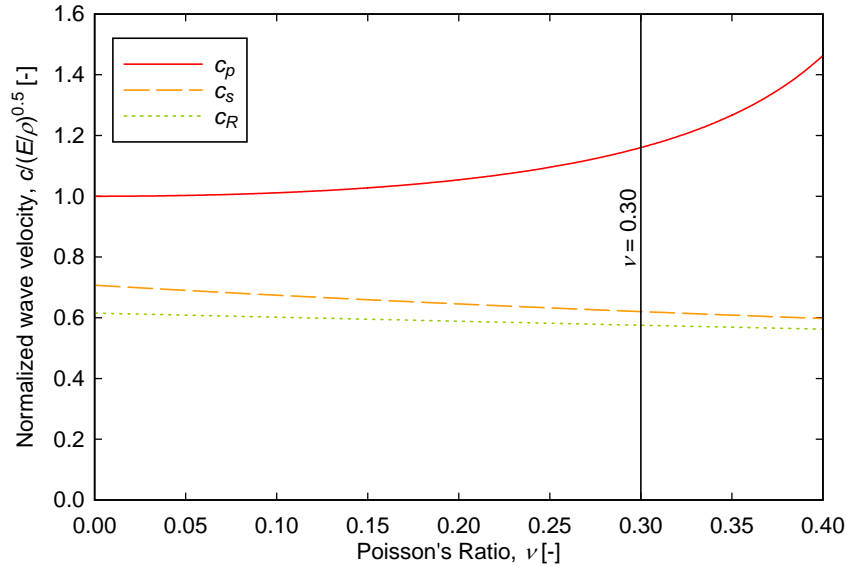


Figure 2.1: Normalized Wave Phase Velocities versus Poisson's Ratio.

A typical mean value for the p -wave velocity observed from several conducted experiments at OSU is $c_p = 3.80$ m/ms (150 in./ms) (*Lovejoy 2006; Schumacher 2006*).

Assuming Poisson's Ratio $\nu = 0.30$, the other two velocities are $c_s = 2.03$ m/ms (80.0 in./ms) and $c_R = 1.88$ m/ms (74.2 in./ms). A more detailed description on how velocities are determined can be found in Section 4.5.3.

2.1.1 Damping

In the previous discussion, homogeneous material characteristics were assumed for wave propagation. Concrete consists of aggregates in different sizes and types as well as cement and water. Conventionally (non-prestressed) reinforced concrete (RC) has its own very unique characteristics due to material heterogeneity and embedded steel reinforcement. In order to activate the steel reinforcement, RC usually cracks at load levels well below capacity. Cracks dampen the progressing wave or, when wide enough, can become insurmountable barriers to wave transmission. All this, plus the fact that concrete is a porous material that can contain water or air or both, influence the propagation of stress waves. Two basic mechanisms cause damping of a stress wave in an infinite medium. The first is geometric attenuation which is due to the fact that as a wave front propagates away from its origin it spreads over a larger volume. The energy density therefore decreases. The geometric attenuation of a body stress wave in an infinite media causes the wave amplitude to decrease proportionally to r^{-1} (spherical). For a surface wave, the wave amplitude decreases proportionally to $r^{-1/2}$ since it propagates on a plane (circular). Geometric attenuation is not frequency dependent. The second kind is material attenuation is caused by absorption and scattering due to internal friction at aggregate boundaries. Material attenuation is frequency dependent and can only be determined experimentally and described with empirical formulas. Generally, higher frequencies attenuate at a higher rate than lower ones. This is because the wave lengths of higher frequencies coincide with the aggregates of equal or bigger size. A comprehensive study on damping characteristics of mortar and concrete can be found in (*Landis 1995*). Damping due to embedded reinforcing bars was studied with an elasto-dynamic code by Schechinger (*2006*) and experimentally by Lovejoy (*2006*). Both showed that there is an influence on the signal amplitude but it is relatively unimportant for small diameter rebars. In these experiments, AE sensors were placed away from the large diameter $\varnothing 35$ mm (#11) rebars to avoid large damping effects.

To evaluate the damping characteristics of the concrete used for this research, an experiment was conducted (see Section 5.1). Pencil lead breaks were performed on concrete specimens with different lengths s to determine material damping characteristics. In Table 5.1, attenuation coefficients α that were computed with a linear least-squares curve-fit are summarized for different AE sensors. Values for the p -wave amplitude vary between $\alpha_{initial} = 80$ and 118 dB/m and $\alpha_{whole} = 42$ and 58 dB/m depending on the type of AE sensor used. Köppel found a value of $\alpha = 45$ dB/m (*Köppel 2002*). Landis found in his experiments attenuation coefficients for concrete with a maximum aggregate size of 10 mm (0.4 in.) around $\alpha = 200$ dB/m (< 125 kHz) (*Landis 1995*).

2.1.2 Reflections of p -Waves on Free Surfaces

When stress waves hit free surfaces or interfaces they go through mode conversions. For instance, when a compression wave hits a free surface, a compression and a shear wave are created plus a surface wave, depending on the incident angle θ as illustrated in Figure 2.2. The same happens vice versa with shear waves. Hence the two independent wave modes become coupled through boundary conditions (*Graff 1991*).

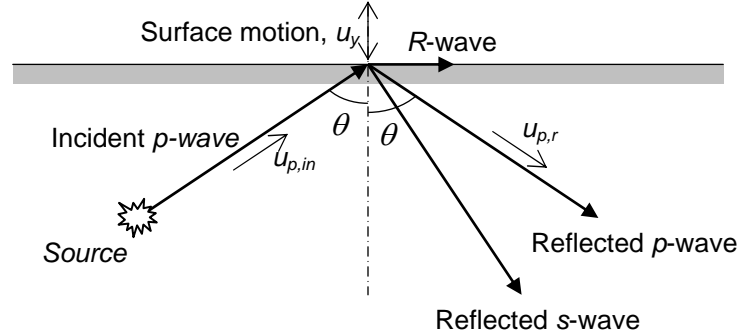


Figure 2.2: Reflections of p -waves on free surfaces.

For the estimation of AE source locations and the application of moment tensor inversions, p -waves are of interest. AE sensors record the surface motion perpendicular to the sensor surface. Therefore, every AE source has a specific distance s and incident angle θ with respect to the sensor. The relationship between the particle displacement due to the incident p -wave $u_{p,in}$, and the resulting surface motion perpendicular to the surface u_y , needs therefore to be known. Köppel (2002) derived the following relationship in terms of the reflection coefficients R_p

$$R_p = \frac{u_{p,in}}{u_y} = \frac{2\kappa^2 \cos(\theta) (\kappa^2 - 2 \sin^2(\theta))}{(\kappa^2 - 2 \sin^2(\theta))^2 + 4 \sin^2(\theta) \sqrt{1 - \sin^2(\theta)} \sqrt{\kappa^2 - \sin^2(\theta)}} \quad (2.11)$$

Where κ is the ratio between p -wave and s -wave velocities as presented in Equation (2.7) and θ the space angle between the normal to the sensor surface and the ray line between AE source and sensor. Through conservation of momentum we find that the surface displacement measured with the AE sensor is twice that of the p -wave amplitude, i.e. the sum of both incident plus reflected surface displacements are recorded. Reflection coefficients R_p can therefore theoretically take values between 0 ($\theta = 90^\circ$) and 2 ($\theta = 0^\circ$). The ratio of the measured p -wave amplitude (perpendicular to the surface) A_p , and the incident p -wave amplitude $A_{p,in}$ is simply $R_p/2$.

Figure 2.3 shows reflection coefficients plotted against incident angle for different Poisson's Ratios.

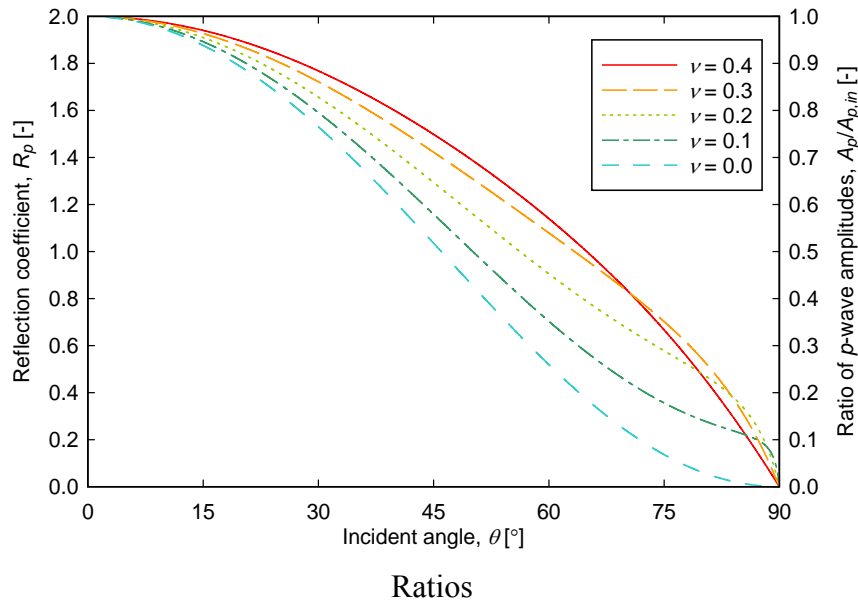


Figure 2.3: Reflection coefficients for different Poisson's Ratios.

Equation 2.11 was validated with an experiment that is described in Section 5.2. Reasonable agreement was found between the theoretical relationship and the observed data with two different sensor types for Poisson's Ratios $0.13 < \nu < 0.21$. These values were determined using the least-squares method. It can easily be recognized that the angle at which a p -wave hits the sensor on the surface (incident angle, θ) greatly influences the recorded p -wave amplitude. Table 2.1 shows the measured p -wave amplitude as a function of different incident angles, θ for the Poisson's Ratios as shown in Figure 2.3.

Table 2.1: Theoretical p -wave amplitude ratios $A_p/A_{p,i}$

Incident angle, $\theta [^\circ]$	Poisson's Ratio, $\nu [-]$				
	$\nu = 0.0$	$\nu = 0.1$	$\nu = 0.2$	$\nu = 0.3$	$\nu = 0.4$
0	1.00	1.00	1.00	1.00	1.00
30	0.77	0.80	0.83	0.86	0.88
45	0.52	0.58	0.65	0.71	0.75
60	0.26	0.35	0.45	0.54	0.57
90	0.00	0.00	0.00	0.00	0.00

This should be always kept in mind when working with p -wave amplitudes. It also opens the discussion on whether calculations of signal energy are a good way to describe the magnitude or strength of an AE event, especially when the source location is unknown. If

the AE source location is estimated, p -wave amplitudes can be corrected using Equation 2.11.

3.0 LITERATURE REVIEW

3.1 EARLY WORK

The fact that material under plastic deformation or when cracking emits audible sounds has been known for centuries. Early investigations were qualitative in character and restricted to the frequency range of the human ear. The necessary tools to measure and record such sounds were finally developed in the early 20th century. Joseph Kaiser from the University in Munich, Germany is considered the pioneer in modern AE research. In 1953, he published his findings of AE measurements during tension tests on metals (*Kaiser 1950*). Thus the Kaiser Effect states that sounds are emitted only when a previous stress level is exceeded. Fowler et al. discovered in the 1960s that this is not always true for composite materials. The Felicity Ratio was born which states that AE starts at a lower stress level than the previous one. This was a major step for Fowler's later work in developing his Historic-Severity analysis procedure (*Fowler 1989*). Green (*1970*) conducted material tests on mortar cylinders for the prestressed concrete pressure vessel reactor industry. He concluded that stress wave emission data can be used to determine the onset and progression of failure processes. Prior loading levels during successive loading could be estimated based on the irreversible nature of stress wave emissions, i.e. a test specimen that had undergone a pressure proof test would have considerably fewer stress wave emissions at operating pressures below the proof level than at pressure levels higher than the proof level.

Presented in the following section is an overview of AE applications to structural reinforced concrete components with a focus on bridges. The first documented AE experiment was conducted in 1980 at the University of Washington to investigate de-bonding of reinforcement during cyclic loading of beam-column joints (*Kobayashi 1980*). After that, AE monitoring has increasingly been utilized to investigate fracture processes and to characterize damage of reinforced concrete elements.

3.2 LABORATORY WORK

3.2.1 Reinforced Concrete

Ohtsu et al. have been conducting research on a variety of reinforced concrete (RC) elements since about 1980 (*Ohtsu 1996*). De-bonding as well as crack formation and propagation have been studied extensively using the AE method. Source location algorithms and a relative moment tensor analysis were developed and implemented in the computer code SiGMA (Simplified Green's Function for Moment Tensor Analysis) (*Ohtsu 1998*). A brief introduction is presented in section 4.5.4. Results were then visualized using the virtual reality modeling language (VRML) (*Shigeishi 2002*). The variety of specimens ranged from unreinforced concrete cylinders with a diameter of 100

mm (~ 4 in.) and a height of 200 mm (~ 8 in.) to an in-service RC pier with a total length of about 25 m (82 ft). Rectangular beams with a single embedded rebar as well as repaired beams were tested.

One of the qualitative assessment criteria for RC beams that emerged was the so called CBI (concrete beam integrity) ratio which is defined as the *ratio of the load at the onset of AE to the maximum prior load* (Yuyama 1998). For a case study involving four test specimens of different size it was found that the CBI ratio decreases with increasing load. The beams were loaded with increasing load steps (followed by unloading) to failure. The pier was loaded with an empty, a half full and a full dump truck. An important observation was that the Kaiser Effect was breaking down after the specimen had seen higher loads, i.e. AE while loading was released prior to the prior maximum load. Also, more AE activity was observed during unloading when approaching capacity. This was attributed to de-bonding or slip of reinforcement and interlock between existing cracks. Based on these observations, a testing standard was proposed. The criteria for a seriously damaged structural element were defined with a CBI ratio < 0.8 and high AE activity during unloading. The next step was the implementation of the above into the *Recommended Practice for In-Situ Monitoring of Reinforced Concrete Structures by Acoustic Emission (NDIS-2421)*. The procedure is also summarized and presented in Section 4.3.3. A description can be found in (Ohtsu 2002). One statement in the paper that may arise concerns is: 'For AE monitoring of existing concrete structures, it is essential to confirm that any AE signals responsible for the damage are not observed under service conditions. When the AE signals detected are due to the deterioration, and not to the noises, the monitoring and analysis should be conducted. Commonly, in-service load tests are conducted under with loads that don't impose new damage to the structure. Otherwise the question can be asked whether this can still be classified as non-destructive testing. The authors mention that the results are still based on laboratory research and in-service tests should be conducted. Furthermore, the applicability of the procedure to heavily deteriorated structures as well as structures that have experienced many load cycles should be verified.

Within the same group, Shiotani et al. developed an *improved b-value analysis* for monitoring of RC structures. Initially used for monitoring of rock slopes, this method appears to have potential for RC structures. An advantage of this method compared to for example a moment tensor analysis is its simplicity since only AE amplitudes are needed. Moment tensor analyses require clean AE signals from at least six sensors for de-convolution. This can become a problem especially when the element under consideration is heavily deteriorated. The *b-value analysis* method is presented in detail in Section 4.3.5. In (Shiotani 2000), results of moment tensor analysis are compared with *b-values*. The authors concluded that *b-values* can be used as a means to evaluate fracture processes in concrete when a moment tensor inversion is not possible. The onset and occurrence of damage is characterized by a sudden drop in the *b-value*.

A research group around M. Forde has investigated the use of the AE technique for monitoring RC bridges since the early 2000s (Colombo 2003, 2004, and 2005). *b-value analysis* was performed on a RC beam with width x height x span length of 125 mm x

270 mm x 2.0 m (4.92 in. x 10.6 in. x 6.56 ft). One 16 mm diameter (#5) rebar was embedded at the bottom. The load protocol consisted of 10 loading and unloading cycles with each subsequent increment applied at higher load magnitude up to 90 kN (20.2 kips). The beam was loaded in four-point bending, having the loading points 250 mm (~10 in.) away from the supports. b -values were computed over 100 AE amplitudes for each of the eight AE sensors. The trend of the b -value was also compared with another damage parameter, called D parameter from seismology. Minimum and maximum b -values were finally computed for each channel and over all AE amplitudes of a whole load cycle (instead of only 100) and plotted against each load cycle. The authors concluded that the development of the b -value over the course of the experiment is in good agreement with the damage observed on the beam. It is further suggested that b -values are well correlated with the degree of damage localization. The following values are presented as quantitative means: b -values between 1.0 and 1.2 imply that macro cracks are forming, b -values between 1.2 and 1.7 mean that there is uniformly distributed cracking (no macro crack growth), and b -values greater than 1.7 suggest that micro cracks are dominant or macro cracks are opening.

A means to predict the ultimate bending capacity of RC beams was suggested by the same group using the so-called *relaxation ratio* (Colombo 2005). The concept is to look at the AE energy that is released during loading and unloading. The equivalent in seismic applications is to look at energy release of fore- and aftershocks of earthquakes. The new parameter introduced was called *relaxation ratio* and simply the ratio of *average energy during unloading* to the *average energy during loading* phase. In collaboration with the research group around Ohtsu, a total of 12 beams were analyzed with this parameter and compared to the NDIS-2421 procedure (2002). The size of those beams is on the same order of the ones used for b -value analysis as described before. The span lengths ranged from 2.0 to 3.0 m (6.56 to 9.84 ft). All beams were loaded in cycles consisting of loading and unloading phases up to failure. Eight beams failed in bending, four in shear mode. For one set of the beams (*Forde*), the relaxation ratio became greater than one (meaning that the aftershock energy is greater than the foreshock energy) after about 45 % of the ultimate capacity was reached. However, for the other set of beams (*Shigeishi*), no clear trend was found and for half of them, relaxation ratio never became greater than one. Discrepancies between the two test sets were attributed to concrete properties, and not data acquisition equipment. Also, the load rate was different and that could have had an influence.

Golaski et al. conducted laboratory as well as field experiments on RC structures in the early 2000s (Golaski 2002). First, a series of full-scale laboratory beams were loaded to failure to determine proper acquisition settings and create a data base. The final goal was to establish guide lines for AE testing for a variety of in-service bridges (conventionally reinforced, prestressed, composite). Similar documents have already been developed in Japan (Ohtsu 2002) and the US (Tinkey 2000). Used for the laboratory testing was a 12 channel system with 55 kHz resonant as well as 150 kHz sensors. Two different types of prestressed beams with lengths of 12 and 18 m (39.4 and 59.1 ft) were tested until failure. The AE sensors were deployed in a linear manner using zonal location, or first-hit sensor approach. The distance between sensors was determined so that the attenuation was less

than 10 dB within each zone. This typically led to spacing's between 1.25 to 1.45 m (4.1 to 4.8 ft). The Historic-Severity Analysis described earlier was then used for evaluation. This method is briefly introduced in Section 4.3.2. Essentially, statistical values are computed based on AE signal strength or energy and plotted in a diagram. Zones from A to E are designated to different stages of damage. This method was adapted from the pressure vessel industry. This method was then used on five in-service bridges in Poland. In addition to testing of existing bridges, new bridges are now regularly tested and assigned an AE certificate before use. In one case of a load test, a girder was repaired after being very active in terms of AE. The authors conclude that AE is a promising tool to evaluate the structural integrity of bridge components while loaded with test trucks or while experiencing overloads. It is also stated that the Felicity Ratio (as described in Section 4.3.3) may not be applicable for in situ bridges as the loading is never exactly determinable.

Since the 1990s, Grosse et al. from the University of Stuttgart, Germany have been working on using AE as a non-destructive testing tool to investigate RC and fiber reinforced concrete. In their early work, they performed rebar pull-out experiments on a specimen 100 x 100 x 100 mm (ca. 4 x 4 x 4 in), rebar \varnothing 16 mm (ca. #5) to investigate the applicability of AE to reinforced concrete (Grosse 1996, 2000; Balazs 1996). A comparison with a non-linear Finite Element (FE) analysis was performed and presented in 1997 based on the idea that the anisotropic fracture model used for the FE model can directly be compared with quantitative AE measurements (Weihe 1997). A new relative Moment Tensor Inversion (MTI) analysis as well as new time picking and 3-D localization algorithms were adapted and incorporated since then. Another field that has been examined is AE signal waveform comparisons with similarity analysis techniques. *b*-value monitoring was investigated for a small concrete specimen (Kurz 2006). It was concluded that this method could have the potential for implementation in a structural health monitoring system as it is able to capture crack initiation. However, studies on large complex structures should be carried out first. Current research is focusing on automation of data acquisition and analysis and development of wireless sensor networks for monitoring bridges using beam theory (Grosse 2007). Implementation methodologies in a condition monitoring system for concrete structures have been presented (Grosse 2006).

Köppel investigated AE on a very fundamental basis in his dissertation (Köppel 2002). Wave motion in general and moment tensor inversion methods were introduced. For his experiments, Köppel chose to work with the relative moment tensor inversion method developed by Dahm/Grosse. The performed experiments include basic investigations with small specimens using artificial sources (pencil lead breaks) to investigate influence of damping and incident angles, determination of *p*-wave velocities and the errors associated with AE source location. Four experiments were performed to investigate AE due to external loads: a double punch test with an unreinforced cube and a rebar pull-out test with an unreinforced cube both of side length 0.20 m (7.87 in.), a symmetric bending test with a beam of width x height x span = 0.15 x 0.20 x 1.60 m (5.91 x 7.87 x 63.0 in.), and an asymmetric bending test with a pre-tensioned T-beam deck of width x height x span 1.78 x 1.45 x 18.7 m (5.83 x 4.76 x 61.4 ft) where the load was applied 3.80 m from

the left support. The influence of the sensor deployment on AE source location was explained: the array was given by the crack pattern, since a group of AE sensors has to be placed within a compression strut in order to ensure reliable source location of the p -wave. A crucial factor was the proper determination of p -wave arrival times. Manual picking as well as the program WinPecker were used. The evaluation performed using relative moment tensor inversion revealed difficulties. Only a few AE events fulfilled the requirements necessary to determine the source mechanism. According to Köppel, AE appears to be a tool for long-term monitoring rather than determining a current state of a structure within a short time. Also, most AE events were generated by crack activity (crack propagation and rubbing of surfaces). This may be of interest when non-ductile failure is associated with that failure mode.

Schechinger continued Köppel's work performing 2-D wave field simulations using an elasto-dynamic finite element code to investigate wave propagation in reinforced concrete (*Schechinger 2006*). Random aggregate patterns as well as reinforcement and pre-stressed strands were modeled. It was shown that conventional rebars don't significantly interfere with the stress wave. However, if an AE source was close to a rebar, these could act as wave guides with a much higher wave speed. This can lead to problems for identification of source locations. Different p -wave arrival time picking methods were compared. Additionally, a probabilistic AE source location scheme was utilized called NonLinLoc where source location results were no longer given as mean values with standard deviation but with probability density functions. Two pre-stressed tension specimens were tested, one $l \times b \times h = 0.44 \times 0.44 \times 5.84$ m (1.44 x 1.44 x 19.2 ft), the other $l \times b \times h = 0.32 \times 0.32 \times 5.84$ m (1.05 x 1.05 x 19.2 ft). Additionally, one bending test was performed with a specimen $l \times b \times h = 0.44 \times 0.44 \times 4.50$ m (1.44 x 1.44 x 14.8 ft). The biggest issue found for locating AE sources was the development of cracks in the higher load steps that effectively altered the medium and introduce boundaries for the stress waves.

Lovejoy has used AE testing to investigate Oregon's diagonally cracked 1950s reinforced concrete deck girder bridges since 2002 (*Lovejoy 2006*). Basic wave propagation studies, as well as laboratory experiments on 31 full scale girders were conducted to investigate the applicability of the AE technique to this specific problem. The NDIS-2421 procedure was used for evaluation. Thresholds that suit the present materials and boundary conditions were established and limits defined. One issue that was revealed is that the Felicity Ratio on undamaged beams decreased with increasing loads (according to theory) whereas on fatigued beams it increased.

The most recent work on large RC beams was conducted by Katsaga et al. at the University of Toronto (*Katsaga 2007*). Lightly reinforced RC beams designed to fail in shear mode were loaded up to failure and monitored using a 24-channel AE system that is capable of recording continuous waveforms. The specimen dimensions were width x height x length = 0.30 x 1.45 x 9.00 m (11.8 in. x 57.1 in. x 29.5 ft). The force was applied at mid-span monotonically up to failure. When a new level was reached, the force was dropped 10 % and cracks were mapped. AE source location was performed and p -wave velocities computed in 15 min. time intervals between two sensors. The estimated

source locations lined up very well with the actual crack surfaces. Furthermore, AE revealed cracking on a level that was not visible by surface inspection. Fracture processes were investigated looking at focal mechanisms. New insights on how coarse aggregates influence shear crack propagation could be won. Using p -wave polarities, AE source mechanisms could be deduced. It was found that in the early stages of fracture propagation tensile events were predominant whereas in later stages the majority of the events were in shear mode (see also Figure 4.29). Studying the predominant source mode during monitoring or inspection could therefore be helpful in determining the stage of fracture development.

Fowler et al. investigated the applicability of the so-called Historic-Severity Analysis for prestressed concrete girder for the Texas Department of Transportation (*Tinkey 2000*). This method is briefly introduced in section 4.3.2. A total of six girders were selected from a batch of 55 that were never put in service because of pre-existing damage. The first type consisted of a prestressed box-girder section. The dimensions were width x height x length = 1.22 x 0.69 x 21.3 m (48 in. x 27 in. x 69.8 ft). The wall thickness was 0.13 m (5 in.) which created a void (to save material and weight) of width x height = 0.97 x 0.41 m (38 x 16 in.). There were four diaphragms total. The second type was a prestressed T-shape (described as C section). Two of those girders were tested with a total height of 1.22 m (4 ft) and lengths of 23.8 and 26.8 m (78 and 88 ft). The deck was cast in place concrete with a thickness of 0.20 m (8 in.). They were first inspected visually and cracks mapped. Most cracks had apparently been caused by delayed ettringite formation (DEF) and alkali-silica reaction (ASR). A series of small unreinforced concrete specimens, width x height x length = 76 x 102 x 406 mm (3 x 4 x 16 in.), were also tested and Historic Index values as well as the CBI index computed to study AE from concrete cracking. The loading protocol for the full-scale beams was of a loading and unloading with increasing amplitude type. A large difference in terms of AE response between damaged and undamaged specimens was found. Mainly, the amount of AE differed as well as the Felicity Effect was not detected before cracking in the heavily damaged specimens. Lovejoy discovered similar problems with this parameter between unloaded and fatigued girder specimens (*Lovejoy 2006*). The authors concluded that AE is a promising tool for evaluating distributed damage in prestressed concrete. The most valuable evaluation criteria appear to be: AE during unloading, Historic Index and hit amplitudes, Felicity Ratio and hit amplitudes.

Continuing the research effort presented in (*Golaski 2002*), test data from six prestressed girders were analyzed using supervised pattern recognition software (*Kalicka 2007*). Seven different classes are recognized by the system and assigned a severity code. Unfortunately, it is not revealed how these signal classes are defined. Laboratory testing of full-scale prestressed concrete beams with lengths of 18.8 (double-tee WBS) and 26.5 m (T-shape) (61.7 and 86.9 ft) were loaded until failure to train the system and create a data base for comparison with in-service proof load testing. From the performed tests it was concluded that the warning time for the observed failures (concrete crushing or lateral buckling) was too short to be helpful. Also, zones that are active in the early loading history can suddenly become quiet and inactive whereas the failure zones

become only active just before failure occurs. Certain classes of AE signals recognized by the software seem to be representative for certain stages of damage.

Fricker investigated the feasibility of AE as a tool to detect wire breaks in deteriorated prestressed concrete bridges (*Fricker 2006*). AE seems to be suited very well for this purpose as ruptures of prestressed wires produce very high energy level signals that can be distinguished easily and located reliably. A system called Sound Print was installed and maintained remotely. In case of a detected wire break, the company called the bridge owner to inform about the event. For verification, some wire breaks were initiated by employing accelerated corrosion. The estimated locations correlated well with the actual location of the initiated break.

3.2.2 Field Applications

The field work of Ohtsu et al. is already presented in Section 3.2.1.

Carpinteri et al. reported the monitoring of a 1950s bridge in Italy in (*Carpinteri 2006 and 2007*). Two columns were instrumented and monitored for 172 days. Nine concrete cores with different diameter to length ratio were produced from the structure and tested in compression in the laboratory. These cylinder tests were then correlated with data collected from the real structure and life limit predictions were made. According to the authors, size effects were taken into using fractal theory. Based on the number of experienced AE events, the life of the two columns was estimated at 2.4 and 3.4 years. It shall not be discussed here whether such extrapolations should be done.

Colombo et al. described the monitoring of the Boghall Bridge in Scottish Borders in (*Colombo 2004*). The bridge consisted of two parts. About half on the road was supported by a masonry arch, the other half by a reinforced concrete deck-girder portion with four beams. Two of those beams were instrumented with AE sensors and monitored. An amplitude attenuation study revealed cracked regions from uncracked ones. AE source location was performed in one dimension. Activity was compared between the two beams and it was found that beam two was very silent whereas beam one showed some emissions which led to the conclusion that beam two was in good condition. A *b*-value analysis was also performed. The authors concluded that the AE results were in agreement with the existing damage on the bridge beams.

The work on in-service load testing performed by Golaski et al. is presented in Section 3.2.1. A series of structural in-service load testing with dump trucks has been performed by Lovejoy et al. on diagonally cracked conventionally reinforced concrete deck girder bridges in Oregon (*Lovejoy 2006*).

Shiotani et al. performed a series of field applications on different types of reinforced concrete structures (*Shiotani 2000, 2004, and 2007*). The latest one was on a 45 m (147.6 ft) long bridge span using a 20 ton mobile crane. 28 AE sensors were placed on the bottom of the girders as linear array to determine the most active regions. Afterwards, the regions with the highest AE activity were selected for closer inspection. Wave velocities

were also computed to reveal regions of deterioration. Velocity is an established indicator for concrete quality where high velocities suggest high and low velocities poor quality. The authors point out the advantage of employing different acoustic techniques at the same time: first, the passive AE technique is used to detect regions in the structure of high activity via controlled loading, and then an active technique such as ultrasonic can be used to evaluate smaller regions for localized damage.

3.2.3 Summary and Limitations

AE work can generally be divided in two major categories: Qualitative vs. quantitative AE analysis methods. Qualitative methods appear to work for defined problems where the boundary conditions (size, geometry, material properties, etc.) do not significantly change over time. For large structures with a number of different potential AE sources such as full-scale reinforced concrete members, they can only give a rough qualitative and relative overview of the AE processes. Quantitative methods try to describe the nature of a source by using moment tensor analysis, for example. A moment tensor analysis is not always easy to perform, especially for large structures and when using only eight sensors. Quantitative methods are the most accurate means to describe processes within a structural element.

There is a controversy between authors whether the current condition of a structural element can be evaluated and classified with AE in-service testing. Recall that AE is often referred to as a *sudden irreversible strain release*, i.e. every AE event is theoretically unique. Clearly, crack formation and propagation can be detected and located when they occur and the sensor array is set up appropriately. However, the evaluation of the severity of deterioration may be difficult as RC structures go through several stages with cracking and redistribution of internal stresses that all create similar AE. Additionally, larger structures have many potential sources of AE that are difficult to separate by using AE parameters. Recall that those parameters also depend on the boundary conditions (crack pattern) which can significantly change over the course of the life of a bridge component, and many other factors such as choice of sensors, material variability, environmental conditions, measurement system, etc.

Nevertheless, useful information can be gained by deploying a network of AE sensor during in-service proof loading. The simple presence or absence of AE during service-level testing says something about the structure. However, the most suitable application for AE appears to be in the field of long term structural health monitoring. AE represents an excellent tool to detect in real-time ongoing fracture processes. It may be beneficial to equip bridges that were designated as critical with a network of AE sensors as additional means.

4.0 ACOUSTIC EMISSION DATA ACQUISITION AND ANALYSIS

4.1 DATA PROCESS CHAIN

4.1.1 Principle

The general principle of the AE technique is that emitted stress waves due to internal strain release processes are recorded, stored, and then analyzed. AE sensors mounted to the surface convert transient surface displacements caused by arriving stress waves into an electrical signal (*Miller 2005*). This signal is then intensified by a pre-amplifier. Usually not only one but several sensors are deployed and record data in parallel. In order to store data on the hard disk, the analog sensor signals must first be digitalized. Typically, AE data is not acquired continuously, since that would yield enormous data files which would be hard to interpret. Pre-selected criteria are used to trigger the system for individual AE burst signals from which descriptive parameters and wave forms are then extracted. All this is done in real-time and requires a powerful data acquisition system. A typical setup is illustrated in Figure 4.1.

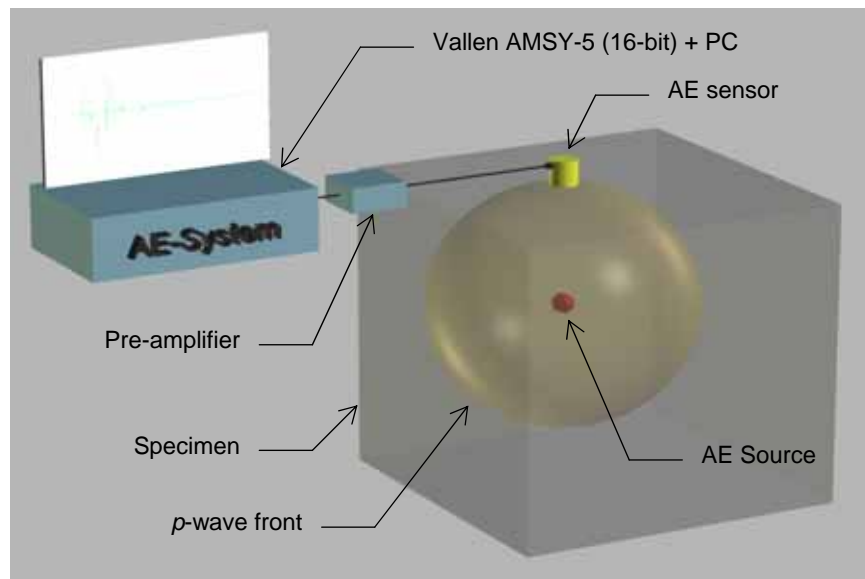


Figure 4.1: AE process chain (for clarity only one channel shown).

The goal of the AE technique is to conclude about ongoing fracture processes within the material. To do this, qualitative (Section 4.3) as well as quantitative procedures (Section 4.4) can be applied during and after data collection.

The typical setup as illustrated in Figure 4.1 can be expressed as an equation called a transmission function for the process chain (*Grosse 1996*) where the source input signal is convolved with the different system component response functions. The recorded signal $R(f)$ is fully described with the input function $S(f)$ of the signal at the source location, and the system functions $TF_M(f)$ of the elastic media, $TF_S(f)$ of the sensor response function, and $TF_{DA}(f)$ of the response function data acquisition system:

$$R(f) = S(f) \cdot TF_M(f) \cdot TF_S(f) \cdot TF_{DA}(f) \quad (4.1)$$

To simplify the matter or when components have little influence on the signal output $R(f)$, they are sometimes neglected which means that these components are set to a value of 1. Solving for the source function $S(f)$ is called signal de-convolution. This can be quite difficult since it ends up being a polynomial division which can be unstable if the data is noisy. This comes into play when a Moment Tensor Inversion (MTI) is performed where the surface motion displacements are used to make conclusions about the initiating fracture process.


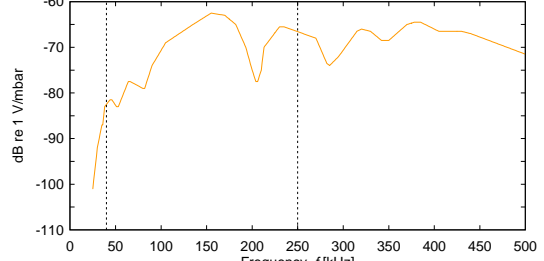

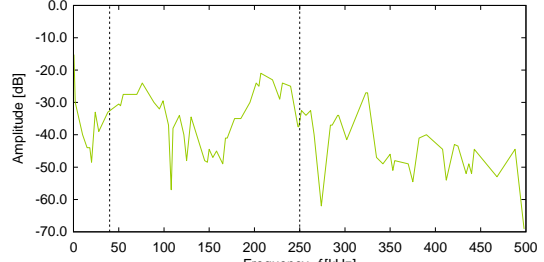

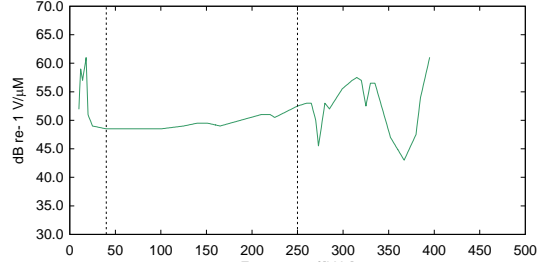
The most important point to keep in mind is that AE signals that are recorded, stored and analyzed are influenced by all elements in the process or measurement chain.

4.1.2 AE Sensors

Sensors mounted to the surface of the specimen represent the first element in the process chain. Piezoelectric transducers are typically used, which produce a voltage-versus-time signal from the dynamic surface motion (*Miller 2005*). The generated voltage signal output is proportional to the surface pressure and dependent on the size and damping characteristics of the sensor. Ideally, a sensor should have a very flat response over the whole frequency range. This is necessary for wave form analyses, but sensors of this kind tend to not be very sensitive which makes it difficult to detect signals at a distance of more than a few meters. Resonant sensors are very sensitive at their resonant frequency and can be used for signal detection. However, wave form analyses with this kind of sensor are not recommended since the signal is heavily biased by the sensor characteristics. Sensors that fulfill both criterion—high sensitivity and fidelity—exist but are not commercially available yet. Glaser et al. developed such a sensor for NIST (from now on referred to as Glaser-NIST sensor) with a conical piezoelectric crystal and built-in high-end pre-amplifier (*Glaser 1998*). This sensor was used for one of the pre-experimental studies on sensor responses (see Section 5.3).

Calibration sheets from the manufacturer show the response for individual AE sensors as illustrated in Table 4.1. Note that the units on the vertical axes (response) vary by manufacturer.

Table 4.1: Commercially available AE sensors with generic calibration sheets

Manufacturer, model	Photo of sensor	Calibration sheet with frequency response, (Only one representative response per sensor type is shown)
Vallen Systeme GmbH, SE150-M		
KRN Services, KRNi060		
Dunegan Engineering Company, Deci SE1000-H		

According to these calibration sheets, the variations in frequency response for a range between 40 and 250 kHz (dotted lines in photos of Table 4.1) are approximately 20 dB, 36 dB, and 4 dB for the Vallen SE150-M, the KRN0i60, and the Deci SE1000-H, respectively.

The SE1000-H sensor is connected to a Vallen AEP4 pre-amplifier with a gain of 34 dB, the other two sensors have integrated pre-amplifiers with gains of 34 dB and 40 dB for SE150-M and KRNi060, respectively.

Proper acoustic coupling of the sensor to the specimen is crucial for the surface motion to propagate into the piezoelectric element (*Miller 2005*). The concrete surface was first smoothed with a grinding stone and checked for voids before the AE sensors were mounted. It is important that no voids are located directly under the sensor because that can heavily dampen the AE signal and thus the sensor response. High-vacuum grease was used as a couplant between the sensor and concrete surface. Proper sensor coupling was verified with pencil lead breaks (Hsu-Nielsen-Source 0.5 mm diameter graphite) located 51 mm (2 in.) away from the center of the piezo-electric sensor element. In the subsequent experiments that are detailed, three pencil lead breaks (PLBs) were performed before every test session at each sensor location such that the peak AE signal amplitudes were within 3 dB.

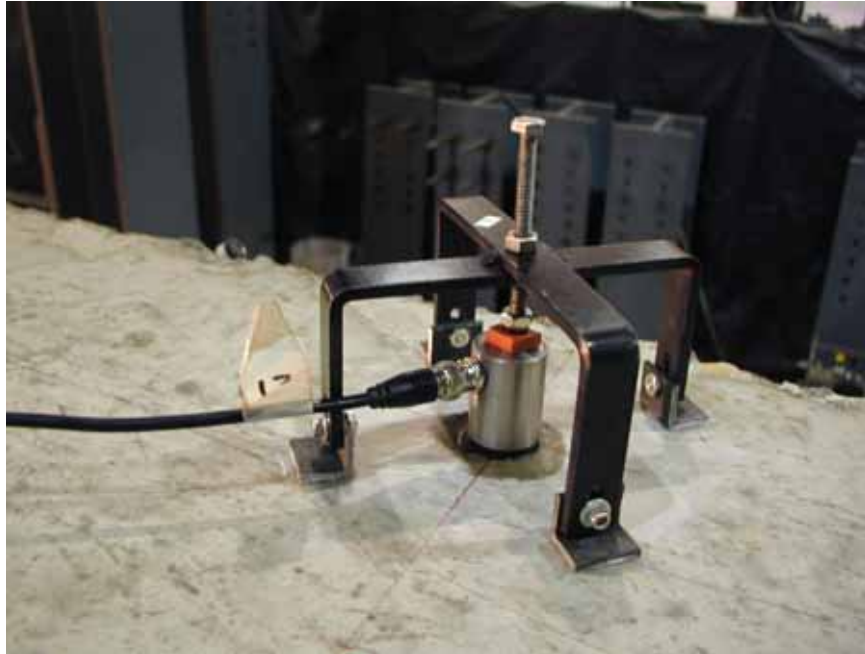


Figure 4.2: AE Sensor (KRNi060) with fixture

A typical setup of an AE sensor with a mounting fixture that was developed for this project is shown in Figure 4.2. The fixture consists of two U-shaped steel parts that were welded together. The horizontal length is about 135 mm (5.3 in.) and the height about 80 mm (3.2 in.). Attached and bonded (with cyanoacrylate glue) to the concrete surface were small steel angles connected to the fixture with little screws. These angles could be removed for stress release when a crack ran through the fixture. An adjustable M6 screw was used to press the sensor to the surface. Between the screw head and the sensor top, a small neoprene pad was placed to isolate potential noise coming in through the fixture.

4.1.3 Pre-amplifiers

Pre-amplifiers intensify the output signal from the AE transducer so it can be measured by the data acquisition system. Some sensors have integrated pre-amplifiers (i.e. Vallen SE150-M and KRNi060), others (i.e. SE1000-H) must be connected to a separate pre-amplifier. The recorded and stored AE amplitude in dB (positive or negative maximum within one AE burst signal) can be expressed as follows:

$$G[dB] = A_o[dB] - A_i[dB] = 20 \cdot \log_{10} \left(\frac{A_o[mV]}{A_i[mV]} \right) \quad (4.2)$$

Where G is the gain (amplification factor) from the pre-amplifier (this value must also be used in the data acquisition settings), A_o is the output voltage ($= A$), and A_i the input voltage from the AE sensor. The maximum input signal from the AE sensor (level of saturation) is ± 50 mV and ± 25 mV for a gain setting of 34 dB and 40 dB, respectively. The maximum output signal range from the pre-amplifier is ± 5000 mV which gives an amplification factor for the signal in [mV] of 100 and 200 for 34 dB and 40 dB, respectively. To calculate the maximum AE signal amplitude in [dB], the following equation can be used:

$$A_o[dB] = 20 \cdot \log_{10} (A_i[mV]) + 60dB - G[dB] \quad (4.3)$$

This yields the following maximum AE signal amplitude values:

- Vallen SE-150M, $G = 34$ dB: $A_o = 99.8$ dB (97.8 mV)
- KRNi060, $G = 40$ dB: $A_o = 93.8$ dB (49.0 mV)
- KRNi060, $G = 44$ dB: $A_o = 89.8$ dB (30.9 mV)
- Deci SE1000-H, $G = 34$ dB: $A_o = 99.8$ dB (97.8 mV)

For the KRNi060, the gain was not known. For AE Specimen #1 and #2 the gain was thus set to 44 dB and 40 dB, respectively. In order to compare the two experiments, a threshold filter in VisualAE was set to 40 dB and 44 dB, for AE Specimen #1 and #2, respectively.

A_i is also used to compute a dynamic (= dependant on the background noise) threshold crossing value THR_{fl} as:

$$THR_{fl} = 20 \cdot \log(Cr \cdot RMS(A_i)) \quad (4.4)$$

Where Cr is the Threshold to Noise Ratio and RMS the root-mean-square of the background noise level calculated over a length of t_{RMS} (see Table 4.4). RMS is continuously evaluated between two subsequent hits. This dynamic threshold can be used

with the Vallen system to improve p -wave arrival detection which is important for AE source location (see Section 4.5.1).

4.1.4 Data Acquisition System

For this project, an eight channel Vallen AMSY-5 AE data acquisition system was used as shown in Figure 4.3. All eight channels were equipped with transient recorders to store full AE wave forms. Every channel consists of an analog frequency band-pass filter, an analog to digital (A/D)-converter, and the capability to extract parameters and record transient AE signals in real time. This is done for AE burst signals that fulfill the user selected trigger criterion (threshold and front-end filters). It is important to know that by establishing these parameters, a certain bias or pre-selection is already imposed in the AE data.

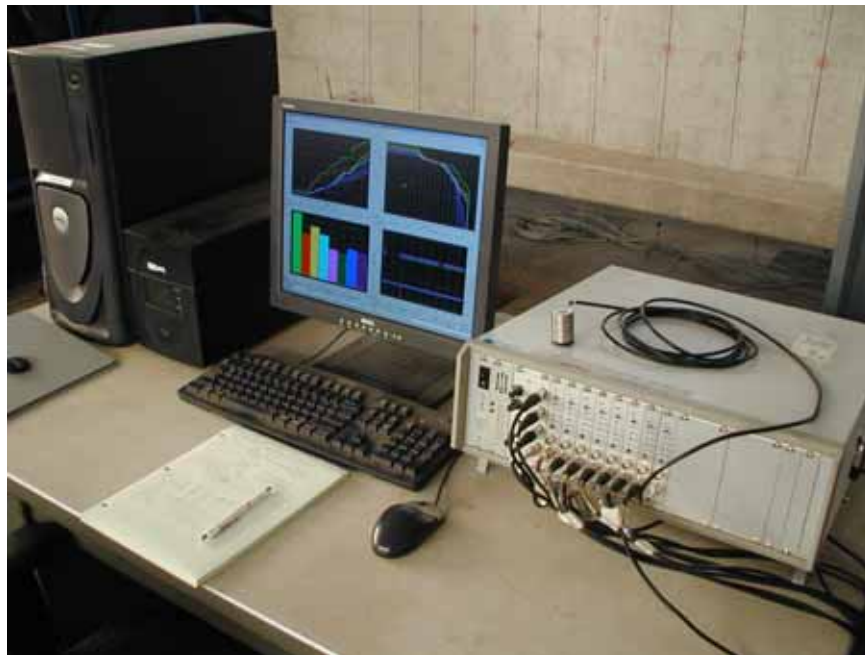


Figure 4.3: AE data acquisition setup

A personal computer is used at the end of the process chain and has data acquisition, analysis, and visualization software (Acquisition32, VisualAE) installed. A commercial Windows XP Professional computer with two Intel Xeon 2.8 GHz processors was connected to the Vallen AE AMSY-5 data acquisition system. With this setup, high-end AE data acquisition can be performed. The system is well documented and even contains some recommendations for settings (Vallen 2003). Table 4.2 lists the hardware elements of the Vallen AMSY-5 system with recommended values that were used for this project.

Table 4.2: Elements of the Vallen AE data acquisition system and settings used for experiments

Element	Description	Used
Frequency filter	Filters undesired noise out of the signal. The filter works as a band pass filter and one can choose between the following two settings: <ul style="list-style-type: none"> - 1-(Hi), 95 to 850 kHz - 2-(Lo), 20/40 to 850 kHz Note: The lower filter setting for '2-(Lo)' is not the same for all channels. For channels 1, 7, & 8 it is 20 kHz, for 2 to 6 it is 40 kHz.	2-(Lo)
A/D-Converter	Converts the analog input signal into a discrete digital signal that can be stored on a hard disk. This system has a 16 bit A/D-converter and can acquire data with a maximum sampling rate of up to 10.0 MHz. <ul style="list-style-type: none"> - Dynamic range: $2^{16} = 65,536$ values (-32,767 to 32,767) - Maximum temporal resolution: $1/10.0 \text{ MHz} = 0.1 \mu\text{s}$ 	2.0 to 5.0 MHz
Parameter extractor	Extracts parameters from AE burst signals, see Figure 4.6. Used for qualitative analyses, see section 4.3.	on
Transient recorder/ Digital signal processor	Stores full wave forms, see Figure 4.6. Used for quantitative analyses, see section 4.4.	on
Parametric recorder	Reads and converts up to four (PA00 to PA03) externally fed in voltage measurements, conversion factors are used to convert into Engineering units such as force, displacement, strain, etc.	on
Data buffer	Pre-stores data before sending it to the computer where it is stored on the hard disk, prevents overflow	on

4.1.5 Final Remarks

A final point to keep in mind is that the Vallen AMSY-5 system was not particularly designed for AE testing of reinforced concrete. This is revealed in some menu points where selectable options only make sense for thin shell structures like pressure vessels. Also, the lower filter setting for the built-in frontend filter '2-(Lo)' is relatively high. Grosse, University of Stuttgart, and Krüger, Smartmote GmbH, found AE signals in reinforced concrete containing frequencies well below 20 kHz. Taking advantage of these low frequency signals recently enabled Grosse et al. to detect AE signals generated as far away as 10 m (*Grosse 2006*). Another issue that is particularly important for *p*-wave arrival time picking as described in Section 4.4 can be the different lower filter settings.

4.2 DATA ACQUISITION

4.2.1 Sources

It is important to know the sources and mechanisms that can produce AE signals in reinforced concrete. RC is a composite material and has a larger number of source mechanisms than steel or plastic for example. An attempt to classify important sources is presented in Table 4.3.

Table 4.3: Overview of possible AE sources in reinforced concrete

Effect	Cause/description	Category
Micro crack generation	Shrinkage, temperature, creep, low load effects	Primary, distributed
Macro crack formation and propagation	Load effect due to shear, moment, or tension forces	Primary, from crack tip
Concrete crushing (plastic deformation)	Concrete in compression zone	Primary
Steel rebar yielding/fracture (plastic deformation)	Steel in tension, overload event, low-cycle fatigue	Primary
Rebar de-bonding (at crack planes, after crack formation)	Repeated differential loads (i.e. live loads)	Primary
Crack surface rubbing, interaction between steel rebars/ concrete	Repeated differential loads (i.e. live loads)	Secondary
Artificially generated signals	Sensor pulse/ pencil break (Hsu Shoe)	Calibration, surface
AE generated from outside the body	Experiment: slip/friction in test frame and bearings Field: tire friction, uneven surface causes vehicle bouncing, studded tires	Undesired noise, surface
Artificial AE from within the electrical circuit/AE system	Power supplies, cables, cell phones	Undesired noise, electr.

4.2.1.1 Primary AE Sources

Primary AE are generated when new damage/disintegration occurs, i.e. by an overload event where the maximum previous stress level is approached or exceeded or by low-cycle fatigue loading. An important distinction to be made here is the one between micro cracks (distributed, practically invisible) and macro cracks (localized, visible). For most RC structures, macro cracking is of more importance for structural evaluation and one method that has the potential to detect macro-crack formation is the so-called *b*-value analysis presented in Section 4.3.4.

4.2.1.2 Secondary AE Sources

On the other hand secondary AE are created at low loadings, i.e. ambient traffic on a bridge where the maximum stress level does not exceed the previous threshold. Kaiser Effect and Felicity Ratio are the well known phenomena associated with this problem (Section 4.3.2).

4.2.1.3 Artificial Sources

Artificial sources are commonly used for calibration purposes or to study wave propagation in solids. Figure 4.4 illustrates the particle displacement pattern of p - and s -wave due to a harmonic point-source excitation (Sansalone 1997). It can be seen that the amplitude of the p -wave is largest at $\theta = 0^\circ$ and does not vary significantly for $-45^\circ < \theta < 45^\circ$. Unfortunately, this smooth radiation pattern is not necessarily the same for real sources (see section 5.2).

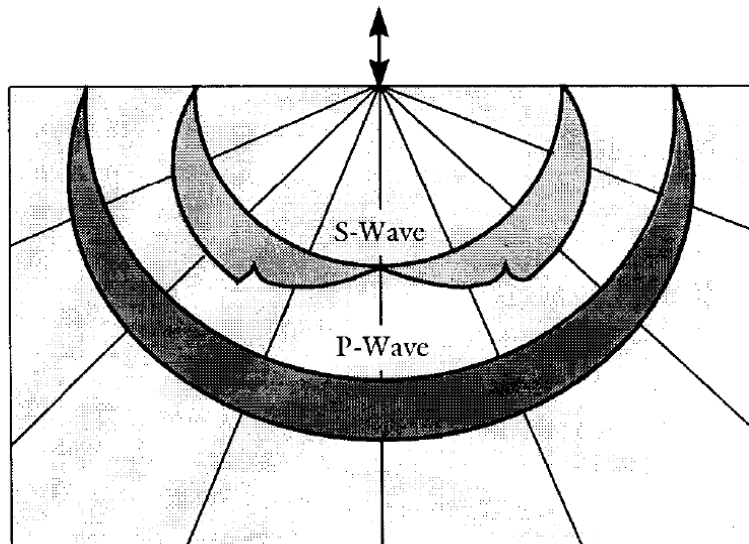


Figure 4.4: Displacement pattern due to harmonic point source (Sansalone 1997)

A selection of artificial sources is presented in Figure 4.5. Figure A shows the force produced by a capillary break. Capillary breaks represent the closest form of a step function where the force is applied and then suddenly released when the capillary breaks. Figure B illustrates the force due to a small ball bearing drop. This forcing is like a haversine and appears especially well suited for numerical modeling since there are no discontinuities. Probably the most used source is presented in Figure C: the pencil lead break (PLB). Again, the force is applied and then suddenly released. The difference to the capillary break is that there is a small negative peak before the force is released. This little peak was observed while performing the attenuation study (see Section 5.1) but it was disregarded since it damps out very quickly. Finally, Figure D shows the amplitude response

due to a pulsed AE sensor (Vallen SE150-M). Notice that this source is not as distinct as the others and it takes a while to dampen out. Nevertheless, it can easily be used for calibration purposes because it is highly repeatable.

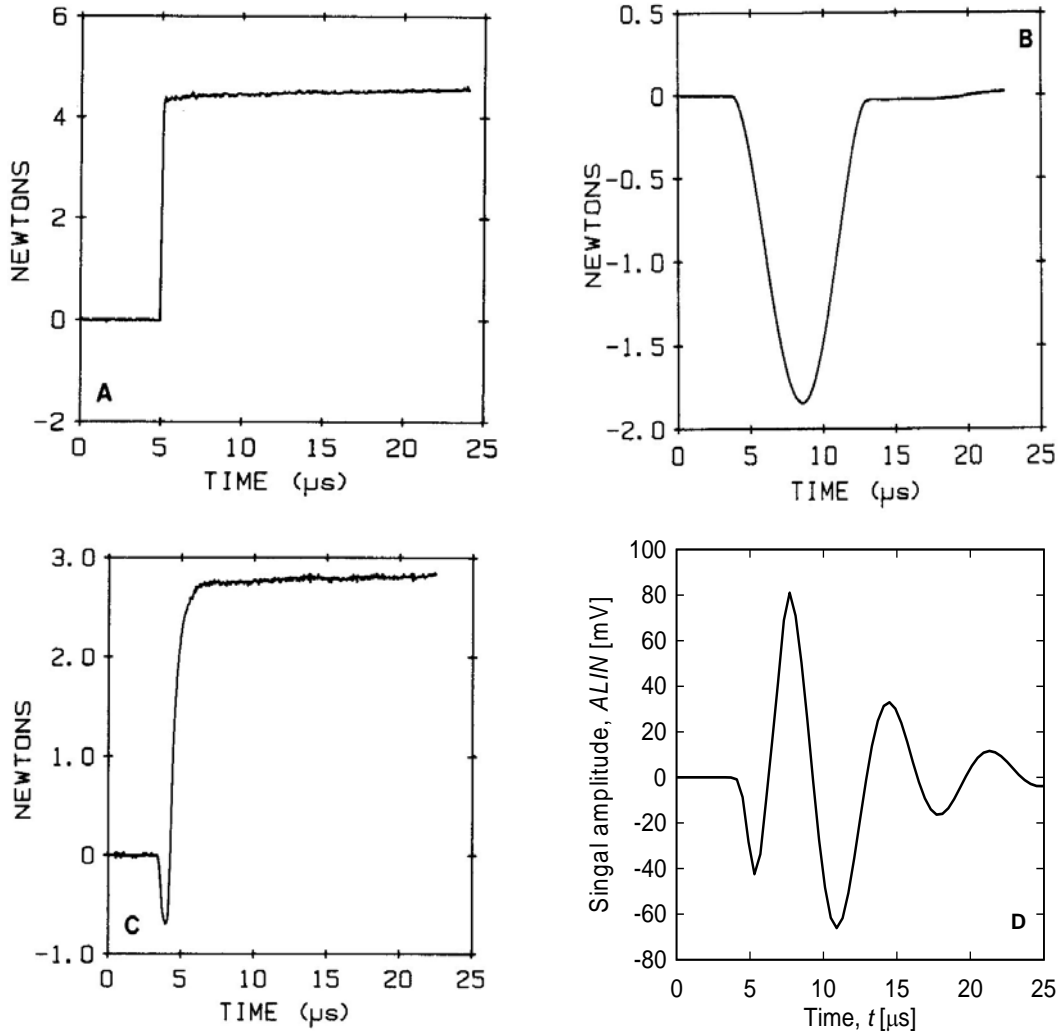


Figure 4.5: Examples of artificial AE sources, A: \varnothing 0.12 mm capillary break, C: 0.5 mm pencil lead break, B: \varnothing 1.6 mm ball bearing drop, D: AE sensor pulse (Breckenridge 1990).

4.2.1.4 Undesired noise

Noise transmitted through the test setup can be isolated using neoprene pads. For this project, neoprene pads with a thickness of 3.2 mm (1/8 in) were placed between the specimen and the force application plates to isolate noise (see Figure 6.1). In field experiments however, it is not possible to prevent the propagation of AE from external sources easily.

4.2.2 Data Acquisition Parameters

Before data can be acquired, several parameters must be selected depending on the particular experiment. These must be chosen very carefully, since post-processing (moving them) is not possible. Table 4.4 gives an overview of the most important parameters. These parameters are unique to the Vallen AMSY-5 system, although the general settings may be applicable broadly to other AE systems as well.

Table 4.4: Overview of data acquisition parameters and recommended values

Acquisition Parameter	Options/max. range	Recommended values
Sampling rate, f_s [MHz]	0.625 (1.6 μ s) to 10.0 (0.1 μ s)	Min. 2.0 or 2.5 for qualitative analysis and source locations, 5.0 or 10.0 for wave form analyses
Samples per TR set, N [-]	256 to 524,288	2048 to 8192
Threshold, THR [dB]	10 to 100, or dynamic	20 to 40 dB, sensor dependent
Threshold to noise ratio, Cr [-]	-	6 to 12, sensor dependent
RMS time constant, t_{RMS} [ms]	40 to 10,000	40/250
Rearm time [ms]	-	1.0, taken from (<i>Koppel 2002</i>)
Duration discrimination time [μ s]	-	250, taken from (<i>Koppel 2002</i>) or 500
Filter setting (Band-pass filter)	1-(Hi) or 2-(Lo)	2-(Lo), 20/40 to 850 kHz
Calculated gain, G [dB]	-	34 for SE-150M, 40 for SE1000-H and KRNi060
Trigger mode	'Normal' or 'Pool'	'Normal'
Pre-trigger samples, N_{Pre} [-]	-	800 to 1200
Frontend filters	AE-Frontend Filter	30 to 40 $\leq A$ [dB] ≤ 100

From AE burst signals, transient wave forms can be digitalized and stored for later interpretation. The parameter ‘*Sampling Rate*’ must be chosen beforehand dependent on the maximum frequency of the AE signal to be correctly represented as illustrated in Figure 4.6.

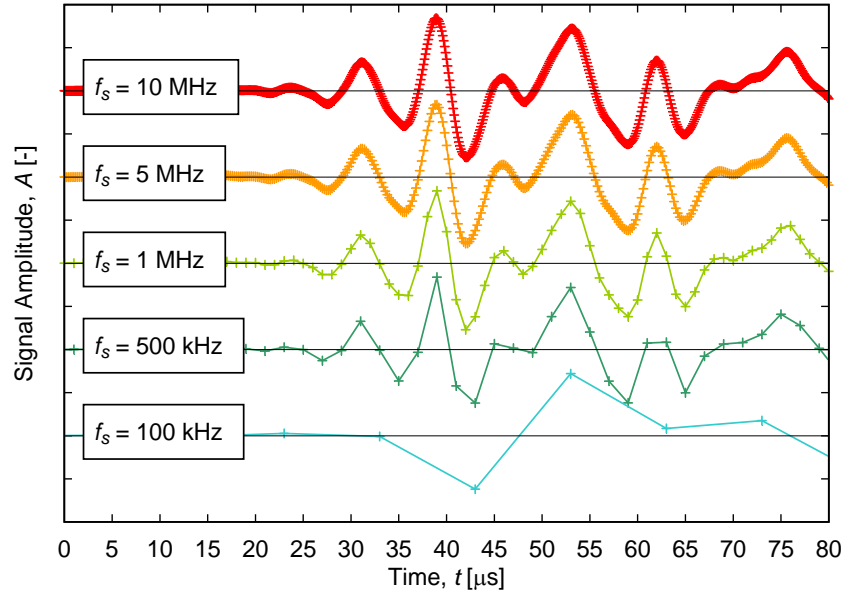


Figure 4.6: Example signal representation with different sampling rates.

Higher frequencies should be filtered out with an analog low-pass filter because they fold in and cause aliasing. Commonly used in AE are sampling rates between 500 kHz and 5 MHz. The highest frequency that can still be properly represented once digitalized is called Nyquist Frequency and depends on the selected sampling rate f_s :

$$f_{Nyq} = \frac{f_s}{2} \quad (4.5)$$

The parameter '*Samples per TR-Set*' in the Vallen system depends on the particular application. If source locations need to be estimated based on *p*-wave arrivals, a recording length of 500 μs is theoretically enough to cover the very first portion of the signal. If whole wave forms are to be analyzed, a longer time window is necessary, since AE signals usually last for approximately 1 to 2 ms. The Vallen parameter '*Pre-trigger Samples*' defines how much time is recorded prior to the *p*-wave detection. This portion also contains the background noise. For post-evaluation with outside programs (i.e. PolarAE), a minimum pre-trigger time of 400 to 800 μs is recommended.

The Vallen parameters '*Threshold*' and '*Threshold to Noise Ratio*' Cr were thoroughly examined in the anchorage project (Schumacher 2006). Appropriately choosing these two parameters enable reasonable p -wave arrival picking if the Vallen software is used. They also represent the starting point for the employment of other methods, e.g. the Matlab picking scheme based on the AIC picking method developed and later presented in section 4.5.1. Table 4.5 gives an overview of threshold and related settings used for the experiments at OSU. These values appeared to work well, but do not necessarily generally apply for every possible application.

Table 4.5: Summary of recommended values for dynamic threshold settings

Sensor	Vallen SE-150M	KRNi060
Threshold, THR [dB]	22 to 26	34 to 36
Threshold to Noise Ratio, Cr [-]	11 to 13	6 to 8
Calculated gain, G [dB]	34	40
Front-end filters	$30 < A$ [dB] < 100	$37 < A$ [dB] < 100

Employing dynamic threshold settings enables for better source location with VisualAE. However, this may have an influence on the consistency of data collection since the threshold is not fixed to a specific value. For instance, when the AE hit rate is high, the background noise increases which consequently increases the detection threshold. This effect is illustrated in Figure 4.7. The influence on qualitative AE parameters was not investigated in the present study. Therefore, if no source location is performed, using a fixed threshold may be the better choice in terms of consistent data acquisition.

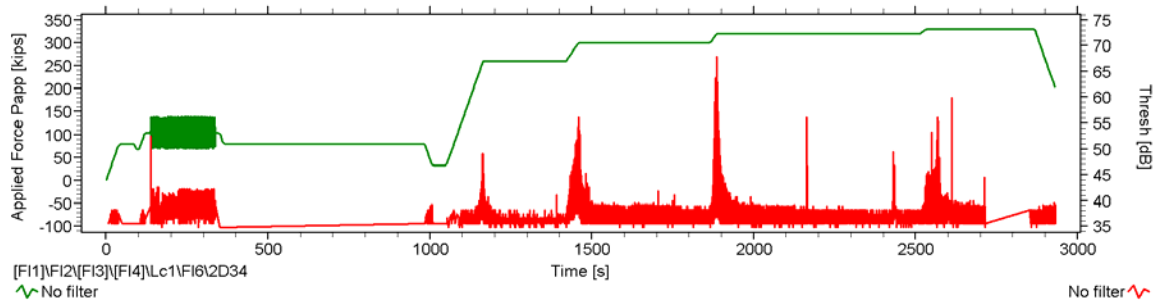


Figure 4.7: Dynamic thresholds for first-hit sensors during an overload event

Vallen parameters '*Rearm Time*' and '*Duration Discrimination Time*' have to be chosen according to the size of the specimen and require some deeper knowledge and experience. The values chosen for these experiments were taken from Köppel's experiments because they appeared to work well on similar large size structures (Köppel 2002).

4.2.3 Wave Form Examples and Filtering

The discrimination of the different AE sources as presented in Section 4.2.1 is often difficult because the recorded surface motions are heavily influenced by the sensor and data acquisition characteristics (see Section 4.1.1). Nonetheless, an attempt was undertaken to present characteristic AE wave forms caused by the different types of sources. In this section, typical wave forms for each AE source type are shown and methods for noise discrimination are discussed.

4.2.3.1 Wave Forms from Primary AE Sources

Typical signal wave forms likely caused by primary AE sources that were recorded with a KRNi060 sensor during the main experiment are illustrated in Figure 4.4. The signal-to-noise ratio is high and medium high for the examples shown in Figure 4.8 (a) and (b), respectively. High signal-to-noise ratios usually allow for more precise p -wave arrival detection with minimal error (see section 4.5.1). The range of amplitude values, A , can span the whole range depending on the signal travel distance. In some cases, they are even clipped, i.e. when the maximum voltage is exceeded.

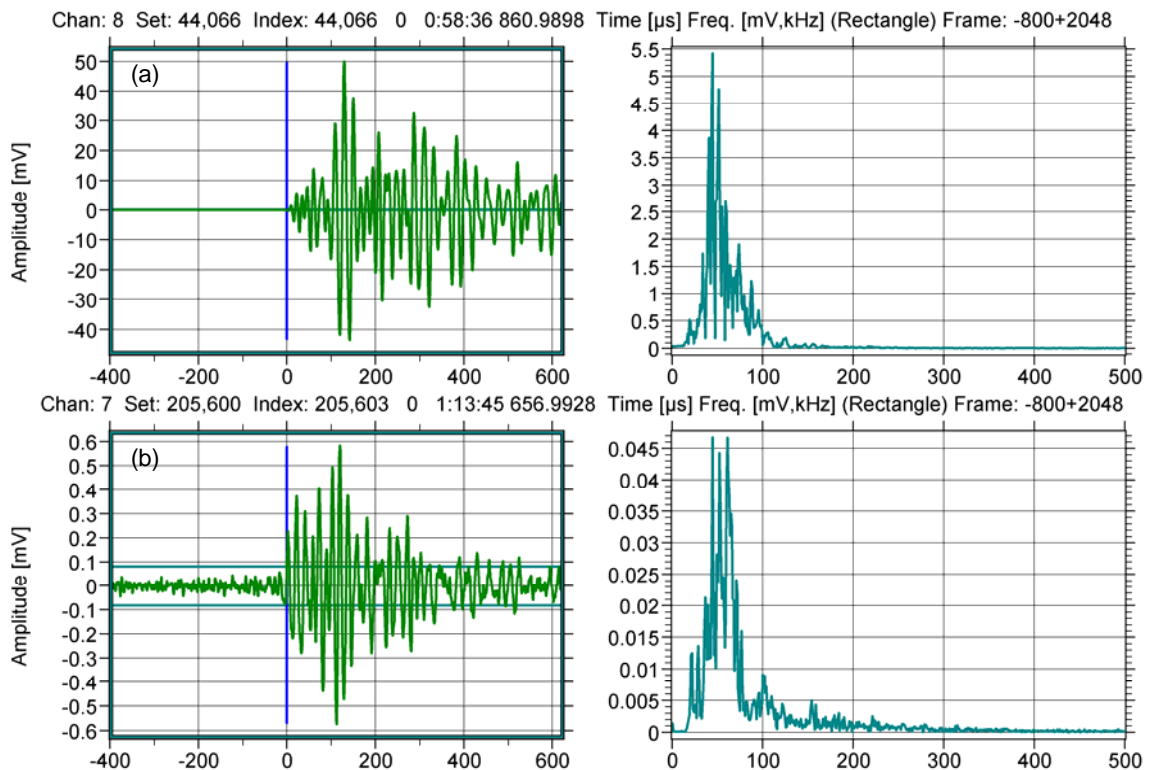


Figure 4.8: Example wave forms likely caused by primary AE sources

4.2.3.2 Wave Forms from Secondary AE Sources

Wave forms from secondary sources are usually of low amplitude and long duration. An example is illustrated in Figure 4.9. In this case, the signal-to-noise ratio is very low and the p -wave arrival may not be determinable.

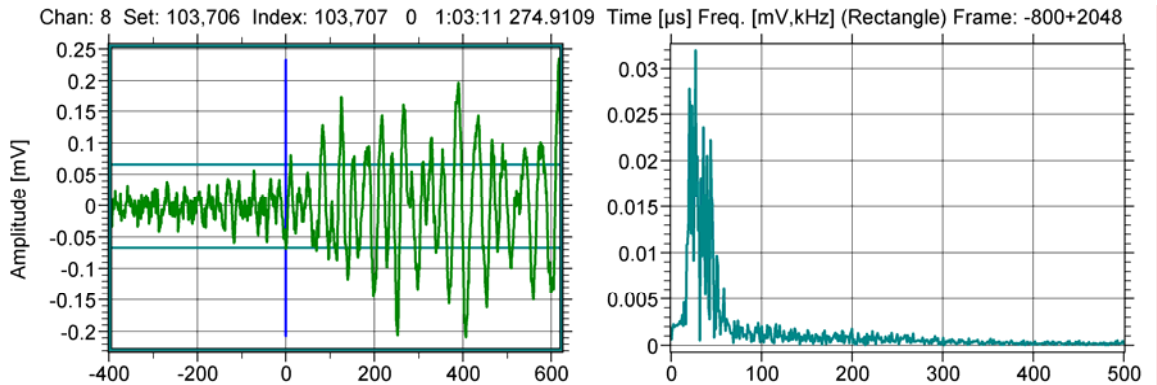


Figure 4.9: Example wave form likely caused by a secondary AE source

4.2.3.3 Wave Forms from Undesired Noise

An example of a wave form likely caused by the electrical circuit is shown in Figure 4.10. In this specific case, the sensor had a bad internal connection and many AE hits with often large amplitude were detected. They were characterized by a very short rise time, R , and a low energy value, E , relative to the measured amplitude, A . A new filter was developed that can filter out a significant number of these false AE events. It may be problematic if such AE hits are not filtered out when applying qualitative analysis procedures such as NDIS-2421 (see Section 4.3.2) or b -value analysis (see Section 4.3.4) because the data can become skewed and that can lead to misinterpretation.

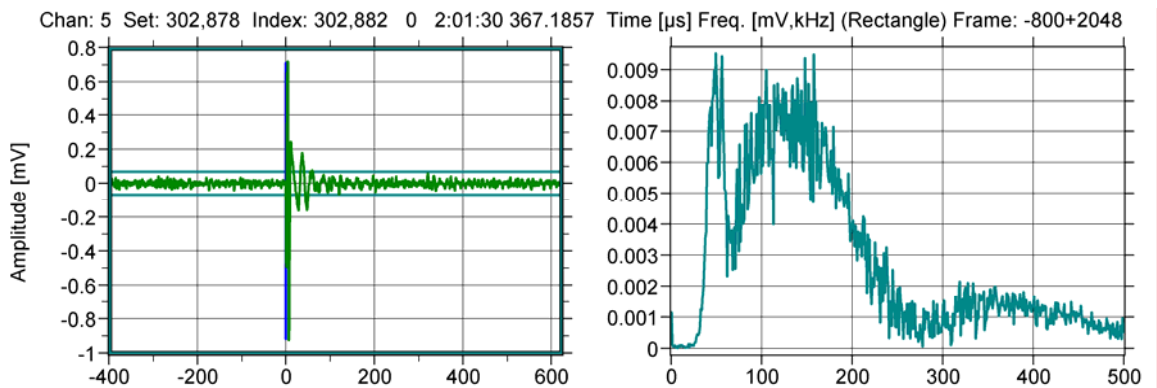


Figure 4.10: Example wave form likely caused by the electrical circuit

The discrimination of noise from primary and secondary sources of interest is important but not an easy task. Filtering of AE data can be achieved on different levels and may be based on:

- AE parameters, e.g. passing of AE hits with $A > 40$ dB, $CNTS > 5$, etc.
- Frequency characteristics, e.g. filter out signals with a flat response, i.e. electrical noise
- Event assembling, i.e. only AE signals that are recorded by a minimum number of sensors, e.g. three, within a given time window are included and designated as AE events

4.2.3.4 Filter to Discriminate Electrical Noise Based on Parameters

Figure 4.11 shows amplitude-energy correlation plots for data that was collected during the main experiment on AE Specimen #2.

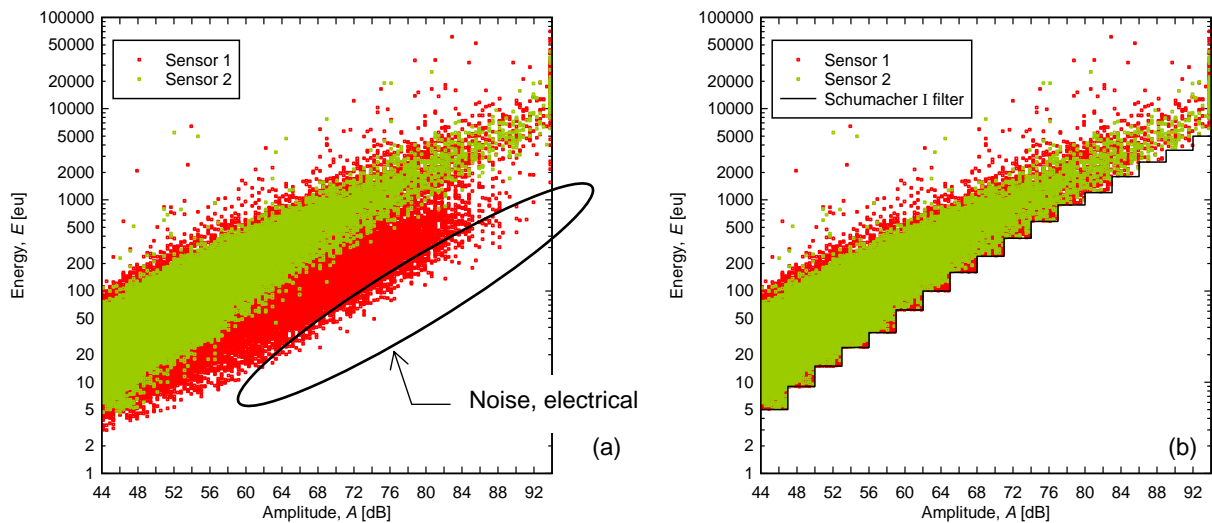


Figure 4.11: Example of filtering with the proposed filter: (a) unfiltered data, (b) filtered data

In Figure 4.11, the red and light green dots represent AE hits detected by sensor 1 and 2, respectively. Sensor 1 had increasingly become noisy towards the end of the tests and detected numerous false AE hits that turned out to be caused by an internal electrical contact that had become loose. The data for sensor 2 was assumed to be reliable and used as reference. The black line represents the proposed filter to exclude undesired noise from the data. The filter worked very well excluding a large number of false AE events such as the one shown in Figure 4.10. Fowler suggests using a so-called Swansong II filter to eliminate external emission from mechanical rubbing (Fowler 1989). For one of his experiments, this noise is visible in a signal duration-amplitude correlation plot. For the present experiments, this was not the case and that filter was therefore not applied.

4.2.3.5 Filtering based on Frequency Content of AE Signals

This method is not explored in the present study since the AE sensors that were used were all resonant sensors that have a significant influence on the recorded wave forms.

4.2.3.6 Natural Filtering by AE Event Assembling

If several sensors are used for AE monitoring, the most effective filter is to employ AE event assembling and perform analysis procedures on AE events rather than AE hits. Noise that occurs only at one sensor is omitted naturally by evaluating events. For sensor arrays where the sensors are spaced far apart, this may not be possible and filters based on AE parameters as presented earlier have to be deployed.

4.3 QUALITATIVE ANALYSIS

For qualitative AE data analysis, only a few key parameters, which are assumed to characteristically describe an AE signal wave form, are extracted and stored. Parameters can be processed and presented in real time and do not require large data storage space. A qualitative AE analysis does not take into account stress wave propagation or the influence of the data acquisition process chain and can be performed with even a single sensor. However, it can be problematic as one may not be able to distinguish between interesting signals and noise or artifacts from external sources since source locations and mechanisms are unidentified. In Table 4.6, the most commonly used parameters for qualitative AE analysis are summarized. Illustrations of these parameters can be found in Figure 4.12.

Table 4.6: Commonly used AE parameters for qualitative AE analysis

Parameter	Symbol	Unit	Description
Hits	<i>HITS</i>	[-]	Number of AE burst signals
Counts	<i>CNTS</i>	[-]	Number of threshold crossings within one discriminated burst signal
Amplitude	<i>A</i> , <i>ALIN</i>	[dB], [mV]	Amplitude of AE signal, relation between <i>A</i> and <i>ALIN</i> : $A = 20 \cdot \log_{10}(ALIN) + 60$,
			$ALIN = 10^{\left(\frac{A-60}{20}\right)}$
Energy	<i>E</i>	[eu] = [1e10 ⁻¹⁴ V ² s]	Signal strength, approximation
Rise time	<i>R</i>	[μs]	Time between 1 st threshold crossing and <i>A_{max}</i>
Duration	<i>D</i>	[μs]	Signal length/time between 1 st and last threshold crossing

Parameter	Symbol	Unit	Description
Threshold	THR	[dB]	Threshold at time of signal detection
Background noise level	RMS	[μV]	Background noise level at pre-amplifier input prior to a hit, calculated with the simplified equation: $RMS = \int_{t_a - t_{RMS}}^{t_a} A_i dt$

AE parameters, as shown in Table 4.6, are influenced by many factors (recall the data process chain, Section 4.1.1) including specimen geometry, variability of material properties, characteristics of AE sensors, amplifiers, and data acquisition system, as well as selection of acquisition parameters (threshold, rearm time, sampling rate, etc.) and must be treated with caution. Köppel showed a large influence from different threshold settings on the parameters as $CNTS$, D , and R (Köppel 2002).

Changing environmental conditions like crack formation and propagation or changing of AE sensor responses can influence AE parameters further and alter them over time. Nonetheless qualitative analysis has shown value and is widely used especially when the problem at hand is well identified and the sensor deployment is always the same.

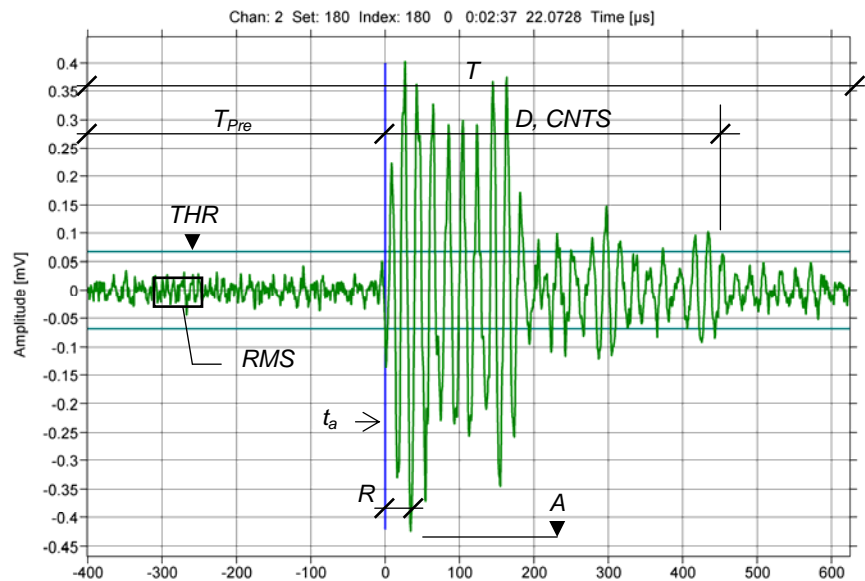


Figure 4.12: Example of an AE signal wave form with parameters

Presented in Figure 4.12 is a typical AE waveform recorded during testing and common qualitative parameters that are extracted from it. The pre-trigger time T_{pre} can be calculated as N_{pre}/f_s (see Table 4.4) and in this case was set as 400 μs . The total recorded length can be determined as N/f_s and in this case was 600 μs . The arrival time t_a and the peak amplitude A are shown for illustrative purpose.

4.3.1 Rate Process Analysis

The most basic way to analyze AE data is to sum parameters such as *HITS*, *CNTS*, or *E* and correlate them with physical measurements from the specimen such as stress, strain, displacements, rotations, etc. Ohtsu et al. (*Ohtsu 2004*) verified an exponential relationship between *N*, the cumulative number of an AE parameter, and the applied compressive stress σ for a concrete cylinder as follows:

$$N(\sigma) = C \cdot \sigma^a \cdot e^{b \cdot \sigma} \quad (4.6)$$

The variables *a*, *b*, and *c* were determined experimentally and it was shown that *a* correlated with the presence of pre-damage. Pre-damaged cores yielded a negative value while undamaged cores produced a positive value for *a*. This method appears to give good results for small specimens.

4.3.2 Historic-Severity Analysis

This analysis method was developed by Fowler et al. and is introduced in detail in (*Fowler 1989*). It consists of two different parameters: the Historic Index and the Severity Index. The Historic Index compares the signal energy, *S* (aka. MARSE = Measured area of the rectified signal envelope) of the most recent hits with the signal energy of all hits up to that point. The equation is:

$$H(t) = \frac{N}{N - K} \left(\frac{\sum_{i=K+1}^N S_{0i}}{\sum_{i=1}^N S_{0i}} \right) \quad (4.7)$$

Where *N* is the current number of hits, and *K* is defined by a table and depends on *N*. This parameter is implemented and can be computed in VisualAE (*Vallen 2003*). The Severity Index, *S_r*, computes the average of the largest signal strengths. The equation is:

$$S_r = \frac{1}{J} \sum_{m=1}^J S_{0m} \quad (4.8)$$

Where *J* is the number of hits over which the average should be computed.

Both indices are computed for each sensor independently. Commonly, a log-log scale chart is then deployed with the Severity Index on the *x*-axis and the Historic Index on the *y*-axis. Zones of different stages of damage are well established from the pressure vessel industry. This method appears to work well, when the loading is controllable and known. The method has recently been evaluated by several research groups for use of structural

in-service testing on bridges (Lovejoy 2006; Nair 2006; Golaski 2002). This method was not used in the present study.

4.3.3 Kaiser Effect and Felicity Ratio

The Kaiser Effect, named after its discoverer, Joseph Kaiser, states that AE signals are only detected when a previous stress level is exceeded (Kaiser 1950). This is true for metals but not for composite materials such as reinforced concrete. The breakdown of the Kaiser Effect is the so-called Felicity Ratio suggested by Fowler (Fowler 1989). It states that AE are produced before a previous stress level is exceeded. Based on these two phenomena, and the observation that the relationship of observed AE hit rates and crack mouth opening is linear, Ohtsu et al. developed a damage assessment criterion for reinforced concrete beams which is established in the recommended practice NDIS-2421 (Ohtsu 2002). Lovejoy tested a total of 31 full-scale bridge girders and showed nicely that the Kaiser Effect is not true for fatigued beams. He also showed that the Felicity Ratio on undamaged beams decreased with increasing loads (according to theory) whereas on fatigued beams it increased (Lovejoy 2006).

Figure 4.13 illustrates the different values that are needed to compute *Load* and *Calm Ratios* as described in NDIS-2421 which are defined as:

$$Load = \frac{P_{onset_AE_activity}}{P_{previous}} = \frac{P_{onset,5\%}}{P_{previous}} \quad (4.9)$$

$$Calm = \frac{\Sigma HITS_{unloading}}{\Sigma HITS_{loading}} = \frac{HITS_{UE} - HITS_{US}}{HITS_{LE} - HITS_{LS}} \quad (4.10)$$

In the equations, $P_{onset_AE_activity}$ is the load at the onset of AE activity in the subsequent loading, $P_{previous}$ the previous load, $\Sigma HITS_{unloading}$ the number of cumulative AE activity during the unloading process, and $\Sigma HITS_{loading}$ the total activity during the last loading cycle up to maximum. $P_{onset_AE_activity}$ was selected as suggested by (Lovejoy 2006) as the force when 5 % of the total cumulative AE hits in the loading phase (named $HITS_{LS,5\%}$) were reached. Also shown in Figure 4.13 are the different phases of one complete loading cycle: ‘1’ represents the unloading phase from a passing vehicle as described in 6.6.2, ‘2’ the loading phase, ‘3’ the holding phase where the load is kept constant and creep occurs, and ‘4’ the unloading phase back to dead load. The computation of cumulative AE hits can be done for each sensor or over all sensors together.

For the present study, *Load* and *Calm Ratios* were computed for sensor array A for the overload events (OL) as well as the simulated test trucks (TT) as defined in section 6.6.4 based on cumulative AE hits and are presented Section 7.

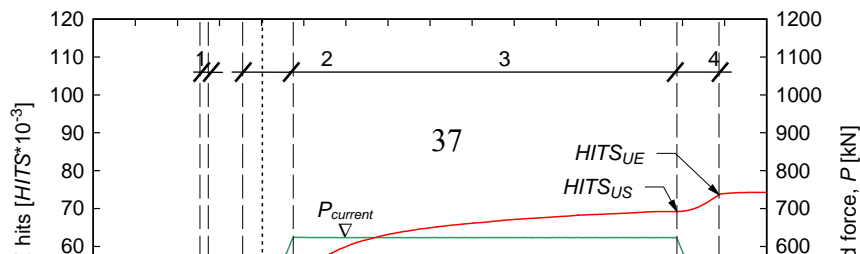


Figure 4.13: Example for evaluation of NDIS-2421 procedure

Figure 4.14 shows the two NDIS-2421 ratios as a function of the used threshold setting. For this example, the third overload from AE Specimen #1 was used. As can be observed, the *Load Ratio* increases and the *Calm Ratio* decreases with increasing threshold values. Critical ODOT ratios based on earlier OSU experiments are shown as defined by Lovejoy (2006). Different experiments should therefore only be compared if the employed thresholds are about the same. Also, there may be other parameters that are not investigated here that could have an influence on these two ratios as well.

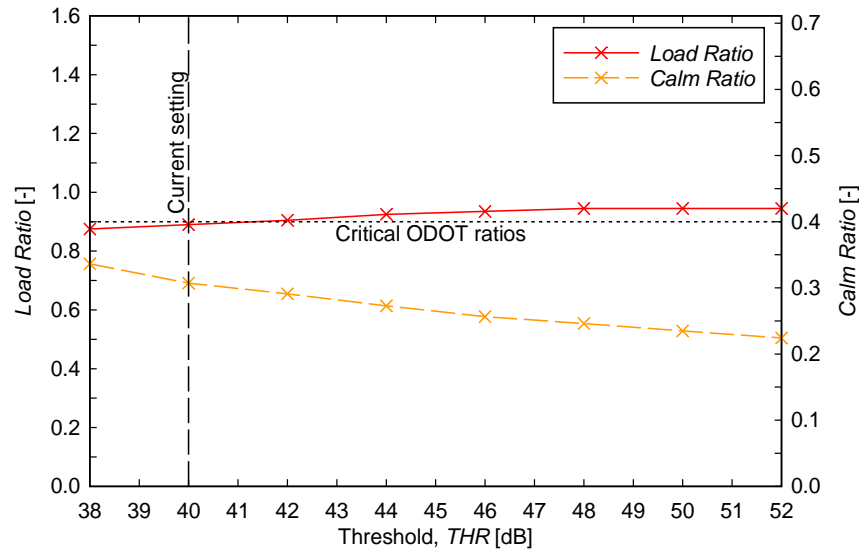


Figure 4.14: Example of Load and Calm Ratios for different threshold settings

4.3.4 Wave Form Analysis

A method somewhat in between qualitative and quantitative AE analysis is a wave form analysis where wave forms are stored and analyzed in addition to discrete parameters. The idea is to identify AE signal groups and distinguish between different AE sources as discussed in Table 4.3. Grosse et al. and Köppel used similarity analysis techniques from signal processing based on magnitude squared coherence functions to compare AE wave signals (*Grosse 1996; Köppel 2002*). The result of such a comparison can be expressed in a similarity value, defined as \hat{C} , with values between 0 and 1 where 1 represents a perfect match and 0 means that the signals are unrelated. Problematic for such an analysis could be the frequency dependent attenuation found in concrete as investigated in Section 5.1. This method was not applied or further investigated in the present study.

4.3.5 b-Value Analysis

A statistical way to look at AE parameter data is the so-called *b*-value analysis. The relationship was established by Gutenberg and Richter in 1949 (*Gutenberg 1949*) and has been used to characterize earthquake amplitude distributions as well as to analyze slope-stability in geotechnical and material science applications (*Rao 2005*). The magnitude-frequency distribution relationship is defined as:

$$\log_{10}(N) = a - b \cdot M_L \quad (4.11)$$

Where M_L is the magnitude of an event on the Richter scale, N is the number of events that lie within $M_L \pm \Delta M_L$. a and b are empirical constants, where b describes the slope of the magnitude-frequency diagram. The basic concept is that this b -value (the slope) drops significantly when stresses are redistributed and damage becomes more localized. In the field of reinforced concrete, b -value analysis has been used by several researchers to monitor structural deterioration (Colombo 2005; Kurz 2006; Shiotani 2000). Commonly in AE applications, the maximum hit amplitude in dB is multiplied by a factor of 1/20 and replaces the earthquake magnitude M_L . This yields b -values in the same range as seen in seismic applications. The b -value for each set of AE amplitude-frequency distributions was estimated with Matlab employing a linear curve-fit over the mean \pm one standard deviation as suggested by Rao et al. (Rao 2005). Standard errors are given as $S_E = b/\sqrt{n}$ where n is the number of samples (consecutive AE hit amplitudes) used. Suggested values for n are 50 to 100. Figure 4.15 visualizes what b -values represent: the slope of the cumulative frequency distribution of a set AE hit amplitudes. For this example, 100 consecutive AE hit amplitudes were selected from AE Specimen #2, Session 7 (see description in section 6). Figure (a) suggests that there is likely no damage occurring whereas Figure (b) with its low b -value suggests that there is likely localized damage occurring. The b -values shown are indicated by vertical lines in Figure 4.16.

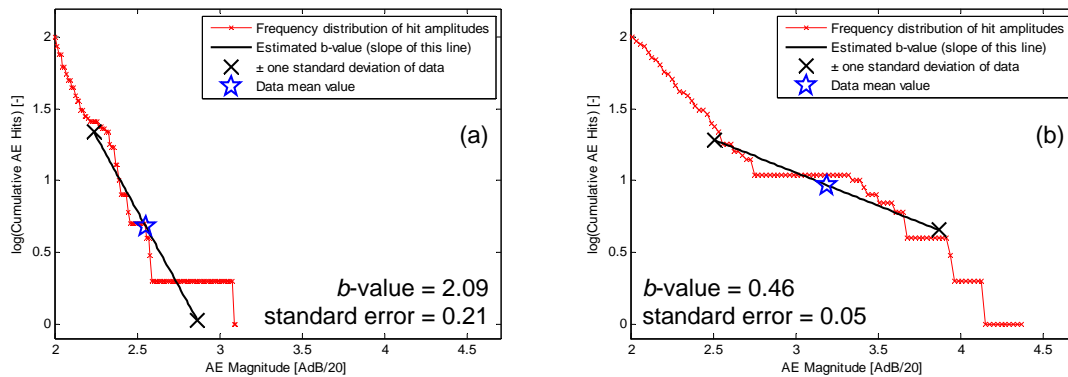


Figure 4.15: Examples of two discrete b -value for 100 consecutive AE hit amplitudes: Likely no on-going damage, (b) likely on-going damage

b -Value analysis appears especially well suited for implementation in a structural health monitoring system since it is computationally inexpensive and, theoretically, only one sensor is needed. Shown in Figure 4.16 is an example of continuous b -value evaluation. In (a) estimated b -values computed over a set of 100 AE hit amplitudes are shown and (b) illustrates the total applied force. In this case, a new overload was applied to the specimen, i.e. a force that the specimen had not experienced before. No new cracks formed in this case, but existing ones further propagated. As anticipated, the b -value drops well below 1 (full line), even below 0.5 (dashed line) when this new load level is reached, suggesting that localized damage is occurring, e.g. cracks are forming or growing. The example was taken from AE Specimen #2, Session 7 with AE hit amplitude data from sensor 4, which was located on top of the web about 1.10 m (43 in.) away from the edge of the left bearing plate (which corresponds to the column face in case of a real

bridge). It was observed that b -value time histories differed from sensor to sensor. This is most likely caused by the different sensor locations which affect the AE hit amplitude data and therefore the b -values as well, i.e. b -values are a function of the sensor location with respect to the damage source. It is therefore probably not meaningful to define an absolute critical b -value.

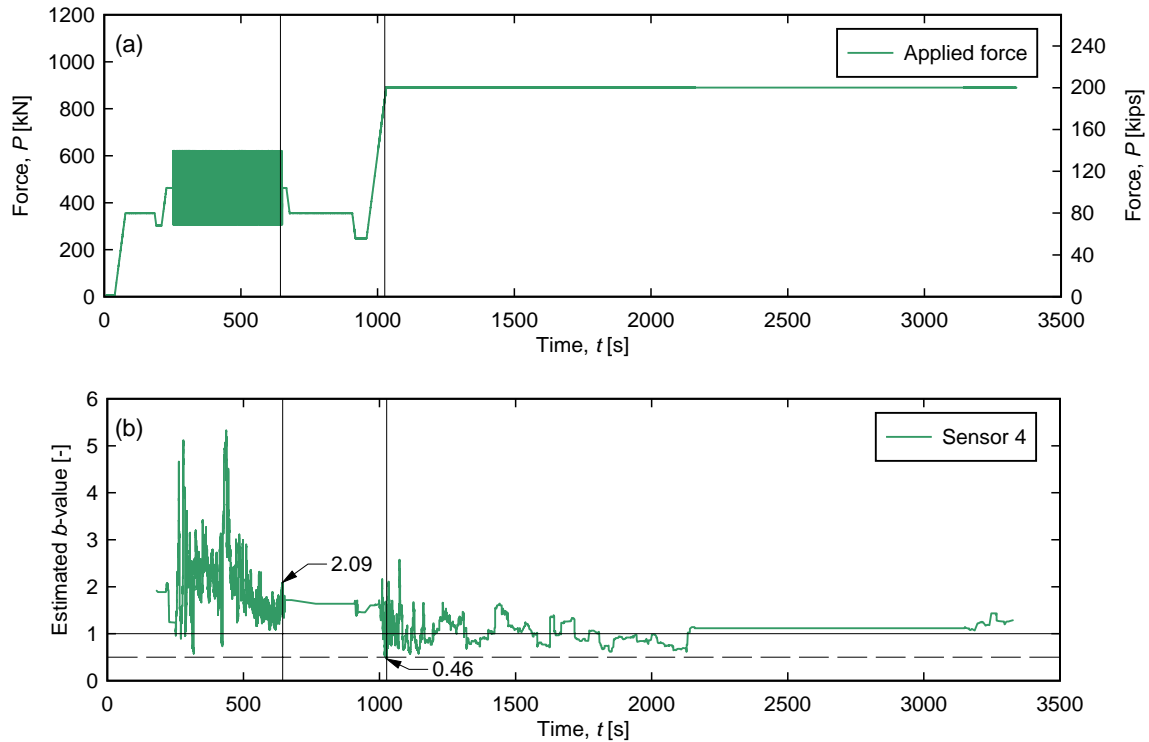


Figure 4.16: Example of continuous b -value monitoring for one AE sensor

A new method to evaluate the impact a passing vehicle has on a monitored bridge component shall be proposed next. As explained earlier, the b -value may indicate the localization of damage, i.e. crack formation and propagation. This may be used in conjunction with applied load cycles, i.e. passing vehicles (ambient or test trucks) to estimate the demand level the bridge is currently operated at. Figure 4.17 shows two examples of applied forcing in the laboratory. In this case, sensor array A was used. b -values are shown as colored lines. The averaged minimum b -value (over 50 AE amplitudes) from one complete loading cycle was computed from all eight sensors. For other sensor arrays, where the sensors are not spaced closely around the volume of interest, the minimum b -value may be computed for each sensor separately, using the standard error as means of uncertainty. For the example below the averaged minimum b -values (and standard deviation) were 0.553 (0.058) and 1.33 (0.307) for the overload and the simulated test truck, respectively. This proposed *minimum b -value analysis* is presented in detail for sensor array A in Section 7.

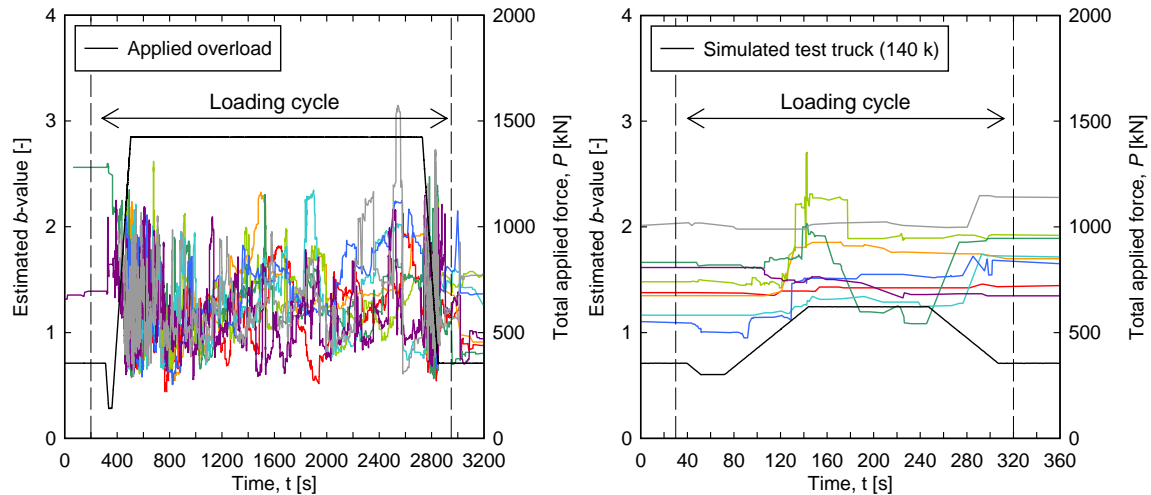


Figure 4.17: Example for evaluation of the proposed *minimum b-value method*

The biggest challenge with the b -value analysis is the discrimination of noise since it is usually performed for each sensor independently. Recall from section 4.2.3 that b -values are sensitive to noise which sometimes can create false AE hits with large amplitudes. Also, maximum AE hit amplitudes are utilized which are often clipped due to channel saturation. The following improvements could be considered in future work:

- Use of p -wave amplitudes rather than maximum signal amplitudes, i.e. no clipped data
- Scaling of p -wave amplitudes according to the signal travel length, i.e. better estimate of strength at the AE source
- Employment of filters

4.4 QUANTITATIVE ANALYSIS

The goal of quantitative AE analysis is to enumerate and explain the source of an AE event. An AE event is defined as the *physical phenomenon giving rise to acoustic emission (EN 2000)*. The principle is that AE burst signals within a given time window are detected by more than one sensor and grouped to an AE event that can be associated with an AE source. Different quantitative methods can then be applied to characterize the source.

A proper source location of AE events is the first important step in quantitative AE analysis. Many approaches exist, ranging from simple zonal methods to sophisticated iterative pin-point hypocenter source location algorithms. Most of the procedures were initially developed for seismic applications and later adopted for use in the field of AE

research. In AE, the first arrival time approach is commonly used where only the information of the first wave mode (or *p*-wave) arrival is taken into account.

4.5 AE SOURCE LOCATION

Common source location techniques and their mathematical background are nicely summarized in Ge's papers (*Ge 2003; Ge 2003*). To estimate pin-point AE hypocenter locations, which is the most commonly used approach for reinforced concrete structures; the following general steps are taken:

1. Group AE burst signals from an AE event (event assembling with time window)
2. Estimate *p*-wave arrival time (time picking)
3. Execute source location scheme (iterative, numerically)
4. Visualize result with estimated mean source location and error estimates

4.5.1 Components of AE Source Location

4.5.1.1 Event Assembling

In a first step, AE burst signals have to be grouped to an AE event. The Vallen parameters which determine the assemblage are *FHCDT* (first-hit channel discrimination time), *DTIX-Max* (maximum allowed Δt between first and last hit within an AE event), and *DTNX-Max* (maximum allowed Δt between two hits). These should be selected according to the geometry of the sensor array. The following values are recommended for use where d_{max} is the maximum distance between two sensors and c_p the *p*-wave velocity:

$$FHCDT = DTIX - Max = DTNX - Max = \frac{1.25 \cdot d_{max}}{c_p} \quad (4.12)$$

4.5.1.2 Arrival Time Picking

Accurate and consistent determination of the arrival time t_a of the p -wave is the second step and crucial for precise AE source location. For example, it takes the p -wave only about 6 μ s to travel a distance of 25 mm (1 in.). In general, only the arrival of the first wave mode (p -wave) is used since the s -wave and R -wave modes are much harder to detect. The list of possible methods for p -wave arrival detection is quite long and ranges from using a simple fixed threshold crossing to advanced energy based methods. For most of the present experiments, a dynamic threshold crossing THR_{η} was used. Threshold to noise ratios Cr , (sometimes called *Crescent Factor*) were determined experimentally for each sensor type. It is important to choose THR_{η} carefully because it cannot be altered in VisualAE once the transient AE data are recorded. Recommended and used values for most of the OSU experiments are presented in section 4.2.2.

Köppel and Schechinger both investigated some available time picking methods for precision and reliability, important from a standpoint of automation (Köppel 2002; Schechinger 2006). A new algorithm recently implemented by Kurz demonstrated excellent performance (Kurz 2006). It is based on the so-called Akaike Information Criterion (AIC). The AIC function value at a time t is defined as:

$$AIC(t) = t \cdot \log_e \left\{ \text{var} \left[U(1:t) \right] \right\} + (T - t - 1) \cdot \log_e \left\{ \text{var} \left[U(1+t:T) \right] \right\} \quad (4.13)$$

Where t is the sample time and varies from 1 to T , where T is the total length of time for the signal and U the AE signal amplitude. Basically, this is the sum of two signal amplitude variances taken over two windows one spanning from $t = 1$ to t the other from $t = t$ to T , each one weighed (i.e. multiplied) by the corresponding window length. The function is evaluated for every t over the length of the signal and the absolute minimum denotes the estimated p -wave arrival time. Typically, the AIC function is not evaluated over the whole recorded length of the waveform. For the present experiments, a window with a length that was half the length of the pre-trigger window T_{pre} was centered over the first p -wave arrival pick determined by the fixed or dynamic threshold for computation of $AIC(t)$.

This criterion was implemented in Matlab and applied to available wave forms to compute a correction time Δt for the arrival times picked based on the dynamic threshold criterion. Unfortunately, full transient AE wave forms are not always available for all sensors of a grouped AE event when the data acquisition system buffer is full. In that case, the AI Criterion cannot be applied and the source location has to be estimated with the arrival times picked by the dynamic threshold method.

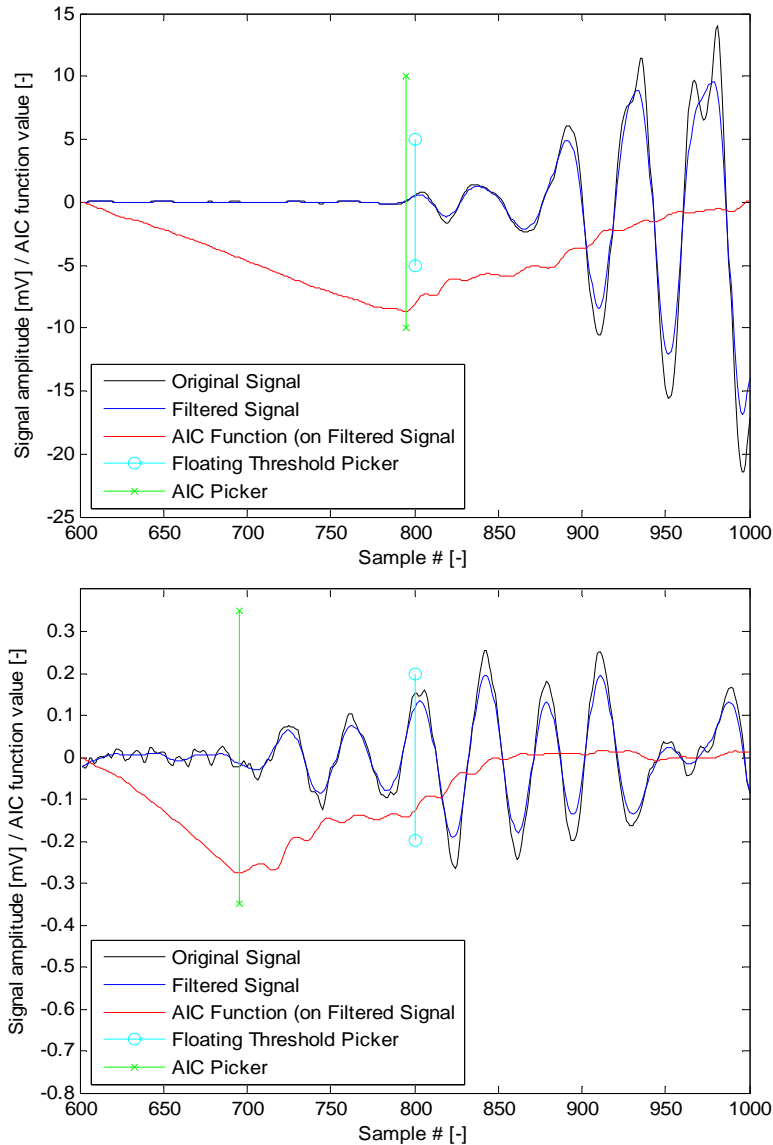


Figure 4.18: Examples of p-wave arrival estimates for two picking methods for signals with high (a) and low (b) signal-to-noise ratio

Figure 4.18 illustrates *p*-wave arrival time picking with this method and offers a comparison with dynamic threshold picking. For an AE signal with a high signal-to-noise ratio as the example shown in Figure 4.18 (a), the difference between the two picking methods is minor. In this case, the time arrival difference is only 2.5 μs , which is still accurate for large specimens. However, for AE waveforms with a low signal-to-noise ratio as the one shown in Figure 4.18 (b), the difference is 52.5 μs which will introduce significant error in the source location result. For both signals, the AIC picking criterion matches well with what would be picked manually. Both signals were smoothed using a zero-lag moving average filter over $2 \times 10 = 20$ amplitude values.

4.5.1.3 Estimation of AE Source Locations

The third step is the execution of a scheme to estimate the source location. Depending on the problem, 1-D (linear), 2-D (planar), or 3-D (solid) source locations can be performed. In AE, normally an approach that uses travel time differences is applied where $n+1$ arrival times are needed to determine a location in an n -dimensional space.

Geiger first suggested the use of the method based on first wave arrival times for the location of earthquake epicenters in 1910 (*Geiger 1910*). It was later adapted by other researchers for the location of AE hypocenters. A summary of this and other popular localization methods in the field of AE can be found in Ge's papers (*Ge 2003; Ge 2003*). For the application in reinforced concrete, it is usually assumed that the material is elastic and homogeneous. In reality reinforced concrete is a composite material with inhomogeneities such as differently sized aggregates, microcracks, voids, and reinforcement bars that cause damping and dispersion of the stress waves as discussed in section 2.2.2. However, many authors have shown that it is justifiable to approximate reinforced concrete as an elastic homogeneous material. Schechinger for example, showed this with her numerical simulations (*Schechinger 2006*). Typically, the stress wave travel path is assumed as a straight line between source and sensor and the velocity of the p -wave as constant with c_p . For the arrival time $t_{a,i}$ at sensor i , the following relationship can be derived:

$$f(x_0, y_0, z_0, t_0) = t_{a,i} = t_0 + \frac{\sqrt{(x_i - x_0)^2 + (y_i - y_0)^2 + (z_i - z_0)^2}}{c_{p,i}} \quad (4.14)$$

Where t_0 is the source time and x_0, y_0 , and z_0 are the AE source coordinates. The coordinates of sensor i are denoted with x_i, y_i , and z_i . This function is often referred to as the arrival time function. For a 3-D problem with the four unknowns x_0, y_0, z_0 , and t_0 , arrival times from at least four sensors must be detected. This inverse non-linear problem can be solved with an iterative algorithm that uses the least-squares solution based on the first-order Taylor Series expansion of the arrival time function. For each iteration step, theoretical arrival times are calculated based on the previous iteration. These are then compared with the observed arrival times to calculate the residual r . The first set is calculated with initial trial location parameters, the following sets with previous source location parameters updated by a correction term δ_x , where δ_x is determined by using the least-squares method. The procedure is discontinued when the event residual s does not significantly change at the next iteration step. The general idea of this source location method is implemented in Vallen's VisualAE and was also directly implemented in a Matlab scheme.

4.5.1.4 Error Estimation with Vallen's VisualAE

If signals from five or more sensors are included, the location uncertainty $LUCY$ can be computed by Vallen's VisualAE. This was used as a quality criterion for AE source location estimations. $LUCY$ represents the root-mean-square of the residuals and is computed as follows:

$$LUCY = \left(\frac{1}{n-1} \right) \cdot \sqrt{\sum (\Delta t_i \cdot c_p - (s_i - s_1))^2} \quad (4.15)$$

Where n is the number of sensors and the distance of the sensor i to the calculated source position s_i . The arrival time difference between sensor i and the first-hit sensor is Δt_i and the speed of the compression wave c_p .

Three quality levels were defined depending on the minimum dimension of the test specimen. In this case this was the web thickness which was 356 mm (14 in.). The following accuracy levels were used for all source location estimations with VisualAE:

- Level 1: $LUCY \leq 36$ mm (0.7 in. = 5 % of web thickness) red '■'
- Level 2: 18 mm (0.7 in.) $< LUCY \leq 36$ mm (1.4 in. = 10 %) yellow '▼'
- Level 3: 36 mm (1.4 in.) $< LUCY \leq 71$ mm (2.8 in. = 20 %) blue '◆'

Spatial clustering of AE events (localization) was computed for a certain number of events that lay within a sphere with a diameter of 71 mm (2.8 in.). The color represents the number of AE events within that circle and is listed in the legend on the right side of the location plots.

Location estimations with only four sensors, which is the minimum number required to define a 3-D location, were not computed because they cannot be evaluated with $LUCY$, their reliability is thus undeterminable.

4.5.1.5 Error Estimation with the Matlab Scheme

If more than four arrival times are available, the system of equations is over-determined and the covariance matrix can be determined from the least-squares solution. The standard deviations in the principal directions σ_1 , σ_2 , and σ_3 can then be obtained by simply solving for the Eigenvalues and Eigenvectors. The obtained standard deviations are a measure of inconsistency in the measured arrival times and not the absolute error associated with a certain location result. For example, systematically delayed arrival times would remain unrevealed.

In order to compare with VisualAE results and to study model and parameter uncertainties, an AE source location scheme was implemented in Matlab. Mean AE hypocenter locations are estimated based Geiger's method and standard

deviations of the least-squares solution are computed. Figure 4.19 shows an example of the output of an AE source location result with this scheme. The estimated AE source location is shown as a ‘★’. First, second, and third principal standard deviations are illustrated with red, blue, and green rays, respectively. The location iteration path is illustrated by a ‘-*-’ line. The iteration is initiated at the mean location of all sensor coordinates.

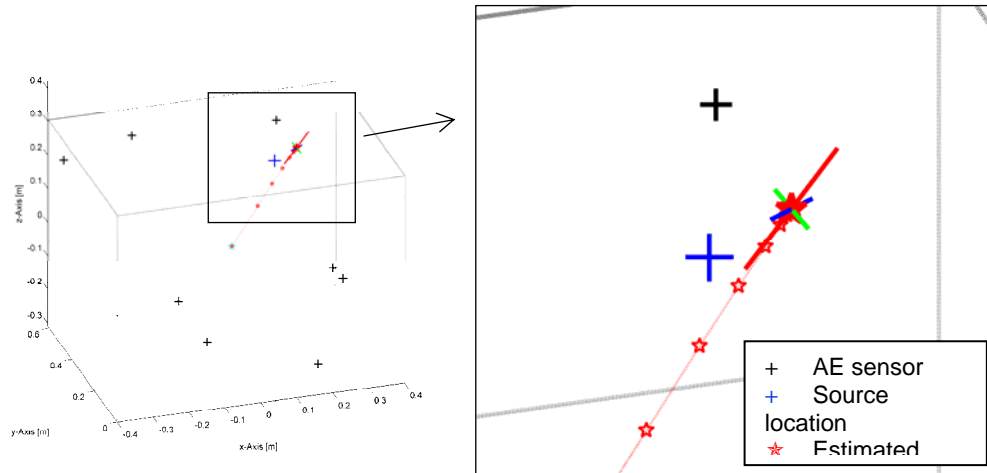


Figure 4.19: Example of a source location result (own scheme)

Vallen’s VisualAE calculates the parameter *LUCY* (Location uncertainty) based on root-mean-square solution for each result that includes more than the required number of signals. This value describes how well a calculated source position compares with the measured arrival time differences (Rao 2005). However, it is not a representation of the absolute error or mis-location and does not contain any directional information.

4.5.1.6 Further Considerations

Köppel showed that AE source locations outside of the sensor array are sensitive to small errors and that not only the accuracy of the *p*-wave detection but also the location of the AE source relative to the sensor array has an influence on the precision of a result (Köppel 2002). To investigate the uncertainties associated with 3-D AE source locations, Monte Carlo simulations were performed using the developed Matlab scheme. The effect of uncertainties such as arrival time picking errors or variation in the *p*-wave velocity due to material inhomogeneities can be studied separately or together. This is the first step towards a probabilistic source location algorithm as developed for earthquake location by Lomax (Schechinger 2006). The simulations were performed for sensor array A of AE Specimen #2 and further discussion can be found in Section 4.5.4.

4.5.2 Used Location Algorithms

4.5.2.1 VisualAE (Vallen software package)

For the main experiments reported here, AE source locations were estimated using a dynamic threshold picker with the embedded 3-D (solid) location software from VisualAE. This can be implemented very easily in real-time so that results become available immediately.

4.5.2.2 Matlab Scheme

Selected data sets were also analyzed with a source location scheme implemented in Matlab for comparison with the VisualAE results. The following steps are necessary for implementation of the source location scheme with Matlab:

1. Define AE event assembling criteria (see Section 4.5.1), copy in Excel spread sheet.
2. Make transient (*.TRA) file with selected events from spread sheet using the Vallen program TR-Copy.
3. Run program w2w.exe to convert transient files from the original Vallen format (*.TRA) into the PolarAE format (*.V01).
4. Use program All2SDF to filter and convert transient files in PolarAE format (*.V01) into Matlab-readable ASCII format (*.TXT), a high-pass filter with a lower cut-off frequency of 40 kHz should be applied to equalize all signals.
5. Pick *p*-wave arrival times with the AIC picker to update arrival times in Excel spread sheet.
6. Run Matlab source location scheme based on updated arrival times.
7. Overlay AE source location results on photo/sketch of specimen using Photoshop.

The whole scheme requires several separate steps that could be automated in future work but it is already effective with this current approach.

4.5.3 Determination of p-Wave Velocities

Before AE sources can be located, average p -wave velocities have to be determined. This can be done based on the following simple approach:

$$c_p = \frac{s_j - s_i}{t_{a,j} - t_{a,i}} = \frac{\Delta s}{\Delta t} \quad (4.16)$$

Where s_i and s_j are the distances between source and sensors, and $t_{a,i}$ and $t_{a,i}$ the p -wave arrival times at the sensors. All possible combinations of sensors were used to cover the entire sensor array. All arrival times were determined manually from the stored wave forms. For AE Specimen #1, the Vallen SE150-M sensors were used as pulsars. A regression analysis over 43 data pairs yielded an average p -wave speed of 3.79 m/ms (149 in./ms) and a standard deviation of 0.04 m/ms (3.15 in./ms). The average p -wave speed for AE Specimen #2 was resolved using pencil lead breaks (PLB) employing the KRNi060 sensors. The average p -wave speed found from 38 data pairs was 3.65 m/ms (144 in./ms) with a standard deviation of 0.04 m/ms (3.22 in./ms). These velocities were used for all source location estimations.

Figure 4.20 illustrates the correlation between compression wave speeds and average concrete compressive strength for the OSU experiments as well as some other experiments from the literature (*Grosse 1996; Köppel 2002; Schumacher 2006*). A square root type curve-fit applied to a selection of average p -wave velocities produced a correlation coefficient of 0.992.

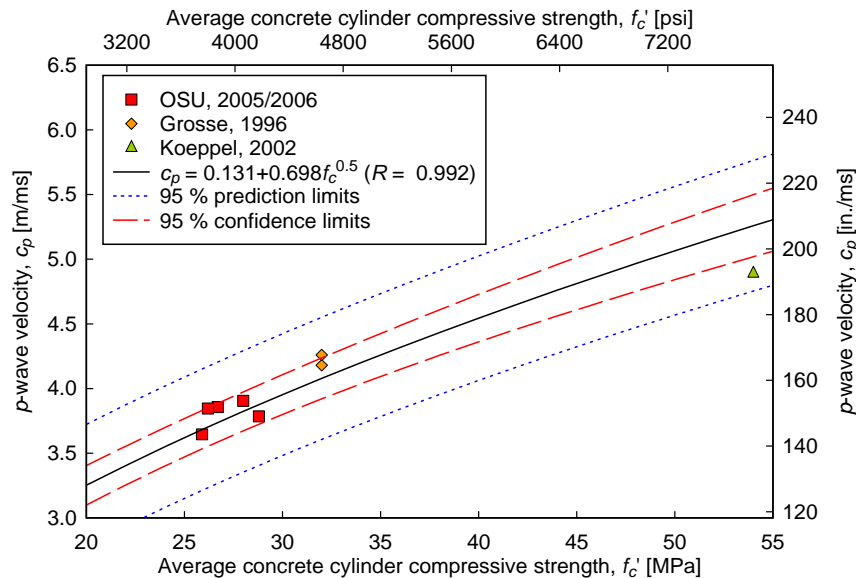


Figure 4.20: p -wave speed vs. concrete strength

4.5.4 Evaluation of Location Uncertainties

Uncertainties are always present and it is important to know which are significant and which can be neglected. Generally, the specimen is assumed to be elastic, isotropic, and homogeneous. But the embedded reinforcement steel, for example, has very different wave propagation properties than the bulk concrete. This would require a non-uniform velocity model which is not easy to implement. Furthermore, numerical simulation of wave propagation has shown that typical reinforcement bar diameters don't change the propagation properties significantly (*Schechinger 2006*).

4.5.4.1 Monte Carlo Simulation

A superior way to visualize uncertainties and errors is by using Monte Carlo Simulation (MCS). Any model or distribution parameter can be assumed as random variable and assigned a probability density function (PDF). In Table 4.7, some of the important parameters are listed and distribution models specified. The three most important uncertainties were assigned PDFs. For the sensor location, a uniform distribution was assigned assuming that AE sensor locations can be determined with an accuracy of 5 mm. The p -wave velocity was modeled according to section 4.5.3 assuming normal distribution. A gamma distribution was fitted manually to a histogram of the correction times determined to compute the p -wave velocities to model arrival time picking errors. A cap value for these arrival time errors was set to 12 μ s to avoid convergence problems. The other uncertainties were assumed to be insignificant and not taken into account. Note that once severe cracks form, travel paths can become longer which will introduce another significant error. This case was not considered here.

Table 4.7: Model parameters and associated uncertainties

Parameter	Comment, influence	Assigned Distribution
Sensor locations, \underline{x}	Measurement errors, inexact placement	$U(a, b)$
p -Wave velocity, c_p	May be non-uniform due to aggregates and steel	$N(\mu, \sigma)$
Travel path along, d	May deviate from straight line due to cracks, etc.	-
Arrival time error, Δt_a	Bad signal to noise ratio, incident angle, distance	$\text{Gam}(k, \lambda)$
Location algorithm	Linearized least-squares solution method	-
Sensor array geometry	Accuracy less for sources outside array	-
Sensor characteristics	Aperture size, resonant behavior	-

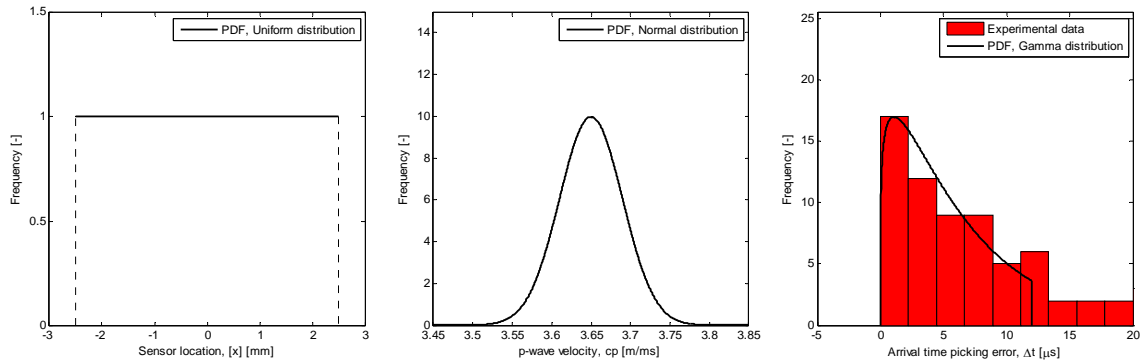


Figure 4.21: Parameter uncertainties with assumed distribution functions

In Figure 4.21, PDFs for the three modeled uncertainties from Table 4.7 are illustrated.

Especially the arrival time errors could be reduced by using a different picking method. However, this is not possible when working with VisualAE. Therefore, for the present simulations a set of picking errors was determined manually from AE wave forms from pencil lead breaks where a dynamic threshold was utilized.

A total of 1000 realizations were run for each location using Matlab with the AE source location scheme implemented for this project. Sensor Array A of AE Specimen #2 was modeled using all eight sensors for each simulation result. Each parameter was assumed as statistically independent for simplicity. Figure 4.22 shows an example of the output for one AE source location. The known source location is denoted with a blue '+', the sensor location with a black '+', red dots represent realizations for one set of random parameters, and the black '★' is the average location of all realizations.

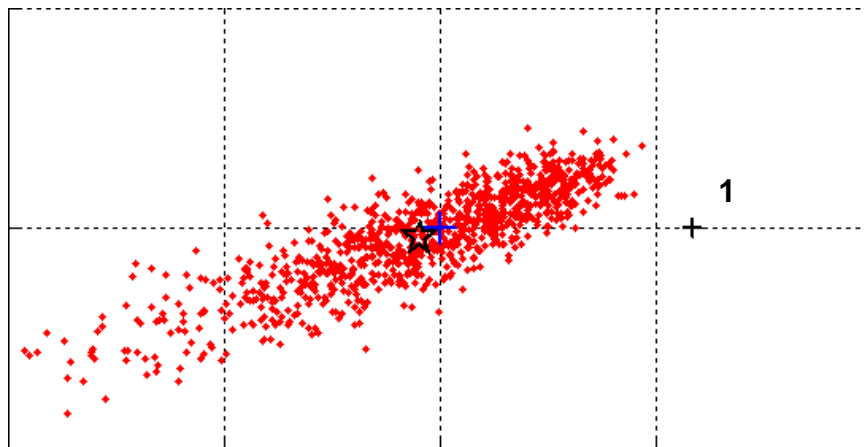


Figure 4.22: Example of the PDF solution of one AE source location

The following parameters were treated as random variables and sampled using Matlab's random number generator with the corresponding distribution function:

1. Sensor locations; x -, y -, z -coordinates $U(a, b) = U(x_i - 2.5 \text{ mm}, x_i + 2.5 \text{ mm})$
2. p -wave velocity $N(\mu, \sigma) = N(3.65 \text{ m/ms}, 0.04 \text{ m/ms})$
3. Arrival time error (dynamic threshold) $LN(\lambda, \zeta) = \text{Gam}(1.2 \mu\text{s}, 5.4 \mu\text{s}) \leq 12 \mu\text{s}$

At first, each parameter was randomized and plotted independently. In a second step, all parameters were sampled at the same time and plotted together. For AE Specimen #2, all AE sensors were placed at or above the center line of the girder ($y = 0$) which is shown in Figure 4.23. The sensors coordinates can be found appendix B, Table B2.1. Source locations were assigned to the intersection points of the existing orthogonal 305 x 305 mm (12 x 12 in.) grid on the specimen (red chalk lines) at the center line ($z = 0$).

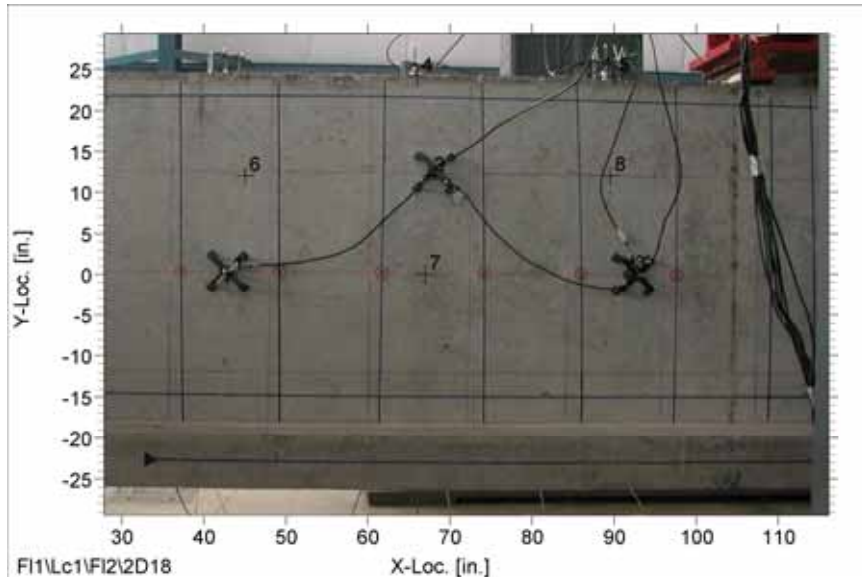


Figure 4.23: East face of AE Specimen #2 with installed sensors.

Figures 4.24, 4.25, and 4.26 show the simulation results for parameter 1 (sensor location), parameter 2 (wave speed), and parameter 3 (time arrivals), respectively. Figure 4.27 illustrates the simulation output if all parameters are kept random at the same time which is what happens in reality. These simulations give a nice qualitative view on the sensitivity of each parameter and the effect on the result.

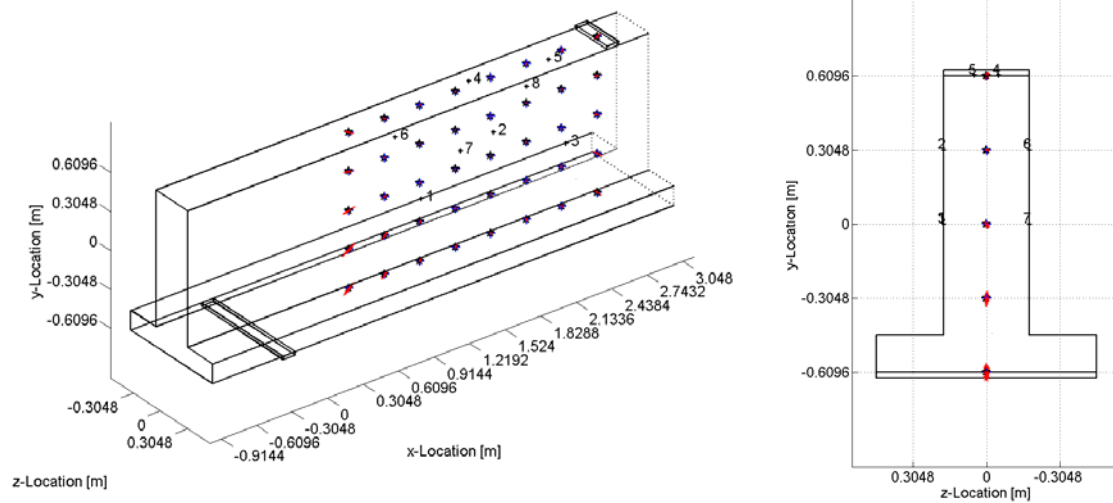
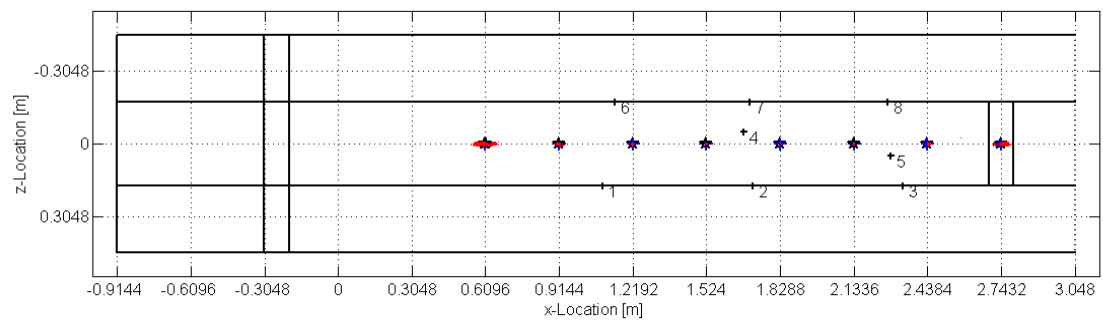
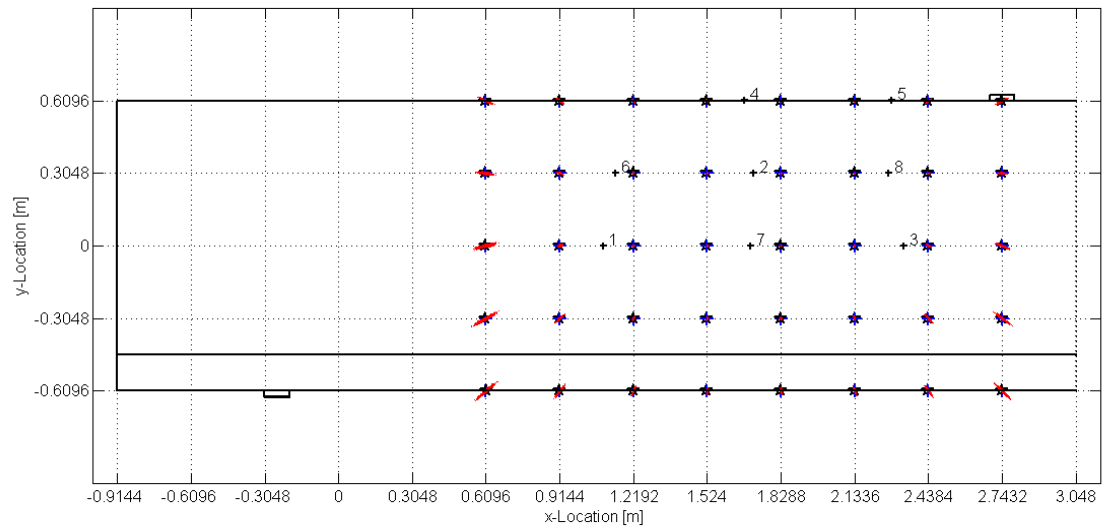


Figure 4.24: Simulation of parameter 1 (sensor locations) at the center line ($z = 0$)

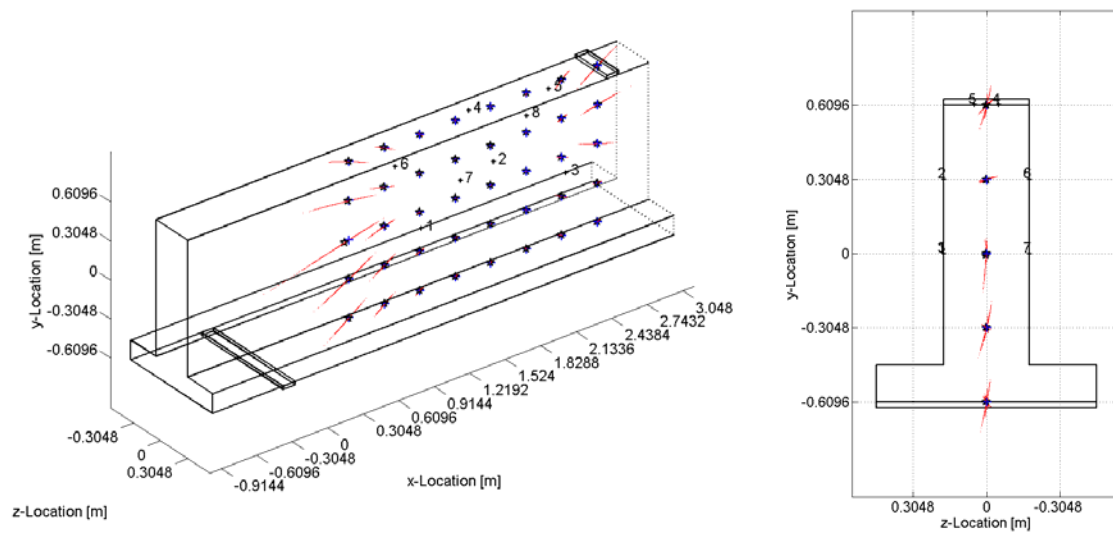
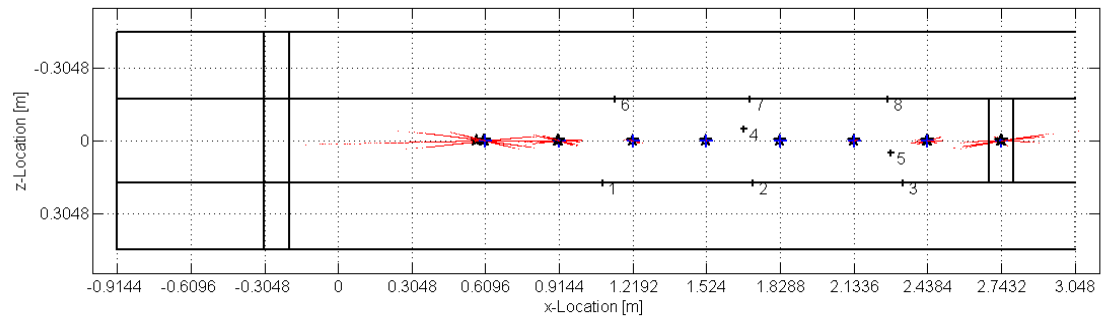
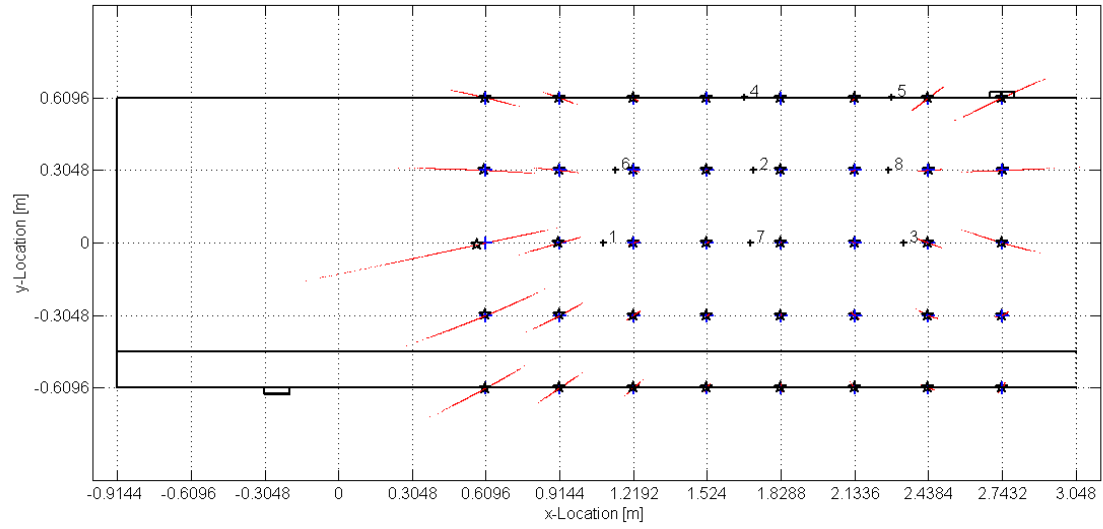


Figure 4.25: Simulation of parameter 2 (wave speed) at the center line ($z = 0$)

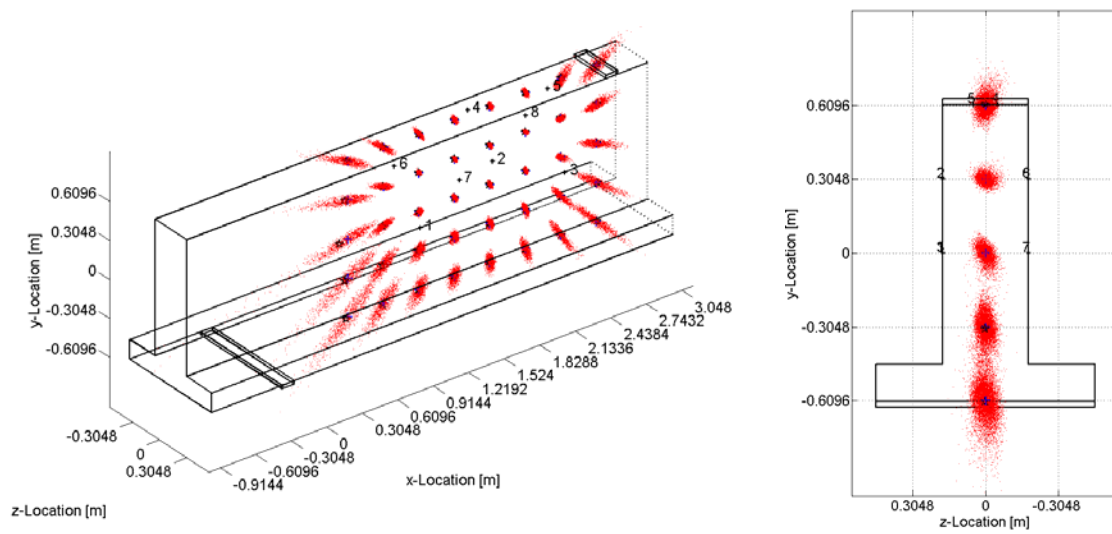
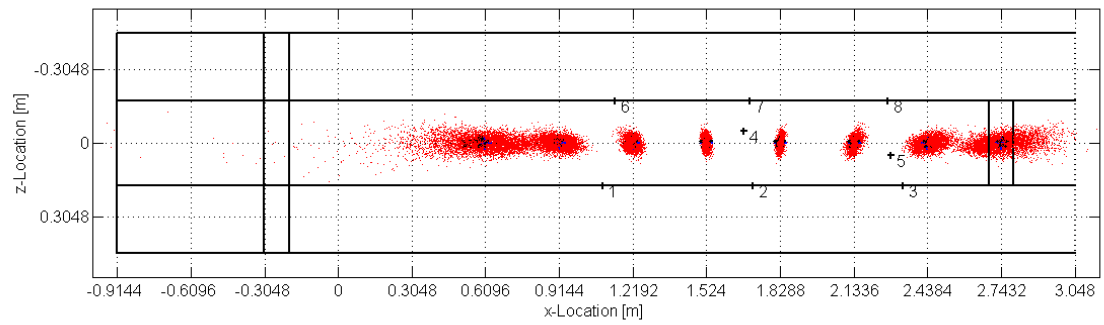
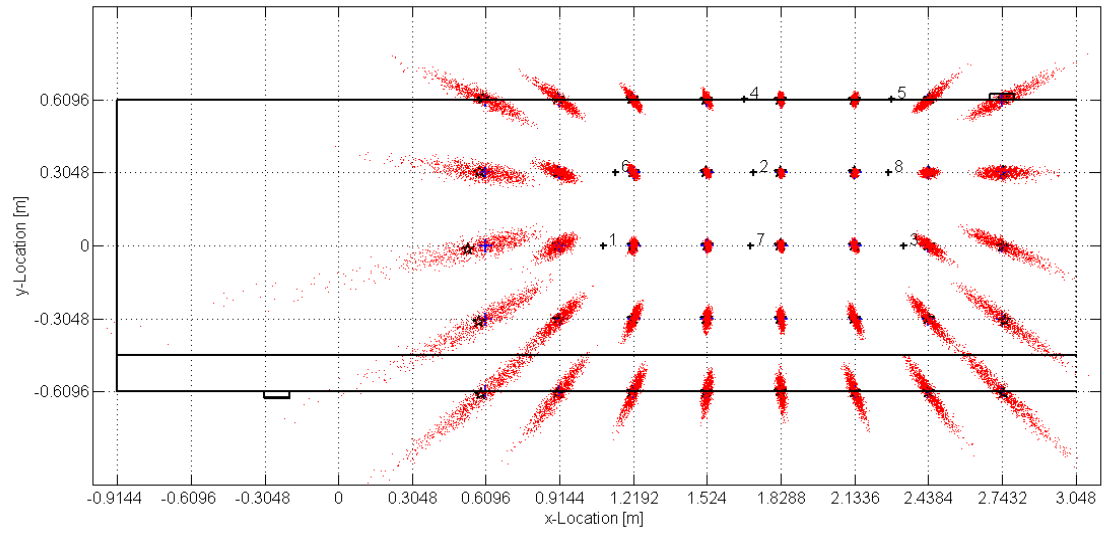


Figure 4.26: Simulation of parameter 3 (time arrivals) at the center line ($z = 0$)

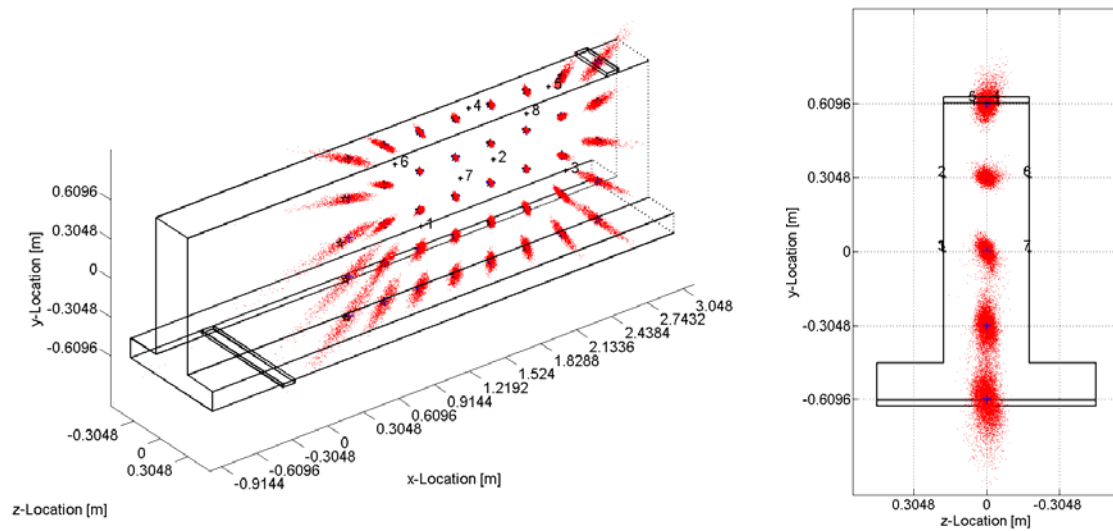
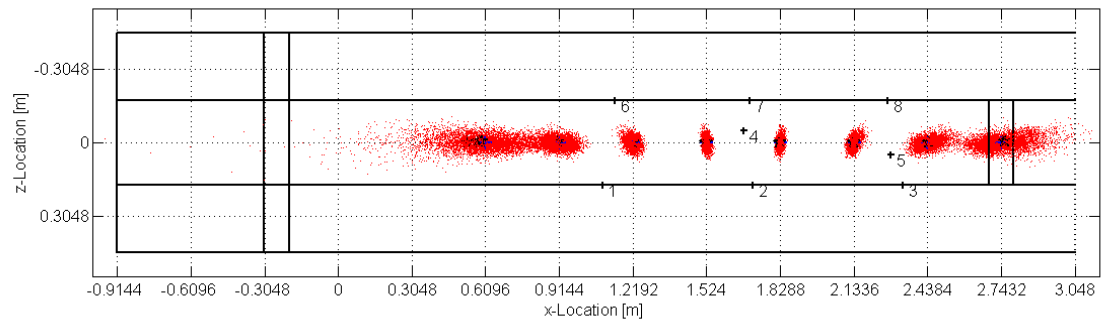
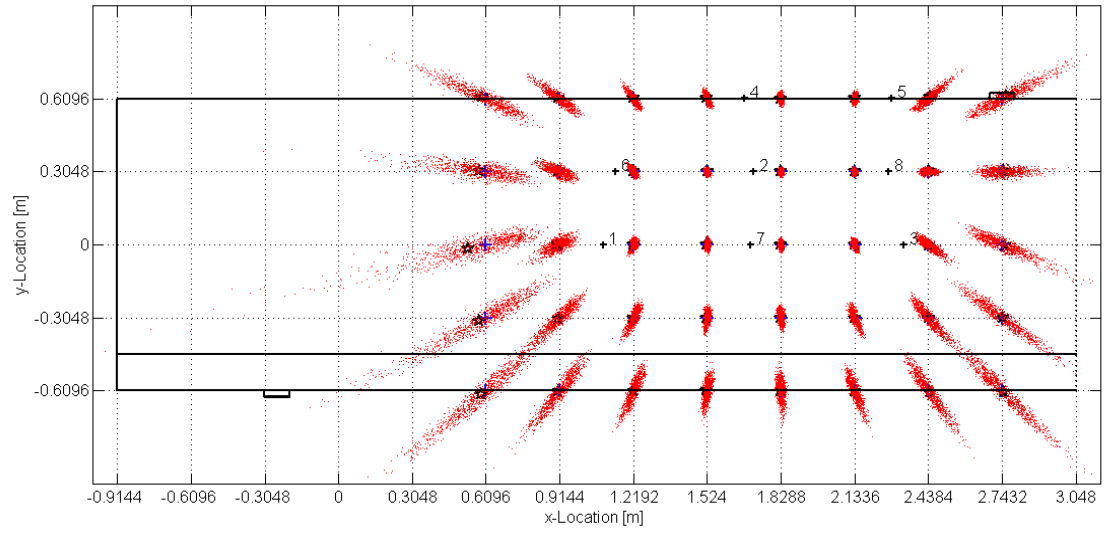


Figure 4.27: Simulation of all parameters simultaneously at the center line ($z = 0$)

4.5.4.2 Comparison with Artificial Sources of Known Location

A practical way to evaluate source location reliability is to perform pencil lead breaks (PLB) on the surface. This was done for AE Specimen #2 in un-cracked condition (before the test). Five individual PLB were performed each on a 152 x 152 mm (6 x 6 in.) grid on the west face of the specimen at $z = 178$ mm (7 in.).

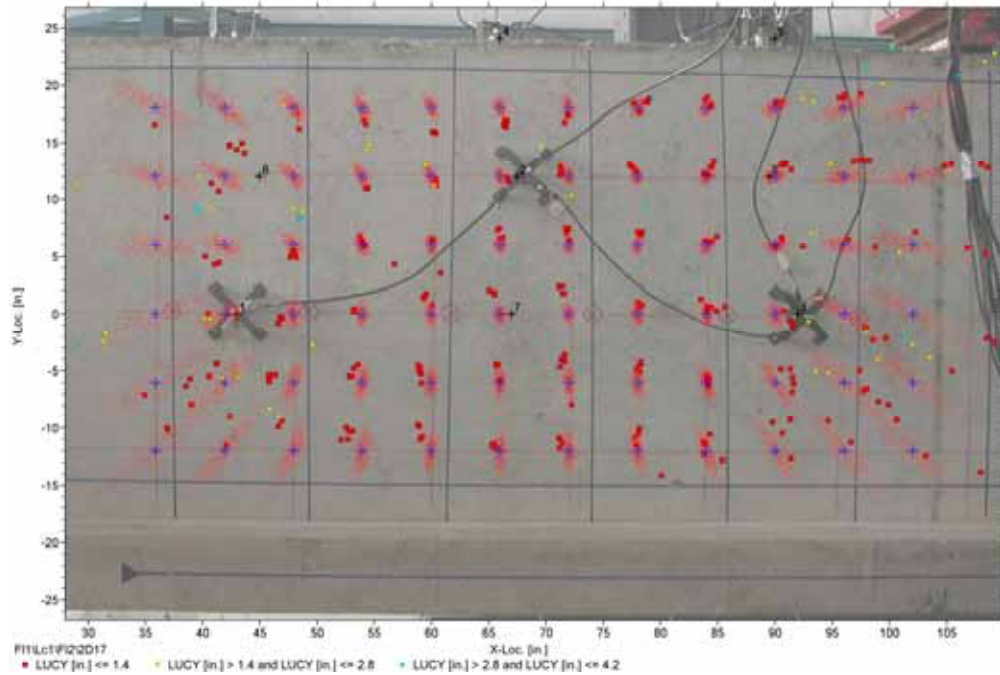


Figure 4.28: Comparison of VisualAE results with MCS for pencil lead breaks

Figure 4.28 shows the results from VisualAE superimposed with MCS. Only the first five time arrivals were included in the computation. The PLB locations are denoted with a blue '+', sensor locations with a black '+', red dots represent MCS realizations (500 per PLB location) for the randomized parameters. The source location results from VisualAE are superimposed and shown with symbols according to the calculated event residual (*LUCY*) as presented in Section 4.5.1.

It can be noticed that the MCS do not always correctly predict the mean location of a group of PLB but the spread is quite accurately simulated. This is due to local effects such as rebars and voids that can bias the mean location. Such off-sets are most probably caused by a systematic arrival time error on one sensor. That's how they could be simulated as well.

The following conclusions can be drawn from the MCS with the given random variables:

1. Sources can be located much more accurately when their origin is inside the sensor array, i.e. locations further away from the sensor array are affected much stronger by parameter variability.

2. The most crucial parameter seems to be the determination of arrival times.
3. The parameter with the least importance is the location of AE sensors.
4. Location results for variable p -wave velocity lie on line paths that point to the center of the sensor array.
5. Locations to the left and right of the sensor array have a much greater uncertainty than the ones that lie above or below, i.e. the outline of the array has an effect (length > height).
6. The relative uncertainty in the shallow direction of the array (z -direction) is much greater than in the other two directions.

4.5.5 Moment Tensor Inversion

An approach to characterize source mechanisms is called Moment Tensor Inversion (MTI), that originally came from quantitative earthquake analysis but was then adapted for AE applications. Aki and Richards first suggested this method to characterize earthquakes. The goal is to determine fracture (cracking) type and orientation. Cracks can be classified according to three modes: pure tension, pure shear, and mixed mode.

After source locations are estimated, a Moment Tensor Inversion (MTI) can be performed. The idea is that the measured transient surface displacements can be de-convolved to characterize the fracture process. To solve for the unknown source mechanism $S(f)$, theoretically all elements of the transmission function (Equation 4.1) must be known. Illustrations of the different source mechanisms are illustrated in Figure 4.29. A representation of the wave propagation function for the media $TF_M(f)$ can be obtained with a set of Green's functions. Because this is very complicated and analytical solutions are available only for the case of an infinite media, relative moment tensor analyses (RMTI) have been developed to simplify the problem or even eliminate the Green's functions. Applications of MTI on small concrete specimens can be found in several publications (*Grosse 1996; Köppel 2002; Landis 1993; Ohtsu 1998; Grosse 2007*). Currently, first large-scale experiments are being conducted applying MTI methods (*Katsaga 2007*). This analysis method was not investigated in this project.

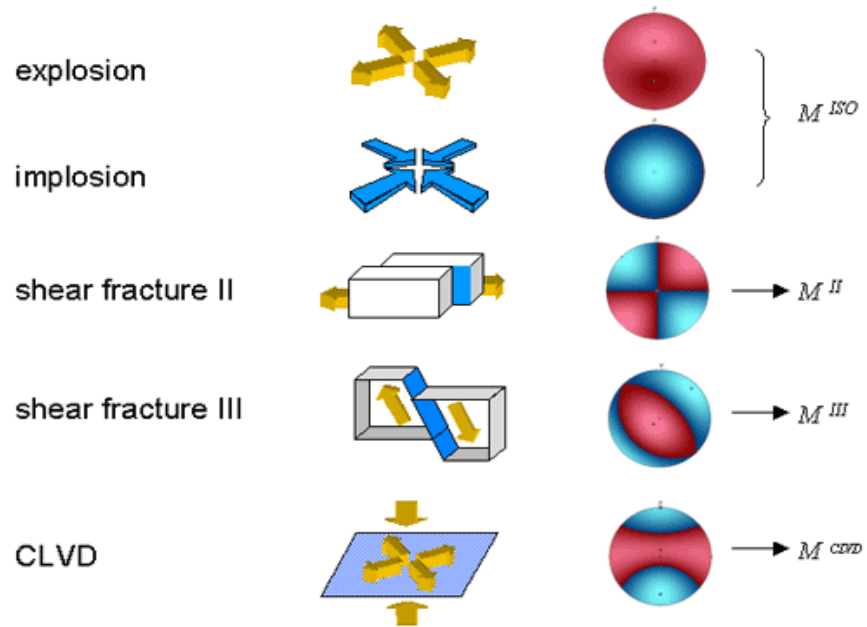


Figure 4.29: Classification of different fracture mechanisms (*Grosse 2001*)

5.0 PRE-EXPERIMENTAL STUDIES

Three additional studies were carried out besides the main experiments on concrete girders to investigate wave propagation in the reinforced concrete (RC) used for construction of the girders. The main objective was to learn about signal attenuation and sensor response and to give guidelines on what sensor types to use and how to deploy them.

5.1 AMPLITUDE ATTENUATION DUE TO MATERIAL DAMPING

A series of 15 concrete cylinders with a diameter $d = 305$ mm (12 in.) and lengths $s = 76/152/305$ mm (3/6/12 in.) were cast and analyzed earlier by Lovejoy (2006) to investigate the influence of concretes with different maximum aggregate sizes on stress wave attenuation. This study was repeated for the three cylinders with concrete used for the girders (mix design see Appendix A) and extended using an additional concrete block $l \times b \times h = 1.14 \times 1.17 \times 0.356$ m (45 x 46 x 14 in.) to get longer signal travel paths which were then $s = 76/152/305/356/1143$ mm (3/6/12/14/45 in.). Data were acquired with a sampling rate of 10 MHz and the total recorded signal length was 204.8 μ s. The pre-trigger was set to 800 samples which produced a pre-trigger time of 80 μ s. One sensor was placed on a face of the block and ten pencil lead breaks (PLB) were performed on the opposite face of the block. PLBs are commonly used because they represent a broad frequency source and they are repeatable. The test specimens and application points of the PLB are illustrated in Figure 5.1.

The PLBs were repeated for each AE sensor type as presented in section 4.1.2. Peak and p -wave amplitude values were then manually extracted from each wave form. Compressive cylinder strengths are the same as those reported for AE Specimen #1 (see Table 6.1).

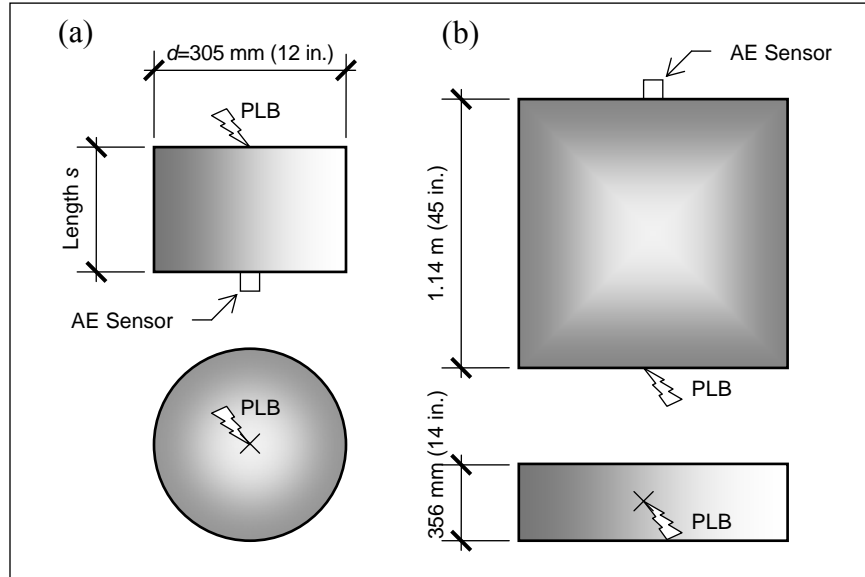


Figure 5.1: Test cylinders (a) and block specimen (b)

Figures 5.2, 5.3, and 5.4 show the results of data regression based on a reciprocal function. Ninety-five percent prediction limits for the whole data set as well as 95% confidence limits for the mean are given as blue dotted and red dashed lines, respectively. The amplitudes were converted into dB by using the first equation in Table 4.5. For each AE sensor, attenuation coefficients were computed employing a linear least-squares curve-fit over signal travel distances up to and including $s = 0.356\text{ m (14 in.)}$ and were called $\alpha_{initial}$. The last data point at $s = 1.14\text{ m (45 in.)}$ was omitted in this case because of the geometry of the block specimen as shown in Figure 5.1 (b). That block specimen is relatively narrow and likely contains reflections of p -waves which were believed to influence the sensor readings.

It can be observed that for all AE sensors, the first peak signal amplitude values (with the shortest signal travel distance) are clipped due to channel saturation, i.e. there is a voltage cap value that cannot be exceeded. This clipping leads to wider confidence and prediction limits compared to the p -wave amplitude data where there is no cap value. However, channel saturation is usually only reached in rare occasions, e.g. during sensor calibration. p -wave amplitudes on the other hand were never found to reach saturation.

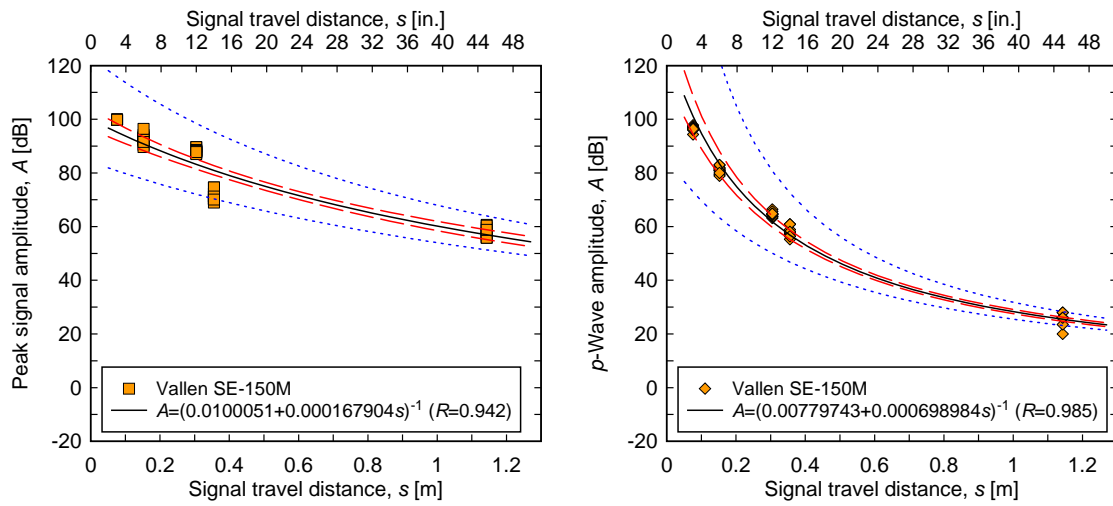


Figure 5.2: Amplitude attenuation curves for the Vallen SE150-M sensor

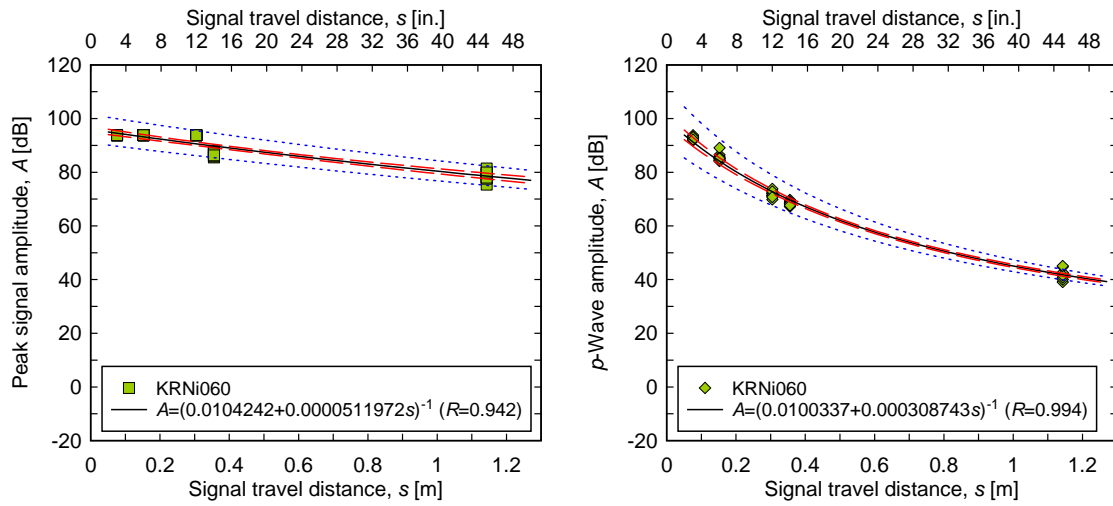


Figure 5.3: Amplitude attenuation curves for the KRNi060 sensor

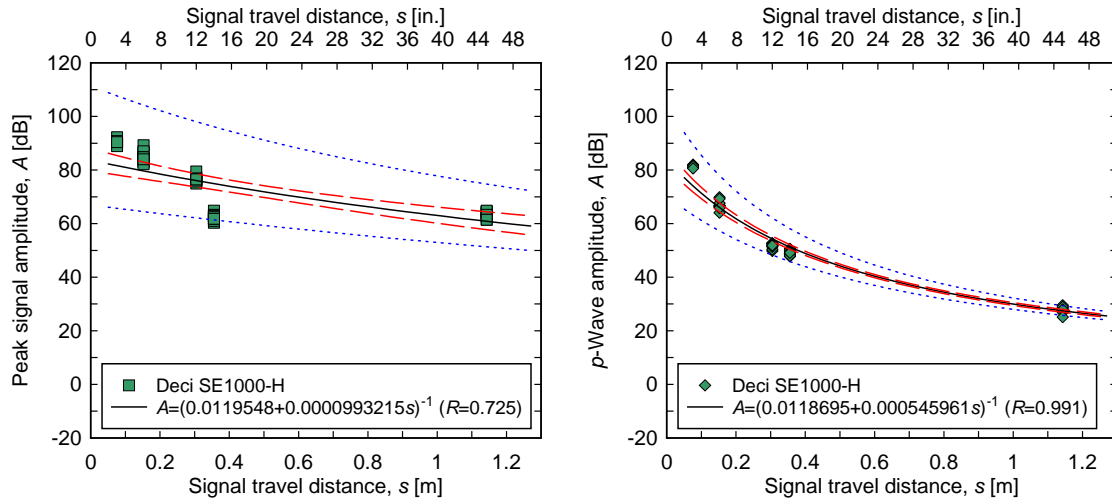


Figure 5.4: Amplitude attenuation curves for the Deci SE1000-H sensor

In Table 5.1, linear attenuation coefficients $\alpha_{initial}$ computed over signal travel lengths up to 0.356 m (14 in.) are listed.

Table 5.1: Attenuation coefficients $\alpha_{initial}$ with correlation coefficients R

AE Sensor	Peak signal amplitude			<i>p</i> -wave amplitude		
	$\alpha_{initial}$	$\alpha_{initial}$	R	$\alpha_{initial}$	$\alpha_{initial}$	R
	[dB/m]	[dB/ft]	[-]	[dB/m]	[dB/ft]	[-]
Vallen SE150-M	83.5	25.5	-0.894	132	40.1	-0.988
KRNi060	18.4	5.60	-0.678	88.5	27.0	-0.994
Deci SE1000-H	88.9	27.1	-0.936	113	34.5	-0.981

Damping is also frequency dependant. Normalized frequency spectra were computed using the Fast Fourier Transformation (FFT) technique and are illustrated in Figure 5.5 from one representative AE waveform from a PLB for each sensor type. It can be observed that frequencies above 200 kHz (shown as vertical dotted line) damp out quickly. This is assuming an average compression wave speed of $c_p = 3.9$ m/ms (154 in./ms) which then corresponds to a frequency of $f = c_p/\lambda = (3900 \text{ m/s})/(0.019 \text{ m}) \approx 200$ kHz where λ is the wave length set to the maximum aggregate size. Therefore for signal travel distances s of more than about 1 m (40 in.) there is not much frequency response. Also, there is almost no power left below 20 kHz since that is the lower analog frequency cut-off filter that applies to channel 1 of the data acquisition system (see Table 4.2). Frequencies above 500 kHz are not shown because very little response was found there for any of the sensors.

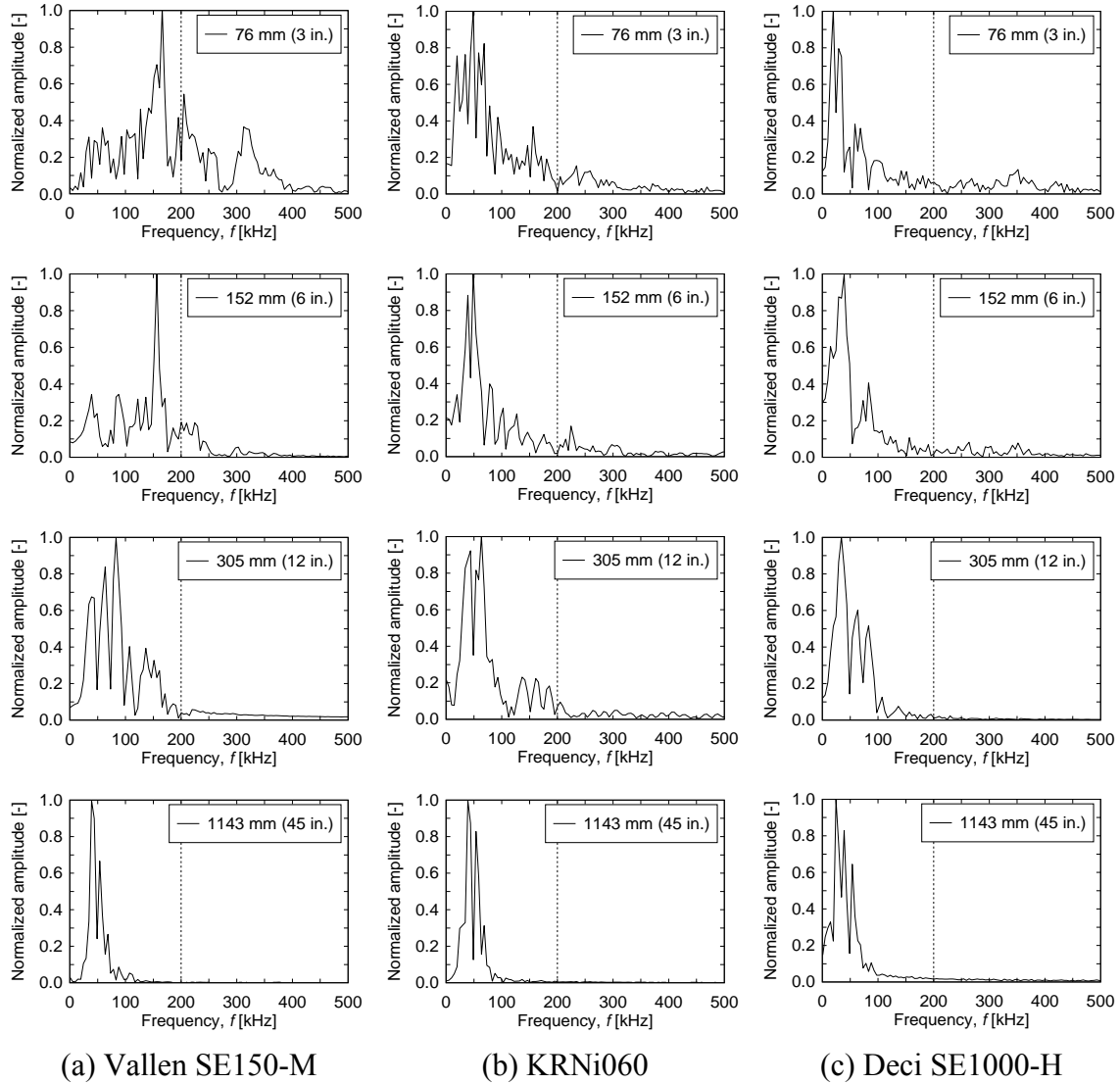


Figure 5.5: Example of normalized frequency responses for one PLB

Figure 5.5 (a) shows the frequency response from a PLB for a Vallen SE150-M sensor. Clearly, frequencies above 200 kHz damp out very quickly. There is also a shift of the amplitude peak response to lower frequencies as the signal travel distance increases. The distinct peaks in the response are mainly due to the sensor characteristics itself (see calibration sheets in Table 4.1). These sensors were found to work well for AE hit detection for intermediate distances up to about 1.0 m (40 in.), i.e. see (Lovejoy 2006; Schumacher 2007). The frequency response for one PLB for a KRNi060 sensor is shown in Figure 5.5 (b). Notice that the peak sensor response is always around 50 to 60 kHz. Frequencies above 200 kHz damp out quickly. This sensor was found to work well for AE hit detection for signals of several meters because of their high sensitivity in the low frequency range (around 60 kHz). Figure 5.5 (c) shows the frequency response from a PLB for a Deci

SE1000-H sensor. Again, frequencies above 200 kHz damp out rapidly. The frequency peak response is always around 20 to 40 kHz. This sensor has a response that is fairly broadband over the range of 40 to 250 kHz (within 4 dB). It can therefore be used for AE waveform analyses but then a high-pass filter should be applied with a cut-off frequency of 40 kHz to data acquisition channels that don't already have an analog low-frequency cut-off set to 40 kHz (channels 3 to 6 in current system).

Finally, the highest frequency component that was still present was estimated for each sensor and signal travel length as shown in Figure 5.7. This frequency was selected from normalized frequency spectra as 5 % of the maximum amplitude as illustrated in Figure 5.6. A logarithmic curve-fit over the entire data set and a linear curve-fit for distances up to $s = 356$ mm (14 in.) was performed. A correlation was found between highest present frequency and signal travel length. In future work, this information may be used to correct p -wave amplitudes where no source location is performed, i.e. in b -value analysis with corrected p -wave amplitudes.

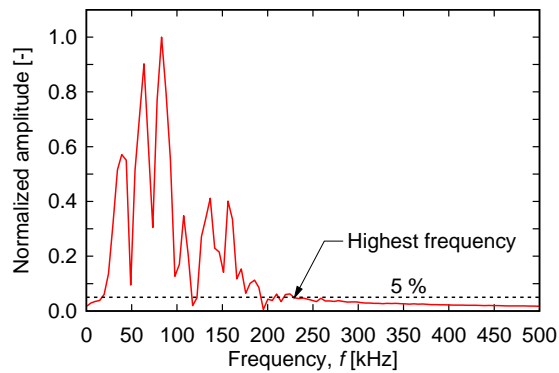


Figure 5.6: Criteria for estimation of highest frequency component

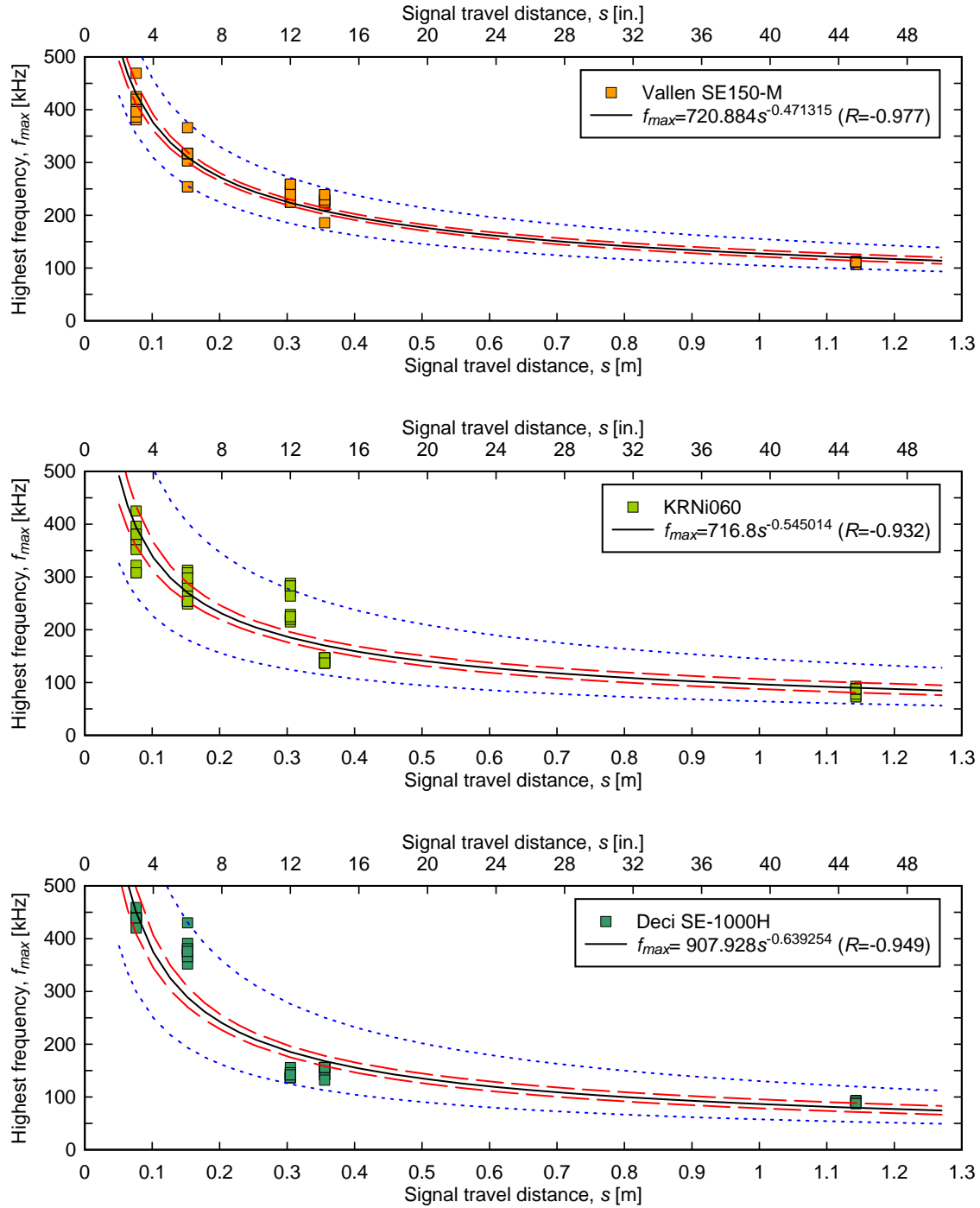


Figure 5.7: Highest detected frequency (5 %) as a function of the signal travel distance

The (linear) frequency attenuation coefficients were named $\beta_{initial}$ and computed over the limited data set were 608 kHz/m (185 kHz/ft), 627 kHz/m (191 kHz/ft), and 1159 kHz/m (353 kHz/ft) for the Vallen SE150-M, the KRNi060, and the Deci SE1000-H sensor, respectively.

5.2 INFLUENCE OF INCIDENT ANGLES ON MEASURED SIGNAL AMPLITUDES

To investigate the influence of the wave incident angle θ on the sensor response, a semi-circular specimen was cast with a diameter $d = 584$ mm (21 in.) and height $h = 305$ mm (12 in.). The experiment was conducted twice, using a broadband Glaser-NIST sensor (Glaser 1998; Weiss 1998) as well as a Vallen SE150-M sensor. The experimental setup is illustrated in Figure 5.8. The sensor was attached to the centerline of the flat face at about mid height. Three pencil lead breaks (PLB) were performed around the circumference of the specimen every 5° at mid-height. Using a semi-circular specimen allowed the signal travel distance to always be $s = 292$ mm (10.5 in.). The specimen was constructed of the same concrete used for the girder experiments with a maximum aggregate size of 19 mm (3/4 in). The concrete mix design can be found in Appendix A.



Figure 5.8: Semi-circular specimen, experimental setup

p -Wave amplitudes were then picked manually for from the recorded AE signal wave forms. The results are shown in Figure 5.9. Given is mean values \pm one standard deviation. It can be observed that for some incident angles there is a large spread in the measured p -wave amplitude data. As expected, the data set is also not perfectly symmetrical. This can be explained by the fact that concrete is not a homogeneous material and contains air voids that can significantly dampen stress waves.

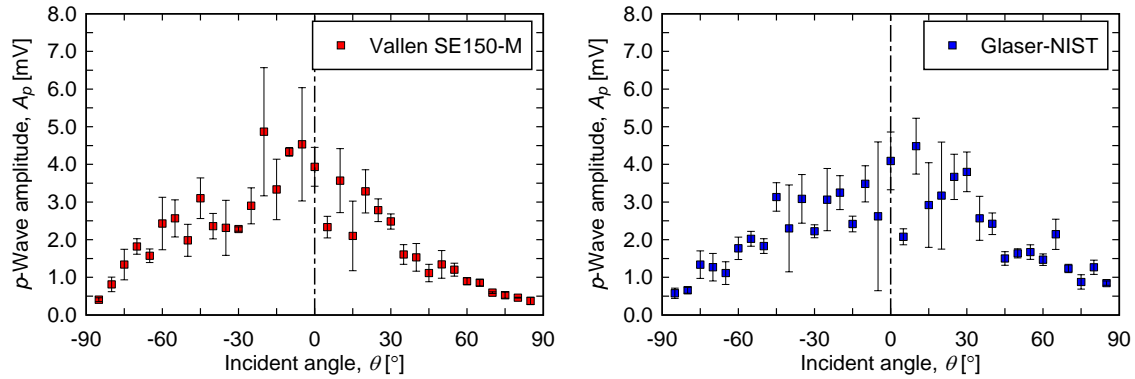


Figure 5.9: Measured p -wave amplitudes vs. incident angles

In a next step, the measured amplitude data were fit to the analytical solution (Equation 2.11) employing a least-squares difference approach. Two procedures were carried out. First, Poisson’s Ratio was kept fixed at $\nu = 0.30$ (as determined earlier) and only a multiplication factor for the measured amplitudes to match the normalized analytical solution were identified. Second, an unconstrained optimization was performed where not only the multiplication factor but also Poisson’s Ratio was assumed unknown. The amplitudes that had the same incident angles but opposite signs were put into one data set assuming symmetry, i.e. $A_p(-\theta) = A_p(\theta)$. Some of the data points that seemed to be outliers were determined manually and then omitted for the optimization process. Figures 5.10 and 5.11 show the results of this optimization.

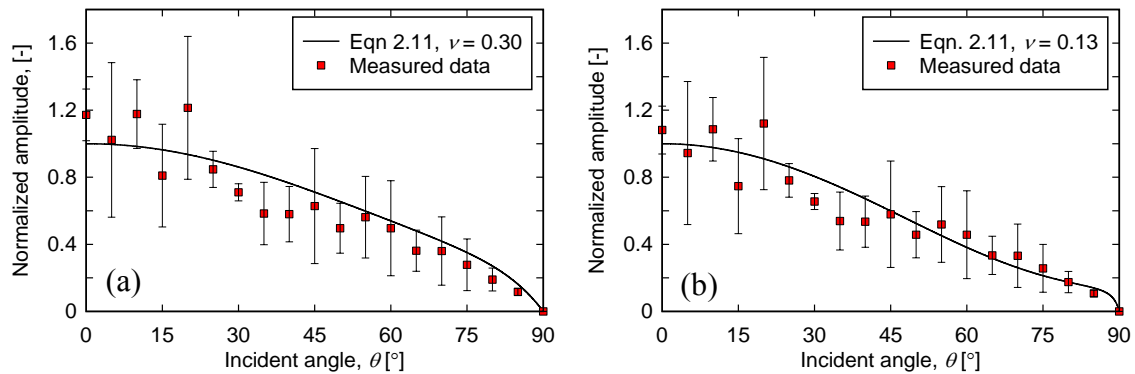


Figure 5.10: Results of data-fitting for the Vallen SE150-M sensor

For the results from the Vallen SE-150-M sensor presented in Figure 5.10 (a), Poisson’s Ratio was fixed at $\nu = 0.30$. Given for the measured data is mean values \pm one standard deviation. The correlation coefficient between observed and analytical data was $\rho = 0.93$. For the unconstrained optimization shown in Figure 5.11 (b), Poisson’s Ratio was found to be $\nu = 0.13$ with a correlation coefficient of $\rho = 0.95$.

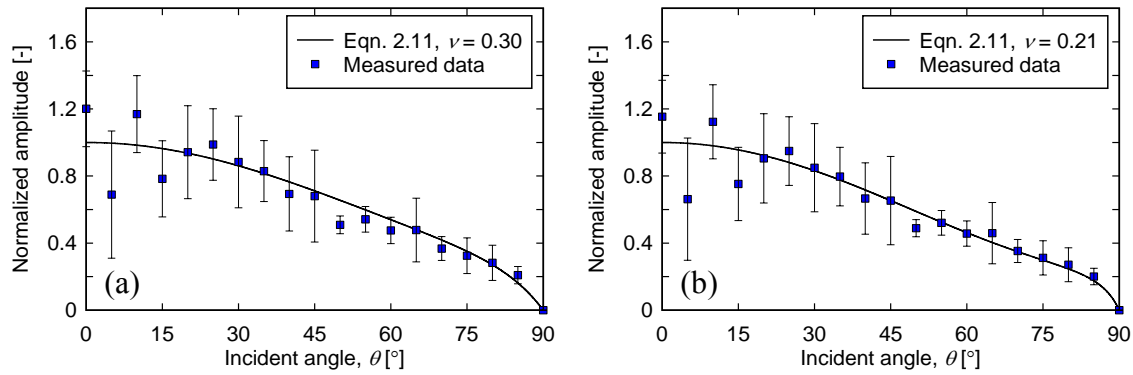


Figure 5.11: Results of data-fitting for the Glaser-NIST Sensor

For the results from the Glaser-NIST sensor presented in Figure 5.11 (a), Poisson's Ratio was fixed at $\nu = 0.30$. Given for the measured data are mean values \pm one standard deviation. The correlation coefficient between observed and analytical data was $R = 0.93$. For the unconstrained optimization shown in Figure 5.11 (b), Poisson's Ratio was found to be $\nu = 0.21$ with a correlation coefficient of $R = 0.94$.

It appears that the choice of Poisson's Ratio is not very sensitive and high correlation coefficients can be achieved even with $\nu = 0.30$ as was found earlier by Lovejoy (2006) via equation 2.7.

5.3 WHAT AE SENSORS MEASURE

Typically, manufacturers state that their AE sensors record surface motion. However, this term could stand for displacements, velocities, or accelerations. This study is an attempt to understand and determine what AE sensors measure and was conducted by the author at UC Berkeley. The three commercially available sensors as presented in Table 4.1 plus a Glaser-NIST (Glaser 1998; Weiss 1998) sensor were compared for this study. The test specimen was a large steel plate (so that wave reflections from edges did not have to be considered) with a thickness of 51 mm (2 in.). AE data for this experiment was acquired at a sampling rate of 5 MHz using a Digital Wave data acquisition system. Ball bearing drops (\varnothing 1.7 mm) were performed on the top of the plate centered about the AE sensors placed on the underside of the plate.

Additionally, the finite difference (FD) program Wave3000 was utilized to simulate 3-D stress wave propagation for comparison. The function used as input was a sine-type over the length of half one time period with a length of 8 μ s as approximation to the forcing function, as illustrated in Figure 4.5 B. The FD solution for the surface displacement due to a ball bearing drop is illustrated in Figure 5.12. A second-order correction term had to be subtracted from the original program output due to rigid body motion as illustrated in

Figure 5.12 (a). Figure 5.12 (b) shows the frequency spectrum of the simulation computed using FFT.

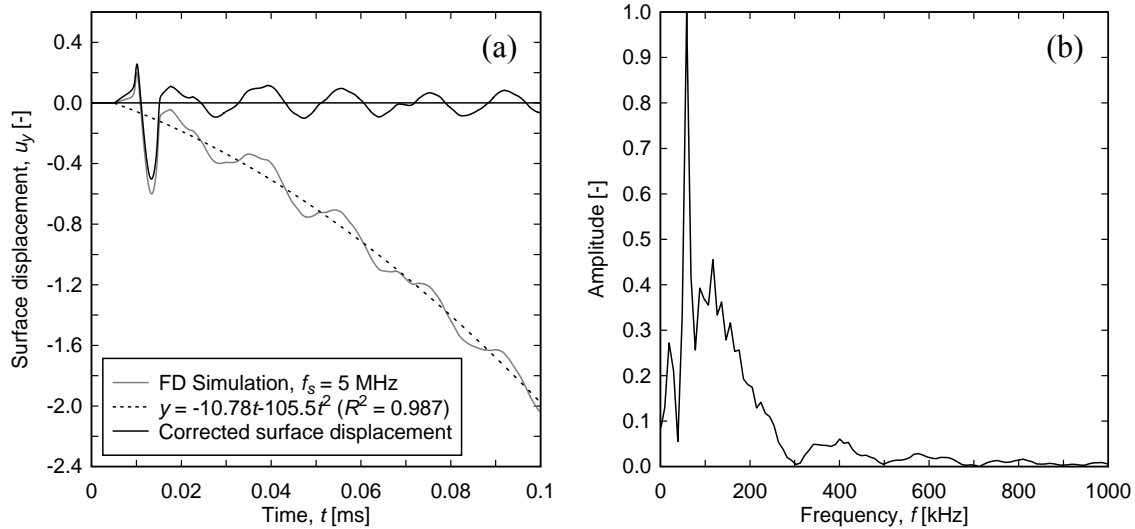


Figure 5.12: FD surface displacement from ball bearing drop (a) with frequency spectrum (b)

Figure 5.13 illustrates the results from the FD simulation (corrected as described above) and the four tested AE sensors. The amplitudes were normalized to one and lined up with respect to time according to the first significant downward motion (assumed as main p -wave response). As can be observed, the Glaser-NIST is able to describe the transient surface displacements quite well. There is no apparent ‘ringing’ showing that this sensor is virtually broad-band over a wide range of frequencies. The only remarkable difference is the one apparent frequency component at about 80 kHz that this sensor does not seem to be able to reproduce. The Vallen SE150-M and KRNi060 sensors match fairly well until slightly after the p -wave arrives, after that the resonant behavior of those sensors takes over and they start ‘ringing’. However, the shape and duration of the p -wave are represented very well in both cases. The Deci SE-1000H sensor appeared to record surface velocities (denoted with ‘rec’) rather than displacements. The surface displacements (denoted with ‘int’) for this sensor were computed by integration of the recorded time series.

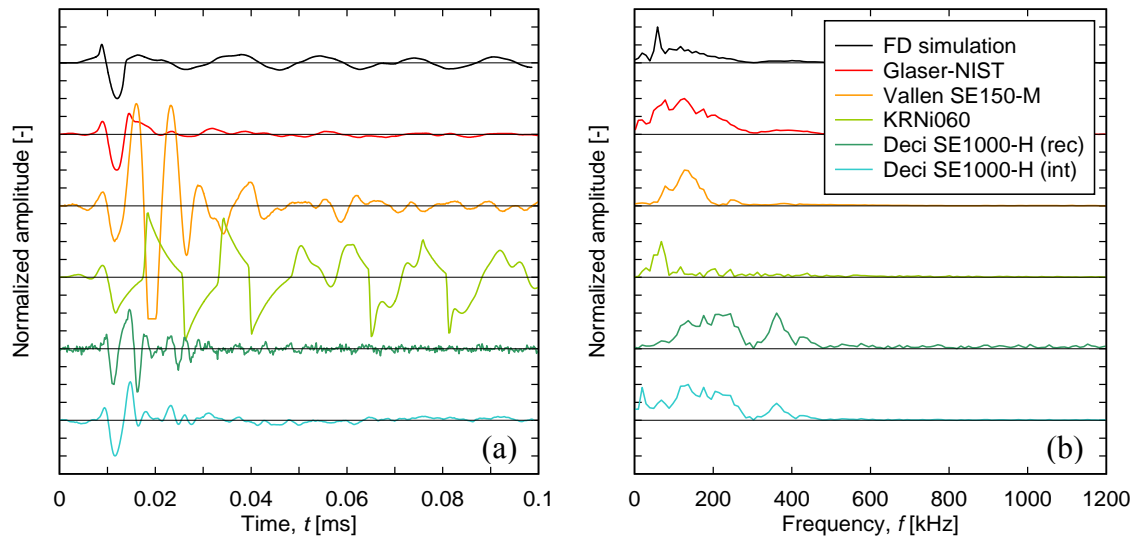


Figure 5.13: Results for ball bearing drop: (a) time history, (b) frequency spectra

A close-up on the p -wave arrival is shown in Figure 5.14. All tested AE sensors appeared to record surface displacements except the Deci SE1000-H which seemed to record surface velocities. As can be observed, the shape and duration of the p -wave is represented fairly well by all sensors and just minor features differ. However after this initial portion of the signal, only the Glaser-NIST sensor and the integrated signal of the Deci SE1000-H come close to the simulation result. The other two sensors start ringing and do not properly represent the solution obtained by finite difference simulation.

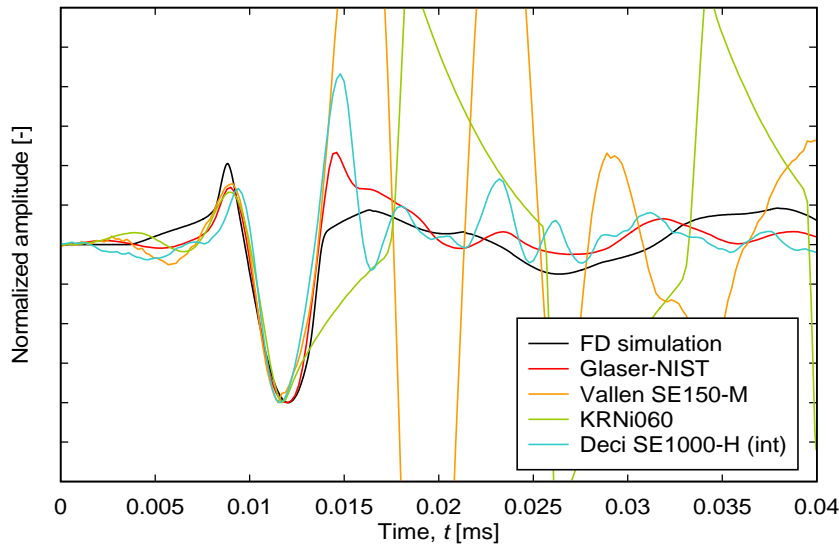


Figure 5.14: Close-up view of p -wave arrival

6.0 MAIN TESTS OF FULL-SIZE REINFORCED CONCRETE GIRDERS

Four full-scale conventionally reinforced concrete (RC) bridge girders were constructed to investigate different aspects of Acoustic Emission (AE) monitoring. Four AE sensor arrays were applied and evaluated for use in structural monitoring. The beam specimens were tested in inverted T (IT) configuration (deck in flexural tension). The IT configuration reflects shear in the presence of negative bending moment, as over continuous support locations such as bents and piers. Incrementally increasing force amplitudes were applied to the specimens. After each peak, forces that are representative of in-service conditions were applied and the AE response investigated.

6.1 SPECIMEN FABRICATION AND MATERIALS

All beam specimens were constructed in the Structural Laboratory at Oregon State University. Concrete was delivered by a local ready-mix concrete supplier. The total length of the beams was 7.92 m (26 ft) and the weight approximately 9.5 t (21,000 lb). Shop drawings and material lists of all specimens are provided in Appendix A.

The specimens were cast in T-position (two at a time) as monolithic beams (no cold joints). The concrete reflects 1950s vintage AASHTO Class-A concrete consisting of Portland Cement, sand, aggregates, and water (*AASHTO 1953*; *AASHTO 1957*). A slight amount of air-entraining admixture was added to obtain desired workability and material properties. The amount of cement and the water-cement ratio were adjusted to provide a relatively low compressive strength typical of the specified 22.8 MPa (3300 psi) concrete strength of the time. The maximum aggregate size was 19 mm (3/4 in.). The plasticity of the concrete was verified just prior to casting with a slump test. The mix design is provided in Appendix A.

Average compressive strengths of concrete for each specimen were determined by ϕ 152 mm (6 in.), 305 mm (12 in.) long cylinder breaks at 3, 7, 14, 28, and at the beginning of the test (test start day) and the end (test end day) using a 1330 kN (300 kip) capacity concrete testing machine. The testing procedure for the concrete compression test was performed in accordance with ASTM C39. The compressive stress-strain curves for the test start days of each specimen are shown in Appendix A. Concrete properties for all specimens are summarized in Table 6.1. The average concrete strength over all specimens was 25.7 MPa (3695 psi) with a coefficient of variation (CV) of 3% and therefore higher than the specified design concrete strength of 22.8 MPa (3300 psi).

Table 6.1: Concrete compressive strength, f_c'

Name	Date of cast	28 days		First test day		Last test day	
		[MPa]	[psi]	[MPa]	[psi]	[MPa]	[psi]
AE Specimen #1	09-09-2005	26.2	3801	30.1	4366	27.5	3993
AE Specimen #2	09-09-2005	26.4	3827	NA	NA	24.7	3580
AE Specimen #3	12-01-2005	24.5	3560	NA	NA	NA	NA
AE Specimen #4	12-01-2005	25.5	3695	NA	NA	NA	NA
Mean		25.7	3721	-	-	26.1	3787
CV		0.03	0.03	-	-	-	-

All reinforcing steel was fabricated by a local rebar fabricator per OSU approved shop drawings. The ϕ 13 mm (#4) Grade 40 bars had a yield stress of 342 MPa (49.8 ksi). They were taken from the lowest yield stress heat of steel produced by a rebar manufacturer during a production run. Miscellaneous remaining ϕ 13 mm (#4) reinforcing steel used for the beams was Grade 60, ASTM A615. Average yield stresses for all reinforcing bars can be seen in Table 6.2.

Table 6.2: Reinforcement steel properties

Steel	Grade	ASTM	Yield stress		Ultimate stress		Failure strain
			f_y		f_u		ϵ_f
	[ksi]	[-]	[MPa]	[ksi]	[MPa]	[ksi]	[-]
ϕ 13 mm (#4)	40	A615	343	49.8	543	78.8	NA
ϕ 19 mm (#6)	60	A706	448	65.0	645	93.5	NA
ϕ 35 mm (#11)	60	A706	480	69.6	700	101.5	NA

6.2 EXPERIMENTAL SETUP

All experiments were conducted in the Structural Laboratory at Oregon State University. The tests were performed with a four-point loading configuration. Force was applied at mid-span through a spreader beam to load points on the specimen spaced 0.61 m (24 in.) apart. The spacing between the supports (span length) was 6.60 m (260 in.). This was necessary to ensure that no anchorage failure in the flexural tension rebars occurs. Applied force was measured with a 2220 kN (500 kip) capacity load cell mounted to the hydraulic actuator. The experiments were conducted with a closed-loop servo-hydraulic system using force-controlled mode. The setup used for all tests is illustrated in Figures 6.1 and 6.2. To minimize noise from the test frame interfering with the Acoustic Emission (AE) measurements, medium stiff neoprene strips were installed between all bearing surfaces (see inset ‘Detail A’ in Figure 6.1).

The data from conventional sensors (described in section 6.3) were acquired using a commercially available data acquisition program installed on a 16-bit personal computer. AE data were recorded with a Vallen AMSY-5 system (described in section 4) connected to a separate 16-bit personal computer.

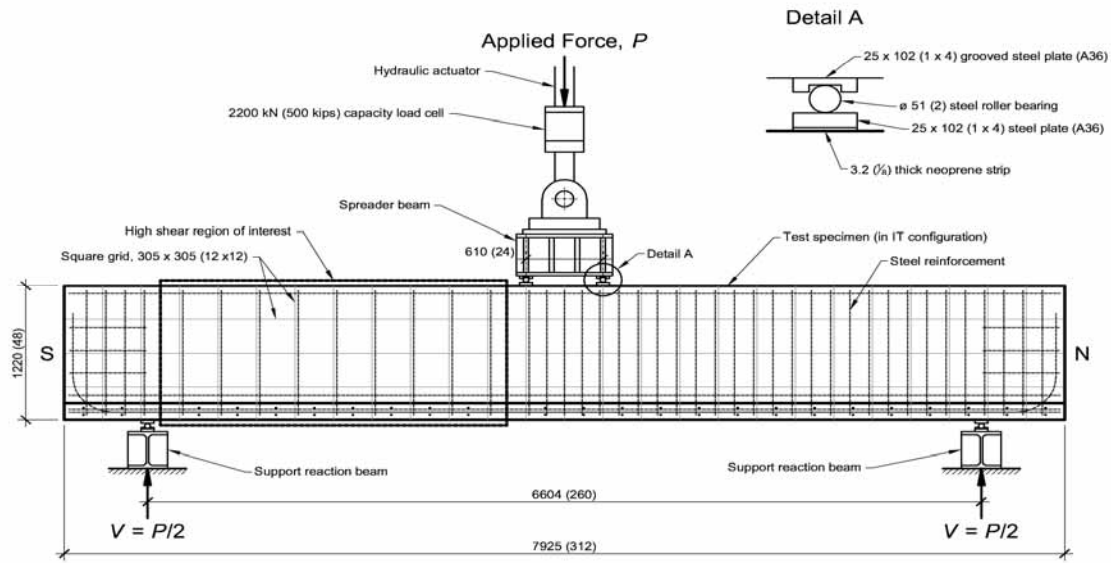


Figure 6.1: Test configuration with typical specimen, dimensions in mm (in.)



Figure 6.2: Test frame with specimen, photo taken from N-E

6.3 INSTRUMENTATION

For each test, data from over 30 conventional sensors were collected. Sensors included load cells, strain gages, concrete clip gages, and displacement sensors. Strain gages were bonded to selected stirrups in the high shear region of interest and installed prior to casting of concrete. Flexural reinforcing bars were instrumented with strain gages at mid-span and at rebar cut-off locations.

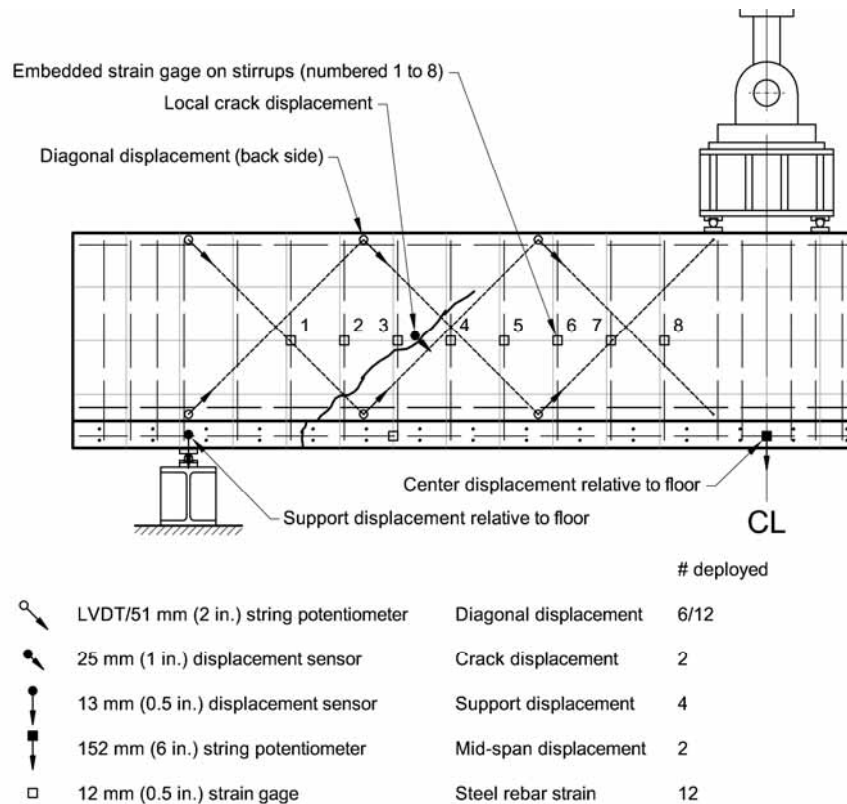


Figure 6.3: Typical instrumentation (conventional sensors) on specimen

Additionally, the specimens were instrumented with eight Acoustic Emission (AE) sensors deployed in different arrays to record stress waves generated during testing. A detailed description of the AE sensor arrays can be found in sections 6.5.1 to 6.5.3.

6.4 TEST SPECIMENS

6.4.1 Cross Section

Illustrated in Figure 6.4 is a cross-section around the center line of the beam specimens used in this project. They were tested in IT-configuration, imposing flexural-tension in the deck. No skin steel was added to the reinforcing cage to reflect 1950s detailing practices. The stirrups were manufactured of Grade 40 ($f_y = 276$ MPa), all other of Grade

60 ($f_y = 414$ MPa) reinforcing steel. Detailed shop drawings of all beam specimens can be found in Appendix A.

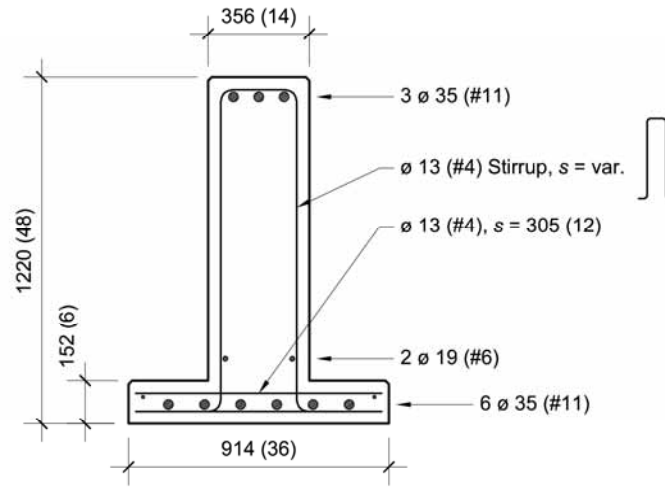


Figure 6.4: Specimen cross-section, dimensions in mm (in.)

6.4.2 AE Specimen #1

AE Specimen #1 was detailed with all 6 ϕ 35 mm (#11) flexural tension rebar's (in the deck) spanning over the whole length of the specimen. Additionally, the two in the middle were bent up 90° into the web. This was done to ensure proper anchorage of the flexural steel bars. The stirrup spacing was 305 mm (12 in.) constant in the high shear region of interest (south side) and 152 mm (6 in.) on the north side to enforce failure in the region of interest.

6.4.3 AE Specimen #2

In AE Specimen #2, the two outer flexural tension rebar (in the deck) were cut-off on the south side at 2.13 m (7 ft) from the center line. These cut-offs were common practice to optimize the steel needed to cover flexural demand on the member. The stirrup spacing was 305 mm (12 in.) constant in the high shear region of interest (south side) and 152 mm (6 in.) on the north side to ensure failure in the region of interest.

6.4.4 AE Specimen #3

This specimen was built identical to AE Specimen #2.

6.4.5 AE Specimen #4

AE Specimen #4 was constructed as the most realistic one with flexural cut-offs as AE Specimen #2 and variable stirrup spacing on the south side (region of interest) ranging from 267 mm (10.5 in.) to 559 mm (22 in.).

6.4.6 Comment

The last two specimens (#3 and #4) have not yet been tested. There was no apparent reason to believe that there would be any benefit in testing all four beams to cover the scope of this project. Recommendations on what could be investigated further will be given in section 8.

6.5 ACOUSTIC EMISSION (AE) SENSOR ARRAYS

Two different sensor arrays were determined to investigate the behavior of AE over the duration of the experiment as described in section 1. Illustrations of the arrays in Figures 6.4 to 6.5 are only of illustrative nature. Some sensors had to be replaced during the experiment due to the development of cracks. The actual sensor location coordinates are listed in Appendix A.

6.5.1 Sensor Array A

Sensor array A is illustrated in Figure 6.5 and represents a three-dimensional array that was selected to mainly estimate 3-D AE source locations while imposing new damage into the specimen (first overload cycle of each session). The sensors were arranged in an anti-symmetric manner around the high shear zone of interest. Eight KRNi060 sensors were deployed.

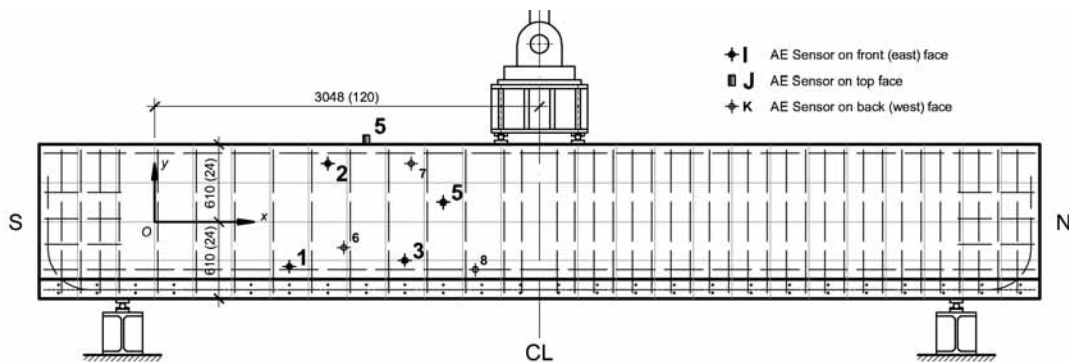


Figure 6.5: AE Specimen #1 with sensor array A, dimension in mm (in)

For AE Specimen #2, AE transducers were only placed at or above the center height of the girder ($y \geq 0$). This was done so that crack interference may be minimized by placing the sensors as far as possible away from where cracks originate (bottom of the girder).

This array is the one that allows for most precise AE source location estimation (in 3-D) and was evaluated more in depth than the other arrays. A very similar array was deployed on the Cottage Grove Bridge, Oregon during a controlled structural in-service testing with test trucks which is reported in (Lovejoy 2006).

6.5.2 Sensor Array B

Figure 6.6 shows sensor array B which is one that can often be found in literature for global AE monitoring (Golaski 2002; Colombo 2003; Shiotani 2007). Both sides (south and north) of the specimen were equipped with AE sensors which allowed comparison of AE response between the two different stirrup spacing's of 305 mm (12 in.) on the south side and 152 mm (6 in.) stirrup spacing on the north side. This array has the advantage that it is easy to apply and replicate on an existing bridge. The KRNi060 sensors were used in this experiment.

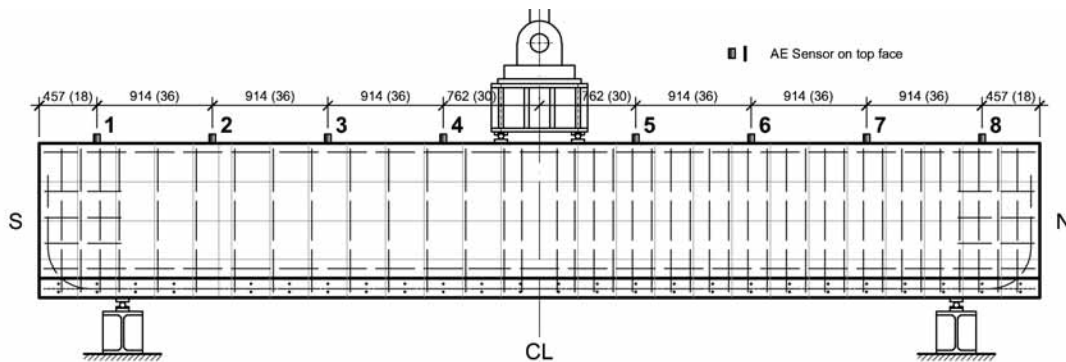


Figure 6.6: AE Specimen #1 with sensor array B, dimension in mm (in)

6.5.3 Comments

The broad-band frequency type Deci SE1000-H transducers were not used for these experiments as they were not sensitive enough to pick the relatively weak signals produced from in-service load conditions applied to the specimens (Lovejoy 2006; Schumacher 2007).

6.6 LOADING PROTOCOL

6.6.1 Introduction

Most of the AE research in laboratories has used loading protocols of loading and unloading cycles with each subsequent increment applied at higher load magnitude, e.g. (Ohtsu 2002; Colombo 2003; Katsaga 2007). Repeated cyclic loading on service level or fatigue loading have rarely been considered. However, such loading history may change the AE behavior significantly as it helps redistribute residual stresses after an overload event, for example. In order to compare the experimental results with in-service conditions, a different approach was therefore chosen. The following general loading procedure was applied to both full-size specimens:

1. Apply equivalent dead load to specimen representative of service level conditions in an actual bridge.
2. Impose new damage by applying a monotonic overload force followed by unloading to the dead load level.
3. Apply load cycles at service level to reach steady-state strain response.
4. Load specimen with ‘test trucks’ to simulate structural load-testing possible on actual bridge structure.
5. Repeat step 2 applying a higher force level.

6.6.2 Unloading effect on indeterminate multi-span bridges

The tested specimens were inverted T-beams which represent longitudinal bridge girders close to transverse supporting elements such as bent caps or abutments where the deck is in flexural-tension. A typical rebar strain response at a diagonal crack due to a 22.7 t (50,000 lb) truck on a multi-span bridge close to a supporting element is illustrated in Figure 6.7.

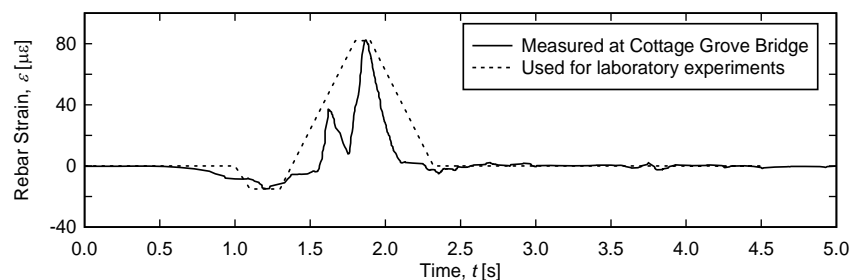


Figure 6.7: Example of rebar strain response at crack location measured at actual in service bridge in Cottage Grove, OR

Notice the negative (compression) relative live load induced strain response as the truck approaches the crack location before the main positive (tension) strain response when the

truck crosses over the crack. In this case the maximum initial compression strain response was 18 % of the following maximum tension strain response. This unloading effect was taken into account and applied to the lab specimens using a rounded value of 20%.

6.6.3 Force effects

To determine realistic force effects, a continuous three-span bridge similar to the McKenzie River Bridge with span lengths of 15.24 m (50 ft) was analyzed. Realistic shear distribution and impact factors recommended by (*Potisuk 2007*) were used. The cross-section of the girders was assumed the same as the AE specimens. The maximum shear force was found in the end spans about d_v away from the face of the column at 31.85 m (104.5 ft). Figure 6.8 shows the force effects due to the self weight of the bridge (a), and the force influence lines for (b) an ODOT dump truck, (c) an HS20-44 truck (c), and (d) a 3-3 truck. The total self weight (DL) of the bridge superstructure was estimated 752 kN (169 kips) which yields 4.11 kN/m/girder (0.28 kips/ft/girder). The weights of the trucks (LL) were 19.1 t (42,000 lb), 32.7 t (72,000 lb), and 36.3 t (80,000 lb), respectively.

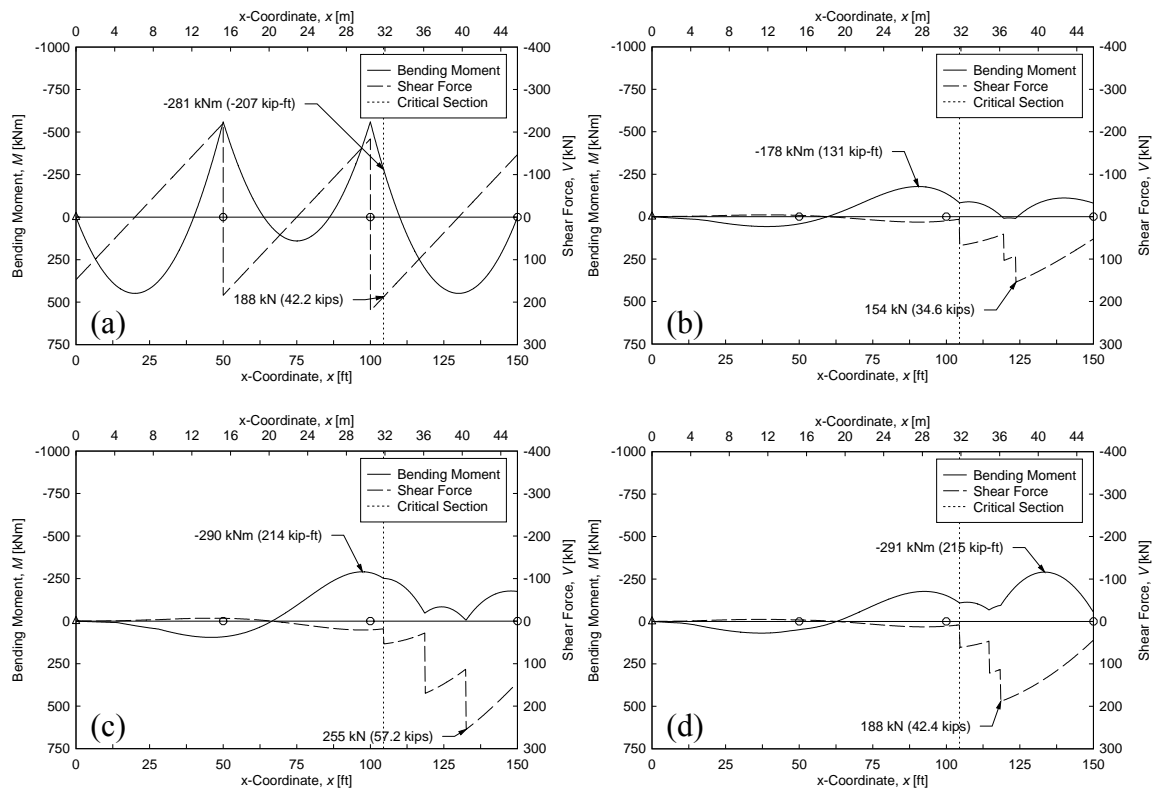


Figure 6.8: Force effects on a three span prototype bridge

The combined service level force effects can be calculated as follows:

$$V_{DL} = V_{DL,tot} / 4 \quad (6.1)$$

$$V_{LL} = IM \cdot DF \cdot V_{LL} \quad (6.2)$$

Where $V_{DL,service}$ is the shear force per girder due to the self-weight of the bridge superstructure (the factor 4 represents the # of girders in the bridge), V_{LL} the shear force due to the trucks, IM the impact factor to account for dynamic amplification of fast moving vehicles, and DF the shear distribution factor. Shear distribution factors DF were taken from (Potisuk 2007) as 0.52 for the combination ‘One truck in lane’ and 0.68 for ‘Two trucks in lane’. The impact factor was defined as 1.00 for the slow moving test trucks and 1.20 for fast moving ambient trucks (according to AASHTO specifications).

The final combined service level force effects per girder are:

- Bridge superstructure self-weight (dead load) $V_{DL} = 188 \text{ kN (42.2 kips)}$
- 1 ODOT dump truck in one lane (slow) $V_{LL} = 1.0 \cdot 0.52 \cdot 154 \text{ kN} = 80.1 \text{ kN (18.0 kips)}$
- (1): 3 ODOT dump trucks (slow) $V_{LL} = 1.0 \cdot 0.52 \cdot (154 + 57.8 + 13.1) \text{ kN} = 117 \text{ kN (26.3 kips)}$
- (2): (1) + 3-3 Truck (fast) $V_{LL} = 117 \text{ kN} + 1.2 \cdot 0.09 \cdot 188 \text{ kN} = 137 \text{ kN (30.9 kips)}$
- (3): 2 ODOT dump trucks side by side (slow) $V_{LL} = 1.0 \cdot 0.68 \cdot 154 \text{ kN} = 105 \text{ kN (23.5 kips)}$
- (4): Ambient 3-3 Truck (fast) $V_{LL} = 1.2 \cdot 0.52 \cdot 188 \text{ kN} = 97.8 \text{ kN (22.0 kips)}$

From these force effects, the following peak forces $P = 2 \cdot V$ were applied to the beam specimens:

- Bridge superstructure self-weight (dead load) $P_{DL} = 2 \cdot 178 \text{ kN} = 356 \text{ kN (80.0 kips)}$
- Simulated test truck (live load, service level) $P_{LL} = 2 \cdot 134 \text{ kN} = 267 \text{ kN (60.0 kips)}$
- 1st elevated simulated test truck $P_{LL} = 2 \cdot 178 \text{ kN} = 356 \text{ kN (80.0 kips)}$
- 2nd elevated simulated test truck $P_{LL} = 2 \cdot 223 \text{ kN} = 445 \text{ kN (100 kips)}$
- 3rd elevated simulated test truck $P_{LL} = 2 \cdot 267 \text{ kN} = 534 \text{ kN (120 kips)}$
- 4th elevated simulated test truck $P_{LL} = 2 \cdot 312 \text{ kN} = 623 \text{ kN (140 kips)}$

The overloads at the beginning of each phase were applied in a similar manner as the test trucks (see section 6.6.2). See Tables 6.3 and 6.4 for the peak values.

6.6.4 Loading Procedure

The loading protocol consisted of several phases, each starting with an overload event (OL) followed by cyclic loading and simulated test trucks. Figure 6.9 illustrates the first phase and the beginning of the second phase that were applied to both AE Specimen #1 and #2.

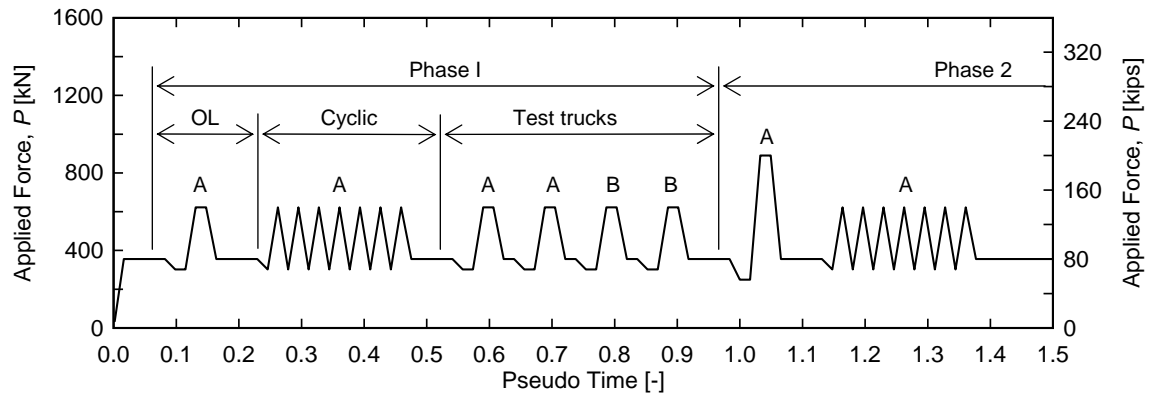


Figure 6.9: Generalized loading protocol with used sensor arrays (designated A to D)

The experiments were divided into phases. At the start of each phase, an overload event (OL) took place to impose new deterioration into the specimen. The procedure for each phase was as follows:

1. Deploy sensor array A (see section 6.5.1), check sensor coupling (PLB)
2. Load specimen up to a force of 356 kN (80 kips) representing the self-weight (DL)
3. Load specimen with overload force (OL) and hold until AE activity (hit rate) diminishes
4. Mark and map newly developed or propagated cracks, take pictures
5. Unload to a force of 356 kN (80 kips) representing the self-weight (DL)
6. Cyclically load specimen between 302 kN (68 kips) and 623 kN (140 kips) until sensor responses (strains, displacements) reach steady state, e.g. 5000 cycles at 1 Hz
7. Load specimen with three individual test trucks, peak force = 623 kN (140 kips)^{*)}
8. Unload specimen completely (in a few cases to DL only)
9. Deploy sensor array B (section 6.5.2), check sensor coupling (PLBs)
10. Load specimen with 100 cycles between 302 kN (68 kips) and 623 kN (140 kips)
11. Load specimen with three individual simulated test trucks to 623 kN (140 kips)^{*)}
12. Load specimen with 100 cycles between 302 kN (68 kips) and 623 kN (140 kips)
13. Check for newly developed cracks, mark and map. Additional elevated test trucks were applied in the later phases (see end of section 6.6.3)

6.6.4.1 AE Specimen #1

Shown in Figure 6.10 is the actual loading protocol that was applied to AE specimen #1. Table 6.3 is a summary of the log file for the entire experiment.

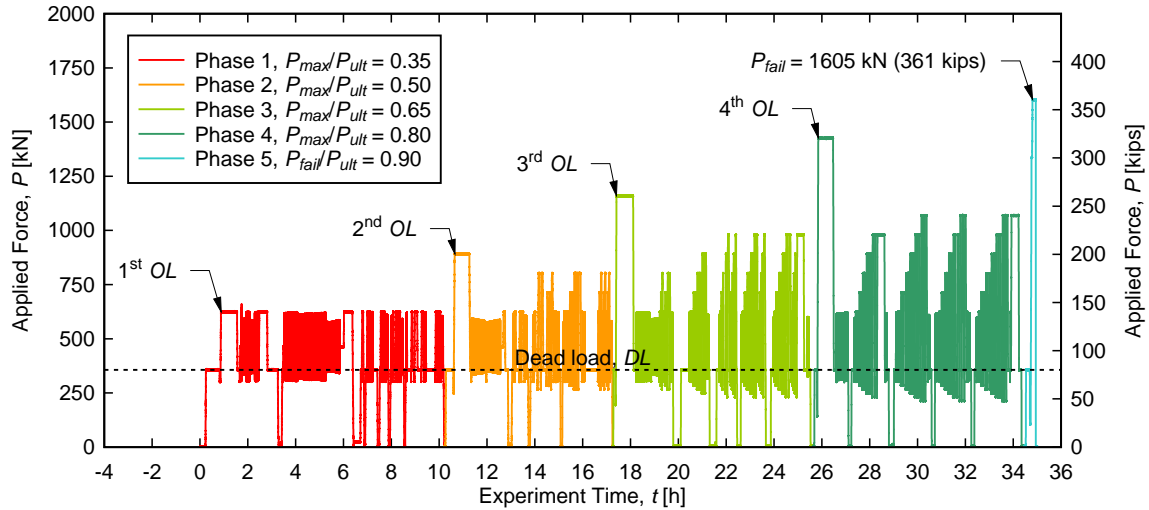


Figure 6.10: Actual loading protocol for AE Specimen #1

Table 6.3: Log File Summary AE Specimen #1 (DL = dead load, OL = overload, TT = test truck)

Ph.	Session	Max. appl. force		P_{max}/P_{ult}	Arra y	Applied forces, comments
		[kN]	[kips]			
1	1	623	140	0.35	A1	1st OL ; 4x250 = 1000 cycles
	2	623	140	0.35	A2	4x1000 = 4000 cycles
	3	623	140	0.35	A2	TT: 3x140 k
	3c	623	140	0.35	B	TT: 3x140 k
2	6	890	200	0.50	A3	2nd OL ; 2x1000 = 2000 cycles
	7	623	140	0.35	A3	TT: 3x140 k
	7b	801	180	0.45	B	TT: 3x140/2x160/3x180 k
3	8	1156	260	0.65	A4	3rd OL ; 1000+500 = 1500 cycles
	8	801	180	0.45	A4	TT: 3x140/3x160/3x180 k
	9	890	200	0.50	B	TT: 3x140/3x160/3x180/3x200 k
4	13	1423	320	0.80	A5	4th OL ; 500+250 = 750 cycles
	14	979	220	0.55	A5	TT: 3x140 to 3x220 k (increment = 20 k)
	15	1068	240	0.60	B	TT: 3x140 to 3x240 k (increment = 20 k)
5	18	1605	361	0.90	A5	Spreader beam slips off specimen
	-	1780	400	1.00	-	Estimated capacity (not reached)

The capacity and failure mode of AE Specimen #1 could not be determined experimentally since the spreader beam slipped off the specimen due to the elastomeric bearing pads at the contact surfaces while reaching an applied force of 1605 kN (361 kips) corresponding to a shear force of 803 kN (181 kips). Therefore the capacity (maximum shear force) was estimated to be about 1780 kN (400 kips) using Response 2000 which has been shown to provide excellent prediction for these specimens [HIG]. This value was then used to compute the force ratios P_{max}/P_{ult} .

6.6.4.2 AE Specimen #2

Illustrated in Figure 6.11 is the actual loading protocol that was applied to AE specimen #2. Table 6.4 shows the summary log file for the whole experiment.

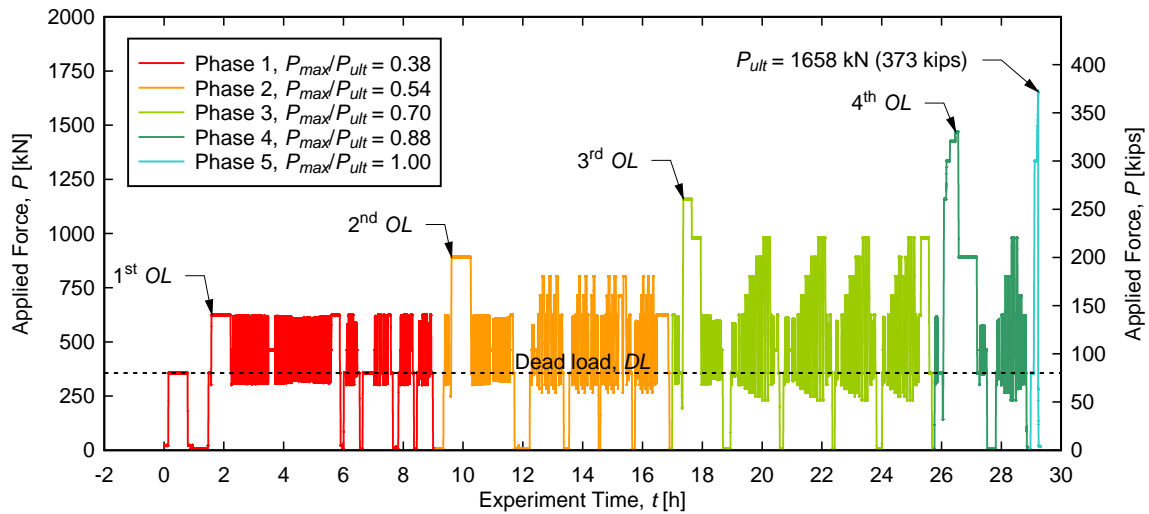


Figure 6.11: Actual loading protocol for AE Specimen #2

The capacity of AE Specimen #2 was found experimentally at a total applied force of 1658 kN (373 kips) which corresponds to a shear capacity of 829 kN (187 kips). Failure occurred in shear-compression mode with the failure crack pattern as illustrated in Figure 6.17.

Table 6.4: Log File Summary AE Specimen #2 (DL = dead load, OL = overload, TT = test truck)

Ph.	Session	Max. appl. force		P_{max}/P_u <i>t</i>	Array	Applied forces, comments
		[kN]	[kips]			
		[-]		[-]	[-]	
1	1	356	80	0.21	A1	1 st DL
	2	623	140	0.38	A1	1st OL ; 2x1000 = 2000 cycles
	2b	623	140	0.38	A1	2x1000 = 2000 cycles
	2c	623	140	0.38	A1	1000 cycles
	3	623	140	0.38	A2	TT: 3x140 k
2	4	623	140	0.38	B	TT: 3x140 k
	7	890	200	0.54	A2	2nd OL ; 2x1000 = 2000 cycles
	8	801	180	0.48	A2	TT: 3x140/3x160/3x180 k
3	9	801	180	0.48	B	TT: 3x140/3x160/3x180 k
	12	1156	260	0.70	A2	3rd OL ; 2x500 = 1000 cycles
	13	979	220	0.59	A3	TT: 3x140 to 3x220 k (increment = 20 k)
4	14	979	220	0.59	B	TT: 3x140 to 3x220 k (increment = 20 k)
	17	1468	330	0.88	A4	4th OL ; 250 cycles
5	18	979	220	0.59	A4	TT: 3x140/3x160/3x180/3x220 k
	19	1658	373	1.00	A4	Ultimate capacity

6.7 SPECIMEN RESPONSE

6.7.1 AE Specimen #1

Illustrated in Figure 6.12 is the mid-span displacement over the whole experiment for AE Specimen #1. Support deflections were subtracted to remove rigid body deformations. Figure 6.14 shows all developed cracks at the end of the experiment. Notice that the average crack angle on the left side (S) where there is less transverse steel (stirrup spacing wider) is shallower compared to the right side (N). No failure crack could be designated since failure was never reached.

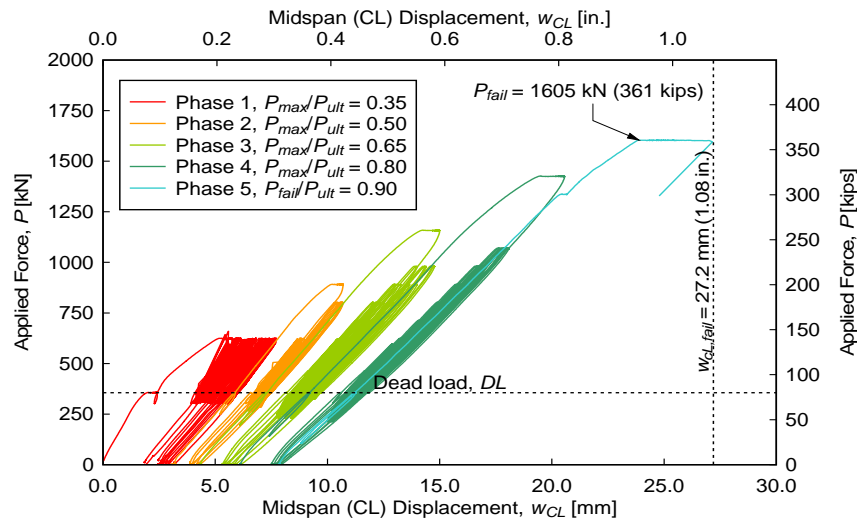


Figure 6.12: Mid-span displacement for AE Specimen #1

Below, the behavior of AE Specimen #1 and key measurements for each phase are summarized. Figure 6.13 shows the crack patterns on the east face that had formed and represents the different stages of deterioration before the simulated service level test trucks were applied. Internal strain gages on stirrups are shown with a red circle where #1 is the first one on the left and #8 the one on the very right. The ratio of applied force to ultimate capacity is given for reference.

6.7.1.1 Phase 1 ($P_{max}/P_{ult} = 0.35$)

Force was applied to the specimen for the first time. Some shrinkage cracks were present but they were distinguishable since they didn't follow the pattern for either shear or moment cracks. Crack initiation occurred at an applied force of about 310 kN (70 kips) which was still below the self weight of 356 kN (80 kips) to be applied. The maximum applied force (overload) was 623 kN (140 kips). Eight major moment and shear cracks had developed at the end. After that, a total of 5000 cycles with a minimum of 302 kN (68 kips) and a maximum of 623 kN (140 kips) were applied to release residual stresses. In addition to the cracks formed before, a few new cracks developed and older ones further propagated. The ones closest to the application point of the force terminated about 0.25 m (10 in.) away from the free surface. The maximum stirrup strains were recorded at strain gage #5 with about 1530 $\mu\epsilon$, followed by strain gage #7 with 595 $\mu\epsilon$. In both cases, diagonal cracks were close to the location of the strain gages. The maximum flexural strains measured were 750 $\mu\epsilon$ and 390 $\mu\epsilon$ at mid-span and the cut-off AE Specimen #1 did not have an actual bar cut-off location, respectively. The maximum mid-span displacement was 6.0 mm (0.238 in.). The maximum measured crack width at the applied self weight (356 kN) was 0.20 mm (0.008 in.).

6.7.1.2 Phase 2 ($P_{max}/P_{ult} = 0.50$)

The maximum applied force was the overload force imposed at the beginning of this phase with an amplitude of 890 kN (200 kips). Except for two cracks in the deck close to the support and one shallow crack originating from the support region, no new diagonal cracks formed. However, existing ones further propagated. After that, a total of 2000 cycles with a minimum of 302 kN (68 kips) and a maximum of 623 kN (140 kips) were applied to release residual stresses. No further crack propagation was found. The maximum stirrup strains were recorded at strain gage #5 with about 2060 $\mu\epsilon$, followed by strain gage #7 with 930 $\mu\epsilon$. The maximum flexural strains measured were 1030 $\mu\epsilon$ and 430 $\mu\epsilon$ at mid-span and the cut-off location, respectively. The maximum mid-span displacement was 7.5 mm (0.296 in.). The maximum measured crack width at the applied self weight (356 kN) was 0.33 mm (0.013 in.).

6.7.1.3 Phase 3 ($P_{max}/P_{ult} = 0.65$)

The maximum applied force was the overload force imposed at the beginning of this phase with an amplitude of 1156 kN (260 kips). Existing cracks further propagated and some started to coalesce. In addition, little branches started to develop from existing cracks near the deck. After that, a total of 1500 cycles with a minimum of 302 kN (68 kips) and a maximum of 623 kN (140 kips) were applied to release residual stresses. No further crack propagation was found. While the overload was applied, strain gage #5 failed most likely due to debonding. The maximum stirrup strains were recorded at strain gage #7 with about 1340 $\mu\epsilon$, followed by strain gage #4 with 880 $\mu\epsilon$. The maximum flexural strains measured were 1360 $\mu\epsilon$ and 630 $\mu\epsilon$ at mid-span and the cut-off location, respectively. The maximum mid-span displacement was 7.5 mm (0.296 in.). The maximum measured crack width at the applied self weight (356 kN) was 0.76 mm (0.03 in.).

6.7.1.4 Phase 4 ($P_{max}/P_{ult} = 0.80$)

The maximum applied force was the overload force imposed at the beginning of this phase with an amplitude of 1423 kN (320 kips). Existing cracks further propagated and some started to coalesce. Cracks branched out and crack edges at some spots started to disintegrate. The longest diagonal crack now turned horizontally towards the compression block, leaving a distance of about 0.10 m (4 in.) to the free surface. After that, a total of 750 cycles with a minimum of 302 kN (68 kips) and a maximum of 623 kN (140 kips) were applied to release residual stresses. No further crack propagation was found. The maximum stirrup strains were recorded at strain gage #4 with about 1750 $\mu\epsilon$, followed by strain gage #7 with 1560 $\mu\epsilon$. Strain gage #4 failed during cyclic loading most likely due to debonding. The maximum flexural strains measured were 1710 $\mu\epsilon$ and 1080 $\mu\epsilon$ at the cut-off and the mid-span location, respectively. The maximum mid-span

displacement was 14.4 mm (0.568 in.). The maximum measured crack width at the applied self weight (356 kN) was 2.0 mm (0.08 in.).

6.7.1.5 Phase 5 ($P_{max}/P_{ult} = 0.90$)

Failure occurred in this phase as the compression block failed at a maximum applied force of 1605 kN (361 kips) causing the spreader beam to slip off the specimen. Ultimate capacity was never reached but estimated using Response 2000. No more test trucks were applied after this point. The final crack pattern is illustrated in Figure 6.15.

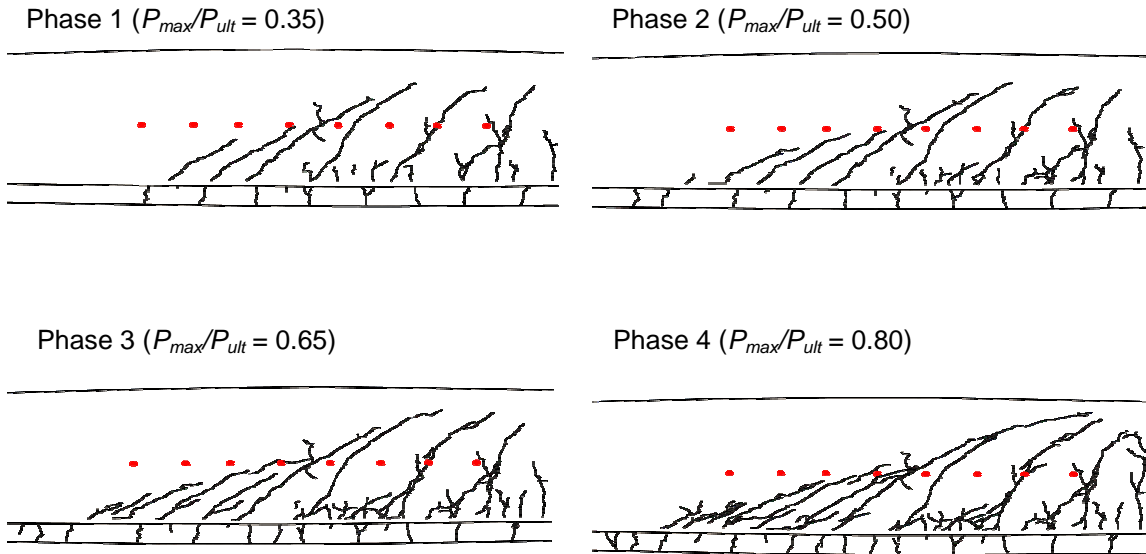


Figure 6.13: Existing cracks for each phase before test trucks were applied for AE Specimen #1 (only cracks on east face shown for clarity)

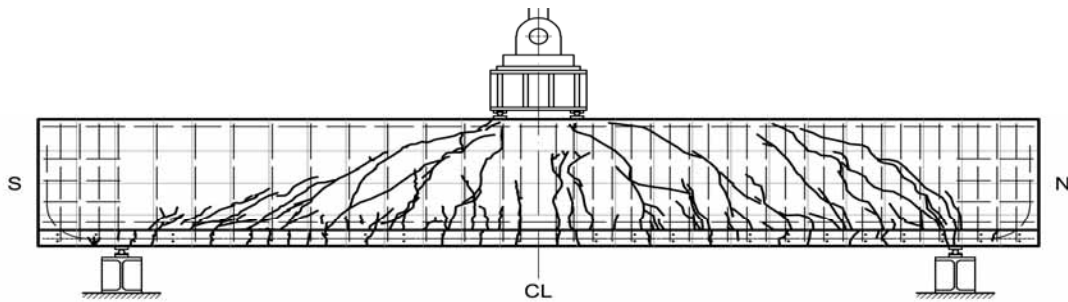


Figure 6.14: Crack pattern at failure for AE Specimen #1 (East face only)

6.7.2 AE Specimen #2

Illustrated in Figure 6.15 is the mid-span displacement over the whole experiment for AE Specimen #2. Support deflections were subtracted to remove rigid body deformations. Figure 6.17 shows all developed cracks at the end of the experiment. The difference between crack angles on the left vs. right side not as pronounced as in AE Specimen #1. Recall that this specimen had the two outer tension rebar's (bottom) cut-off 2.13 m (7ft) away from the center line (marked with a vertical arrow). The failure crack is shown with a thick line.

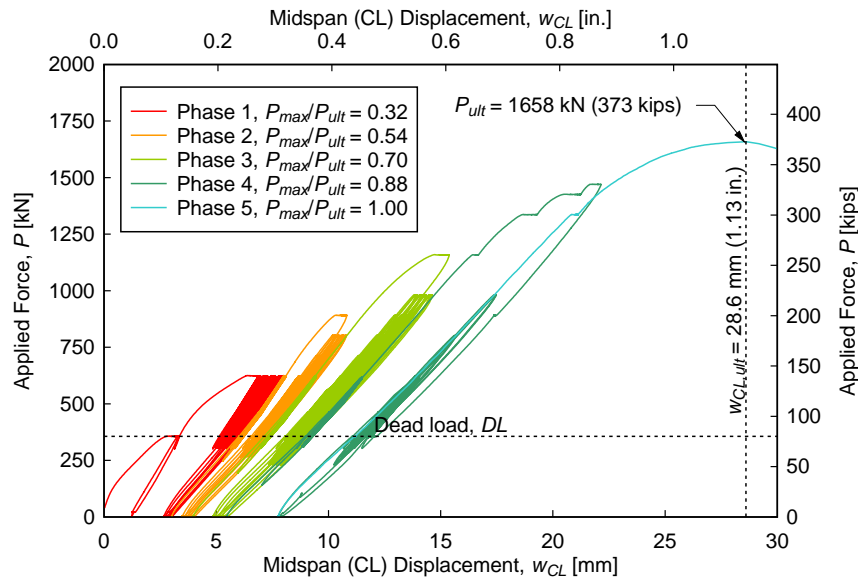


Figure 6.15: Mid-span displacement for AE Specimen #2

Below, the behavior of AE Specimen #2 and key measurements for each phase are summarized. Figure 6.16 shows the crack patterns on the east face that had formed and represents the different stages of deterioration before the simulated service level test trucks were applied. Internal strain gages on stirrups are shown with a red circle where #1 is the first one on the left and #8 the one on the very right. The ratio of applied force to ultimate capacity is given for reference.

6.7.2.1 Phase 1 ($P_{max}/P_{ult} = 0.38$)

Force was applied to the specimen for the first time. Some shrinkage cracks were present and marked for easier distinction from new forced cracks. Crack initiation occurred at an applied force of about 320 kN (72 kips) which was still below the self weight of 356 kN (80 kips) to be applied. The maximum force applied was 623 kN (140 kips). Eight major moment and shear cracks had developed at the end. After the first applied overload, a total of 5000 cycles with a range between of 623 kN (140 kips) were applied of the same amplitude to release residual

stresses. In addition to the cracks formed before, new cracks developed and older ones further propagated. The ones closest to the application point of the force terminated about 0.18 m (7 in.) away from the top surface. The maximum stirrup strains were recorded at strain gage #7 with about 1990 $\mu\epsilon$ which is close to yielding, followed by strain gage #7 with 1560 $\mu\epsilon$. In both cases, diagonal cracks were close to the location of the strain gages. The maximum flexural strains measured were 650 $\mu\epsilon$ and 750 $\mu\epsilon$ at mid-span and the cut-off location, respectively. The maximum mid-span displacement was 6.2 mm (0.244 in.). The maximum measured crack width at the applied self weight (356 kN) was 0.64 mm (0.025 in.).

6.7.2.2 Phase 2 ($P_{max}/P_{ult} = 0.54$)

The maximum applied force was the overload force imposed at the beginning of this phase with an amplitude of 890 kN (200 kips). A few new cracks formed in the deck close to the support and existing cracks further propagated. After the first applied overload, a total of 2000 cycles with a range between of 623 kN (140 kips) were applied of the same amplitude to release residual stresses. No further crack propagation was observed. The maximum stirrup strains were recorded at strain gage #7 with about 1610 $\mu\epsilon$, followed by strain gage #3 with 1080 $\mu\epsilon$. Strain gage #4 failed during the overload most likely due to de-bonding. The maximum flexural strains measured were 920 $\mu\epsilon$ and 890 $\mu\epsilon$ at mid-span and the cut-off location, respectively. The maximum mid-span displacement was 7.8 mm (0.307 in.). The maximum measured crack width at the applied self weight (356 kN) was 1.02 mm (0.04 in.).

6.7.2.3 Phase 3 ($P_{max}/P_{ult} = 0.70$)

The maximum applied force was the overload force imposed at the beginning of this phase with an amplitude of 1156 kN (260 kips). A completely new crack formed in a so far uncracked region in the middle of the high shear region. Existing cracks further propagated and started to coalesce. After the first applied overload, a total of 1000 cycles with a range between of 623 kN (140 kips) were applied of the same amplitude to release residual stresses. No further crack propagation was observed. While the overload was applied, strain gage #7 failed most likely due to de-bonding. The maximum stirrup strains were recorded at strain gage #6 with about 3070 $\mu\epsilon$ (well above yielding), followed by strain gage #3 with 1480 $\mu\epsilon$. The maximum flexural strains measured were 1190 $\mu\epsilon$ and 1240 $\mu\epsilon$ at mid-span and the cut-off location, respectively. The maximum mid-span displacement was 11.4 mm (0.449 in.). The maximum measured crack width at the applied self weight (356 kN) was 1.02 mm (0.04 in.).

6.7.2.4 Phase 4 ($P_{max}/P_{ult} = 0.88$)

The maximum applied force was the overload force imposed at the beginning of this phase with an amplitude of 1468 kN (330 kips). Existing cracks further

propagated and started to coalesce. More cracks branched out and crack edges at some spots started to disintegrate. The longest diagonal crack now turned horizontally towards the compression block, leaving a distance of about 0.10 m (4 in.) to the free surface. The maximum stirrup strains were recorded at strain gage #5 with about $640 \mu\epsilon$, followed by strain gage #1 with $450 \mu\epsilon$. Strain gage #3 and #6 failed during the overload most likely due to de-bonding. The maximum flexural strains measured were $1490 \mu\epsilon$ and $1430 \mu\epsilon$ at mid-span and the cut-off location, respectively. The maximum mid-span displacement was 16.7 mm (0.658 in.). The maximum measured crack width at the applied self weight (80 kips) was $> 2.0 \text{ mm}$ ($> 0.08 \text{ in.}$).

6.7.2.5 Phase 5 ($P_{max}/P_{ult} = 1.00$)

The specimen failed in shear-compression mode at a maximum applied force of 1658 kN (373 kips). No more test trucks were applied after this point. The final crack pattern is illustrated in Figure 6.19.

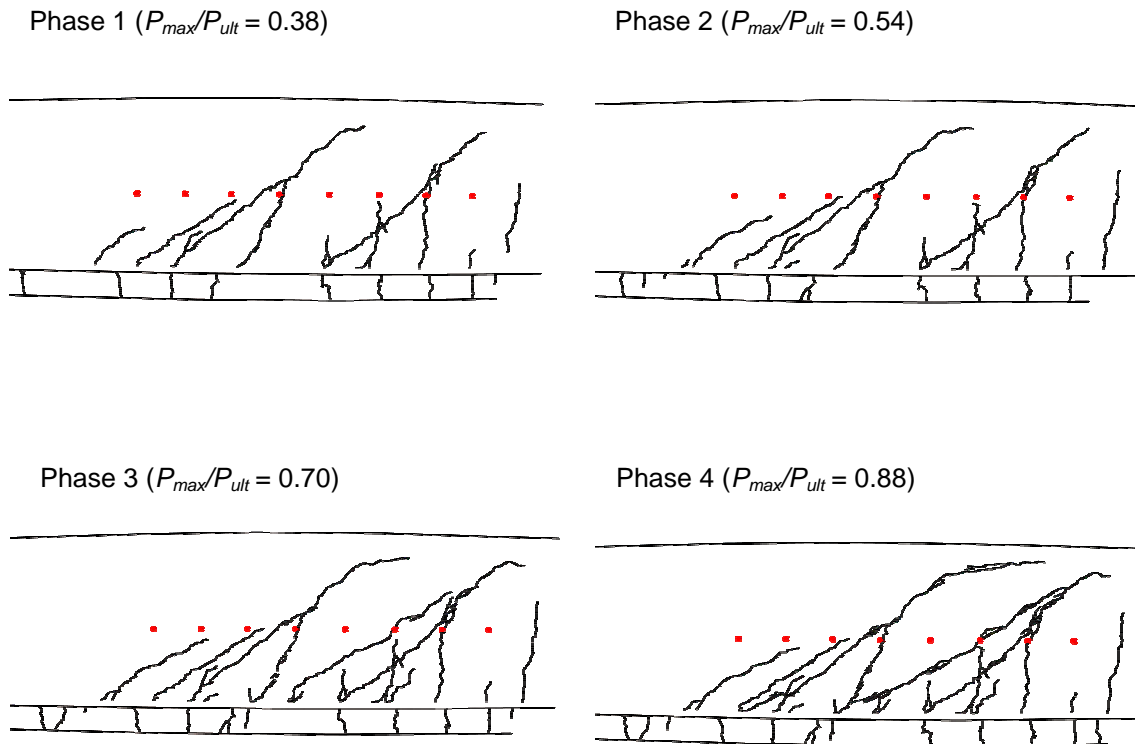


Figure 6.16: Existing cracks for each phase before test trucks were applied for AE Specimen #2 (only cracks on east face shown for clarity)

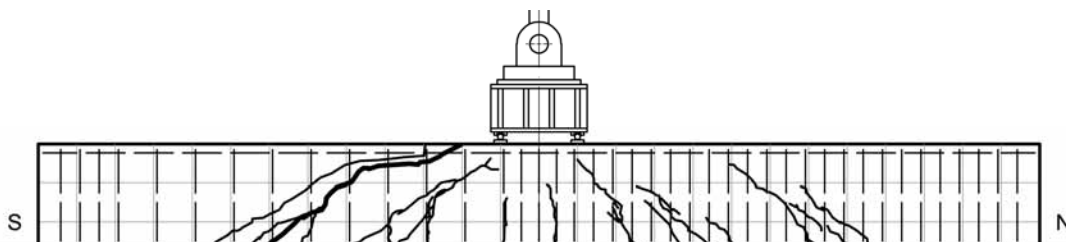


Figure 6.17: Crack pattern at failure for AE Specimen #2 (East face only)

7.0 SENSOR ARRAY A

Sensor array A was used to evaluate overload (OL) events, cyclic loading, and simulated test trucks as described in section 6.6.4. Qualitative as well as quantitative procedures were applied to this array as described in sections 4.3 and 4.4. This sensor array covers the most data and was therefore examined more in depth than the other arrays.

7.1 AE HIT RATES

7.1.1 AE Specimen #1

The most basic method for qualitative AE analysis is by looking at total number of AE hits during loadings and AE hit rates, i.e. how many AE hits are detected per second over time. Figures 7.1 and 7.2 shows the different overloads and subsequently applied service level test trucks. AE hit rates were computed as the sum of all eight sensors. AE hit rates are significantly higher for overload events (right column), where the current force exceeds the maximum previous force, than loads on service level (left column), where the previous maximum force is not reached. Peak AE hit rates between different overloads do not significantly vary and do not have a trend to increase when going to higher loads. What can be observed is that the unloading portion becomes more active towards ultimate capacity. This phenomenon is well known and likely due to the increasing number of cracks and locked-in residual strains and therefore also increasing number of potential sources for AE. Typically, the AE hit rate increases during loading, then decreases during the holding phase to reach steady state, indicating that there is still some (stable) creep occurring. This relaxation phase during holding may be indicative of how close the currently applied force is to ultimate capacity. Figure 7.3 illustrates the development of AE hit rates in the holding phase.

The simulated test trucks were in some cases (e.g. Figure 7.1, phase 3) not applied in increasing order to study whether that influences the AE hit response. It was found that when three trucks of the same magnitude are applied subsequently, the AE hit rate and number of hits decreases, i.e. the first truck produces the most AE, the third the fewest. Figure C3.1 in Appendix C illustrates maximum AE hit rates for all applied load cycles. There was no trend for trucks of the same magnitude to produce less AE hits in later phase, i.e. after the element had experienced higher forces.

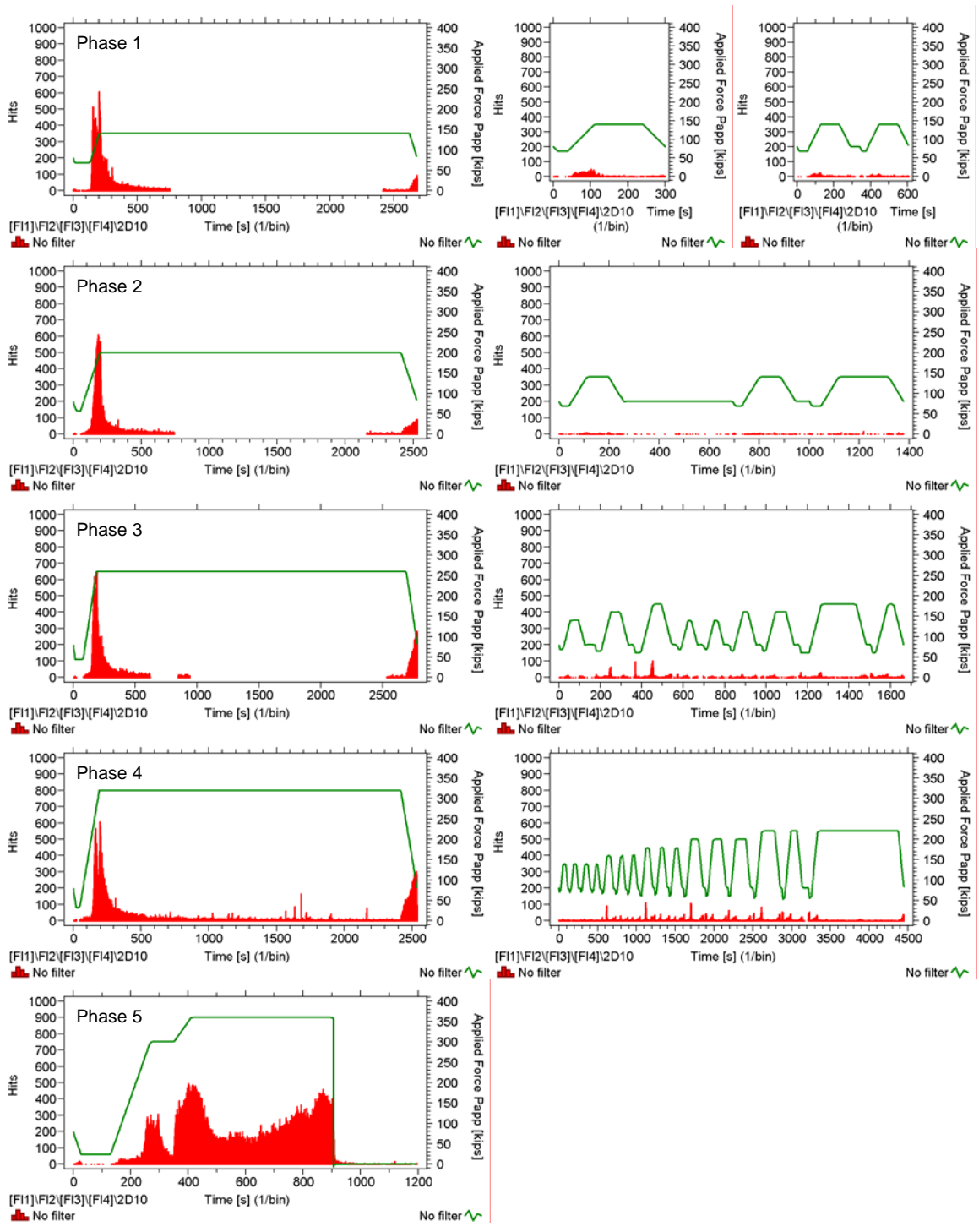


Figure 7.1: Cumulative AE hit rates (from all eight sensors) for AE Specimen #1: left column: overloads; right column: simulated service level test trucks

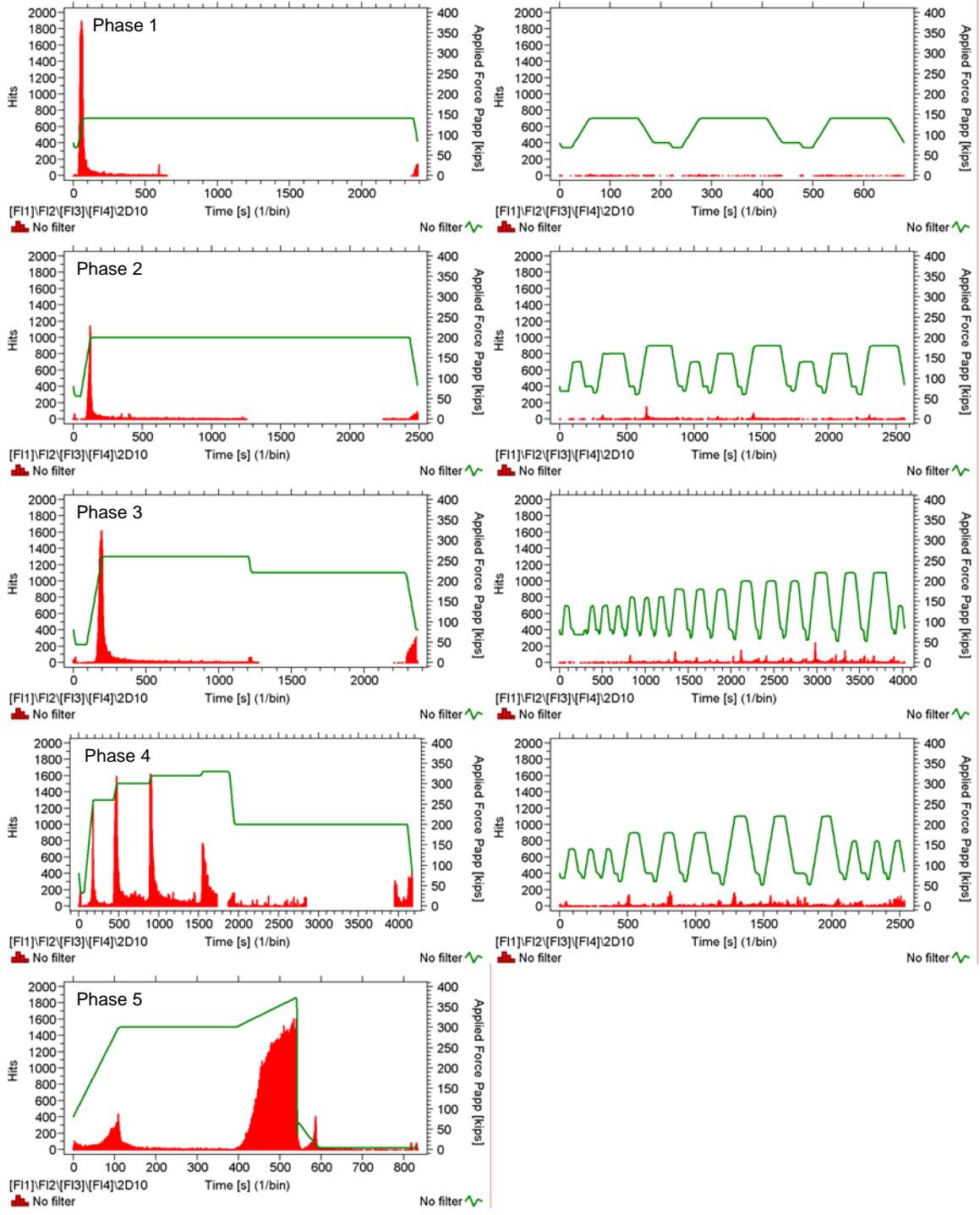


Figure 7.2: Cumulative AE hit rates (from all eight sensors) for AE Specimen #2: left column: overloads; right column: simulated service level test trucks

As can be observed from Figures 7.1 and 7.2, the AE hit rates for the two specimens are quite different (also see Figure C3.1 in Appendix C). Even though the different initial gain settings (44 dB vs. 40 dB) was accounted for by setting different threshold levels (40dB vs. 44 dB), AE Specimen #2 produced up to three times higher AE hit rates compared to AE Specimen #1. It is therefore always recommended to work with dimensionless ratios (like *Calm* or *Load*) when comparing different specimens and not absolute values (like number of AE hits or AE hit rates). See section 4.1.3 for details on sensor pre-amplifiers.

Figure 7.3 illustrates cumulative AE hits recorded from all eight sensors during the holding phases (shown as phase ‘3’ in Figure 4.8). For both specimens, the second overload produced less cumulative AE hits than the first one. However, after that second phase, AE activity increases with higher applied forces. This can be explained by the fact that the redistribution of stresses (creep) takes longer as ultimate capacity of the member is approached. During the last overload of AE Specimen #2, the AE hit rate reached steady state after some time but then started to increase again before the compression block failed and the actuator slipped off the bearing plate. The cumulative AE hit rate in this case correlated well with the redistribution of stresses (creeping) and announced upcoming (partial) failure. Unfortunately, this ‘warning time’ was very short and could therefore probably not be used as indicator for failure.

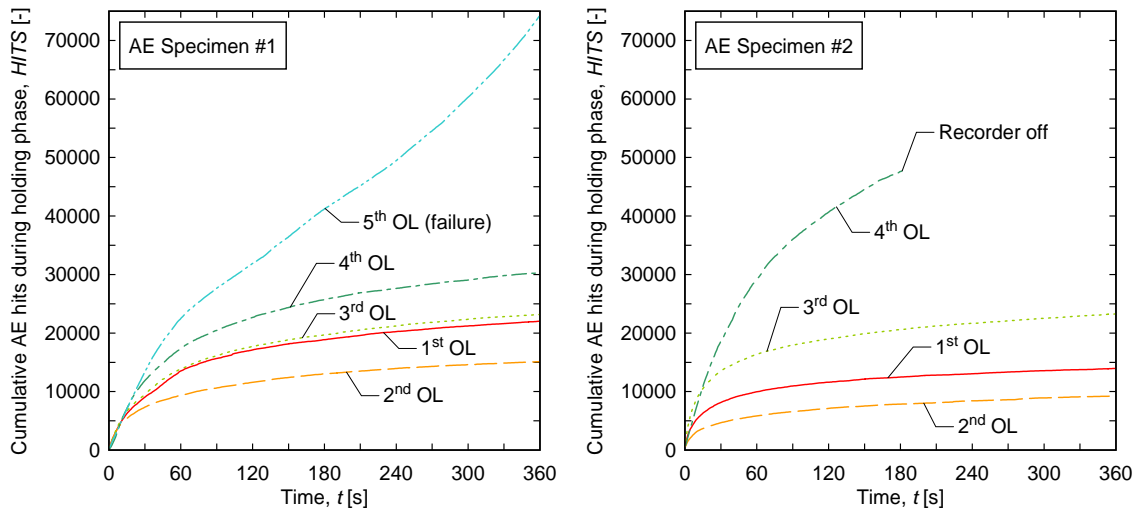


Figure 7.3: Cumulative AE hits during holding phase

7.2 KAISER EFFECT AND FELICITY RATIO

Illustrated in Figure 7.4 are the results obtained from the NDIS-2421 damage assessment procedure based on the Kaiser Effect and the Felicity Ratio as presented in section 4.3.3. A threshold to reject AE hits having amplitudes below 40 dB and 44 dB was applied to AE Specimen #1 and #2, respectively. All sensors were included in the computation (sum of hits of all eight sensors). The critical values that define regions of minor / intermediate / heavy damage as (damage as defined in (*Ohtsu 2002*)) were chosen according to Lovejoy's recommended values (*Lovejoy 2006*).

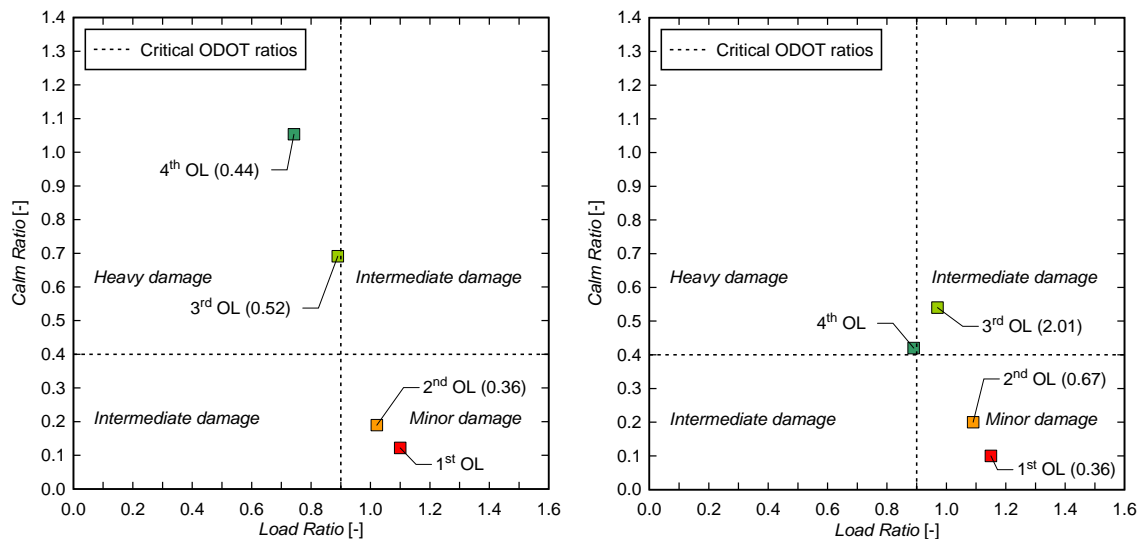


Figure 7.4: Evaluation of AE Specimen #1 (a) and #2 (b) according to the NDIS-2421 procedure

For AE Specimen #1 (a), a very high correlation was found between *Load* and *Calm Ratio* for the different overloads (OL). The corresponding maximum relative crack mouth opening displacements (*CMOD*) in millimeter for crack clip #1 are presented in parentheses. *Load* and *Calm Ratios* for AE Specimen #2 (b) fit well in the graph up to the third overload. The last data point (4th overload) appears to be too low. Overall, the procedure appears to work for overloads even when cyclic loadings in between these damage inducing loads are imposed to remove residual stresses.

However, this kind of procedure could not easily be applied to an in-service bridge test since new damage has to be imposed in order to get meaningful results. The procedure was initially applied to the service-level loads as well but the data turned out to be not very conclusive. When looking at the average ratios of all test truck groups for each phase, the *Load Ratio* showed a decreasing trend, whereas the *Calm Ratio* did not show a definite trend. This is illustrated in Figures 7.5 and 7.6. However, the *Load Ratio* is not easily applicable in the field as the previous maximum load is usually unknown. Maps of the developed cracks for each phase are shown in Figures 6.15 and 6.18 for AE Specimen #1 and #2, respectively.

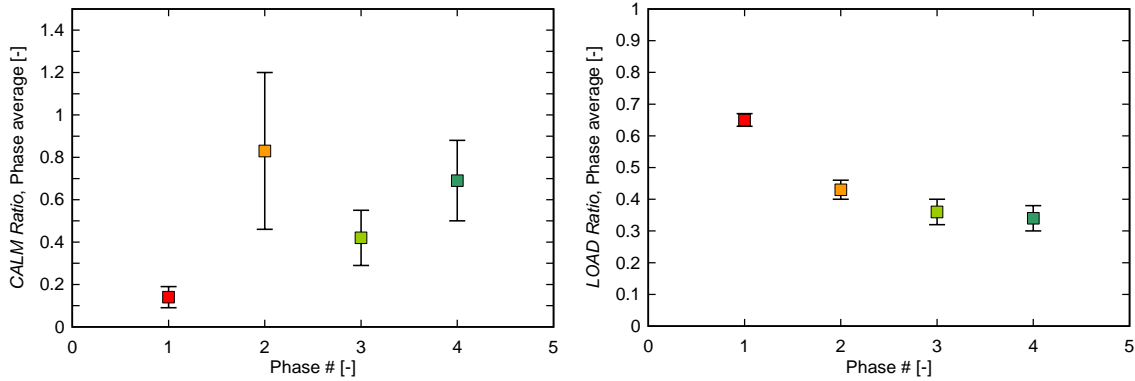


Figure 7.5: Average *Calm* and *Load Ratios* for each phase for AE Specimen #1

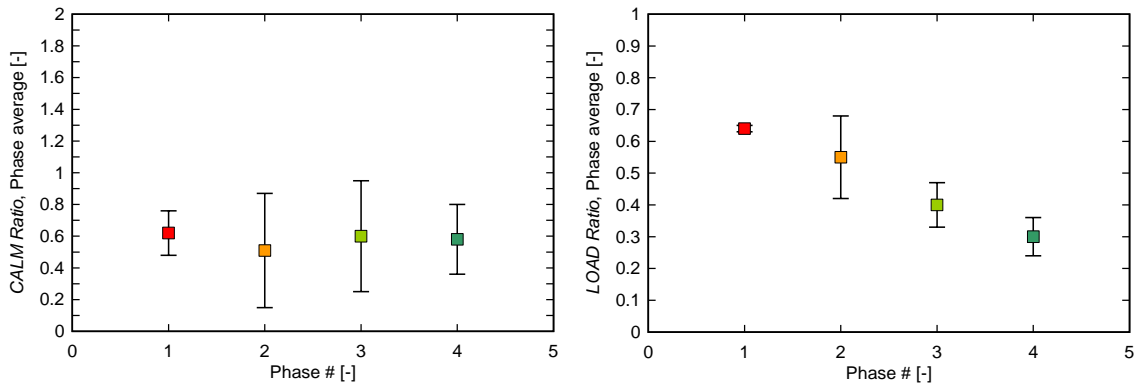


Figure 7.6: Average *Calm* and *Load Ratios* for each phase for AE Specimen #2

Figures C4.1 and C4.2 in Appendix C show the individual *Calm* and *Load Ratios* for each truck group.

7.3 MINIMUM *B*-VALUE ANALYSIS

Summarized in this section are results from the proposed minimum *b*-value analysis for the entire experiment. Minimum *b*-values were computed according to section 4.3.5 with 50 consecutive AE hit amplitudes included in the computation. Minimum *b*-values of all applied load cycles are shown in Appendix C5.1 and C5.2. In the following figures, individual *b*-values (from one sensor) are shown as black dots and mean *b*-values (computed by taking the average from all eight sensors) as colored squares. Error bars represent one standard deviation and are shown for each individual load cycle. Curve-fits (prediction of mean) are represented by a full black line and 95 % confidence limits as red dashed lines. 95 % prediction limits for the entire data set are shown as dotted blue lines. The following ratios are used subsequently to normalize forces:

$$LR = \text{Applied force} / \text{Ultimate capacity} \quad (7.1)$$

$$LR2 = \text{Applied force} / \text{Previous maximum applied force} \quad (7.2)$$

Figure 7.7 shows the results from applied overloads for both specimens. It can be observed that forces that are higher than previously applied ones produce minimum b -values well below a value of 1, even below 0.5, which was suggested earlier by other researchers (*Kurz 2006; Rao 2005*). Also, there is an overall trend for minimum b -values to decrease as ultimate capacity is approached.

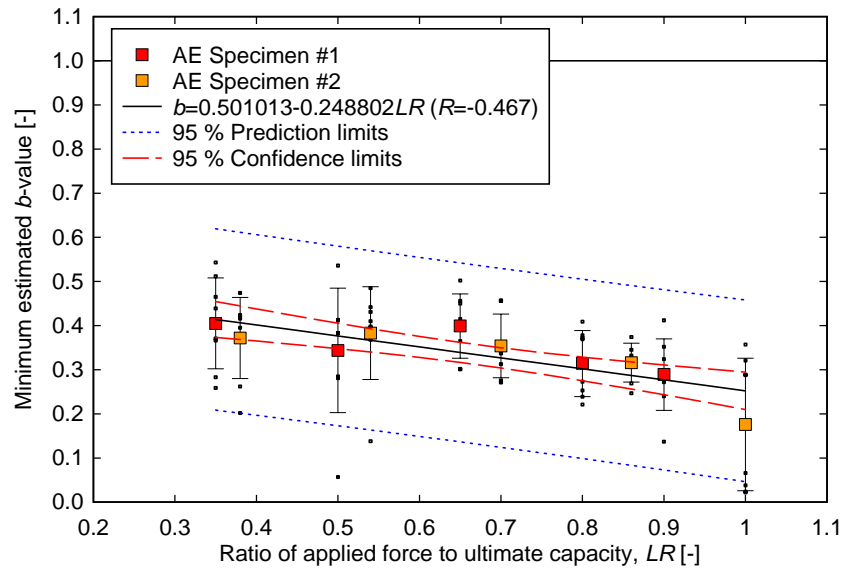


Figure 7.7: Minimum estimated b -values from overloads for both specimens

Figures 7.8 and 7.9 show minimum b -values for the simulated test trucks for each phase for AE Specimen #1 and #2, respectively. Minimum b -values from all three individual test trucks were lumped into one data set. For the later phases where test trucks with different magnitudes were available, a clear trend was present for the minimum b -value to decrease with increasing loads and this is true for both specimens. It can also be observed that the data variation (or scatter) decreases as higher forces are applied which suggests that damage becomes more localized.

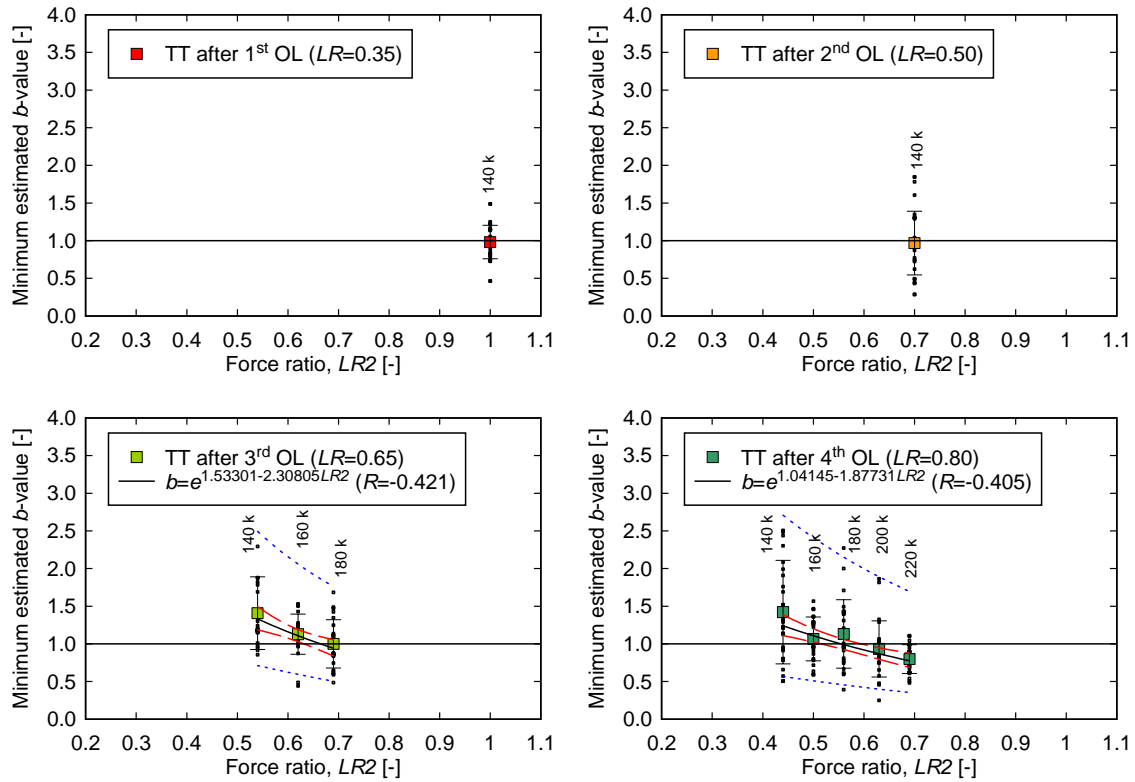


Figure 7.8: Minimum averaged b -values from applied test trucks for AE Specimen #1

Physical measurements such as rebar strains, diagonal displacements, and crack motions remained fairly constant (difference $< 2\%$) over a series of equally high test trucks. Maximum stirrup strains ranged between about 300 and 900 $\mu\epsilon$ (which corresponds to a stress range of about 8.5 to 26 ksi), depending on the applied force and the stage of deterioration (phase). The b -value response on the other hand differed up to 25% for some test truck groups. Therefore it is very important to always show some measure for data variability (e.g. one standard deviation) and not only the mean.

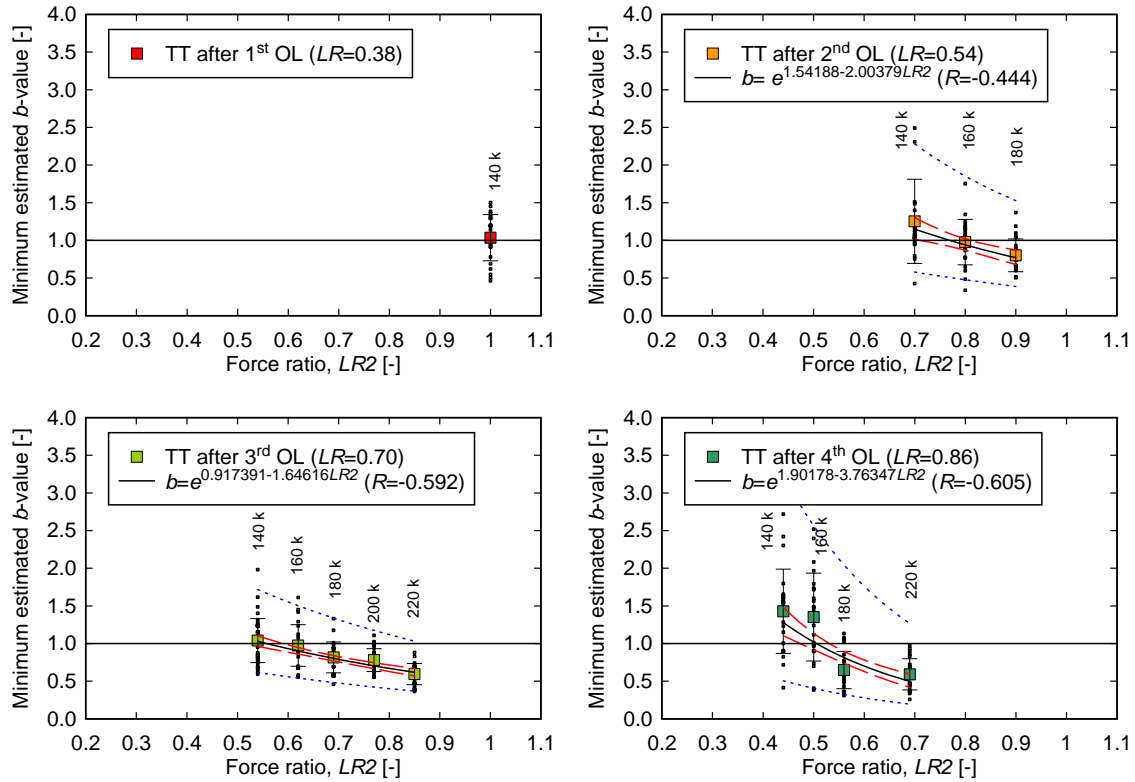


Figure 7.9: Minimum averaged b -values from applied test trucks for AE Specimen #2

In Figure 7.10, minimum b -values for the 140 kip test truck are plotted against the stage of damage (phase). A clear trend for the minimum b -value to increase as the specimen has experienced higher loads in the past can be observed for that truck type, which is the most realistic one in terms of weight. For some of the heavier test trucks (160 to 220 kips), there were too few data points generated to draw conclusions. More important, in terms of the applied load compared to the previous maximum load (named $LR2$ Ratio), the same is true: As that ratio decreases, the minimum b -value increases. This observation could be taken advantage of to develop a tool for estimating the load history a bridge girder has experienced or the load level it is currently operating at. If the minimum b -value response due to a certain imposed test truck is high (e.g. > 1.2), it can be assumed that that bridge girder must have seen much higher loads before. If the minimum b -value is low (e.g. 1.0 to 1.2), the bridge may be operating at a similar load level than the applied test truck. A very low minimum b -value (e.g. < 0.90) suggests that deterioration occurred as the test truck was applied which implies that the operating level was lower than the test truck.

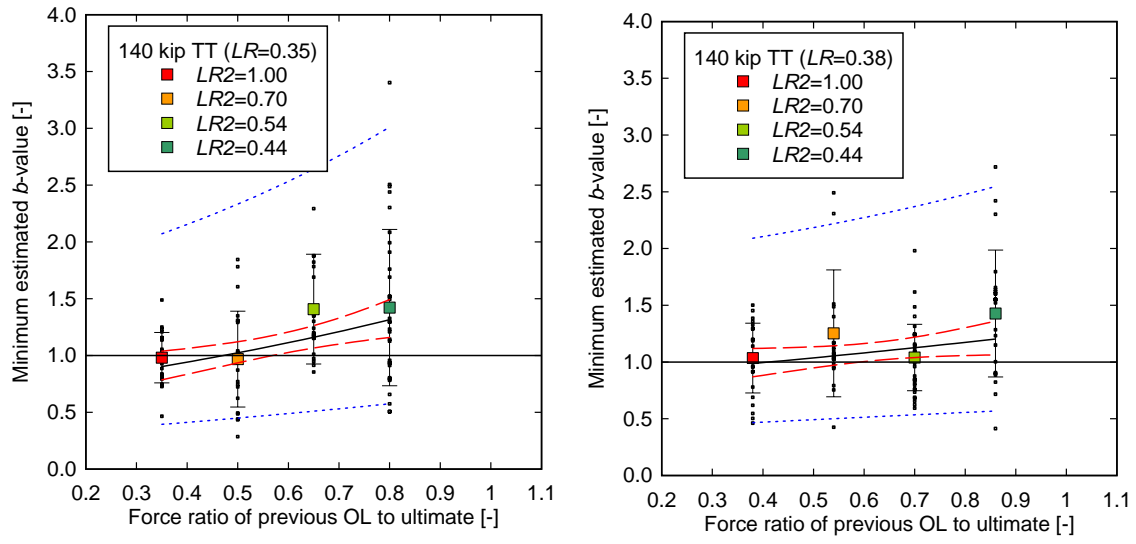


Figure 7.10: Minimum averaged b -values for the 140 kip test truck for AE Specimen #1 (left) and #2 (right) Estimation of 3-D AE Source Locations

7.3.1 AE Specimen #1

Presented in this section are estimated 3-D AE source locations found with sensor arrays A1 to A5 as presented in section 6.5.1 using the KRNi060 sensors. Table 7.1 shows the number of located AE events classified by their level of quality as specified in section 4.5.1. All results were computed and visualized with VisualAE inserting photos that were taken during the experiment as background images. Only AE events with five signals were included in the event assembling to maximize the number of events while still having a measure for their uncertainty (see section 4.5.1). AE events that were located more than 36 mm (1.4 in.) outside of the specimen were rejected via spatial filtering. Data acquisition settings and options are listed in Table B3.1 in Appendix B.

Table 7.1: Summary of located AE events (DL = dead load, OL = overload, TT = test truck)

Ph.	Session	Load type	P_{max}/P_{ult}	Array	Number of located AE events			
					Level 1	Level 2	Level 3	Total
	[-]		[-]	[-]				
1	1	DL	0.20	A1	83	56	42	181
	1	1st OL	0.35	A1	62	48	32	142
	1	4 x 500 cycl.	0.35	A2	16	16	15	47
	2	4 x 1000 cycl.	0.35	A2	53	61	43	162
	3	3 TT	0.35	A2	1	4	6	11
2	6	2nd OL	0.50	A3	80	59	64	203
	6	2 x 1000 cycl.	0.35	A3	25	17	32	74
	7	3 TT	0.35	A3	1	1	0	2
3	8	3rd OL	0.65	A4	87	57	81	225
	8	1000 + 500 cycl.	0.35	A4	19	24	16	59
	8	9 TT	0.45	A4	5	4	6	15
4	13	4th OL	0.80	A5	96	62	57	215
	13	500 + 250 cycl.	0.35	A5	14	8	6	28
	14	16 TT	0.55	A5	4	4	10	18
5	18	5th OL	0.90	A5	96	59	91	246
		Located, total			642	480	501	1623
		Percentages [%]			39.5	29.6	30.9	100

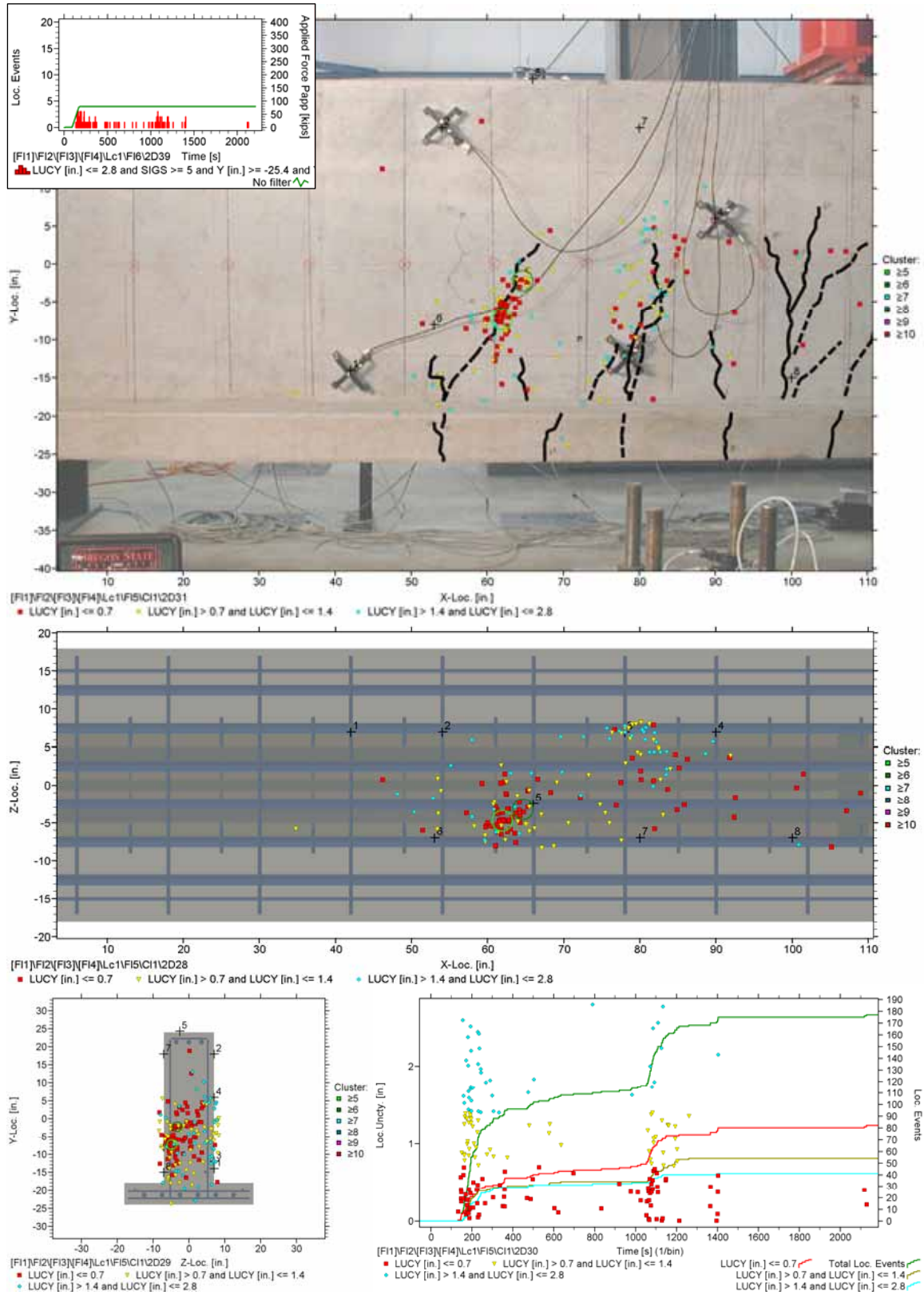


Figure 7.11: Estimated Source Locations, Session 1 (DL)

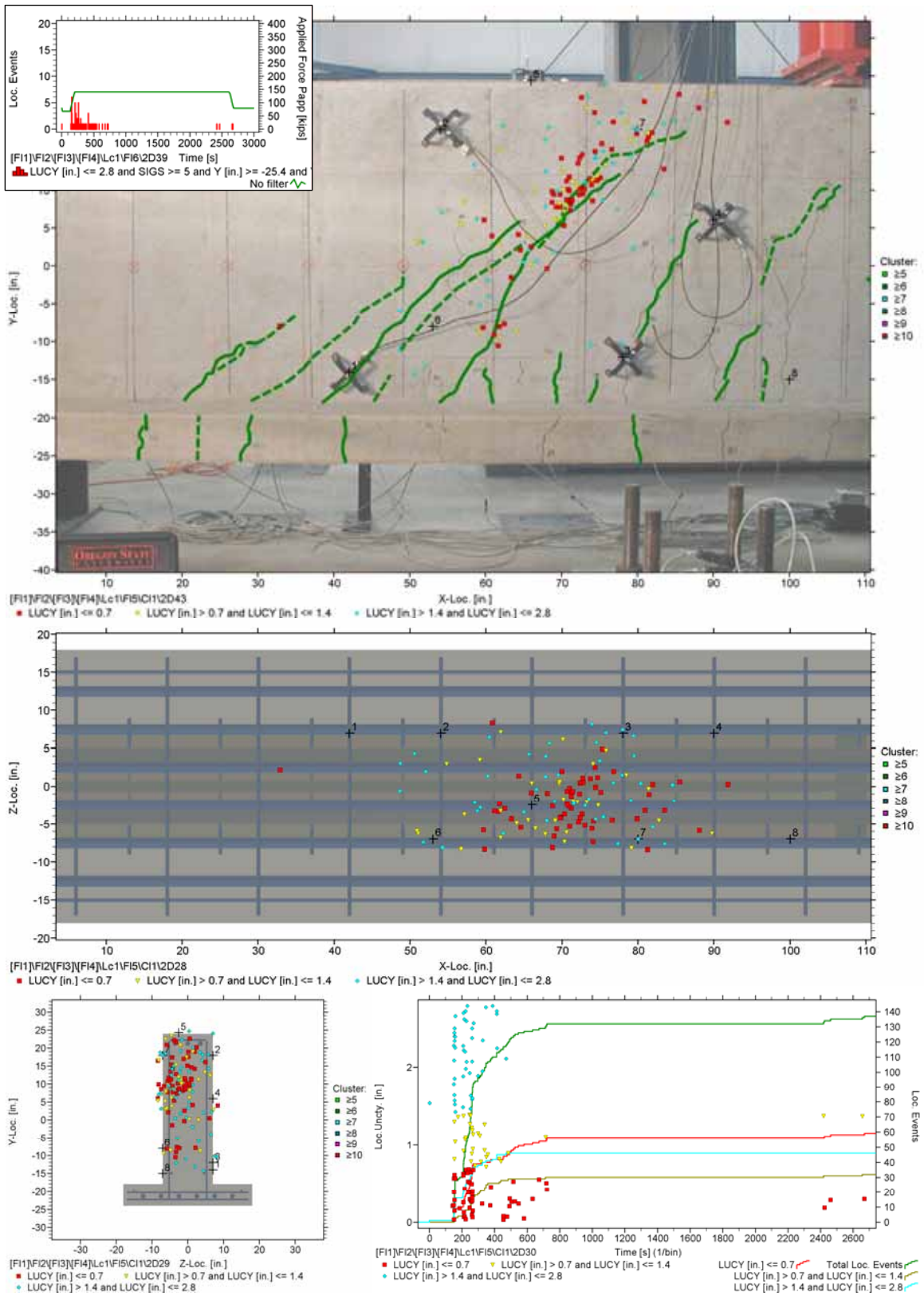


Figure 7.12: Estimated Source Locations, Session 1 (1st OL)

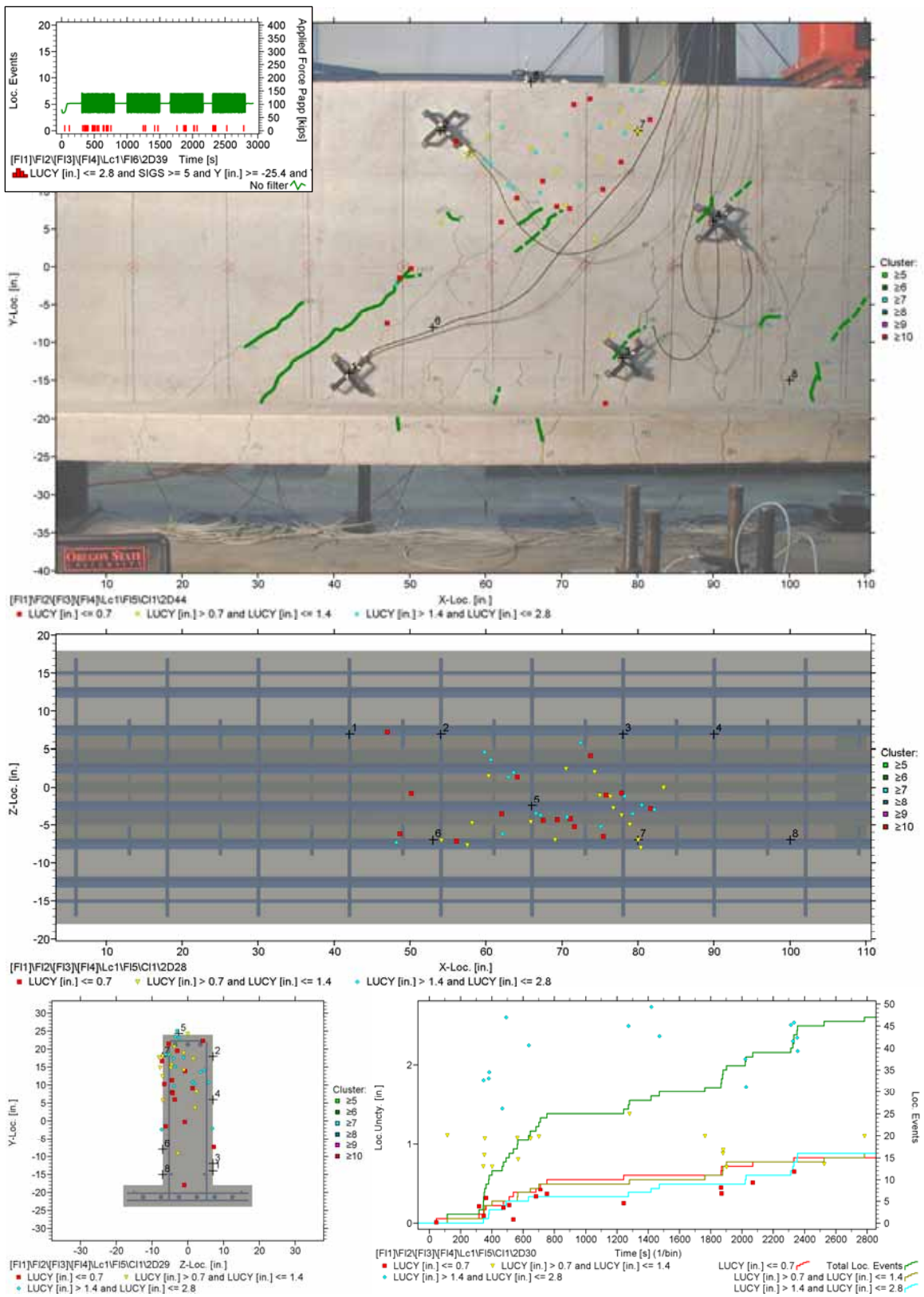


Figure 7.13: Estimated Source Locations, Session 1 (4 x 500 cycles)

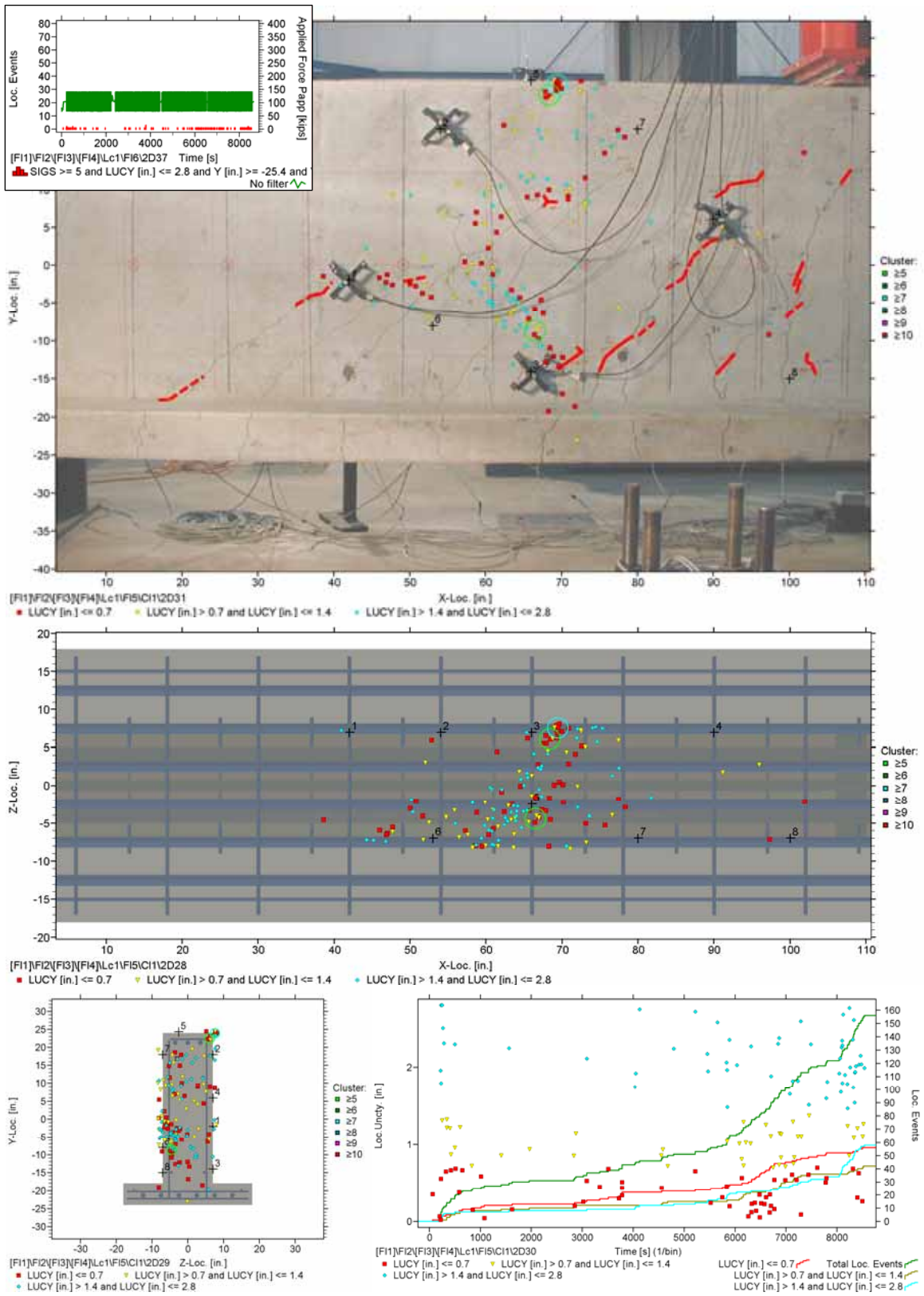


Figure 7.14: Estimated Source Locations, Session 1 (4 x 1000 cycles)

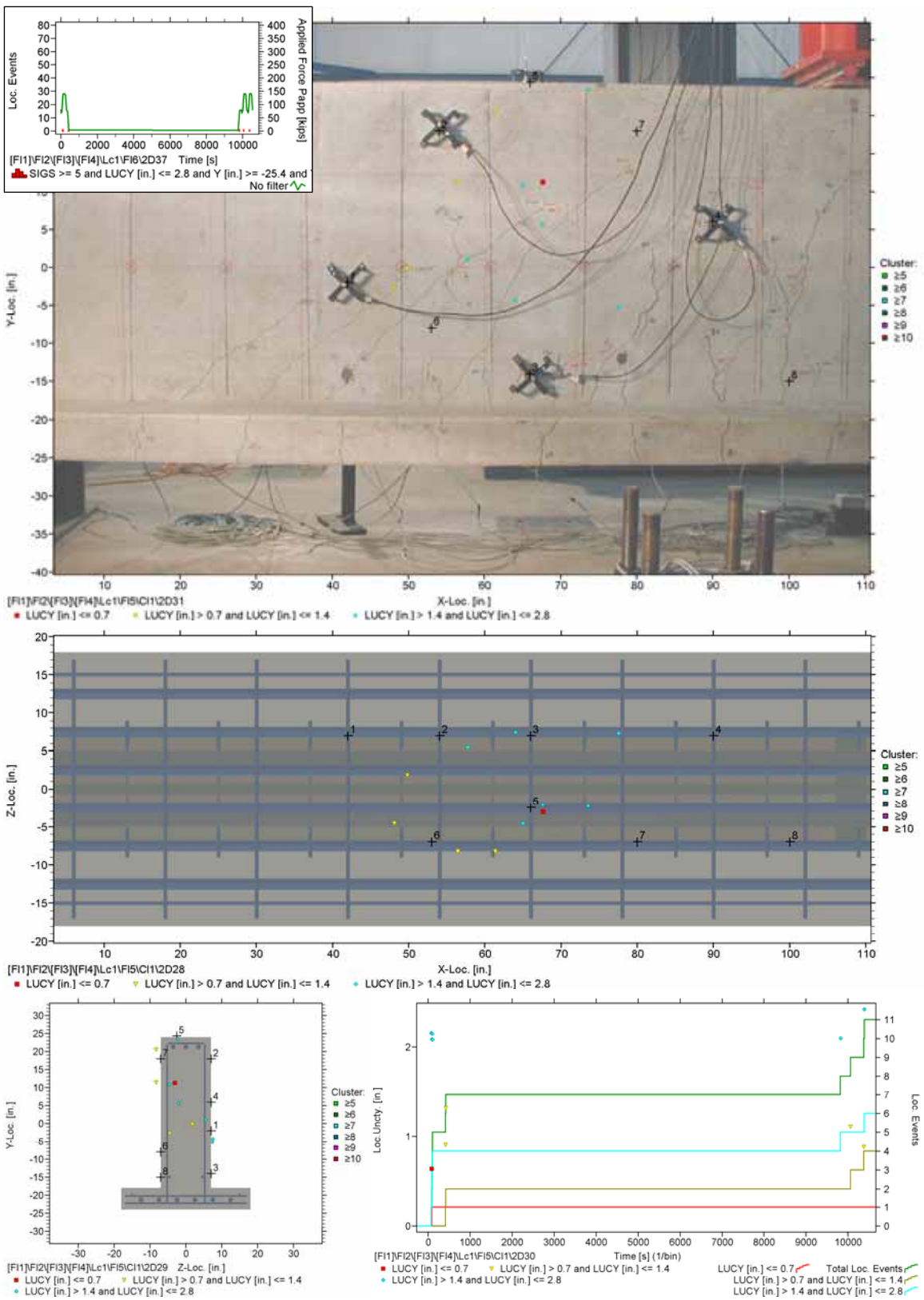


Figure 7.15: Estimated Source Locations, Session 3 (3 TT)

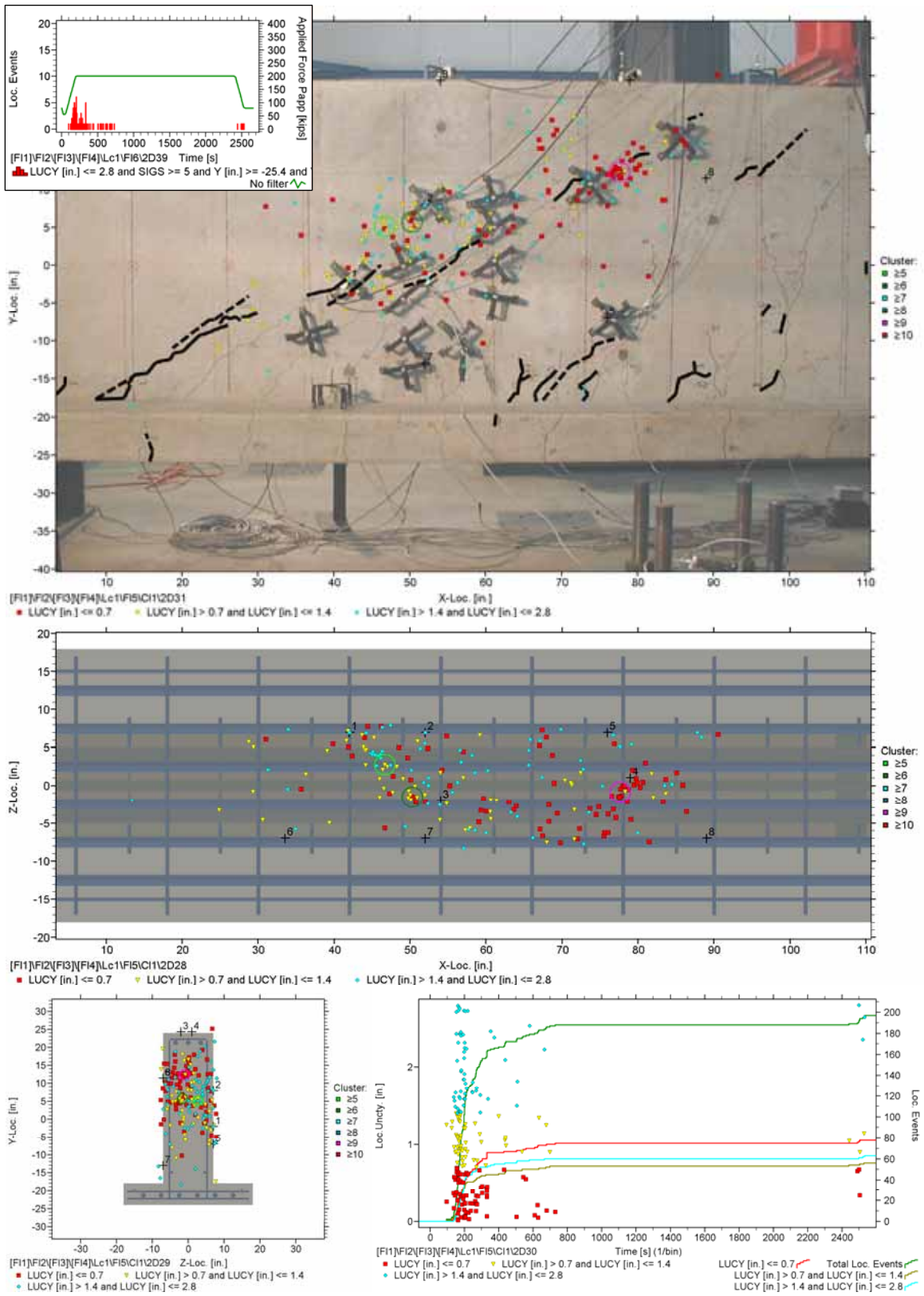


Figure 7.16: Estimated Source Locations, Session 6 (2nd OL)

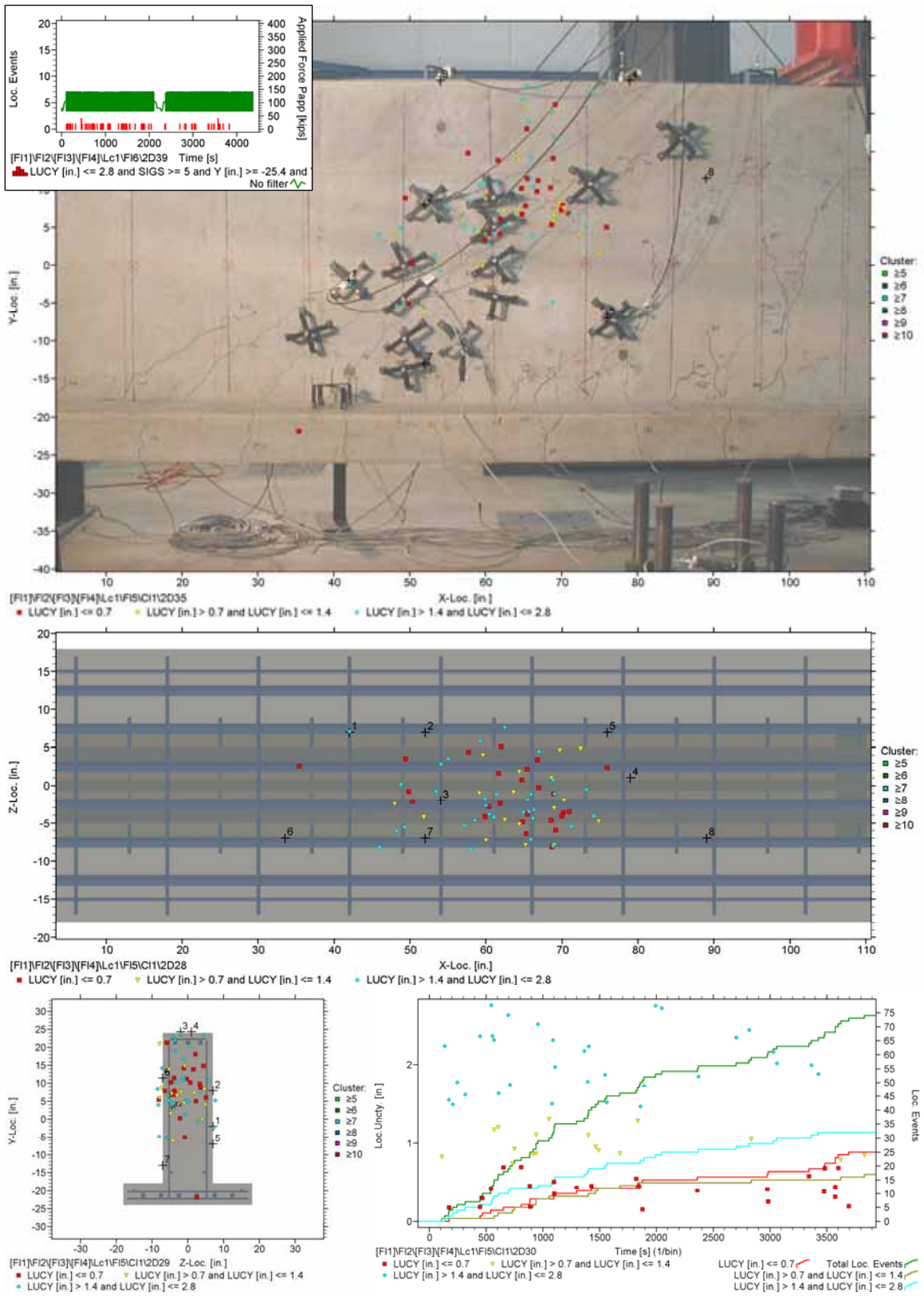


Figure 7.17: Estimated Source Locations, Session 3 (2 x 1000 cycles)

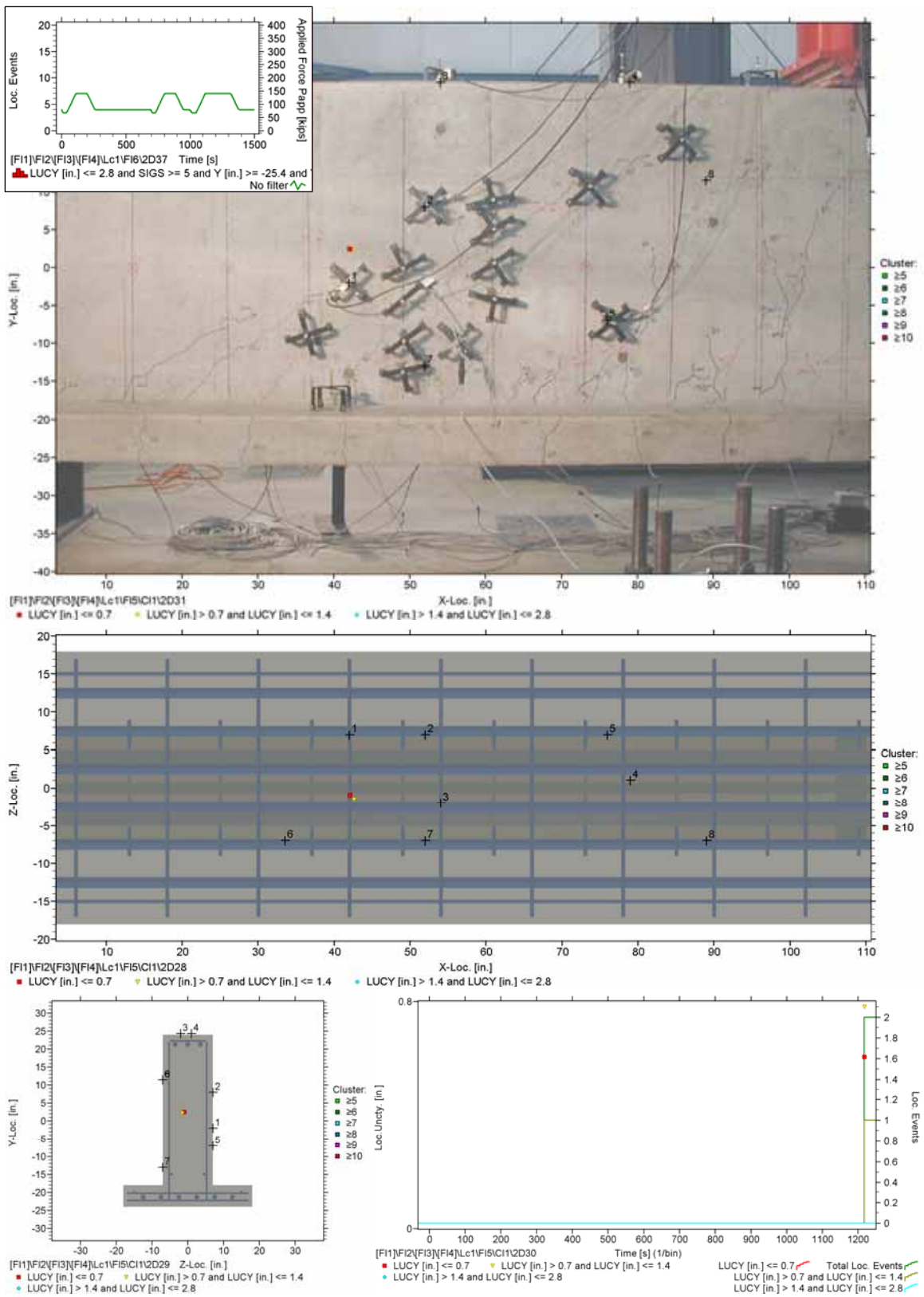


Figure 7.18: Estimated Source Locations, Session 7 (3 TT)

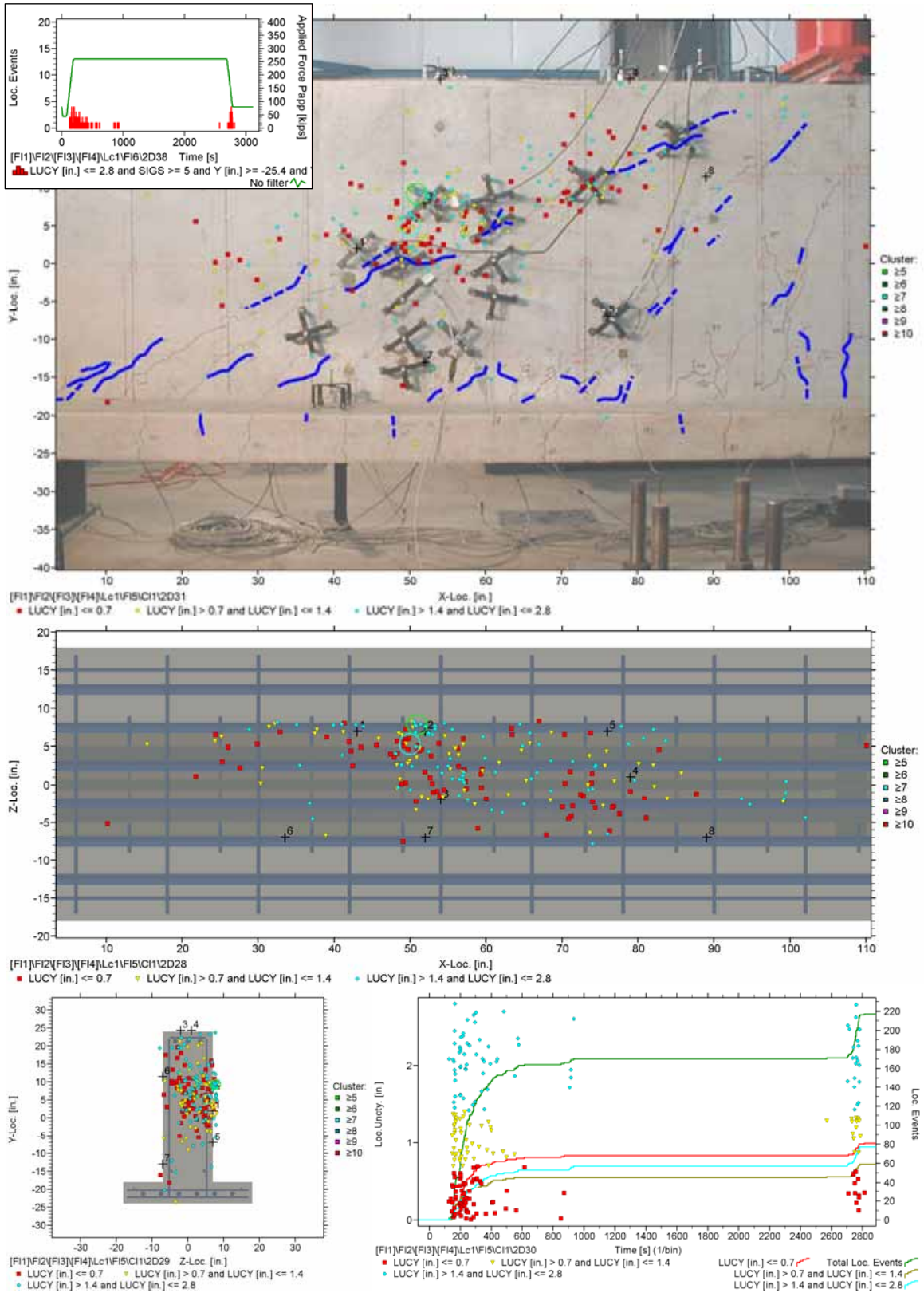


Figure 7.19: Estimated Source Locations, Session 8 (3rd OL)

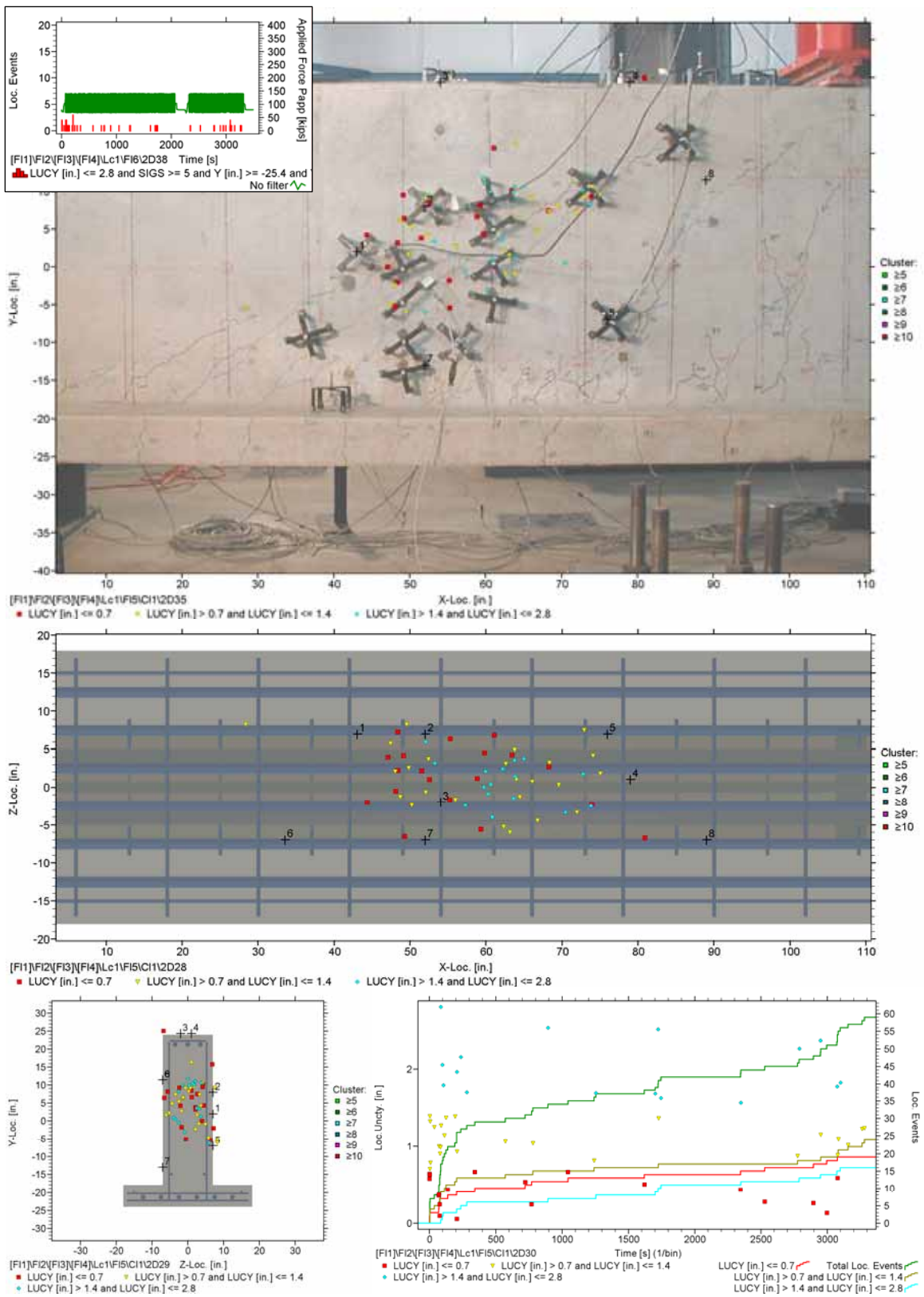


Figure 7.20: Estimated Source Locations, Session 8 (1000 + 500 cycles)

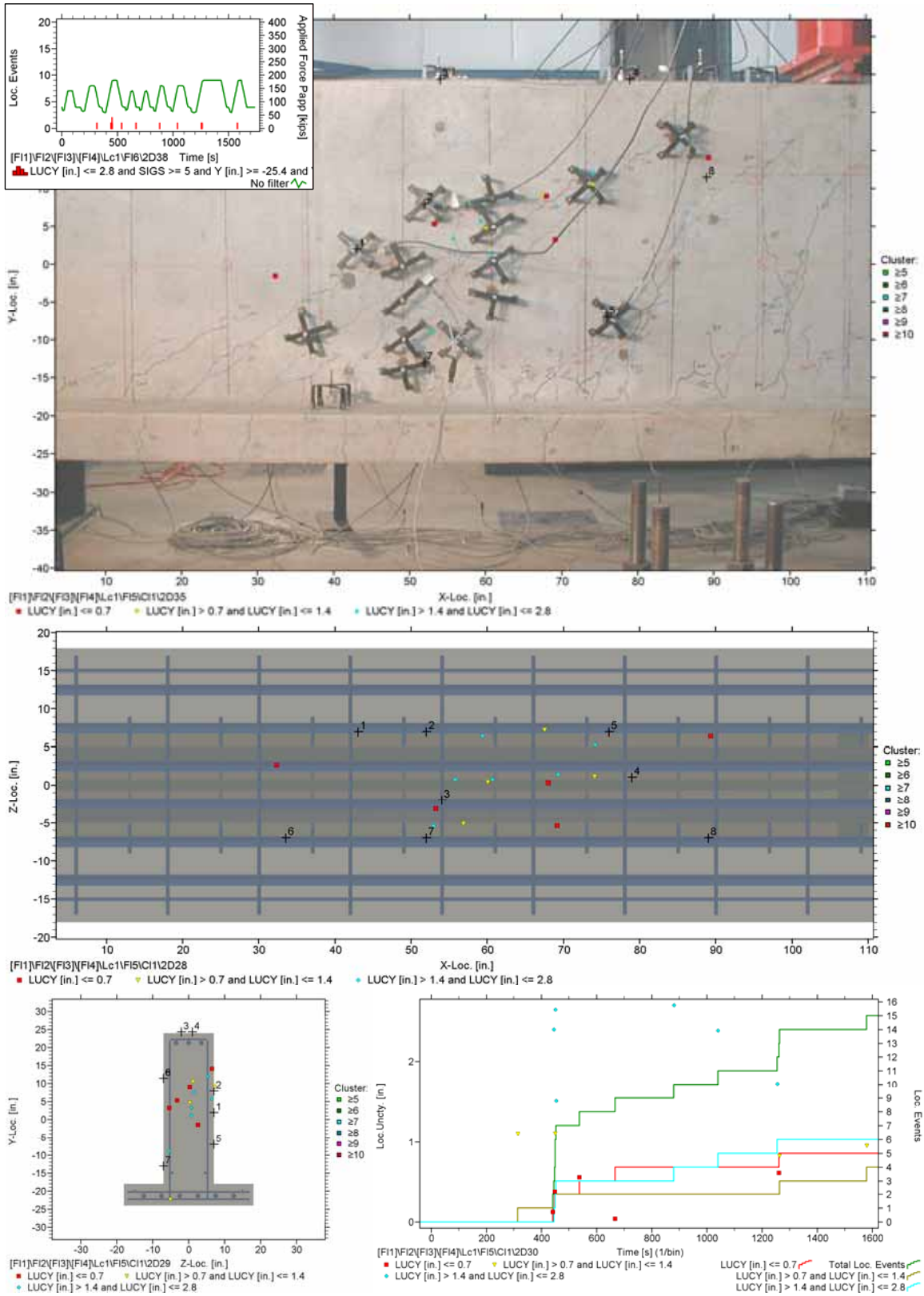


Figure 7.21: Estimated Source Locations, Session 8 (9 TT)

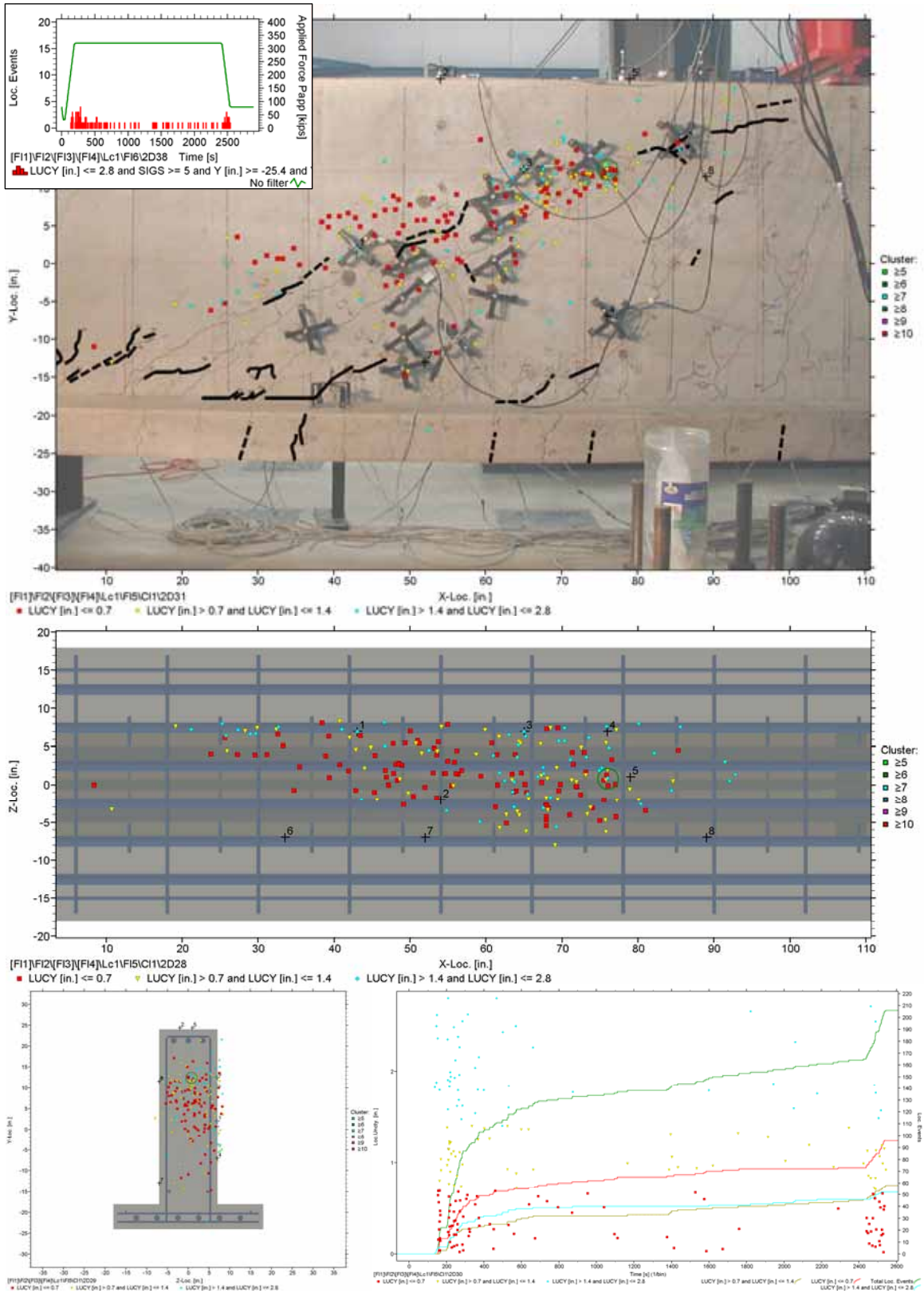


Figure 7.22: Estimated Source Locations, Session 13 (4th OL)

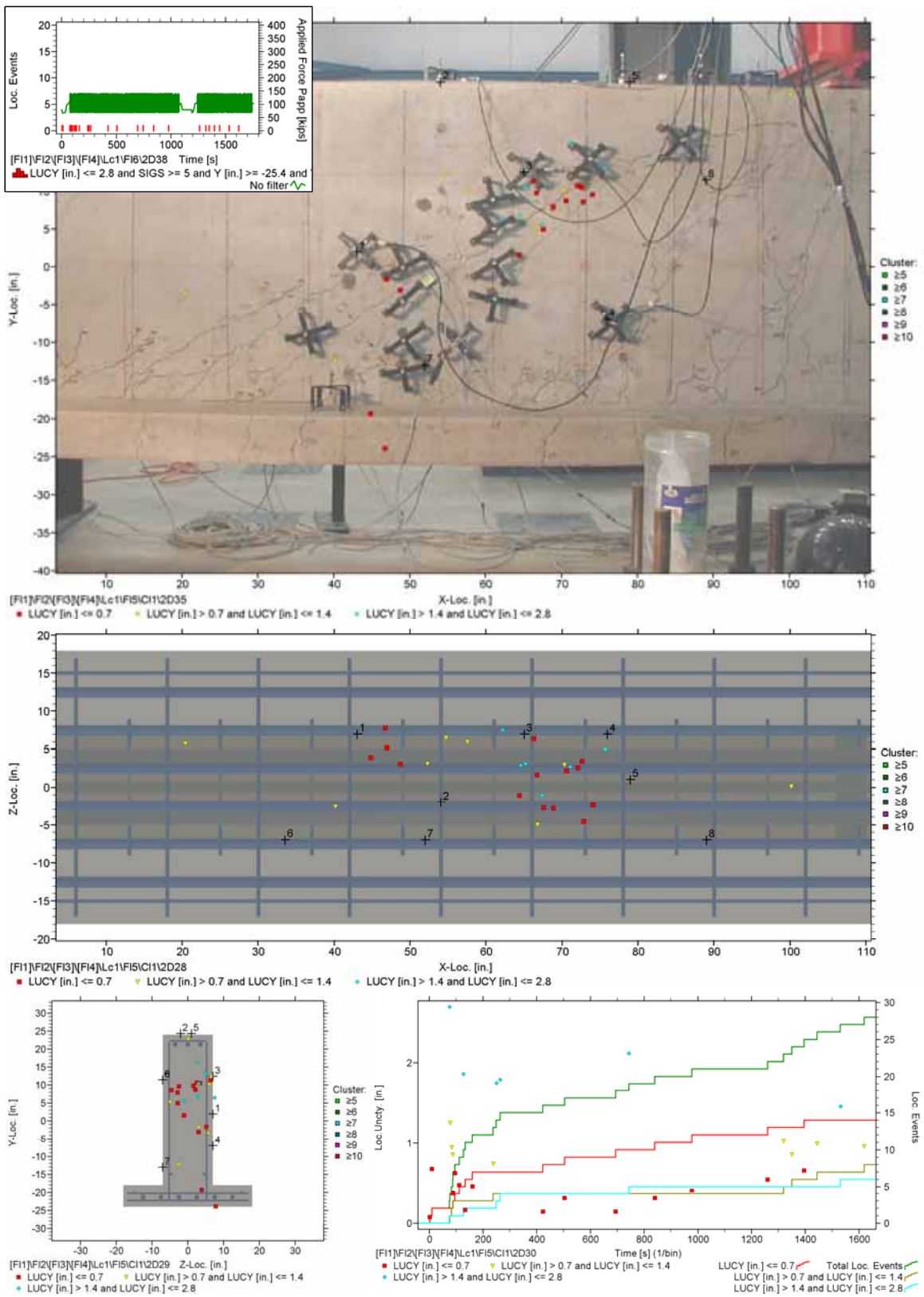


Figure 7.23: Estimated Source Locations, Session 13 (500 + 250 cycles)

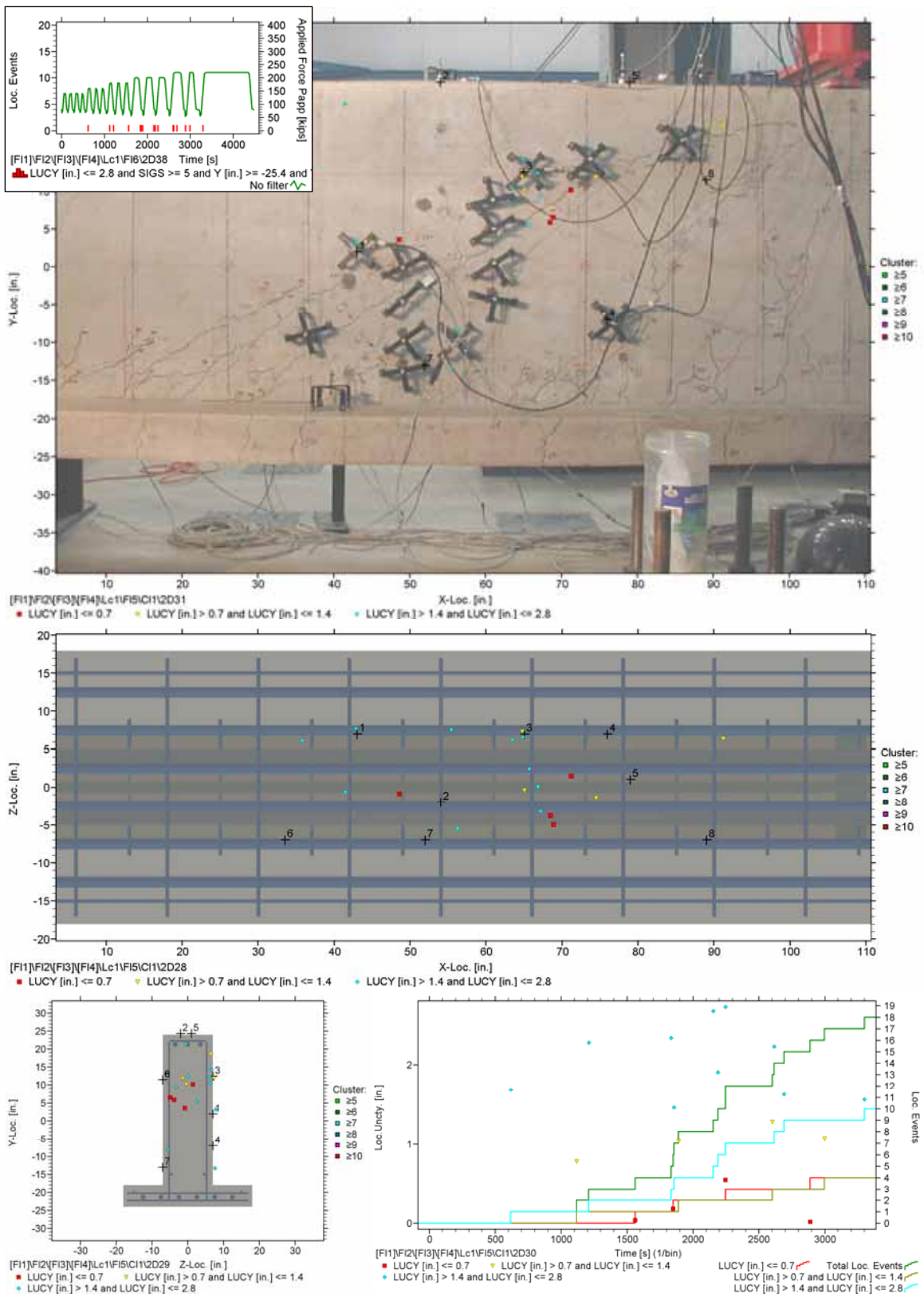


Figure 7.24: Estimated Source Locations, Session 14 (16 TT)

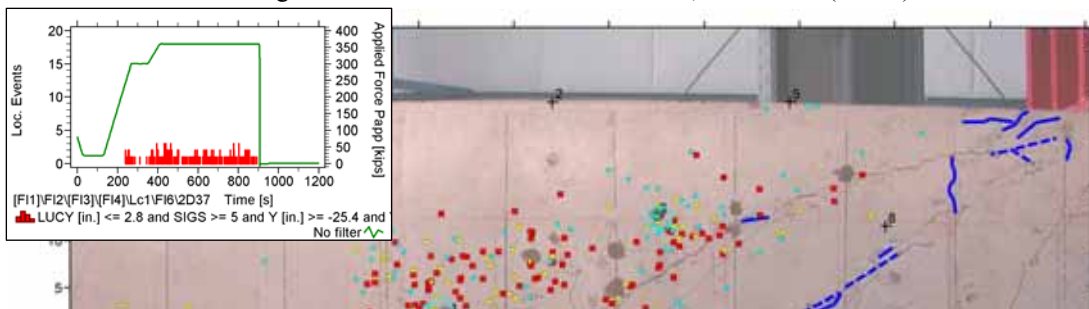


Figure 7.25: Estimated Source Locations, Session 18 (5th overload, failure)

7.3.2 AE Specimen #2

Presented in this section are estimated 3-D AE source locations found with sensor arrays A1 to A4 as presented in section 6.5.1 using the KRNi060 sensors. Table 7.2 shows the number of located AE events classified by their level of quality as specified in section 4.5.1. All results were computed and visualized with VisualAE using background photos that were taken during the experiment. Only AE events with five signals were included in the event assembling. AE events that lied more than 36 mm (1.4 in.) outside the body of the specimen were filtered out. Data acquisition settings and options are presented in Appendix B.

Table 7.2: Summary of located AE events (DL = dead load, OL = overload, TT = test truck)

Ph.	Session	Load type	P_{max}/P_{ult}	Array	Number of located AE events			
					Level 1	Level 2	Level 3	Total
1	1	DL	0.21	A1	186	139	129	454
	2	1st OL	0.38	A1	116	92	85	293
	2	2 x 1000 cycl.	0.38	A1	235	241	264	740
	2b	2 x 1000 cycl.	0.38	A1	582	221	245	1048
	2c	1000 cycl.	0.38	A1	155	49	67	271
2	3	3 TT	0.38	A2	5	2	0	7
	7	2nd OL	0.54	A2	130	88	113	331
	7	2 x 1000 cycl.	0.38	A2	95	68	89	252
3	8	9 TT	0.48	A2	31	23	36	90
	12	3rd OL	0.70	A2	165	84	105	354
4	12	2 x 500 cycl.	0.38	A2	23	27	31	81
	13	17 TT	0.59	A3	178	125	157	460
	17	4th OL	0.88	A4	744	756	1010	2510
5	17	250 cycl.	0.38	A4	3	9	10	22
	18	12 TT	0.59	A4	9	18	24	51
	19	5th OL (failure)	1.00	A4	63	82	113	258
	Located, total					2720	2024	2478
Percentages [%]					37.7	28.0	34.3	100

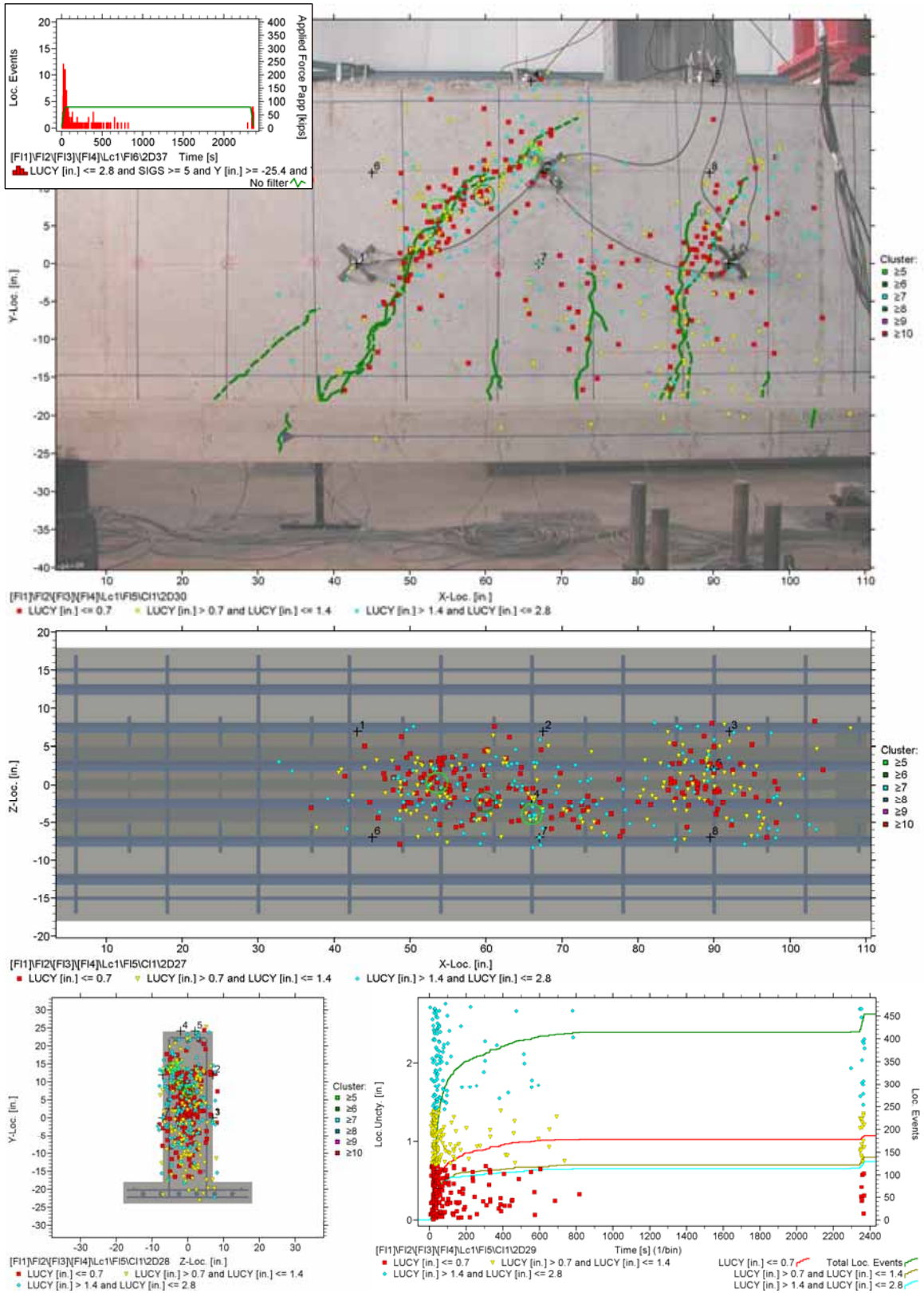


Figure 7.26: Estimated Source Locations, Session 1 (DL)

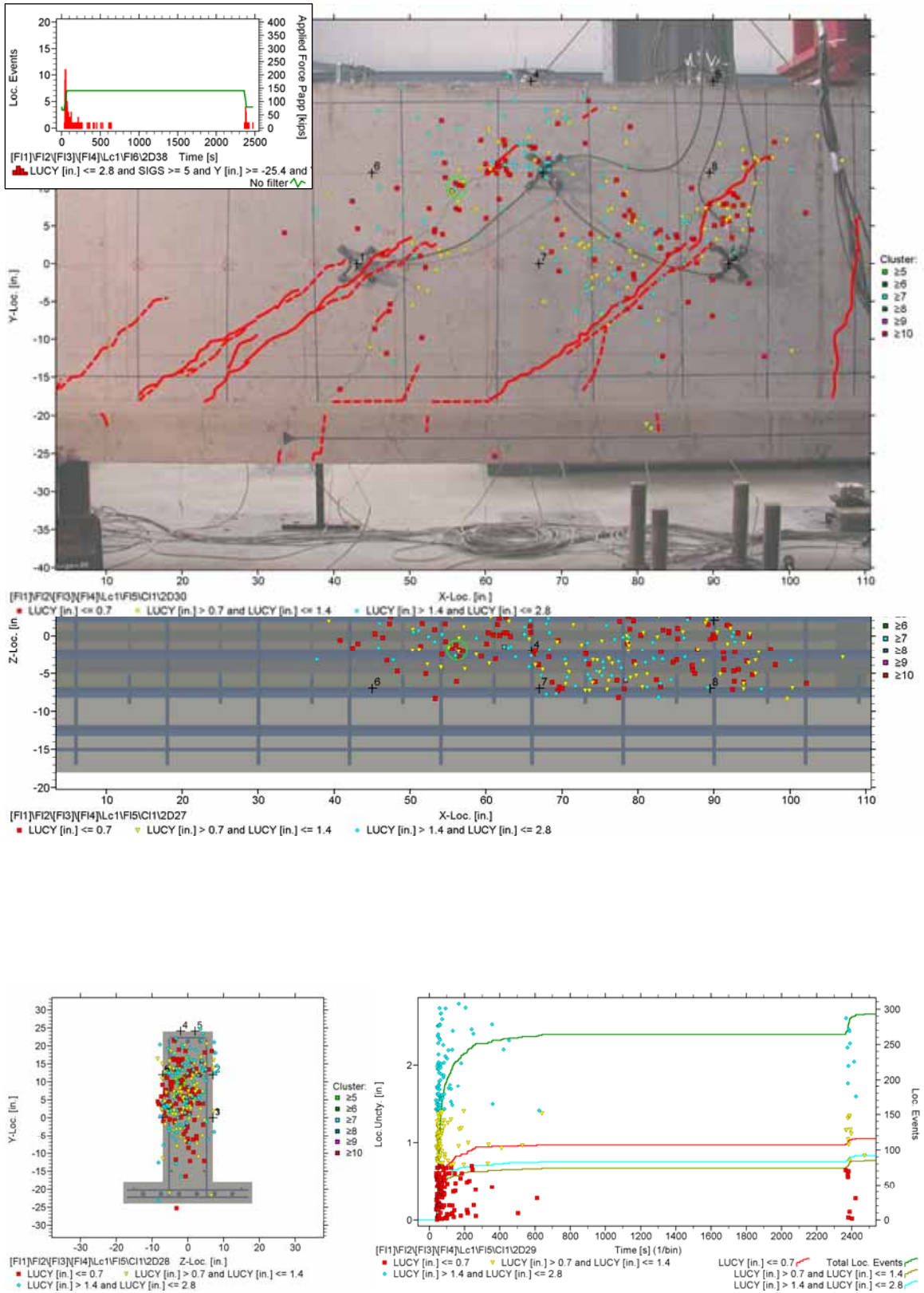


Figure 7.27: Estimated Source Locations, Session 2 (1st OL)

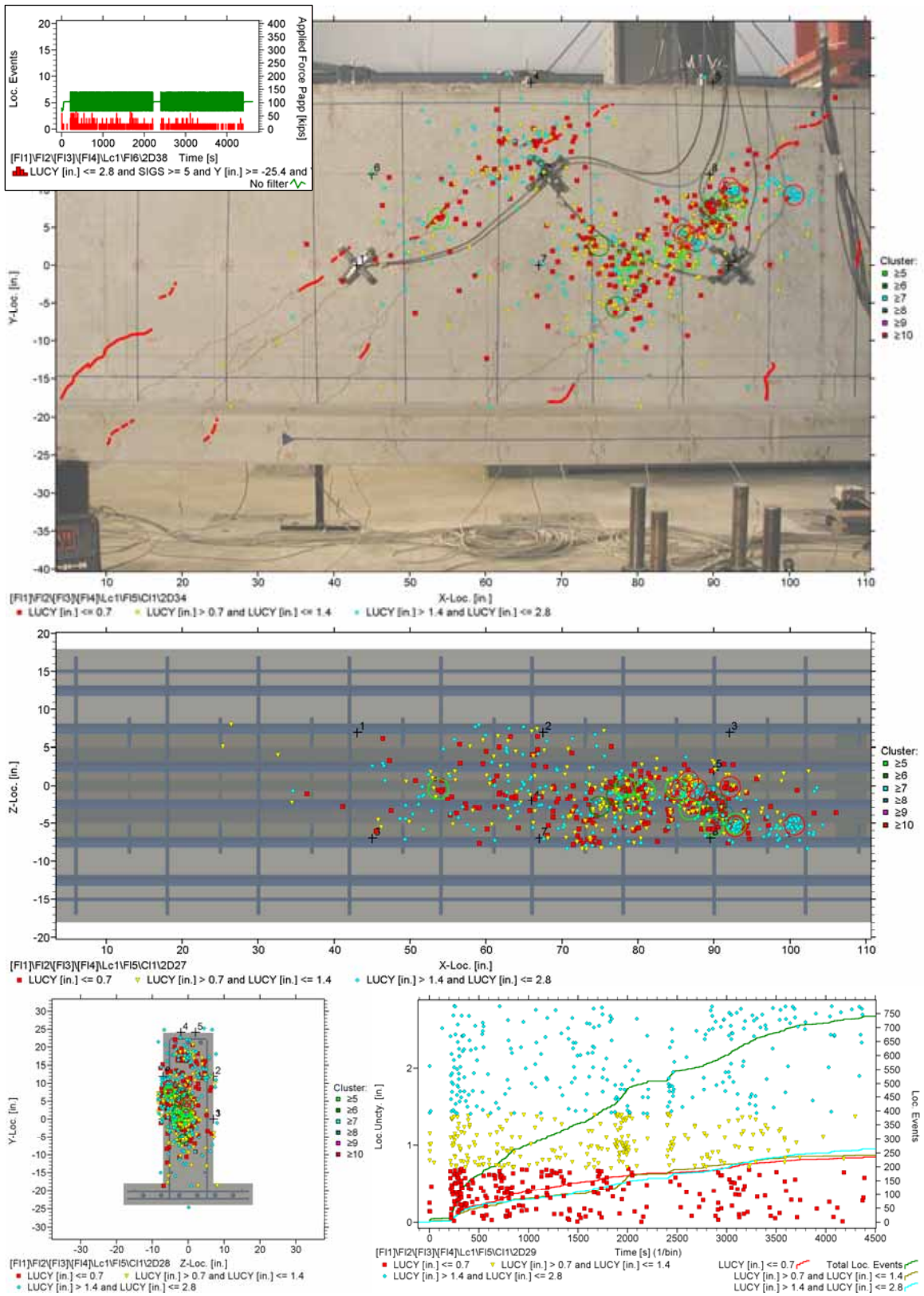


Figure 7.28: Estimated Source Locations, Session 2 (2 x 1000 cycles)

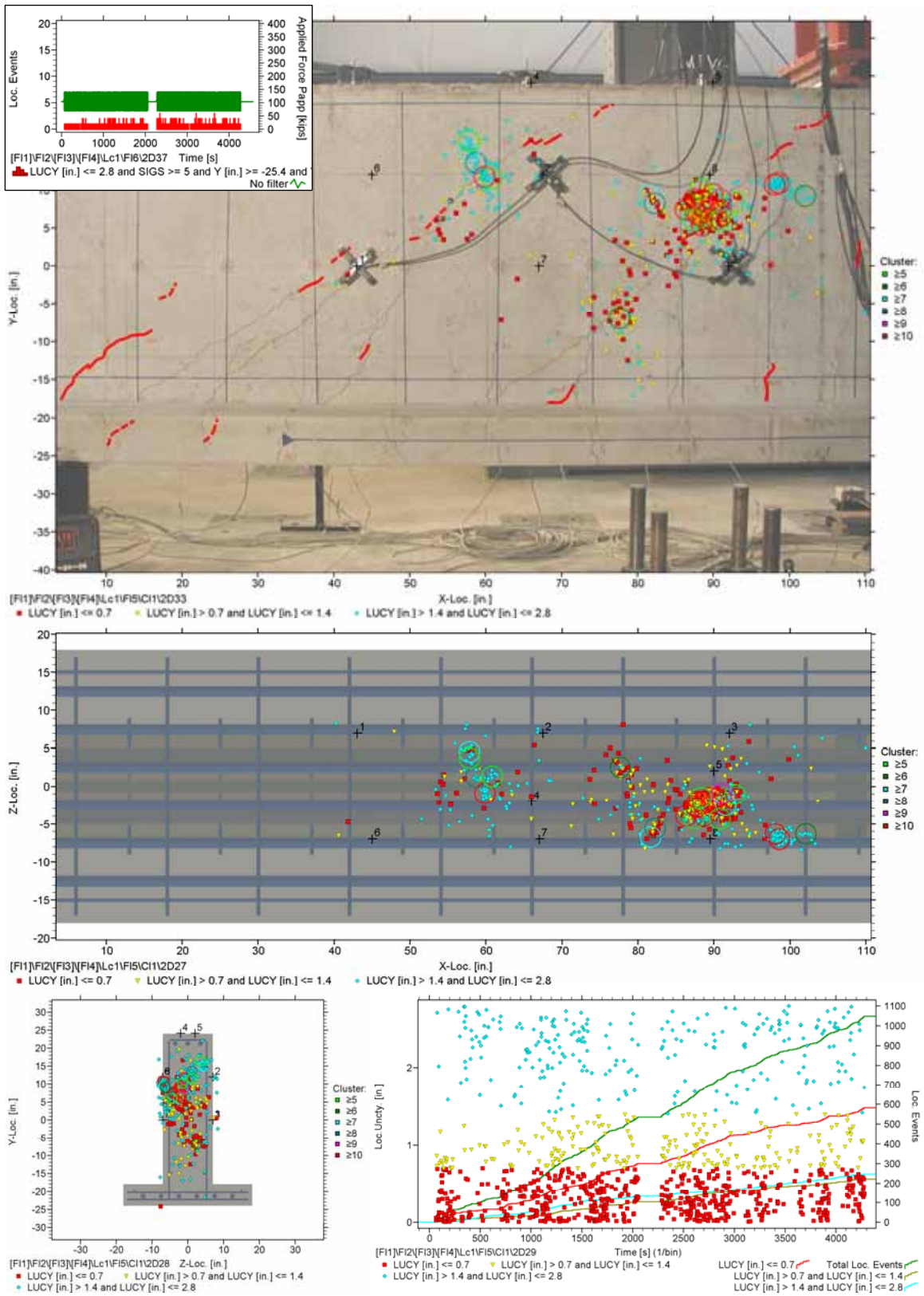


Figure 7.29: Estimated Source Locations, Session 2b (2 x 1000 cycles)

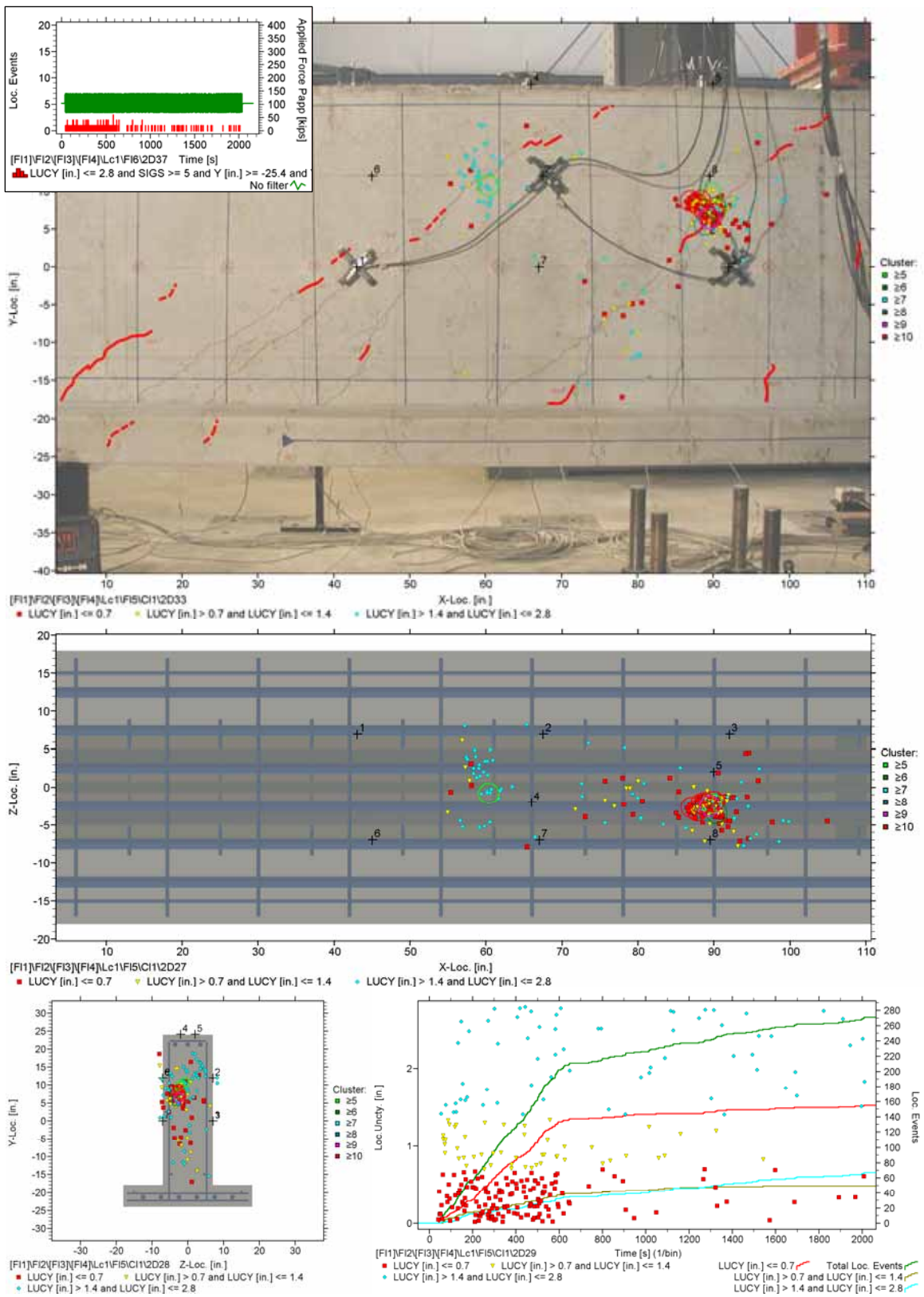


Figure 7.30: Estimated Source Locations, Session 2c (1000 cycles)

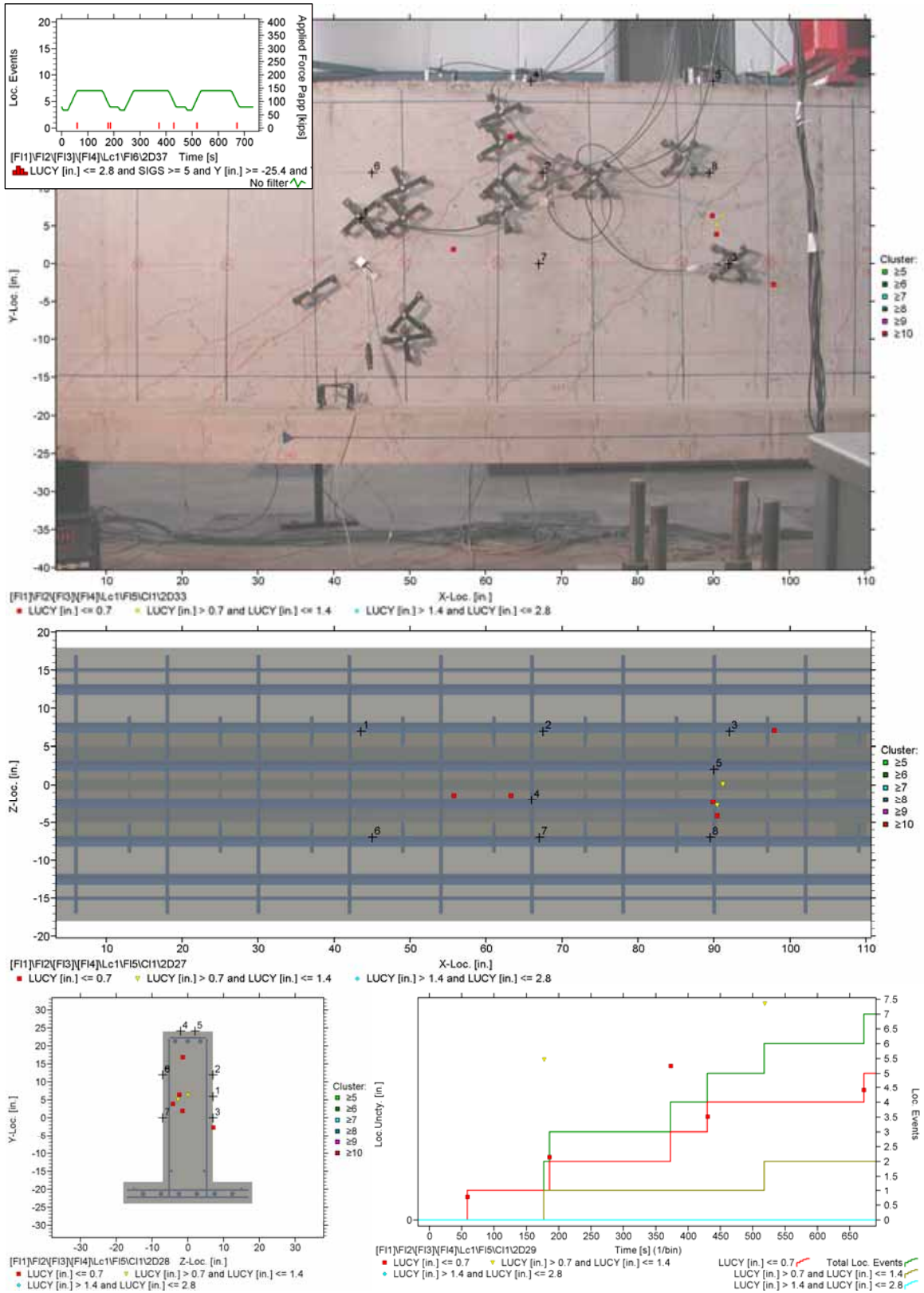


Figure 7.31: Estimated Source Locations, Session 3 (3 TT)

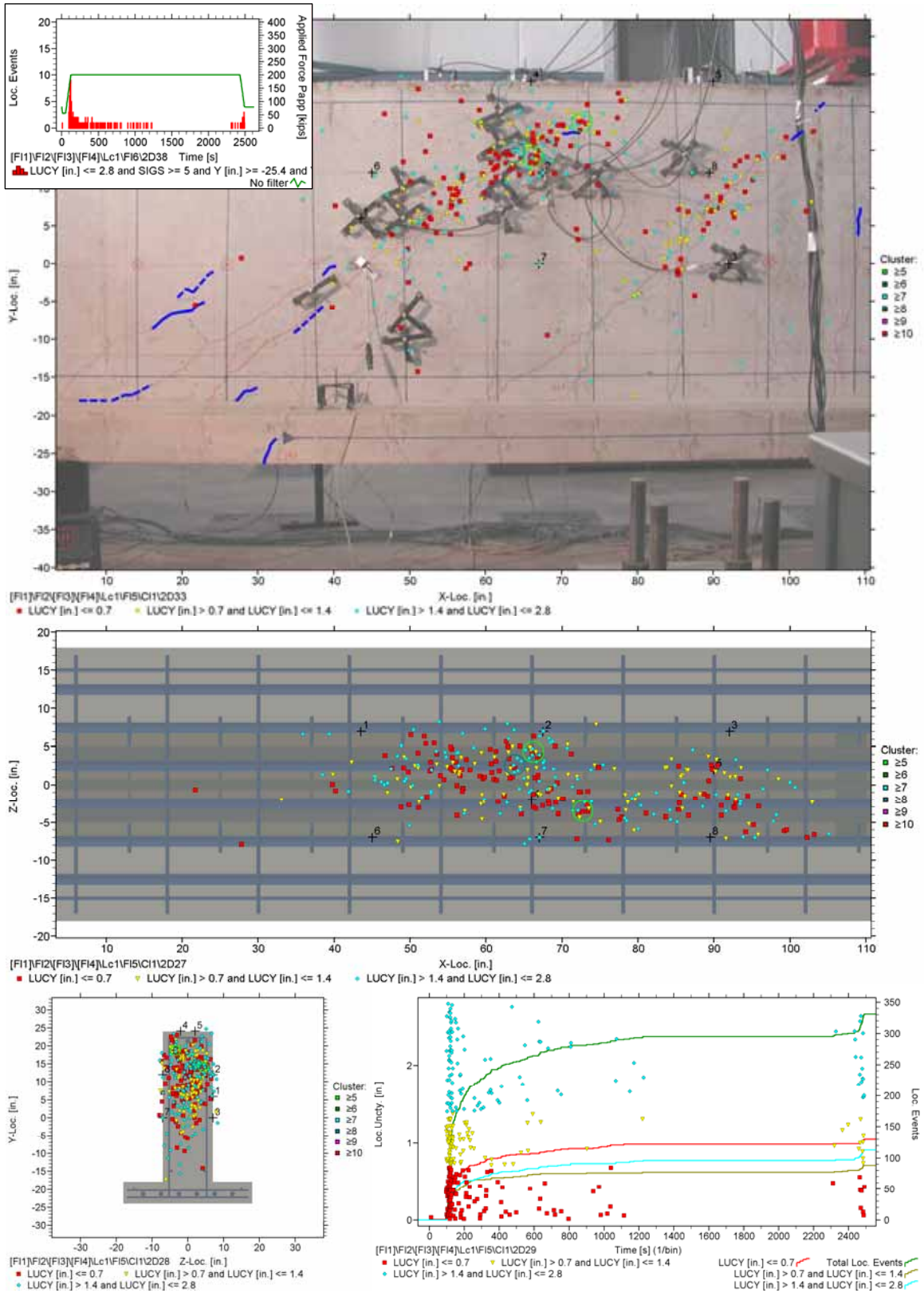


Figure 7.32: Estimated Source Locations, Session 7 (3rd OL)

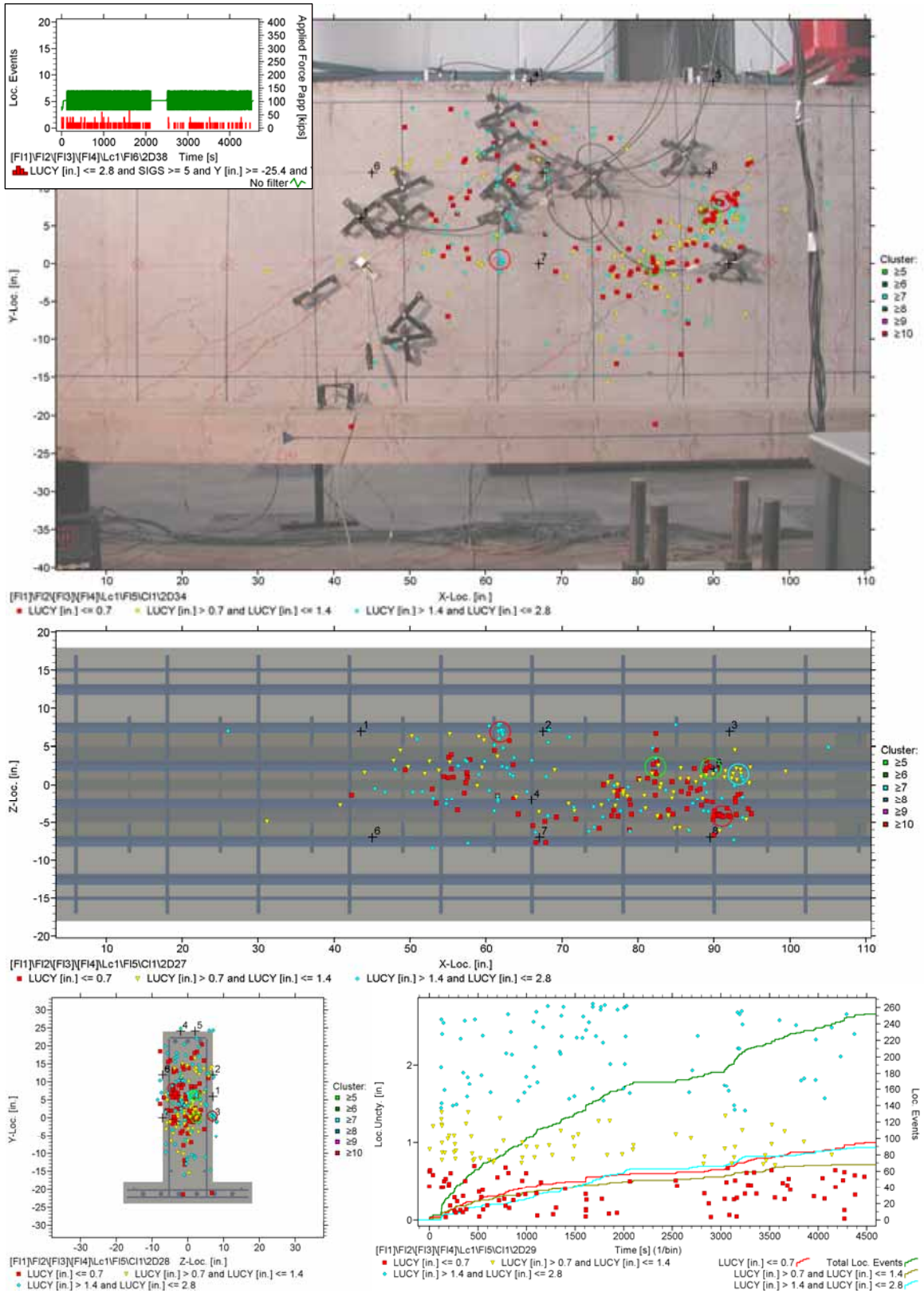


Figure 7.33: Estimated Source Locations, Session 7 (2 x 1000 cycles)

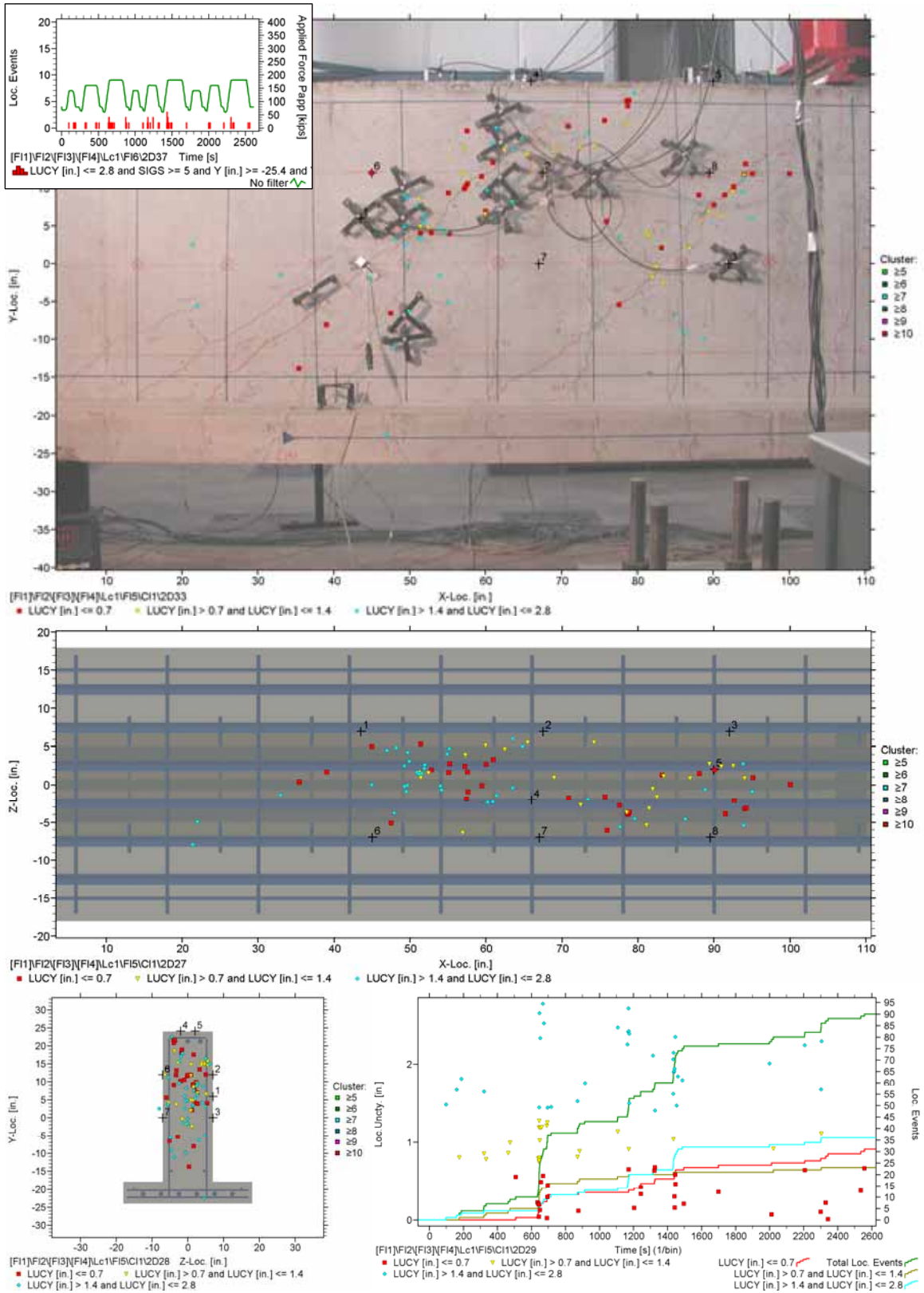


Figure 7.34: Estimated Source Locations, Session 8 (9 TT)

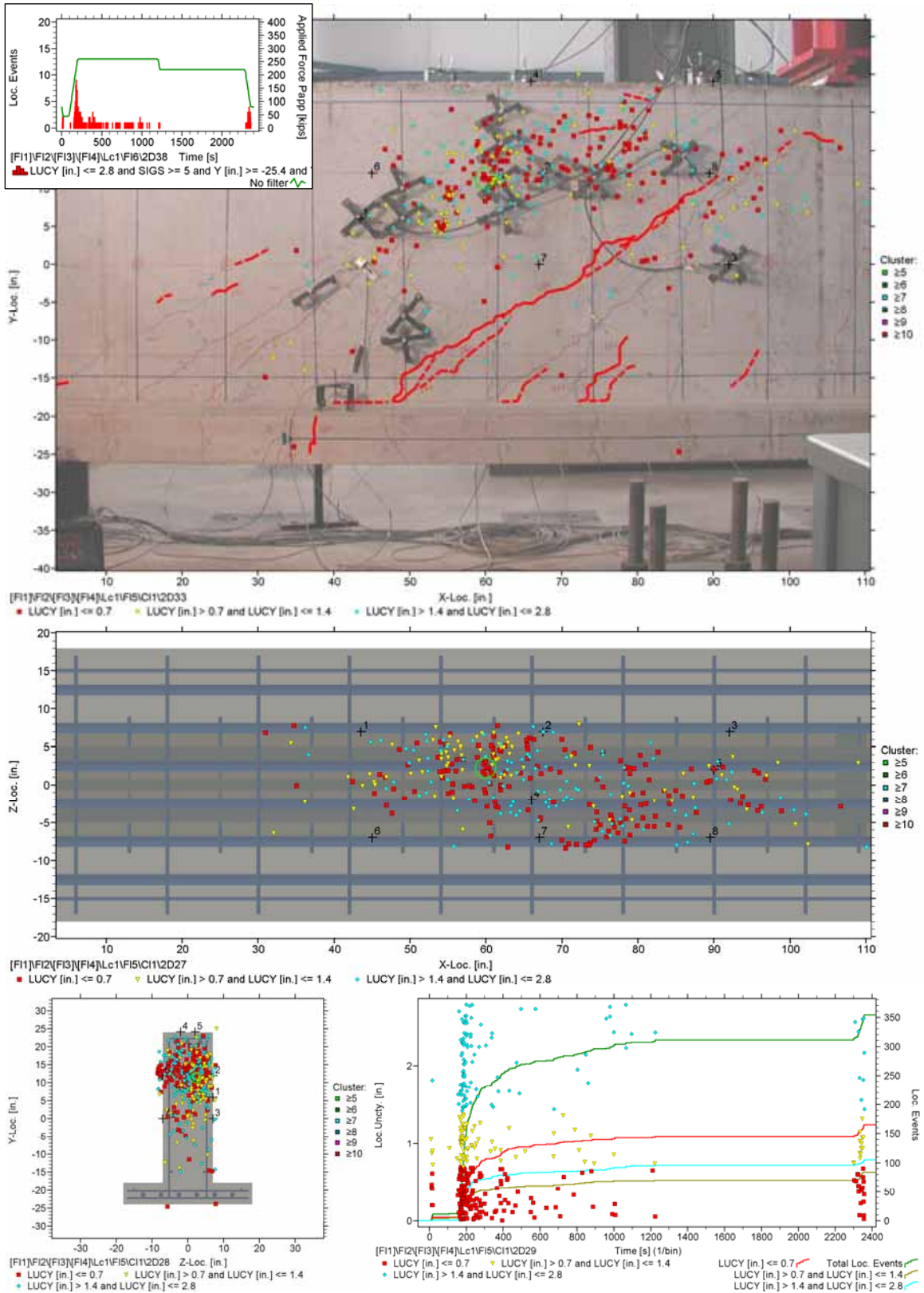


Figure 7.35: Estimated Source Locations, Session 12 (3rd OL)

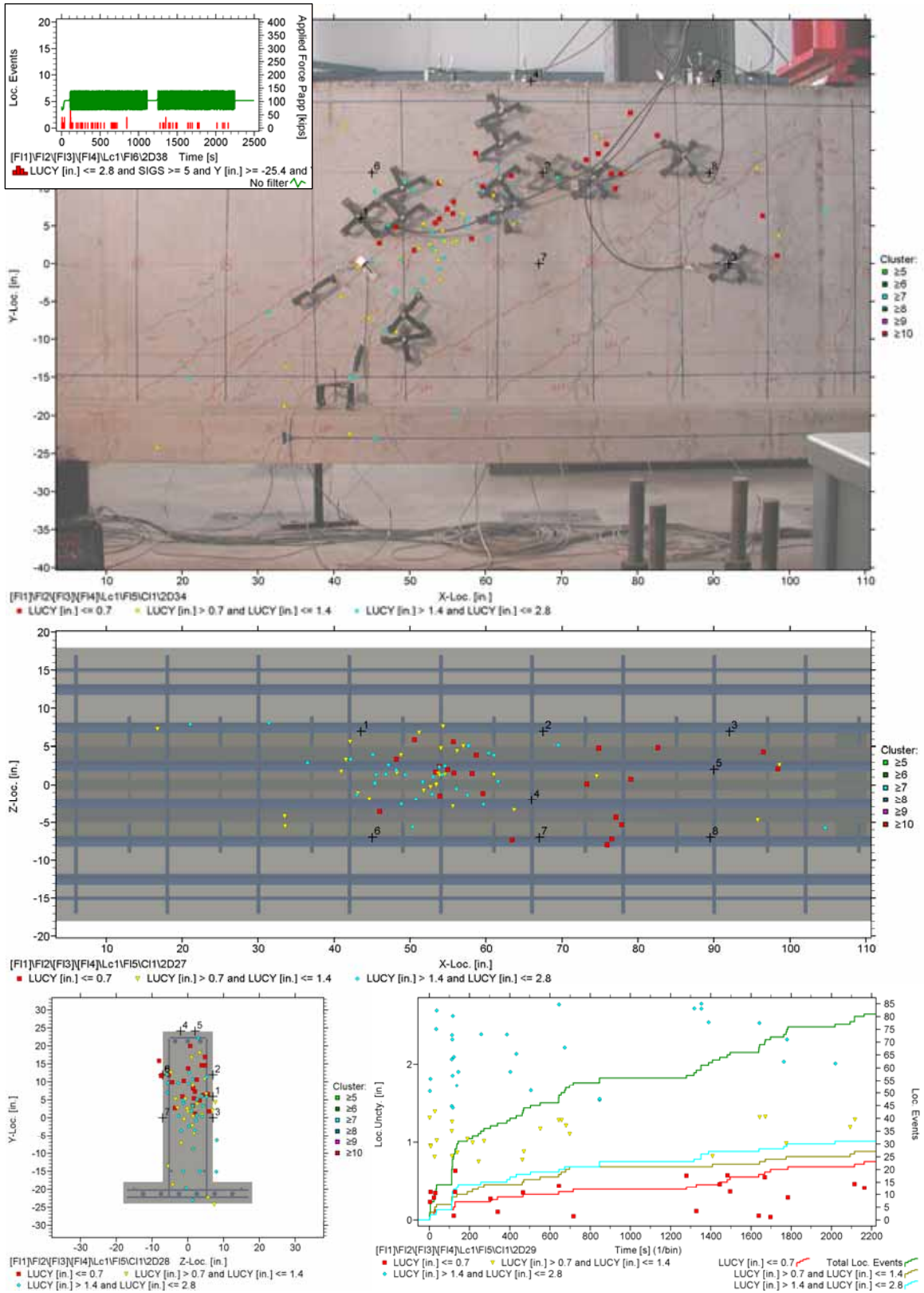


Figure 7.36: Estimated Source Locations, Session 12 (2 x 500 cycles)

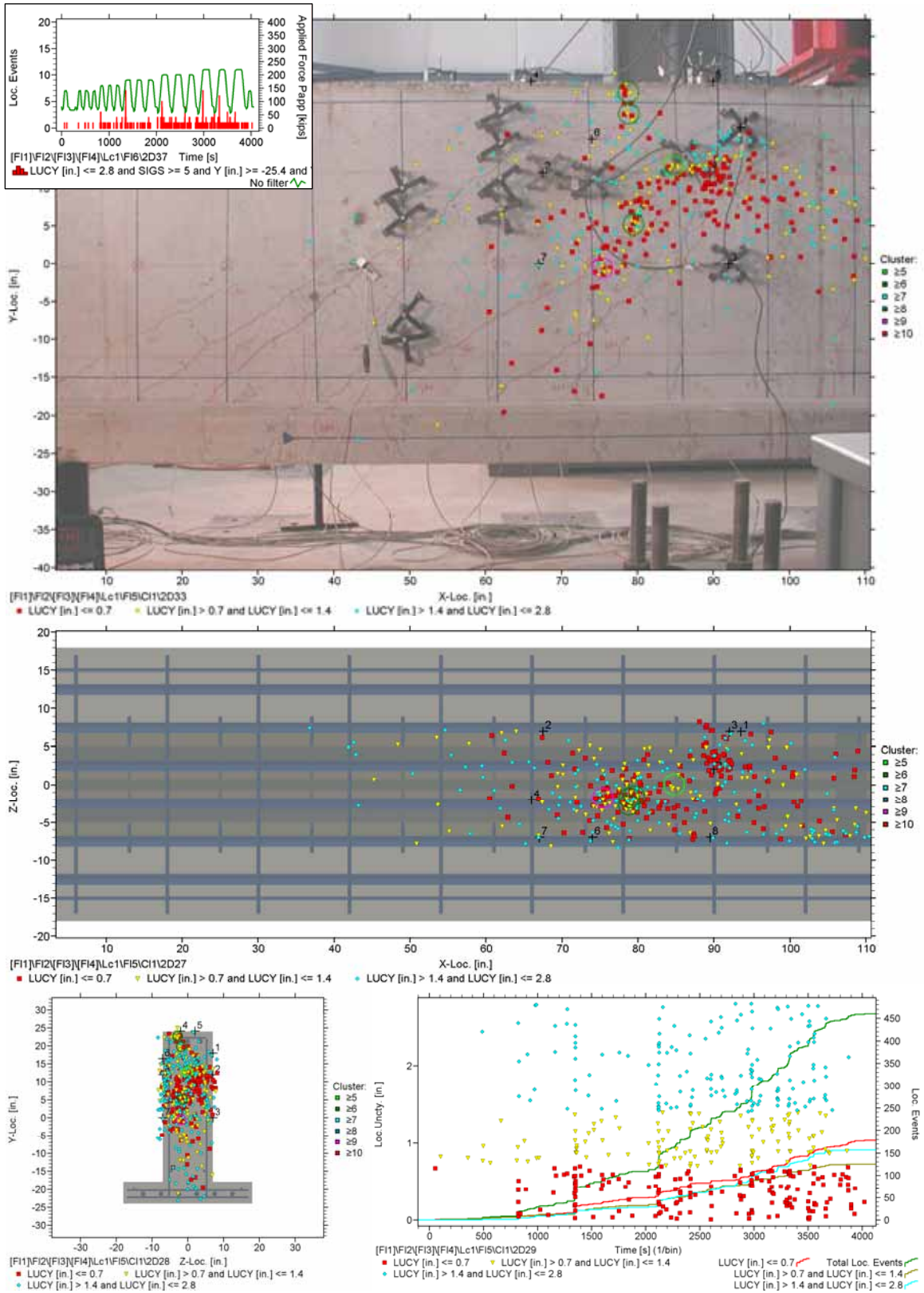


Figure 7.37: Estimated Source Locations, Session 13 (17 TT)

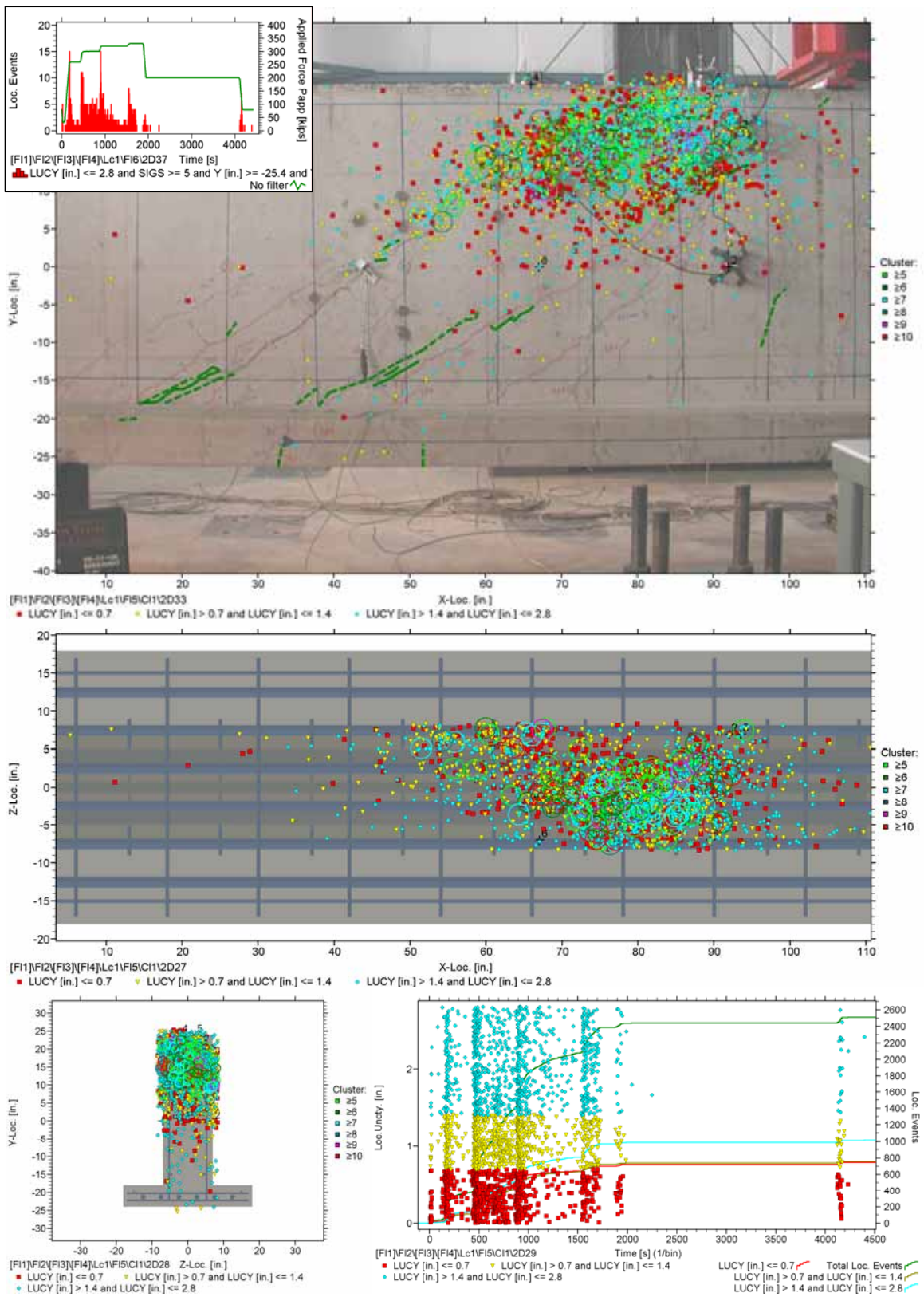


Figure 7.38: Estimated Source Locations, Session 17 (4th OL)

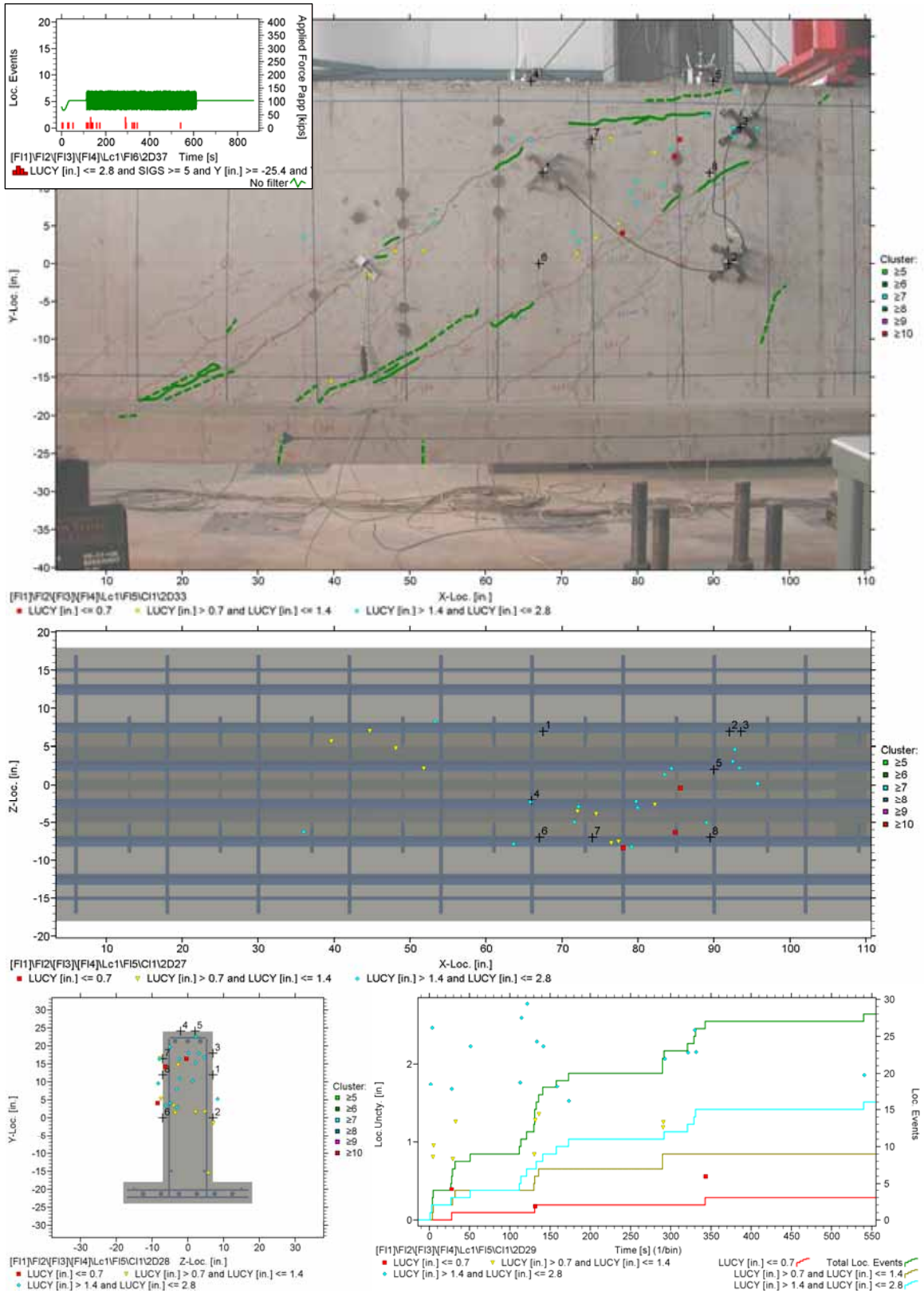


Figure 7.39: Estimated Source Locations, Session 17 (250 cycles)

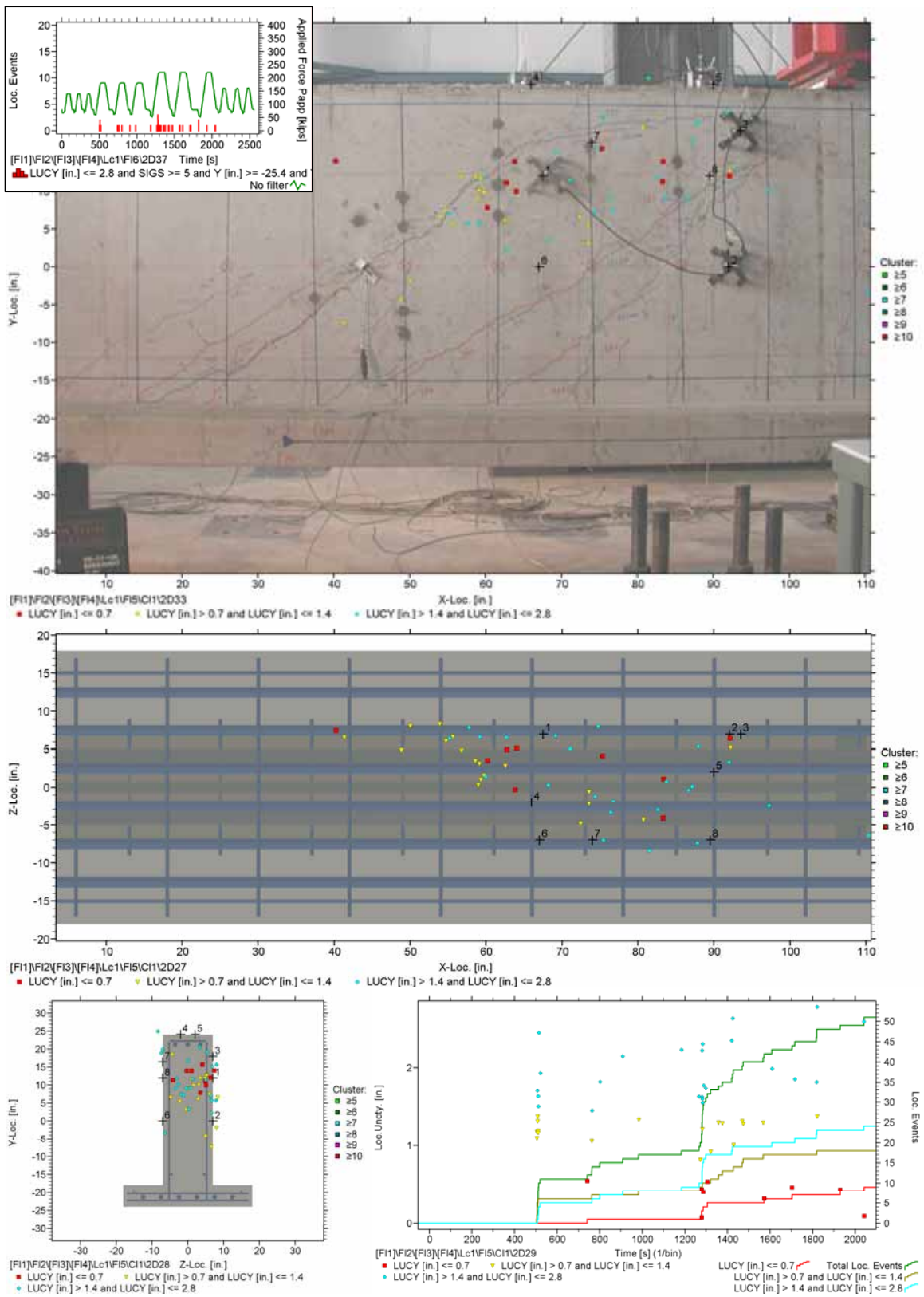


Figure 7.40: Estimated Source Locations, Session 18 (12 TT)

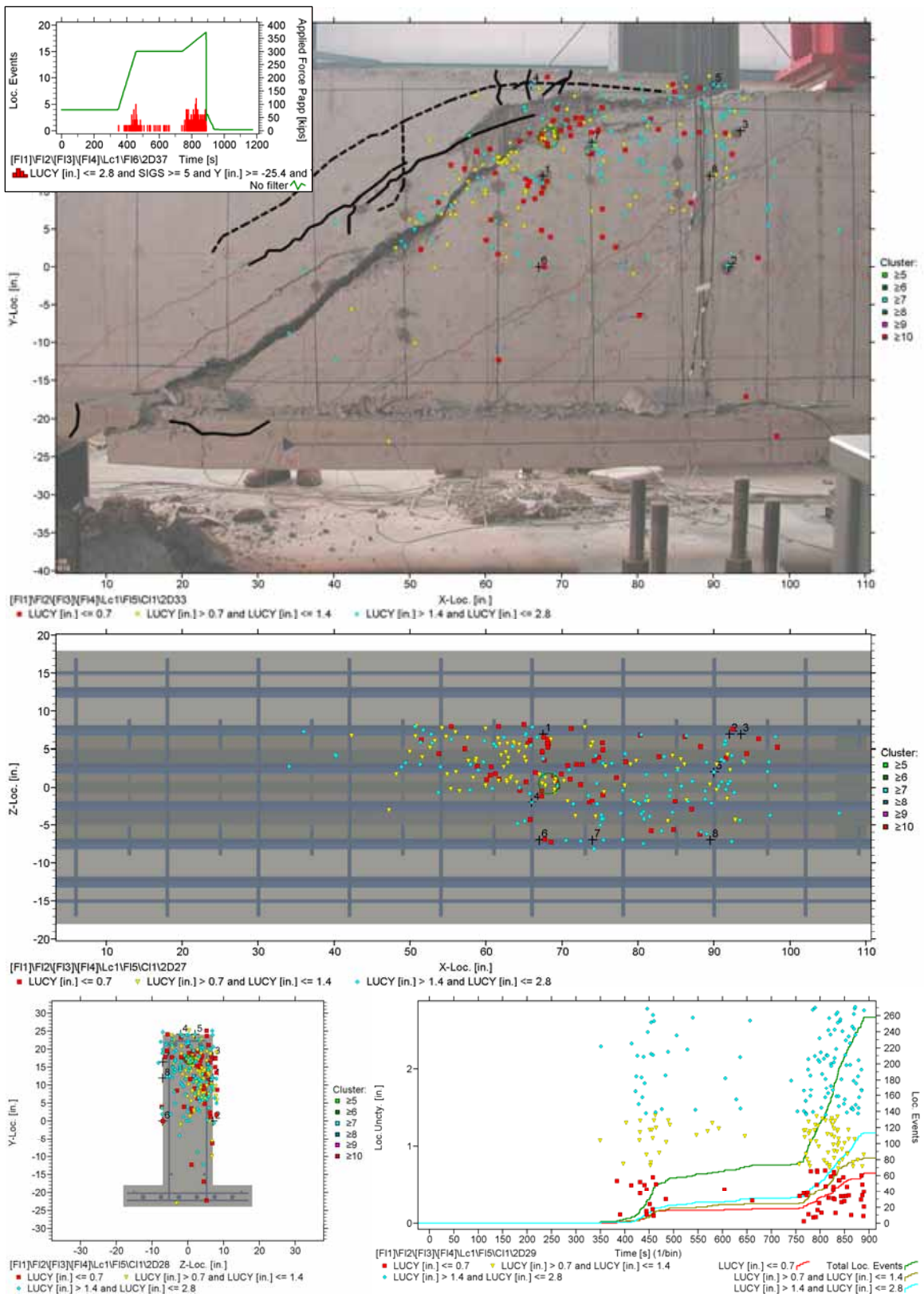


Figure 7.41: Estimated Source Locations, Session 19 (5th OL, failure)

7.3.3 Summary and Comments

As can be observed, overloads produce many more locatable AE events than test trucks. This is the case because most AE in RC is related to crack initiation or propagation and these mechanisms are not necessarily anticipated to be found from low level loads. Especially when force is applied for the first time to the specimen, located AE events line up very well with propagated cracks (e.g. see Figures 7.11, 7.12, 7.26). AE clusters line up as well with cracks. As the crack patterns become more complex, stress wave travel paths become more convoluted and that introduces bias in the measurements. One way to address the problem would be to adapt the sensor array more rigorously. For the present study, the array was replaced only when cracks propagated too close by a sensor in order to not change the boundary conditions for the qualitative procedures. For cyclic loading, the located AE events couldn't always be explained. For example Figure 7.29 produced a cluster of many AE events where no source would be expected. On the other hand, Figure 7.28 shows located AE events around the two major cracks which would be explainable by crack activity.

Estimation of AE source locations is a major field of application. Crack tips can be monitored for propagation, for instance. Combined with *b*-value analysis, this may provide a very reliable detection tool. Not only the spatial distribution of a crack, but also the temporal evolution of the crack can be studied as illustrated in Figure 7.42. The example is the application of the first dead load and then overload up to 623 kN (140 kips) for AE Specimen #1. Green dots represent early events, red dots the last events that occurred. It can be observed that first, the smaller crack (on the right) formed, then the longer to the left initiated and propagated up towards the compression block. That longer crack has a color gradient ranging the whole spectrum from green (bottom) to red (top) which is in agreement with how it developed.

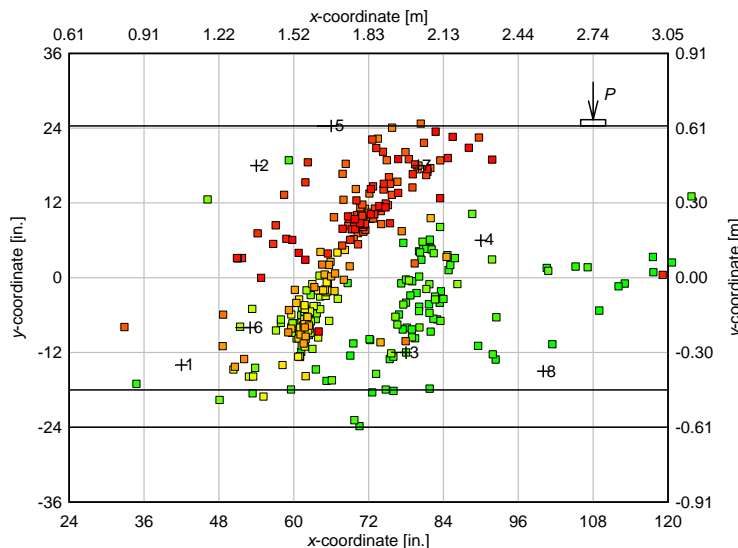


Figure 7.42: Elevation view of AE Specimen #1

8.0 SENSOR ARRAY B

Sensor array B as presented in section 6.5.2 was used to evaluate simulated test trucks as described in section 6.6.4. Basic qualitative plots were generated and a linear location performed. This type of sensor array can often be found in the literature for global monitoring of structures (*Golaski 2002; Shiotani 2007*). Basic results are presented and recommendations on how this type can be used for global monitoring are suggested.

8.1 AE HITS AND HIT RATES

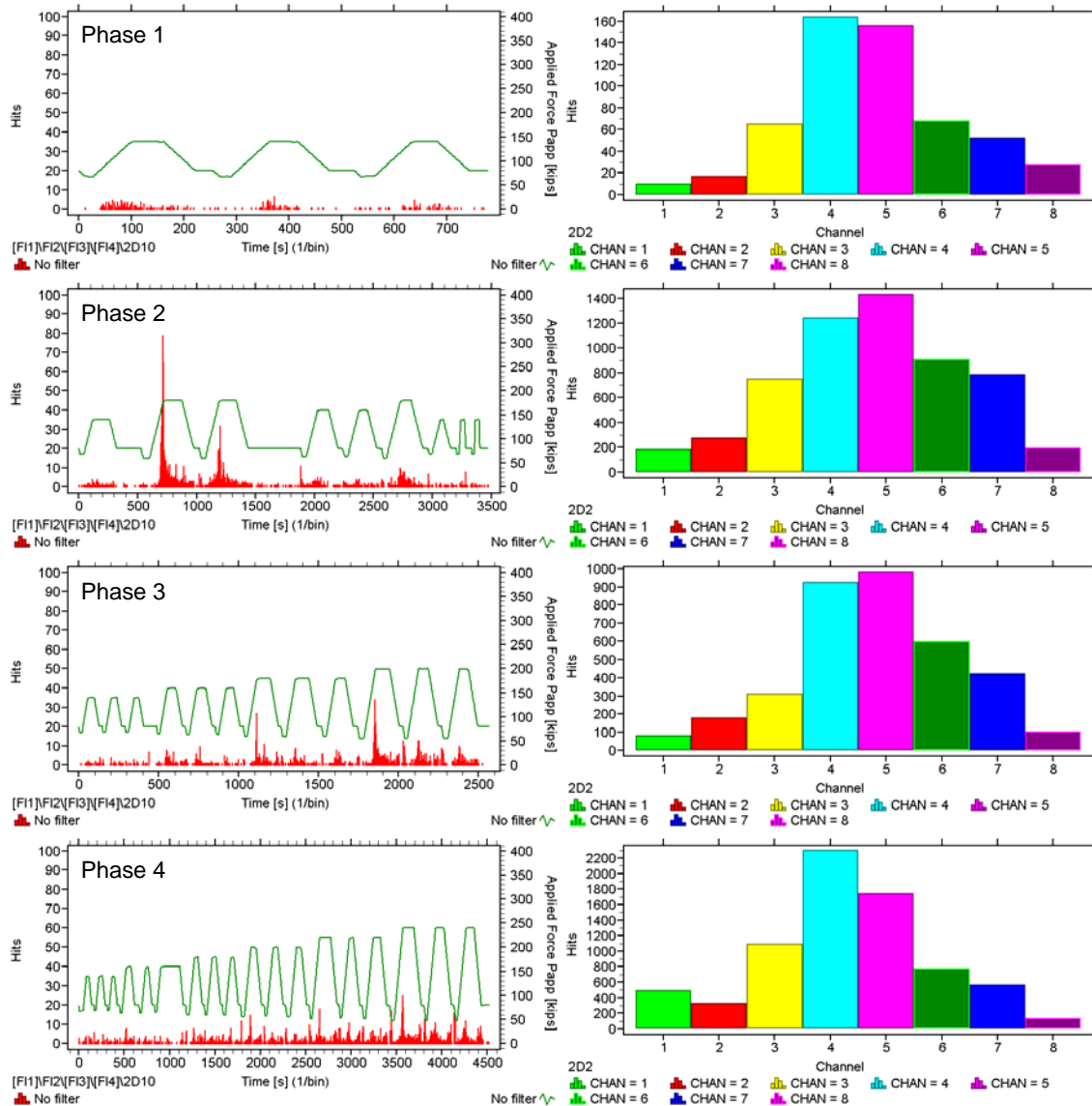


Figure 8.1: Total AE hit rates (left column) and total AE hits (right column) for AE Specimen #1

Figures 8.1 and 8.2 illustrate AE hit rates (left column) and total AE hits recorded (right column) during application of the simulated test trucks. AE hit rates are computed from the total response of all eight sensors to give a general overview. The sensors in the middle of the specimen, however, detected the most AE hits. During the application of some of the heavier test trucks, it was noticed that some noise from the left support was picked up. Notice the relatively high level of AE activity of sensor 1 (compared to sensor 2) in Figure 8.1, phase 4 and Figure 8.2, phase 3. The same problem was found at sensor 7 for AE Specimen #2. A major issue of widely space sensor arrays is the rejection of noise. If 3-D sensor arrays are used (like sensor array A), AE events can be grouped and noise such as the one discussed above is filtered out automatically.

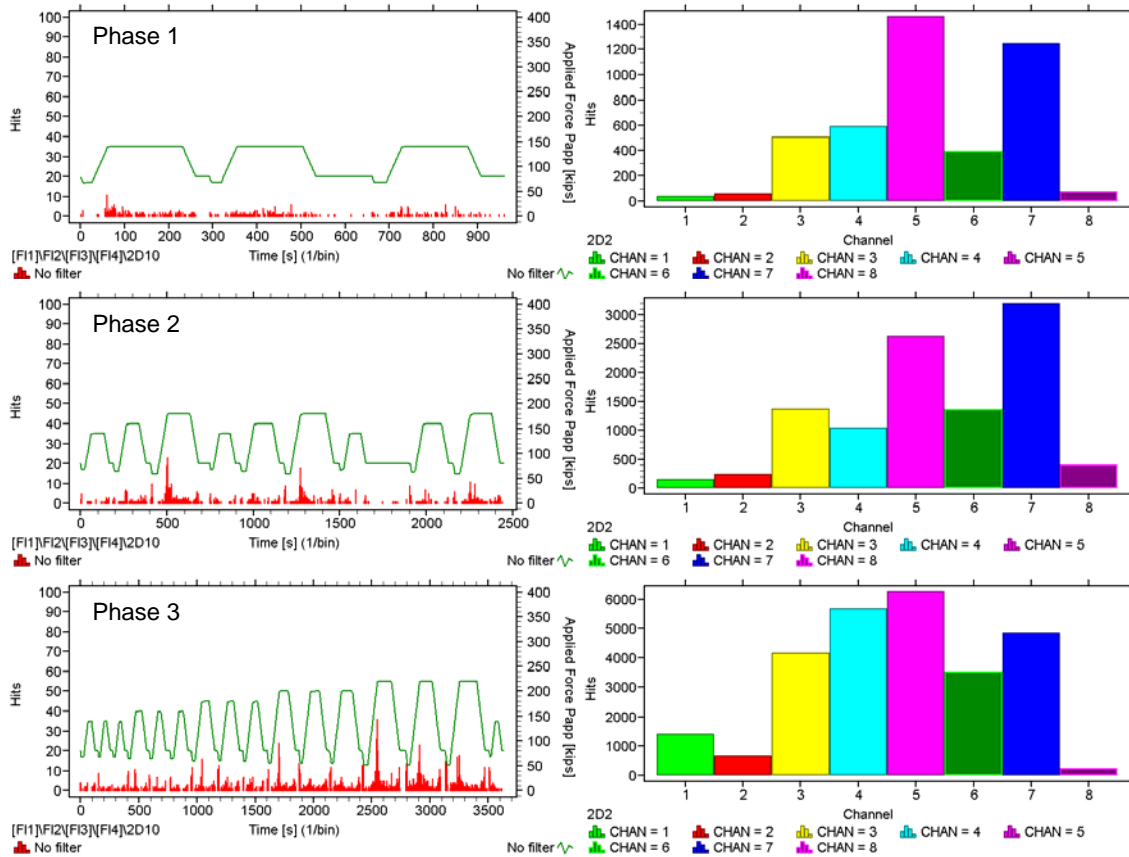


Figure 8.2: Total AE hit rates (left column) and total AE hits (right column) for AE Specimen #2

8.2 KAISER EFFECT AND FELICITY RATIO

These parameters were not computed since only AE data from service-level loads were detected which means that previous loads were never exceeded.

8.3 B-VALUE ANALYSIS

For this type of array, *b*-values can be monitored as presented in section 4.3.5 for each sensor individually for long term monitoring. The proposed minimum *b*-value method could be performed comparing the different zones on the girder. The standard error could be used as measure of uncertainty in this case.

8.4 ESTIMATION OF LINEAR AE SOURCE LOCATIONS

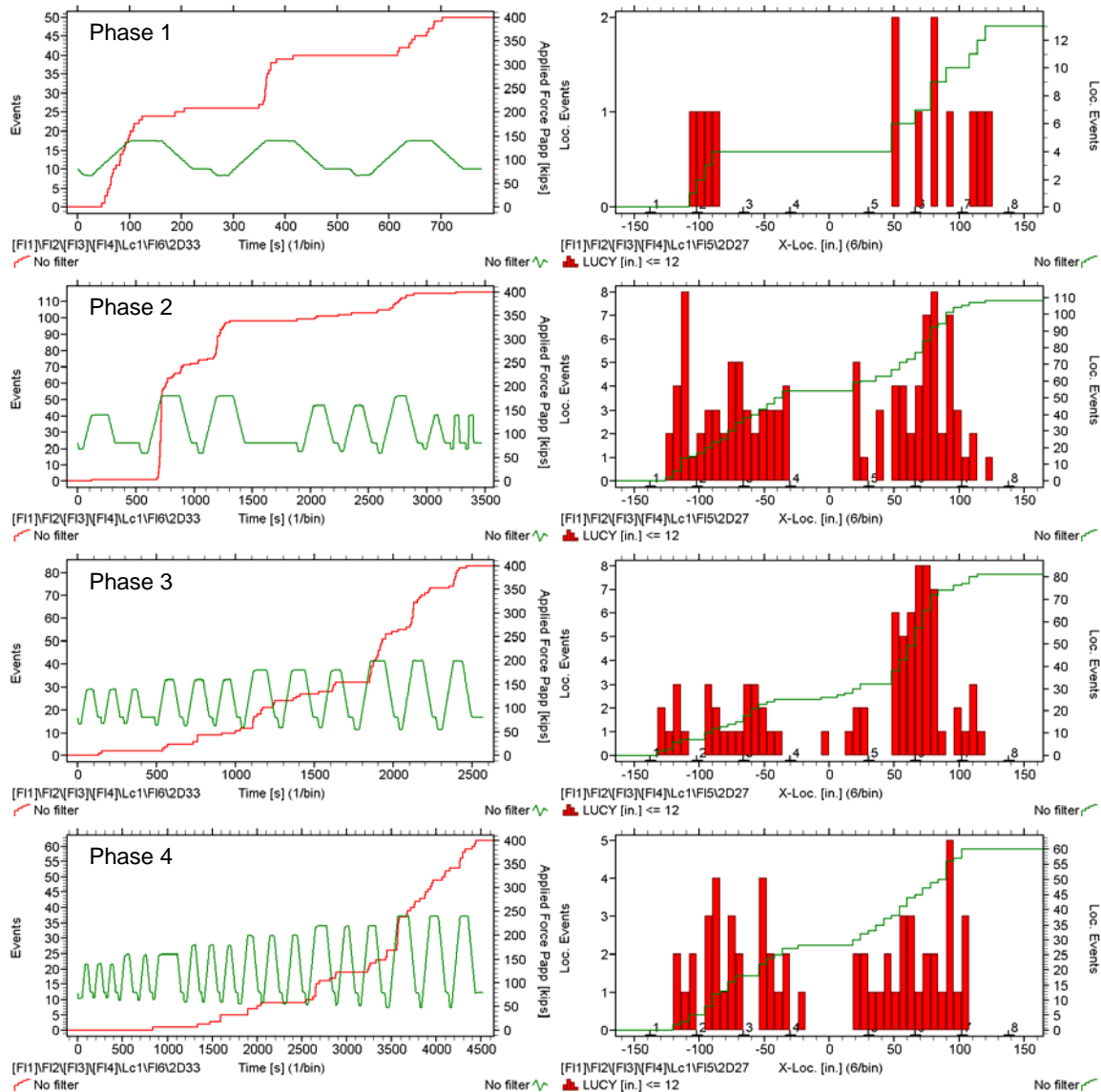


Figure 8.3: AE Events (left column) and AE event locations (right column) for AE Specimen #1

Grouped AE events and locations of these are presented in Figures 8.3 and 8.4. It can be observed that there is a difference between sensor locations from 1 to 4 and 5 to 8 which would be expected since the stirrup spacing on the two sides is not the same.

Interestingly, only very few AE events were located to originate from the center of the beam where the force was applied. This is also the region with the highest moment and no shear force. This suggests that the diagonal shear cracks are ‘noisier’ during service level operation than the moment induced cracks, which can be explained by the different motion behavior of the two crack types.

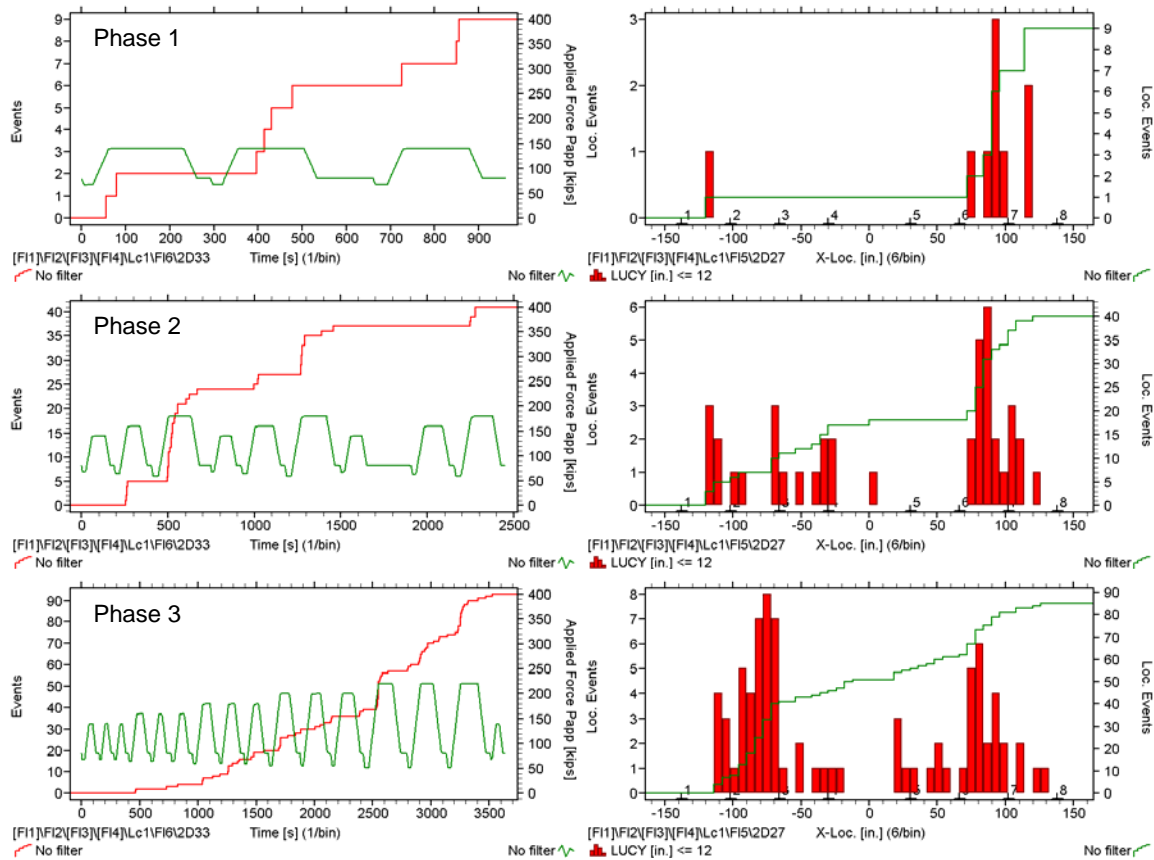


Figure 8.4: AE Events (left column) and AE event locations (right column) for AE Specimen #2

A trend that can be observed is that AE locations tend to be more distributed in later phases of the experiment. In the first phase, AE events are located away from the center of the beam where the first shear cracks have developed (crack patterns can be found in section 6.7). Once the specimen is more deteriorated, AE sources are then present more distributed over the whole specimen.

9.0 SUMMARY AND CONCLUSIONS

Maintaining aging bridge populations have become a major issue worldwide. Numerous reinforced concrete bridges were built in the beginning of the last century and are reaching, or have already passed the expected service life limit. Additionally, traffic volumes have increased almost everywhere drastically since those structures were built. The Oregon Department of Transportation (ODOT) has over 1800 conventionally reinforced concrete deck-girder (RCDG) bridges in its inventory that were built during the 1950s. Many of these bridges are exhibiting diagonal tension cracking in the high shear regions of the girders. Conventional load rating methods have found many of these structures to be deficient for current loading conditions. In response, a very large bridge replacement program was initiated in 2003, with a total cost exceeding 1.6 billion US dollars. However, these resources are insufficient to replace all the cracked bridges and large numbers of these will be required to remain in-service. A need exists to better predict the capacity and remaining life for the bridges that will stay in service to prioritize future replacements, repairs and impose load restrictions when required.

In the present study, the Acoustic Emission (AE) Technique was evaluated on two RC bridge girders that were built so that they are representative of those found in Oregon's bridge inventory. The main goal was to determine in what way AE can assist in maintaining the State of Oregon's diagonally cracked RCDG bridges. AE based methods have become popular tools worldwide for monitoring aging structures. AE are elastic waves traveling through a solid that are released due to a sudden energy release. In RC, potential sources are for example crack formation and propagation (on micro and macro level) or interaction between reinforcement and concrete. The so produced stress waves are then recorded by sensors attached to the surface and analyzed. The AE technique as such is a passive tool that documents the change of a state in the structure as it occurs.

Wave propagation theory and basic relationships were studied first and are presented in section 2. Waves in finite solids generally consist of three different wave modes (or types): the compression (p -) wave, the shear (s -) wave, and the surface (R -) wave. The most important wave mode in quantitative AE analysis (e.g., estimation of source locations, moment tensor inversions) is the compression wave as it represents the first, undisturbed arrival of a wave front.

The data process chain and aspects that arise when performing AE data acquisition are discussed in section 4. Recommended options and settings for the Vallen system are provided. Different qualitative and quantitative analysis methods are explained and examples shown. Explored in detail was the estimation of AE source locations in 3-D. Using Monte Carlo Simulations, sources of uncertainty were visualized and observations presented. One new qualitative method based on b -value analysis for estimating the current load operating level of a bridge girder is proposed and was given the name *minimum b-value analysis*.

Certain aspects unique to wave propagation in RC were studied by conducting separate experiments in section 5. Damping characteristics of concrete were studied on a series of different concrete cylinders and attenuation coefficients determined. Frequency dependant attenuation was characterized as well. The influence of measured signal amplitudes due to incidental angles was studied on a semi-circular specimen. The sensor response due to a known source was simulated with a finite difference program and then compared with the experimental data. It was found that the response greatly varies between sensors and depends on the sensor characteristics (i.e. broad band vs. resonant).

In section 6, the experimental procedure is explained. For the present study, a unique loading protocol was used to simulate realistic in-service conditions while going through different phases of structural deterioration of the specimens. By applying thousands of cycles after the overloads, residual strains were released to simulate realistic boundary conditions within the specimens for the simulated test trucks.

Results from sensor array A are presented in section 7. Qualitative methods were applied to the overloads at the beginning of each phase. The load holding phase after reaching a new peak load was found to give some insight as to the proximity of failure for the specimens. The newly proposed *minimum b-value analysis* appears to have potential as a tool to estimate the operating load level of a RC bridge component. As for AE source locations, it was shown that located AE events line up well with newly developed cracks. Only few AE events were located during the simulated test trucks at service level. The temporal evolution of a propagating crack could be captured and visualized.

Sensor array B is evaluated in section 8. This array can commonly be found in literature for global monitoring. Linear source location was performed to expose zones of AE activity.

The following conclusions and recommendations can be drawn from the present study:

- AE are the result of a change in the current state which suggests that the main application lies therefore mainly in long-term monitoring and real-time detection of occurring deterioration.
- The main source of AE for reinforced concrete (RC) comes from the mechanics of crack formation and propagation. Friction between crack surfaces and interaction of reinforcing bars and concrete, as well as plastic deformation and shrinkage of concrete are other potential sources.
- Due to the complexity and uniqueness of large structures many potential sources (of interest and noise) are present and can overwhelm the data acquisition system.
- Discrimination of different sources is a difficult task since recorded wave forms are highly dependent on the entire data process chain. The media (e.g. cracked concrete) as well as the characteristics of the sensors can alter the signal significantly.
- AE parameters such as signal energy, amplitude, counts, etc. depend on boundary conditions, specimen size, load rate, choice of sensor, material inhomogeneities, etc. and can only give a rough qualitative measure of the ongoing processes.

- Estimation of 3-D AE source locations from crack formation and propagation works well and located AE sources correspond with observed cracks and crack surfaces. However, it is important that the sensor network is established so that potential sources or zones of interest are not shaded by existing cracks. Also, not using all eight sensors in the network enabled maximization of detection and minimization of location errors. This is because the signals with the largest arrival time errors could be omitted from location estimations.
- The proposed *minimum b-value analysis* has the potential as a tool to help estimate the operating load level a RC bridge element. This method is based on minimum, averaged *b*-values from the whole sensor network during a load event. Use of test trucks to obtain such controlled service-level input loads is within the range of that available to almost all transportation agencies.
- Interpretation of AE data requires experience. It is not possible to determine critical values for qualitative procedures (e.g. *Historic-Severity Analysis*, *b*-value monitoring) prior to monitoring. Broad input information including inspection data, engineering rating calculations, and other available performance records must also be gathered because each structure is unique and different potential failure mechanisms may affect deployment of AE.

10.0 REFERENCES

Codes and Standards

ASTM E569-02; *Standard Practice for Acoustic Emission Monitoring of Structures During Controlled Stimulation*; ASTM International; West Conshohocken 2002.

ASTM E650-97 (Reapproved 2002); *Standard Guide for Mounting Piezoelectric Acoustic Emission Sensors*; ASTM International; West Conshohocken 2002.

ASTM E2374-04; *Standard Guide for Acoustic Emission System Performance Verification*; ASTM International; West Conshohocken 2004.

EN 1330-9; *Non-destructive testing-Terminology-Part 9: Terms used in acoustic emission testing*; European Committee for Standardization (CEN); Brüssel 2000.

Books and Dissertations

Graff, K. F.; *Wave Motion in Elastic Solids*; Dover Publications; New York 1991.

Grosse, Ch.; *Quantitative zerstörungsfreie Prüfung von Baustoffen mittels Schallemissionsanalyse und Ultraschall*; PhD Dissertation Universität Stuttgart; Stuttgart 1996.

Gutenberg, B.; Richter, C. F.; *Seismicity of the Earth and Associated Phenomena*; Princeton University Press, 1949.

Kaiser, J.; *Untersuchungen über das Auftreten von Geräuschen beim Zugversuch*; PhD Dissertation Technische Hochschule München; München 1950.

Köppel, St.; *Schallemissionsanalyse zur Untersuchung von Stahlbetontragwerken*; PhD Dissertation Eidgenössische Technische Hochschule Zürich; IBK Bericht Nr. 272; February 2002.

Kurz, J. H.; *Verifikation von Bruchprozessen bei gleichzeitiger Automatisierung der Schallemissionsanalyse an Stahl- und Stahlfaserbeton*; PhD Dissertation Universität Stuttgart; Stuttgart 2006.

Lovejoy, St., C.; *Development of Acoustic Emissions Testing Procedures Applicable to Conventionally Reinforced Concrete Deck Girder Bridges Subjected to Diagonal Tension Cracking*; PhD Dissertation Oregon State University; Corvallis 2006.

Miller, R. K.; Hill, E. v. K.; *Acoustic Emission Testing*; ASNT Nondestructive Testing Handbook, Vol. 6; Third Edition; Colombo 2005.

Nair, A.; *Acoustic Emission Monitoring and Quantitative Evaluation of Damage in Reinforced Concrete Members and Bridges*; M.S. Thesis Louisiana State University; December 2006.

Sansalone, M. J.; Streett, W. B.; *Impact-Echo, Nondestructive Evaluation of Concrete and Masonry*; Bullbrier Press; Ithaka, N.Y. 1997.

Schechinger, B.; *Schallemissionsanalyse zur Überwachung der Schädigung von Stahlbeton*; PhD Dissertation Eidgenössische Technische Hochschule Zürich; IBK Bericht Nr. 295; February 2006.

Schumacher, Th.; *Acoustic Emission Monitoring of Flexural Tension Reinforcement Anchorage Zones in Full-Scale Bridge Bent Caps*; M.S. Project Report Oregon State University; Corvallis 2006.

Technical Publications

Balazs, G. L.; Grosse, Ch. U.; Koch, R.; Reinhardt, H. W.; *Damage accumulation on deformed steel rebar to concrete interaction detected by acoustic emission technique*; Magazine of Concrete Research, Vol. 48, No. 177, December 1996; pp 311-320.

Carpinteri, A.; Lacidogna, G.; Niccolini, G.; *Critical Behavior in Concrete Structures and Damage Localization by Acoustic Emission*; Key Engineering Materials Vol. 312 (June 2006); pp. 305-310.

Carpinteri, A.; Lacidogna, G.; Pugno, N.; *Structural damage and life-time assessment by acoustic emission monitoring*; Engineering Fracture Mechanics, Volume 74, Issues 1-2; January 2007; pp. 273-289.

Colombo, S.; Main, I. G.; Forde, M. C.; *Assessing Damage of Reinforced Concrete Beam Using "b-value" Analysis of Acoustic Emission Signals*; ASCE Journal of Materials in Civil Engineering, May/June 2003; pp. 280-286.

Colombo, S.; Forde, M. C.; Main, I. C.; Shigeishi, M.; *Predicting the ultimate bending capacity of concrete beams from the "relaxation ratio" analysis of AE signals*; Construction and Building Materials; 19, 2005; pp. 746-754.

Ge, M.; *Analysis of Source Location Algorithms, Part I: Overview and Non-iterative Methods*; Journal of Acoustic Emission, No. 21, 2003; pp. 14-28.

Ge, M.; *Analysis of Source Location Algorithms, Part II: Iterative Methods*; Journal of Acoustic Emission, No. 21, 2003; pp. 29-32.

- Geiger, L.; *Herdbestimmung bei Erdbeben aus den Ankunftszeiten*; Nachrichten von der Königlichen Gesellschaft der Wissenschaften zu Göttingen, Mathematisch-Physikalische Klasse, Heft 1; Göttingen 1910;
- Glaser, St. D.; Weiss, G. G.; Johnson, L. R.; *Body waves recorded inside an elastic half-space by an embedded, wideband velocity sensor*; Journal of Acoustical Society of America; 104 (3); Sept. 1998.; pp. 1404-1410.
- Golaski, L.; Gebiski, P.; Ono, K.; *Diagnostics of Reinforced Concrete Bridges by Acoustic Emission*; Journal of Acoustic Emission, No. 20, 2002; pp. 83-98.
- Green, A. T.; *Stress Wave Emission and Fracture of Prestressed Concrete Reactor Vessel Materials*; June 1969.
- Grosse, Ch. U.; Glaser, St. D.; Krüger, M.; *Condition Monitoring of Concrete Structures Using Wireless Sensor Networks and MEMS*; Not yet published; 2006.
- Katsaga, T.; Sherwood, E. G.; Collins, M. P.; Young, R. P.; *Acoustic emission imaging of shear failure in large reinforced concrete structures*; International Journal of Fracture; Volume 148; Number 1 / November, 2007; pp. 29-45.
- Kurz, J. H.; Finck, F.; Grosse, Ch. U.; Reinhardt, H. W.; *Stress Drop and Stress Redistribution in Concrete Quantified Over Time by the b-value Analysis*; Structural Health Monitoring 5(1); 2006; pp. 69-81.
- Kobayashi, A. S.; Hawkins, N. M.; Chan, Y.-L.; Lin, I.-J.; *A Feasibility Study of Detecting Reinforcing-Bar Debonding by Acoustic-Emission Technique*; Experimental Mechanics, Vol. 20, No. 9; September 1980; pp. 301-308.
- Landis, E. N.; Shah, S. P.; *Recovery of Microcrack Parameters in Mortar Using Quantitative Acoustic Emission*; Journal of Nondestructive Evaluation, Vol. 12, No. 4, 1993; pp. 219-232.
- Landis, E. N.; Shah, S. P.; *Frequency-Dependant Stress Wave Attenuation in Cement Based Materials*; Journal of Engineering Mechanics; June 1995; pp. 737-743.
- Ohtsu, M.; *The history and development of acoustic emission in concrete engineering*; Magazine of Concrete Research, Vol. 48, No. 177, December 1996; pp. 321-330.
- Ohtsu, M.; Okamoto, T.; *Moment Tensor Analysis of Acoustic Emission for Cracking Mechanisms in Concrete*; ACI Structural Journal, March-April 1998; pp 87-95.
- Ohtsu, M.; Uchida, M.; Okamoto, T.; Yuyama, Sh.; *Damage Assessment of Reinforced Concrete Beams Qualified by Acoustic Emission*; ACI Structural Journal, July/August 2002; pp. 411-417.

Potisuk, T.; Higgins, Ch. C.; *Field Testing and Analysis of CRC Deck Girder Bridges*; Journal of Bridge Engineering, January/February 2007; pp 53-63.

Rao, M. V. M. S.; Prasanna Lakshmi, K. J.; *Analysis of b-value and improved b-value of acoustic emissions accompanying rock fracture*; Current Science, Vol. 89, No. 9, 10 November 2005; pp. 1577-1582.

Shiotani, T.; Aggelis, D. G.; Makishima, O.; *Global Monitoring of Concrete Bridge Using Acoustic Emission*; Journal of Acoustic Emission Vol. 25, January-December 2007; pp. 308-315.

Weiss, Gregory, G.; Glaser, Steven, D.; *Design and Absolute Calibration of an Embedded, Wideband Velocity Sensor*; Transportation Research Record 1614, August 1998; pp. 43-51.

Research Reports

Fricker, St.; Vogel, Th.: *Feldversuche mit dem akustischen Überwachungssystem SoundPrint*; Eidgenössische Technische Hochschule Zürich; IBK Forschungsauftrag Nr. AGB 2002/009; August 2006.

Köppel, St.; *Schallemissionsanalyse bei Versuchen an Stahlbeton*; Eidgenössische Technische Hochschule Zürich; IBK Bericht Nr. 259; November 2000.

Oregon Department of Transportation; *Assessment Methods for Diagonally Cracked Reinforced Concrete Deck Girders*; SPR-350; 2005.

Tinkey, B. V.; Fowler, T. J.; Klingner, R. E.; *Nondestructive Testing of Prestressed Bridge Girders with Distributed Damage*; Research Report 1857-2, Texas Department of Transportation, November 2000; pp. 17-67.

Conference Proceedings

Breckenridge, F. R.; Proctor, T. M.; Hsu, N. N.; Fick, S. E.; Eitzen, D. G.; *Transient Sources for Acoustic Emission Work*; Progress in Acoustic Emission V, The Japanese Society for NDT, 1990; pp. 20-37.

Fowler, T. J.; Blessing, J. A.; Conlisk, P. J.; *New directions in testing*; AECM-3: 3rd International Symposium on Acoustic Emission from Composite Materials Paris, France; July 1989; pp. 16-27.

Green, A. T.; *Stress Wave Emission and Fracture of Prestressed Concrete Reactor Vessel Materials*; Interamerican Conference on Materials Technology, Mexico City, Mexico; August 24-27, 1970; pp. ???-649.

- Grosse, Ch. U.; Köppel, St.; *Schallemissionsmessungen an Stahlbeton–Untersuchungs der Lokalisierungsgenauigkeit als Grundlage für quantitative Analysen*; 12. Kolloquium Schallemission Jena; March 2000; Beitrag 2.
- Grosse, Ch. U.; Reinhardt, H. W.; Finck, F.; *Signal-Based Acoustic Emission Techniques in Civil Engineering*; Journal of Materials in Civil Engineering; May/June 2003; pp. 274-279.
- Grosse, Ch. U.; Krüger, M.; Glaser, St. D.; McLaskey, G.; *Structural health monitoring using acoustic emission array techniques*; The 6th International Workshop on Structural Health Monitoring, Stanford University; September 2007.
- Grosse, Ch. U.; Krüger, M.; Chatzichrisafis, P.; *Acoustic emission techniques using wireless sensor networks*; International Conference on Sustainable Bridges; Wroclaw, Poland; October 2007.
- Kalicka, M.; *Defect Development and Failure Evaluation in Prestressed Concrete Girder by Acoustic Emission*; The sixth International Conference on Acoustic Emission; Lake Tahoe, October/November 2007; pp. 384-389.
- Ohtsu, M.; Suzuki, T.; *Quantitative Damage Estimation of Concrete Core based on AE Rate Process Analysis*; 26th European Conference on Acoustic Emission Testing, Berlin; September 2004.
- Shigeishi, M.; Ohtsu, M.; Shimazaki, J.; *Three-Dimensional Visualization of Acoustic Emission Moment Tensor Solutions by VRML*; The e-Journal of Nondestructive Testing; Issue Vol. 7 No. 9; September 2002.
- Shiotani, T.; Yuyama, S.; Li, Z. W.; Ohtsu, M.; *Quantitative Evaluation of Fracture Processes in Concrete by the Use of Improved b-Value*; Non-Destructive Testing in Civil Engineering 2000; Seiken Symposium No. 26; Tokyo, Japan. April 2000; pp. 293-302.
- Shiotani, T.; Nakanishi, Y.; Luo, X.; Haya, H.; *Damage Assessment in Railway Sub-Structures Deteriorated using AE Technique*; 26th European Conference on Acoustic Emission Testing, Berlin; September 2004.
- Weihe, S.; Ohmenhäuser, F.; Kröplin, B.-H.; Grosse, C., U.; Reinhardt, H.-W.; *Characterization of damage and failure during the pull-out of a reinforcement bar by acoustic emission und numerical simulation*; 1st International Conference on Damage and Failure of Interfaces; Vienna 1997.

Yuyama, Sh.; Okamoto, T.; Shigeishi, M.; Ohtsu, M.; Kishi, T.; *A Proposed Standard for Evaluating Structural Integrity of Reinforced Concrete Beams by Acoustic Emission*; Acoustic Emission: Standards and Technology Update, Symposium in Plantation, Florida; January 1998.

Manuals

Vallen Systeme GmbH; *AMSY-5 System Documentation*; München 2003.

Figures

Grosse, Ch. U.; Non-destructive testing techniques; Acoustic emission; Fault plane; Figure 4; *4_classifi_kl.gif*; <http://www.iwb.uni-stuttgart.de/grosse/aet/>; Updated June 12, 2001;

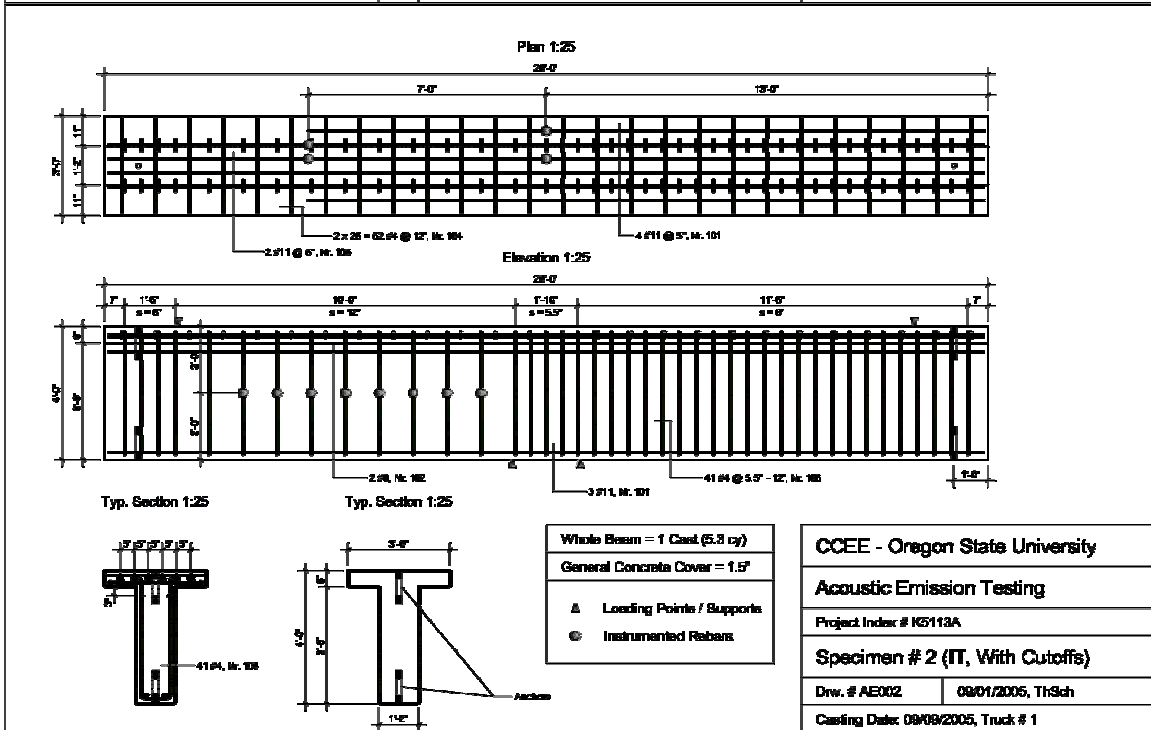
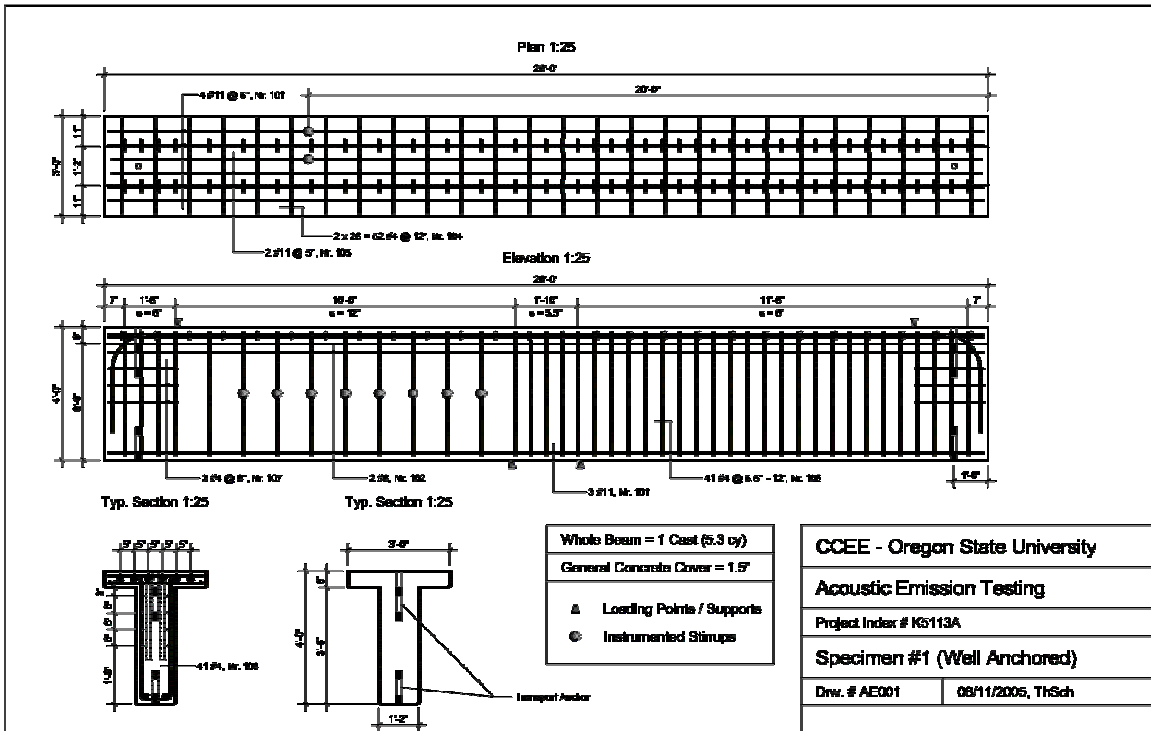
Internal Correspondence and Conversations.

Colombo, S.; Forde, M. C.; Main, I. G.; Hill, B.; *AE Monitoring of Boghall Concrete Bridge, Scottish Borders*; Draft Report; Received from Lovejoy, S.; September 2004.

Conversation with Grosse, Ch. & Krueger, M.; *Sensors and Filter Settings Used for AE Data Acquisition*; University of Stuttgart, Germany; September 18 & 19, 2006.

**APPENDIX A:
MATERIALS AND SETTINGS**

A1: Specimen Shop Drawings



A2: Concrete Mix Design

The aggregate composition for the mix was reported by the supplier to be: 97 % passing the 3/4 in. sieve (19 mm), 82 % passing 5/8 in. (16 mm), 57 % passing 1/2 in. (12.5 mm), 33 % passing 3/8 in. (9.5 mm), 21 % passing 5/16 in. (8 mm), 9.3 % passing 1/4 in. (6.3 mm), 3.0 % passing #4 (4.75 mm), 0.6 % passing #8 (2.36 mm) and 0.3 % passing the #200 (0.075 mm) sieve. The sand composition of the mix was also reported as: 99.7 % passing the 1/4 in. sieve (6.3 mm), 96.8 % passing #8 (2.36 mm), 59.4 % passing #16 (1.18 mm), 44.9 % passing #30 (0.600 mm), 17.9 % passing #50 (0.300 mm), 3.7 % passing #100 (0.150 mm) and 1.7 % passing the #200 (0.075 mm) sieve. The coarse aggregate was from Willamette River bed deposits and was smooth rounded basaltic rock.

A3: Stress-Strain Curves from Concrete Cylinder Tests

In Figures A1 and A2, stress-strain curves are illustrated for both specimens for the test end day. Moduli of Elasticity were determined via linear least-squares curve-fitting over a stress range from 0 to $0.4f_c'$. Mean Moduli of Elasticity were 18,770 MPa (2722 ksi) and 19,290 MPa (2798 ksi) for AE Specimen #1 and #2, respectively.

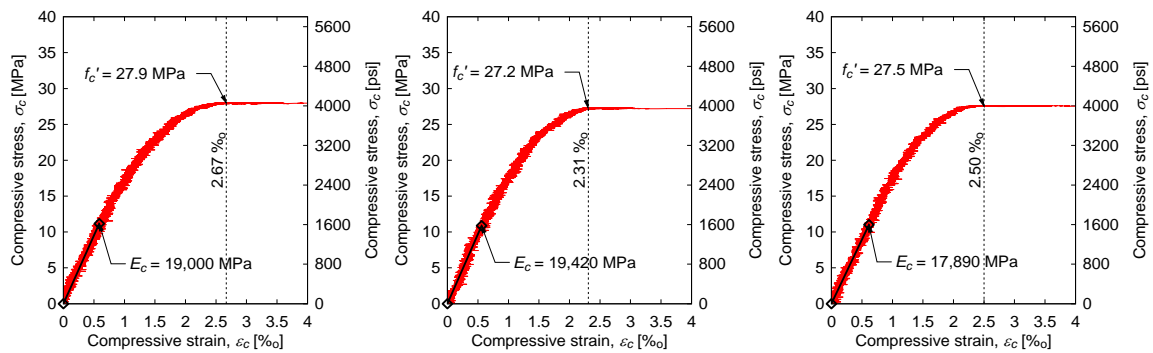


Figure A1: AE Specimen #1, concrete cylinders at test end day

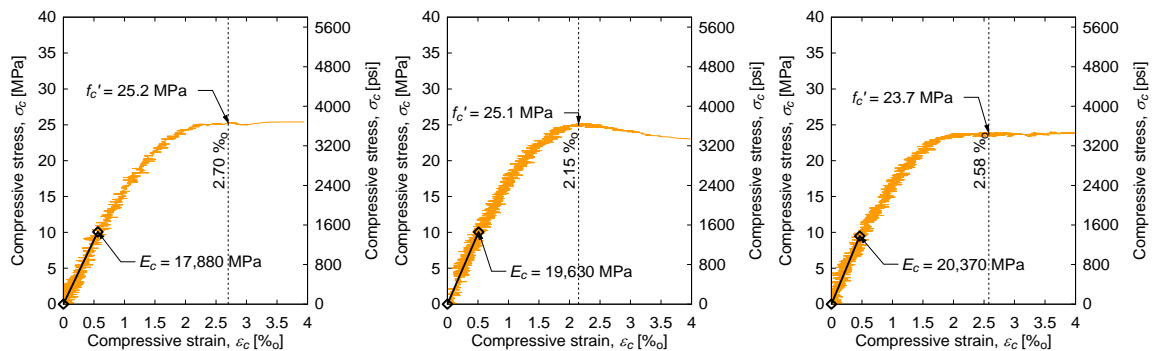


Figure A2: AE Specimen #2, concrete cylinders at test end day

**APPENDIX B:
AE SETTINGS**

B1: Sensor Array Coordinates AE Specimen #1

Table B1.1: Sensor Array A1 (Session 1)

S#	Metric			U.S. Customary			d_{max} [m]/ [in.]	KRNi060 Serial #	G [dB]
	x [m]	y [m]	z [m]	x [in.]	y [in.]	z [in.]			
1	1.067	-0.356	0.178	42.0	-14.0	7.0		03026	44
2	1.372	0.457	0.178	54.0	18.0	7.0		03027	44
3	1.981	-0.305	0.178	78.0	-12.0	7.0		03028	44
4	2.286	0.152	0.178	90.0	6.0	7.0	1.91/	03029	44
5	1.676	0.619	-0.064	66.0	24.4	-2.5	75	03030	44
6	1.346	-0.203	-0.178	53.0	-8.0	-7.0		03031	44
7	2.032	0.457	-0.178	80.0	18.0	-7.0		04036	44
8	2.540	-0.381	-0.178	100.0	-15.0	-7.0		04037	44

Table B1.2: Sensor Array A2 (Session 2 & 3)

S#	Metric			U.S. Customary			d_{max} [m]/ [in.]	KRNi060 Serial #	G [dB]
	x [m]	y [m]	z [m]	x [in.]	y [in.]	z [in.]			
1	1.067	-0.051	0.178	42.0	-2.0	7.0		03026	44
2	1.372	0.457	0.178	54.0	18.0	7.0		03027	44
3	1.676	-0.356	0.178	66.0	-14.0	7.0		03028	44
4	2.286	0.152	0.178	90.0	6.0	7.0	1.94/	03029	44
5	1.676	0.619	-0.064	66.0	24.4	-2.5	76	03030	44
6	1.346	-0.203	-0.178	53.0	-8.0	-7.0		03031	44
7	2.032	0.457	-0.178	80.0	18.0	-7.0		04036	44
8	2.540	-0.381	-0.178	100.0	-15.0	-7.0		04037	44

Table B1.3: Sensor Array A3 (Session 6 & 7)

S#	Metric			U.S. Customary			d_{max} [m]/ [in.]	KRNi060 Serial #	G [dB]
	x [m]	y [m]	z [m]	x [in.]	y [in.]	z [in.]			
1	1.067	-0.051	0.178	42.0	-2.0	7.0	1.76/ 69	03026	44
2	1.321	0.203	0.178	52.0	8.0	7.0		03027	44
3	1.372	0.619	-0.051	54.0	24.4	-2.0		03028	44
4	2.007	0.619	0.025	79.0	24.4	1.0		03029	44
5	1.930	-0.178	0.178	76.0	-7.0	7.0		03030	44
6	0.851	0.292	-0.178	33.5	11.5	-7.0		03031	44
7	1.321	-0.330	-0.178	52.0	-13.0	-7.0		04036	44
8	2.261	0.292	-0.178	89.0	11.5	-7.0		04037	44

Table B1.4: Sensor Array A4 (Session 8)

S#	Metric			U.S. Customary			d_{max} [m]/ [in.]	KRNi060 Serial #	G [dB]
	x [m]	y [m]	z [m]	x [in.]	y [in.]	z [in.]			
1	1.092	0.051	0.178	43.0	2.0	7.0	1.76/ 69	03026	44
2	1.321	0.203	0.178	52.0	8.0	7.0		03027	44
3	1.372	0.619	-0.051	54.0	24.4	-2.0		03028	44
4	2.007	0.619	0.025	79.0	24.4	1.0		03029	44
5	1.930	-0.178	0.178	76.0	-7.0	7.0		03030	44
6	0.851	0.292	-0.178	33.5	11.5	-7.0		03031	44
7	1.321	-0.330	-0.178	52.0	-13.0	-7.0		04036	44
8	2.261	0.292	-0.178	89.0	11.5	-7.0		04037	44

Table B1.5: Sensor Array A5 (Session 13, 14, & 18)

S#	Metric			U.S. Customary			d_{max} [m]/ [in.]	KRNi060 Serial #	G [dB]
	x [m]	y [m]	z [m]	x [in.]	y [in.]	z [in.]			
1	1.092	0.051	0.178	43.0	2.0	7.0	1.76/ 69	03026	44
2	1.372	0.619	-0.051	54.0	24.4	-2.0		03027	44
3	1.651	0.318	0.178	65.0	12.5	7.0		03028	44
4	1.930	-0.178	0.178	76.0	-7.0	7.0		03029	44
5	2.007	0.619	0.025	79.0	24.4	1.0		03030	44
6	0.851	0.292	-0.178	33.5	11.5	-7.0		03031	44
7	1.321	-0.330	-0.178	52.0	-13.0	-7.0		04036	44
8	2.261	0.292	-0.178	89.0	11.5	-7.0		04037	44

Table B1.6: Sensor Array B (Session 3c, 7b, 9, & 15)

S#	Metric	U.S. Customary	d_{max}	KRNi060	G
	x	x	[m]/	Serial #	[dB]
	[m]	[in.]	[in.]		
1	-3.505	-138		03026	44
2	-2.591	-102		03027	44
3	-1.676	-66.0		03028	44
4	-0.762	-30.0	3.05/	03029	44
5	0.762	30.0	120	03030	44
6	1.676	66.0		03031	44
7	2.591	102		04036	44
8	3.505	138		04037	44

B2: Sensor Array Coordinates AE Specimen #2

Table B2.1: Sensor Array A1 (Session 1, 2, 2b, & 2c)

S#	Metric			U.S. Customary			d_{max} [m]/ [in.]	KRNi060 Serial #	G [dB]
	x [m]	y [m]	z [m]	x [in.]	y [in.]	z [in.]			
1	1.092	0.0	0.178	43.0	0.0	7.0		03026	40
2	1.715	0.305	0.178	67.5	12.0	7.0		03027	40
3	2.337	0.0	0.178	92.0	0.0	7.0		03028	40
4	1.676	0.613	-0.051	66.0	24.1	-2.0	1.69/	03029	40
5	2.286	0.613	0.051	90.0	24.1	2.0	66	03030	40
6	1.143	0.305	-0.178	45.0	12.0	-7.0		03031	40
7	1.702	0.0	-0.178	67.0	0.0	-7.0		04036	40
8	2.273	0.305	-0.178	89.5	12.0	-7.0		04037	40

Table B2.2: Sensor Array A2 (Session 3, 7, 8, & 12)

S#	Metric			U.S. Customary			d_{max} [m]/ [in.]	KRNi060 Serial #	G [dB]
	x [m]	y [m]	z [m]	x [in.]	y [in.]	z [in.]			
1	1.105	0.152	0.178	43.5	6.0	7.0		03026	40
2	1.715	0.305	0.178	67.5	12.0	7.0		03027	40
3	2.337	0.0	0.178	92.0	0.0	7.0		03028	40
4	1.676	0.613	-0.051	66.0	24.1	-2.0	1.60/	03029	40
5	2.286	0.613	0.051	90.0	24.1	2.0	63	03030	40
6	1.143	0.305	-0.178	45.0	12.0	-7.0		03031	40
7	1.702	0.0	-0.178	67.0	0.0	-7.0		04036	40
8	2.273	0.305	-0.178	89.5	12.0	-7.0		04037	40

Table B2.3: Sensor Array A3 (Session 13)

S#	Metric			U.S. Customary			d_{max} [m]/ [in.]	KRNi060 Serial #	G [dB]
	x [m]	y [m]	z [m]	x [in.]	y [in.]	z [in.]			
1	2.375	0.457	0.178	93.5	18.0	7.0		03026	40
2	1.715	0.305	0.178	67.5	12.0	7.0		03027	40
3	2.337	0.0	0.178	92.0	0.0	7.0		03028	40
4	1.676	0.613	-0.051	66.0	24.1	-2.0	1.17/	03029	40
5	2.286	0.613	0.051	90.0	24.1	2.0	46	03030	40
6	1.880	0.419	-0.178	74.0	16.5	-7.0		03031	40
7	1.702	0.0	-0.178	67.0	0.0	-7.0		04036	40
8	2.273	0.305	-0.178	89.5	12.0	-7.0		04037	40

Table B2.4: Sensor Array A4 (Session 17, 18, & 19)

S#	Metric			U.S. Customary			d_{max} [m]/ [in.]	KRNi060 Serial #	G [dB]
	x [m]	y [m]	z [m]	x [in.]	y [in.]	z [in.]			
1	1.715	0.305	0.178	67.5	12.0	7.0		03026	40 ¹⁾
2	2.337	0.0	0.178	92.0	0.0	7.0		03027	40
3	2.375	0.457	0.178	93.5	18.0	7.0		03028	40
4	1.676	0.613	-0.051	66.0	24.1	-2.0	1.17/	03029	40
5	2.286	0.613	0.051	90.0	24.1	2.0	46	03030	40
6	1.702	0.0	-0.178	67.0	0.0	-7.0		03031	40
7	1.880	0.419	-0.178	74.0	16.5	-7.0		04036	40
8	2.273	0.305	-0.178	89.5	12.0	-7.0		04037	40

¹⁾ For session 19, this sensor was replaced by a Vallen SE150-M (gain = of 34 dB)

Table B2.5: Sensor Array B (Session 4, 9, & 14)

S#	Metric	U.S. Customary	d_{max} [m]/ [in.]	KRNi060 Serial #	G [dB]
	x [m]	x [in.]			
1	-3.505	-138		03026	40
2	-2.591	-102		03027	40
3	-1.676	-66.0		03028	40
4	-0.762	-30.0	3.05/	03029	40
5	0.762	30.0	120	03030	40
6	1.676	66.0		03031	40
7	2.591	102		04036	40
8	3.505	138		04037	40

B3: Data Acquisition Settings for Sensor Array A

Table B3.1: Data acquisition settings used for AE Specimen #1

Settings	Parameter	Symbol	Unit	Value/Setting	
Acquisition	Sample rate	f_s	MHz	2.0	
	Samples per TR-set		-	2048	
	Pre-trigger samples		-	800	
	Threshold	THR	dB	$2 - 6^{1)}$	
	Threshold to noise ratio	Cr	-	$1)$	
	Gain	G	dB	44	
	Duration discrimination time		μs	250	
	Rearm time		ms	1.0	
	Location	First-hit discrimination time	$FHCDT$	ms	
		Max. Δt to first-hit	$DTIX-Max$	ms	$\frac{1.25 \cdot d_{max}}{c_p}$
Max. Δt to previous hit		$DTNX-Max$	ms		
p -wave velocity		c_p	m/ms (in./ms)	3.79 (149)	
Max. neighborhood distance			m (in.)	$1.25 \cdot d_{max}$	
Algorithm type			-	Solid 3D (steps)	
Min. signal hits			n	5	
Max. signal hits			n	5	
Frnt. Filter		Signal amplitude	A	dB	$40 < A < 100$

¹⁾ Values for threshold and crescent factor vary throughout the experiment since the most suitable values had to be determined first. Recommended values can be found in section 4.

Table B3.2: Data acquisition settings used for AE Specimen #2

Settings	Parameter	Symbol	Unit	Value/Setting	
Acquisition	Sample rate	f_s	MHz	2.0	
	Samples per TR-set		-	2048	
	Pre-trigger samples		-	800	
	Threshold	THR	dB	1)	
	Threshold to noise ratio	Cr	-	1)	
	Gain	G	dB	40 (34) ²⁾	
	Duration discrimination time		μ s	250	
	Rearm time		ms	1.0	
	Location	First-hit discrimination time	$FHCDT$	ms	
		Max. Δt to first-hit	$DTIX-Max$	ms	$\frac{1.25 \cdot d_{max}}{c_p}$
Max. Δt to previous hit		$DTNX-Max$	ms		
p -wave velocity		c_p	m/ms (in./ms)	3.65 (144)	
Max. neighborhood distance			m (in.)	$1.25 \cdot d_{max}$	
Algorithm type			-	Solid 3D (steps)	
Min. signal hits			n	5	
Max. signal hits			n	5	
Frnt. Filter		Min. signal amplitude	A	dB	$40 < A < 100$

**APPENDIX C:
DATA SENSOR ARRAY A**

C1: Basic AE response plots and physical measurements for AE Specimen #1

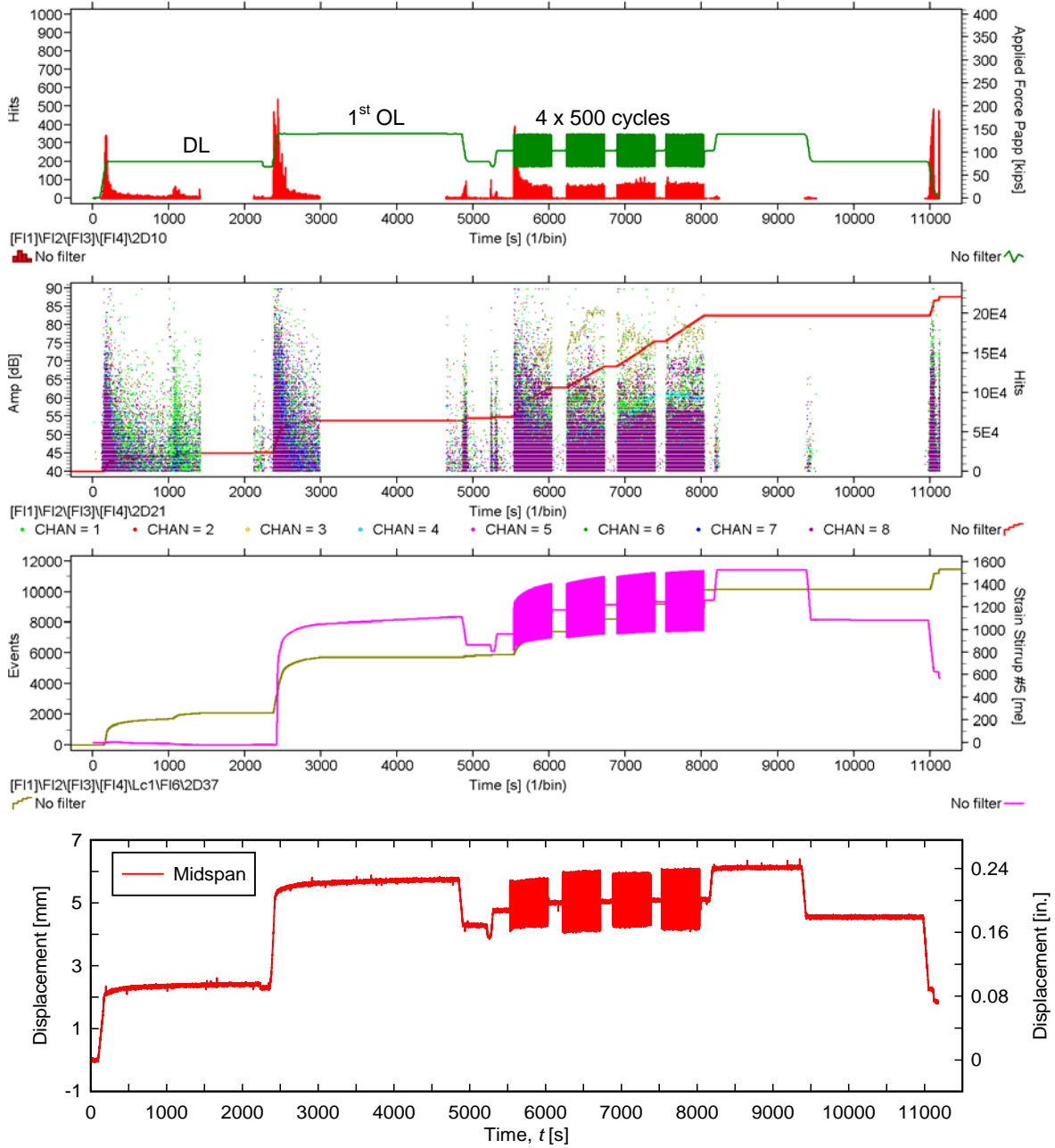


Figure C1.1: Basic AE data and physical measurements, Session 1

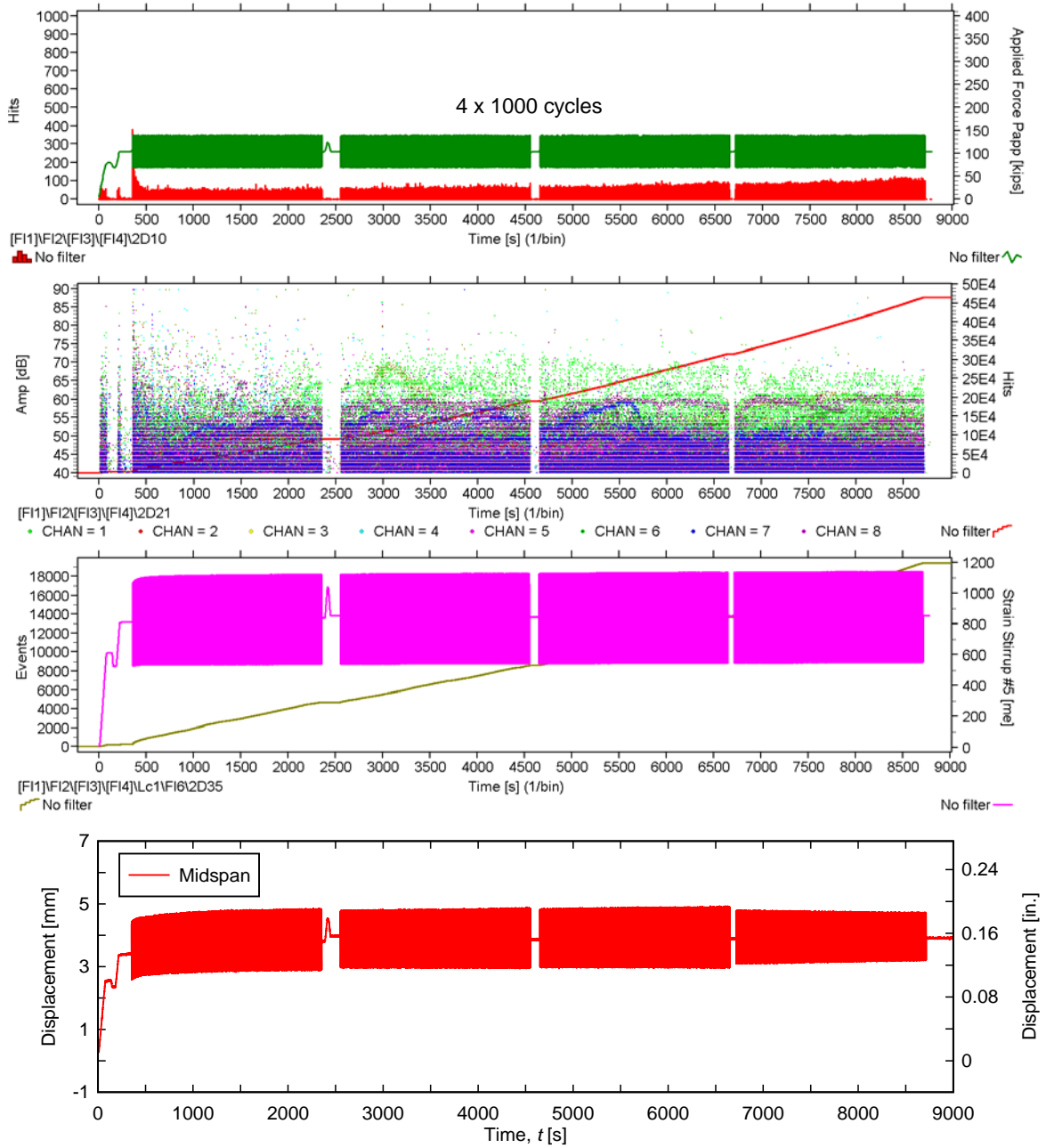


Figure C1.2: Basic AE data and physical measurements, Session 2

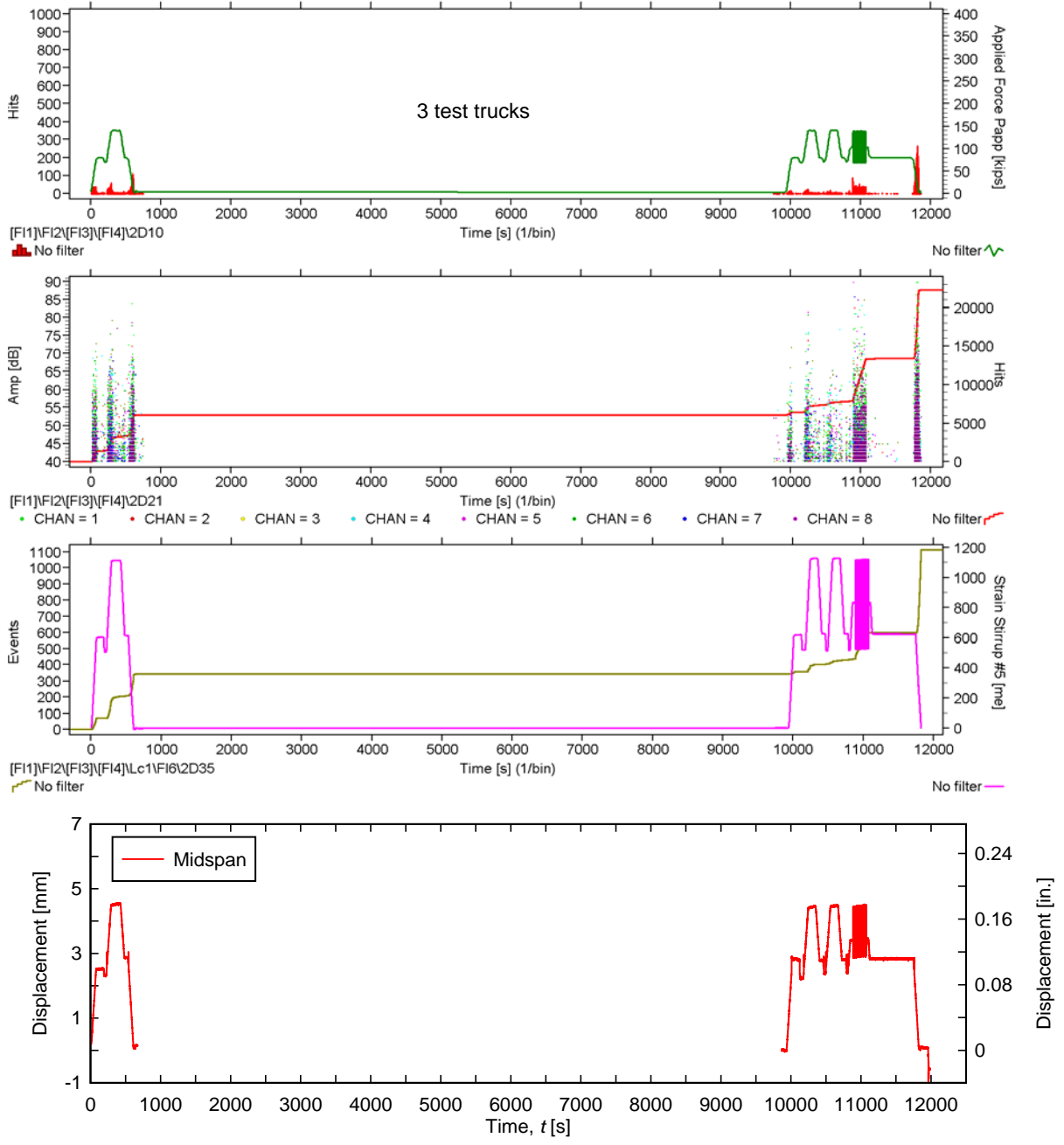


Figure C1.3: Basic AE data and physical measurements, Session 3

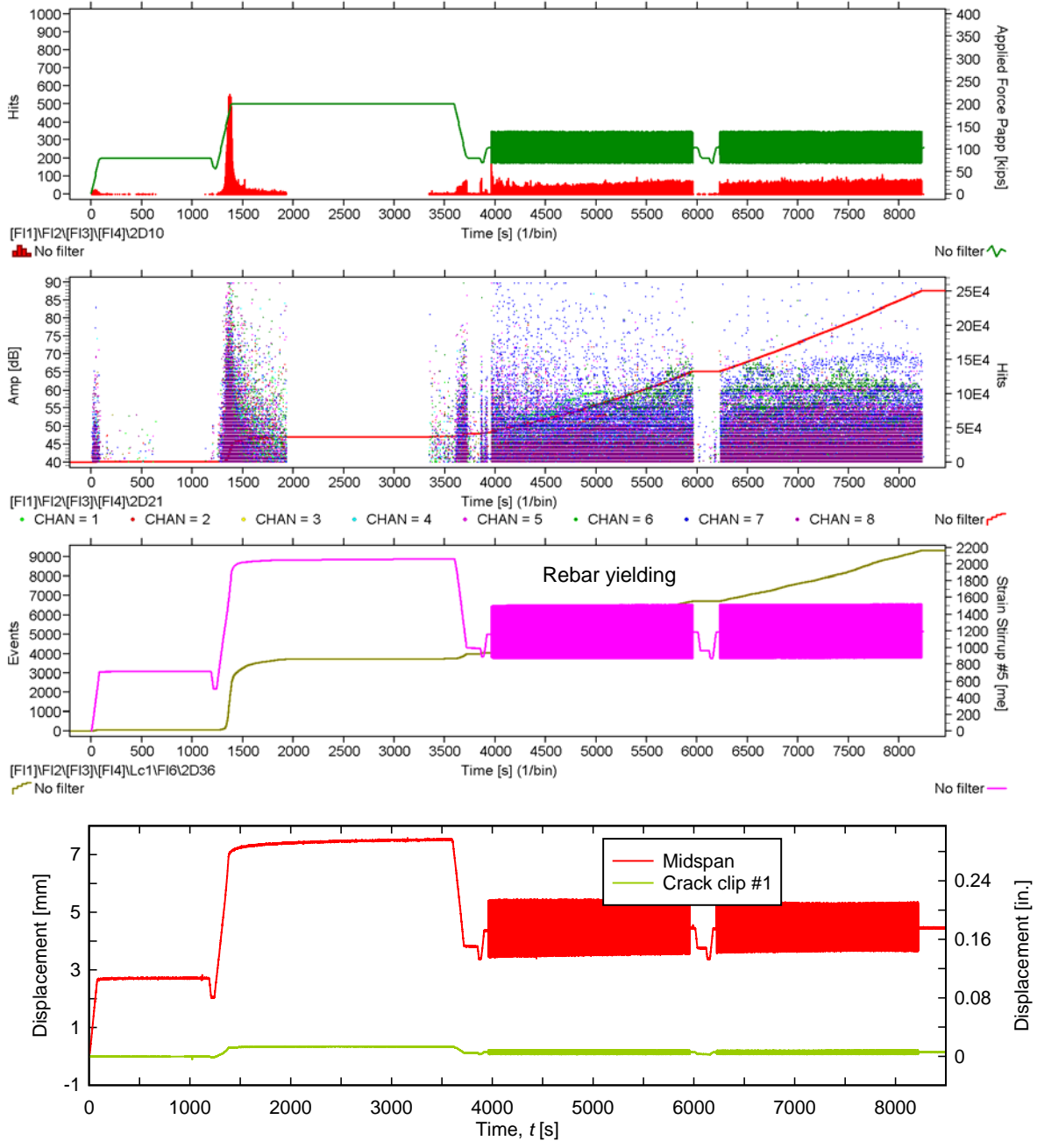


Figure C1.4: Basic AE data and physical measurements, Session 6

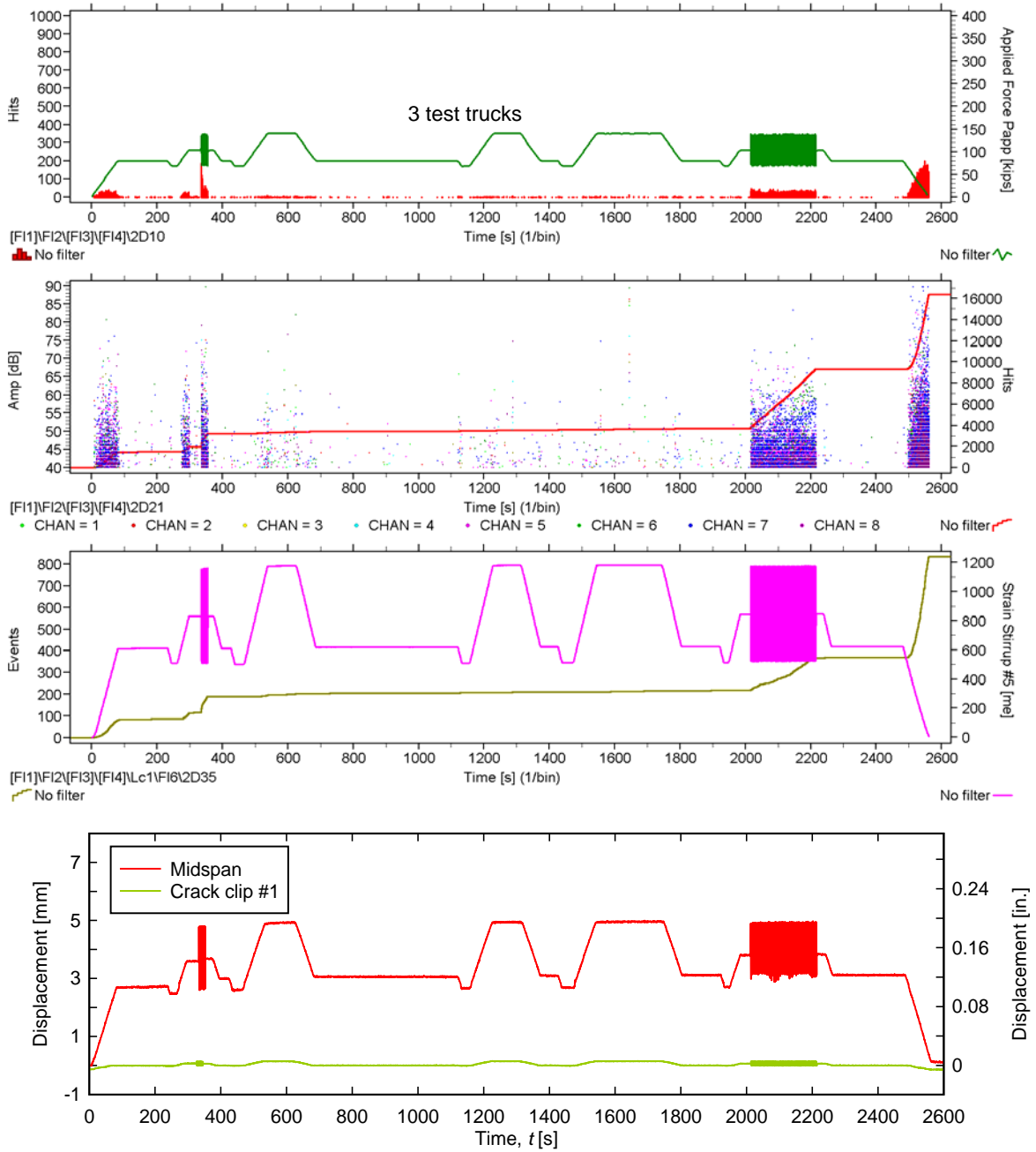


Figure C1.5: Basic AE data and physical measurements, Session 7

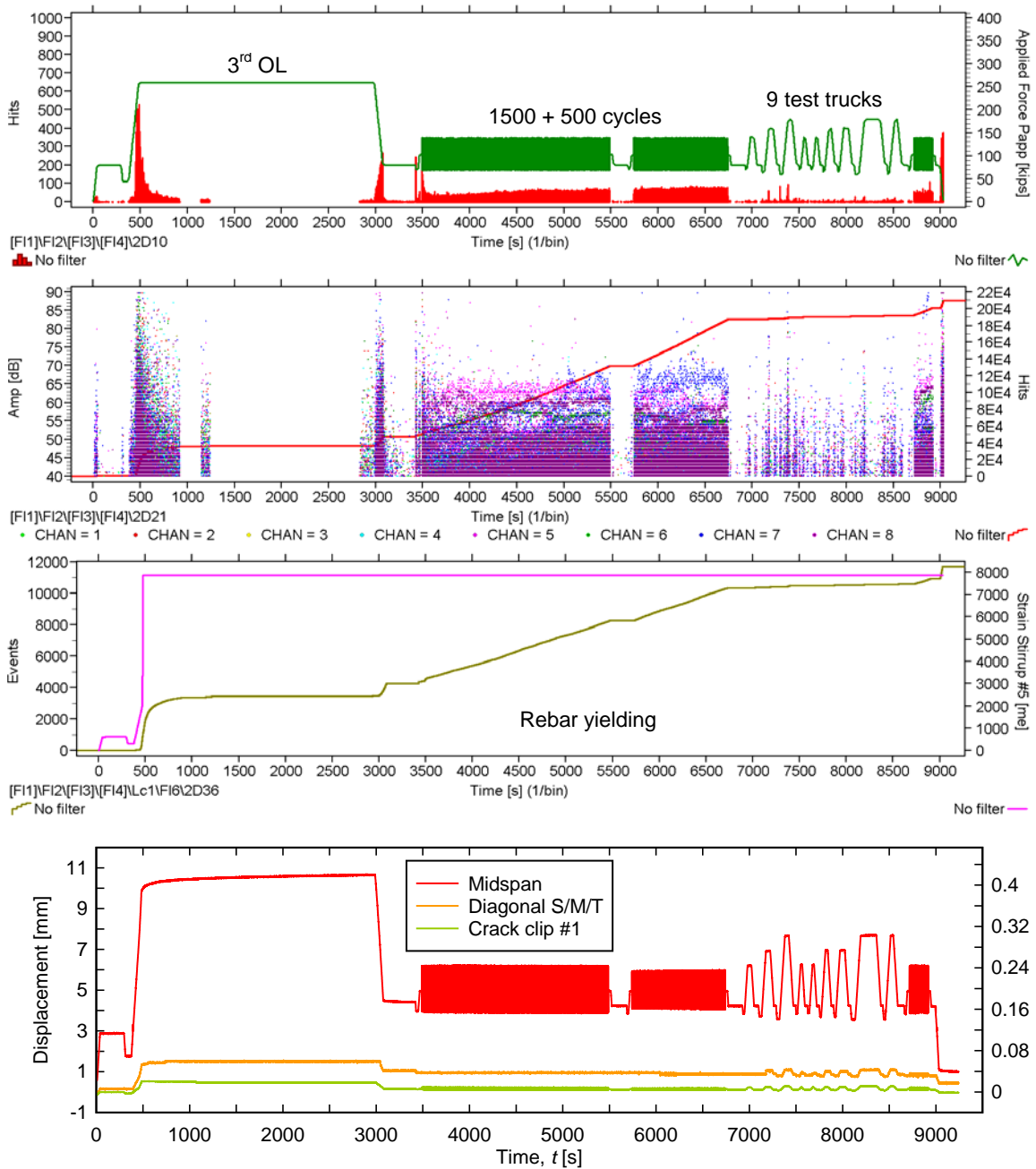


Figure C1.6: Basic AE data and physical measurements, Session 8

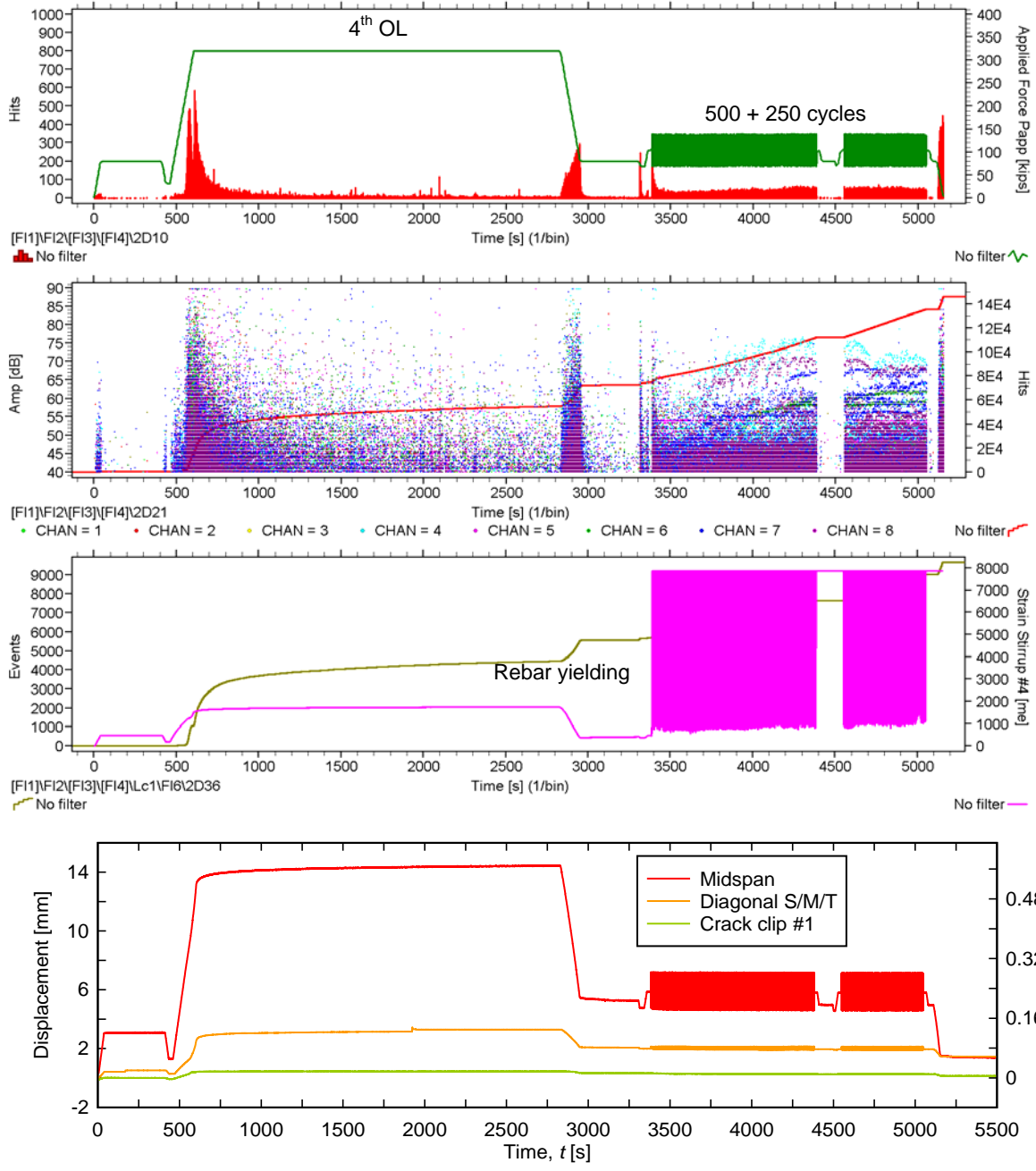


Figure C1.7: Basic AE data and physical measurements, Session 13

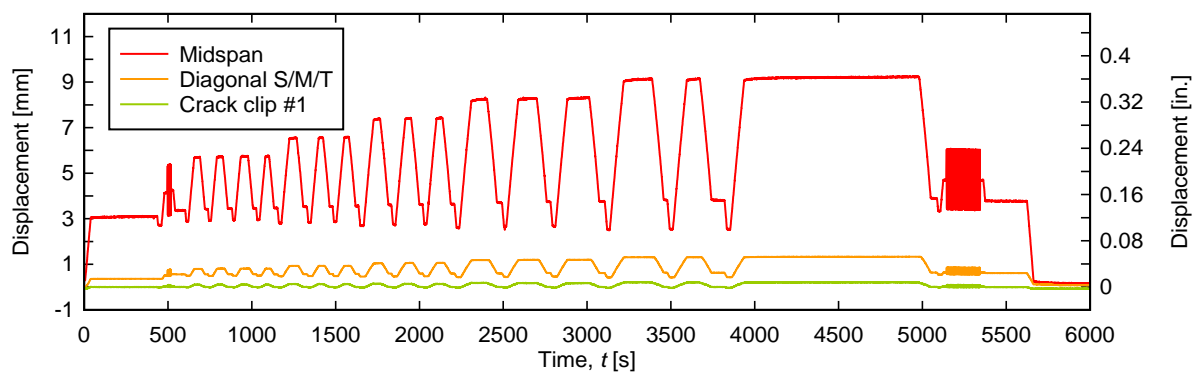
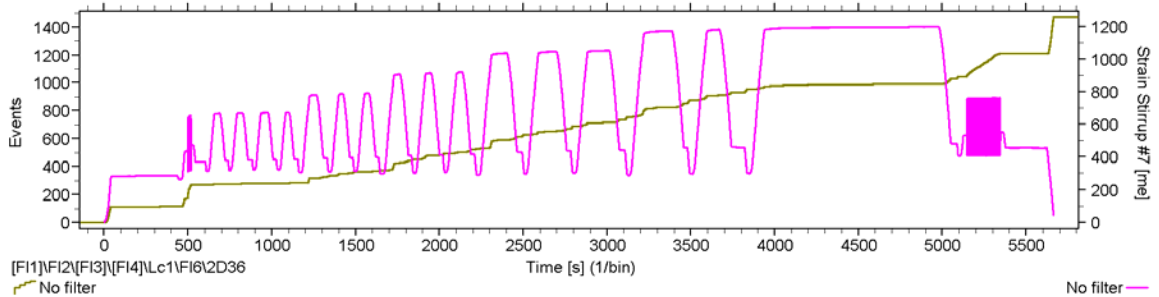
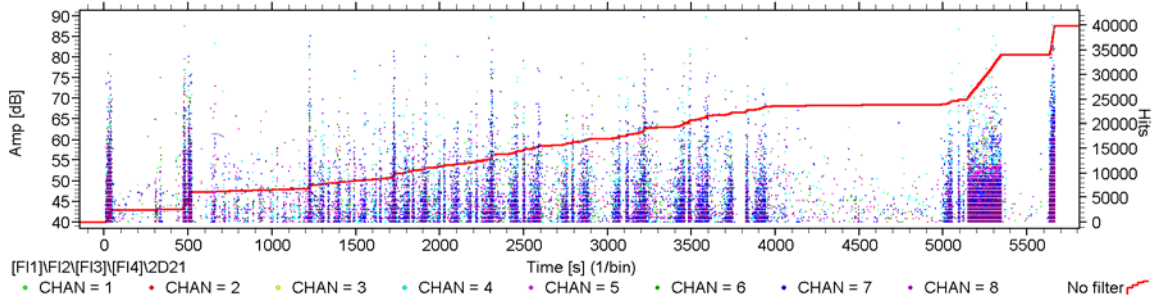
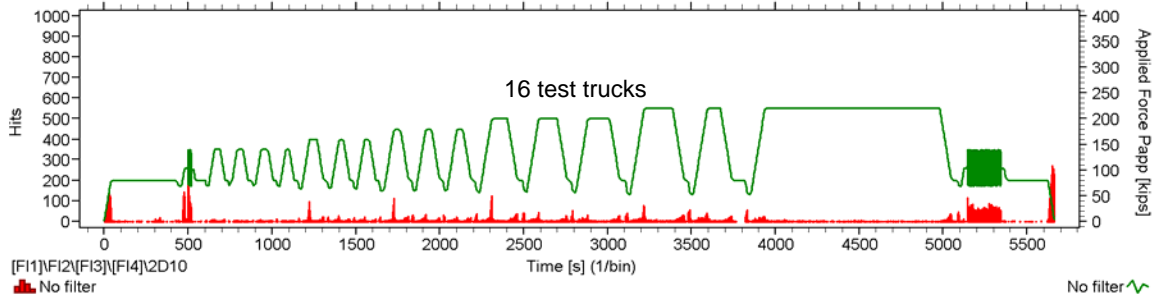


Figure C1.8: Basic AE data and physical measurements, Session 14

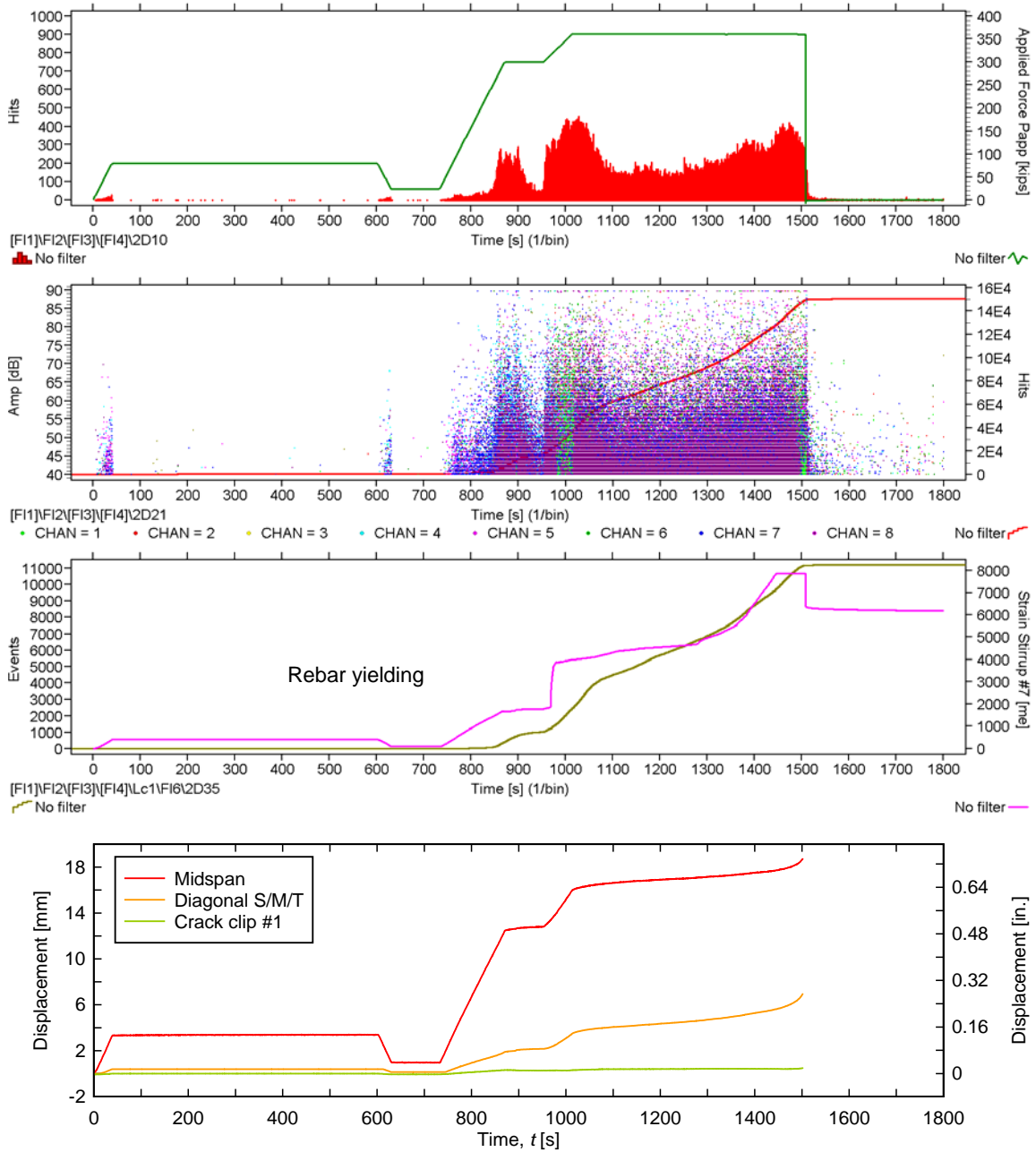


Figure C1.9: Basic AE data and physical measurements, Session 18

C2: Basic AE response plots and physical measurements for AE Specimen #2

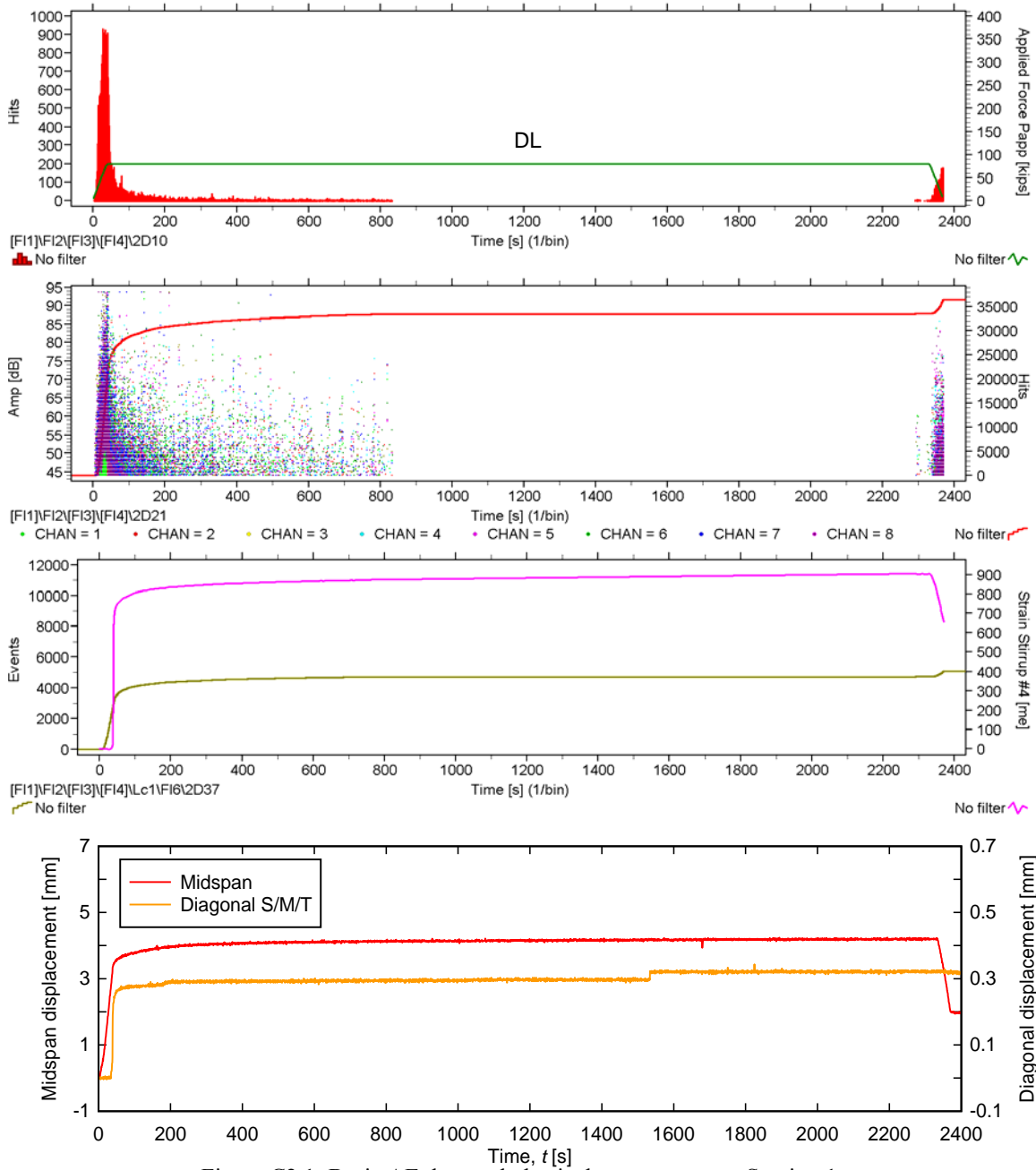


Figure C2.1: Basic AE data and physical measurements, Session 1

C3: AE Hit Rate Data

Shown in Figure C3.1 are mean maximum AE hit rates from all applied load cycles (except the cyclic loadings). Error bars represent one standard deviation.

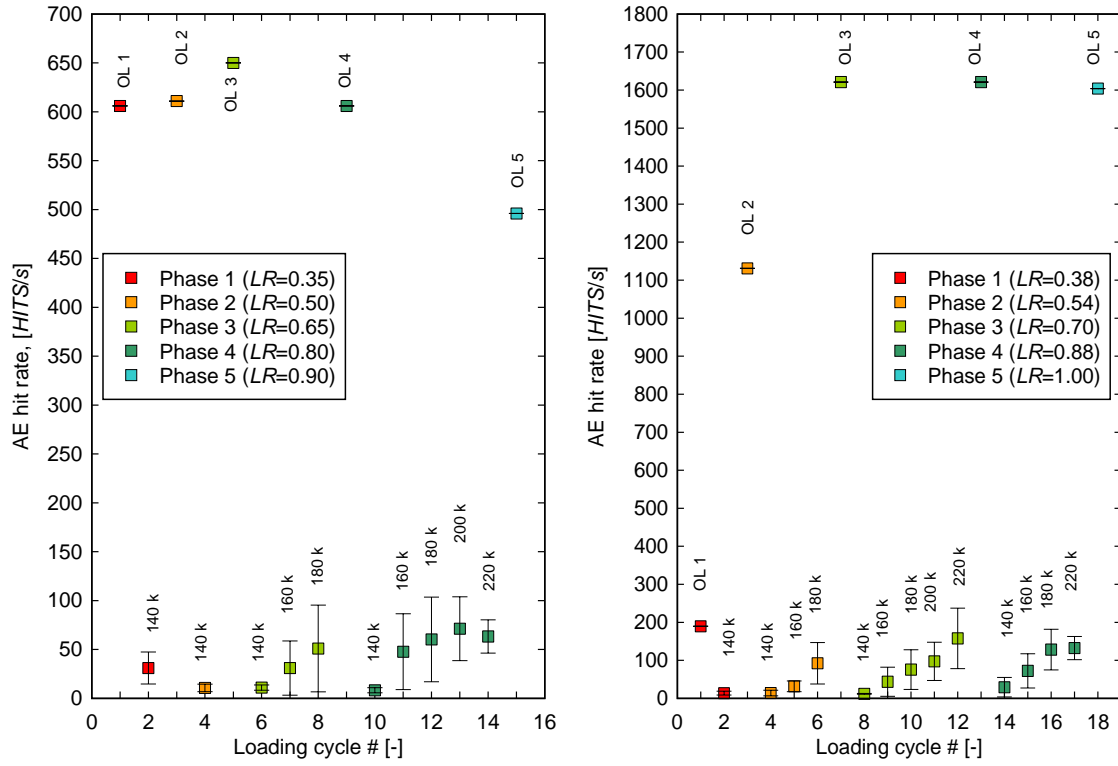


Figure C3.1: AE hit rates for all applied load cycles for AE Specimen #1 (left) and #2 (right)

C4: Calm and Load Ratios for Service-Level Test Trucks

Presented below are average *Load* and *Calm Ratios* for truck groups (trucks with of same magnitude). Error bars represent one standard deviation.

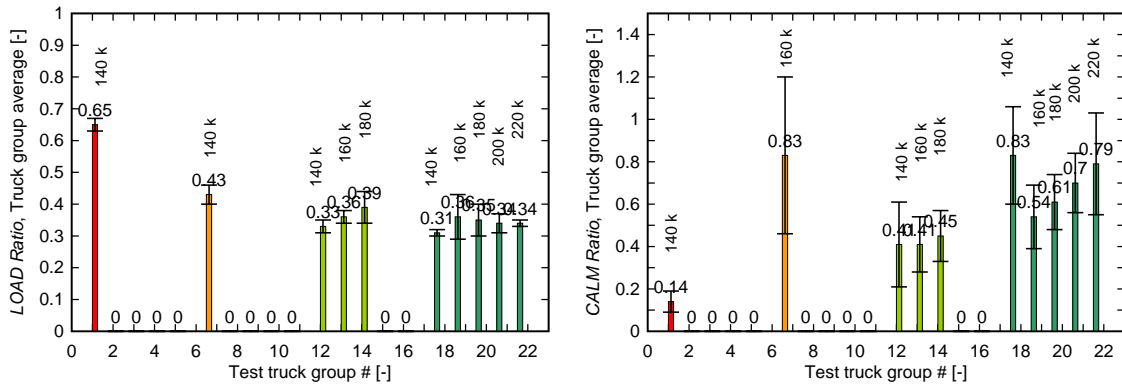


Figure C4.1: Load and Calm Ratios for simulated test truck groups for AE Specimen #1

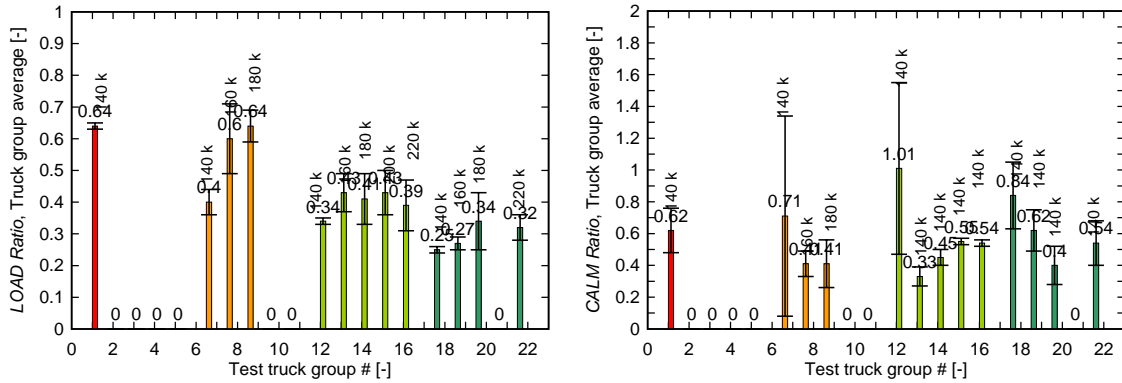


Figure C4.2: Load and Calm Ratios for simulated test truck groups for AE Specimen #2

C5: Minimum b -Value Analysis

Shown below are computed minimum b -values from all applied load cycles (except the cyclic loadings). Error bars represent one standard deviation.

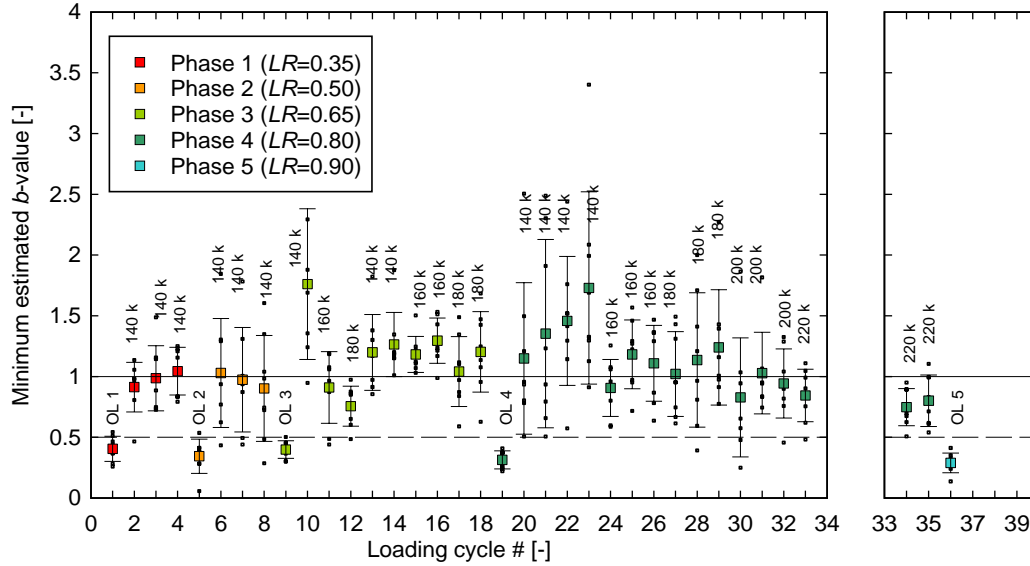


Figure C5.1: Minimum b -values for applied load cycles for AE Specimen #1

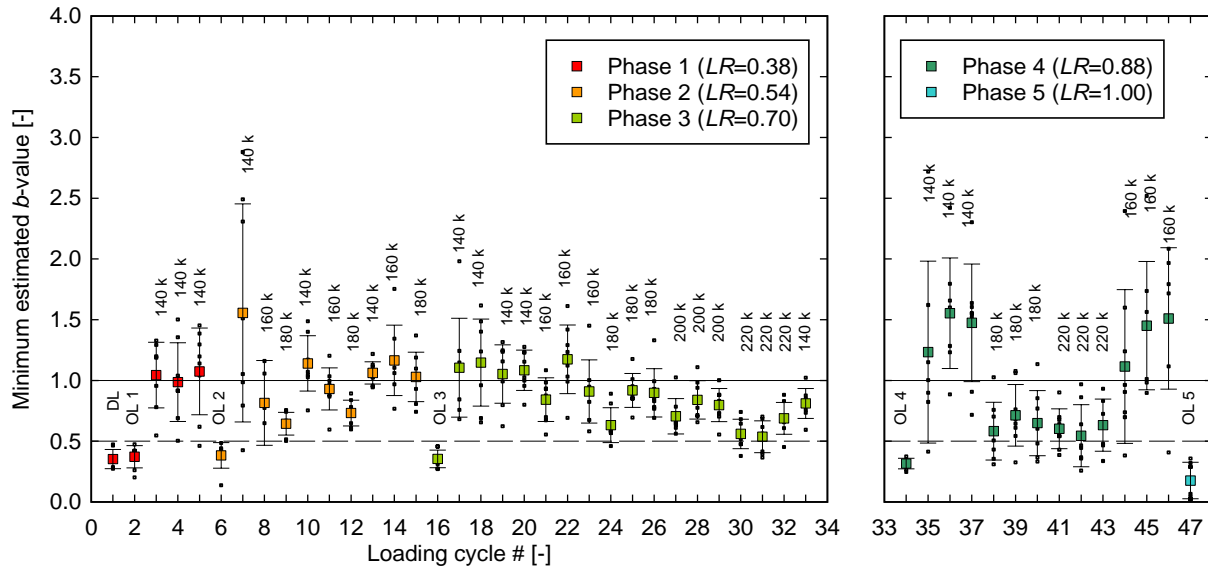


Figure C5.2: Minimum b -values for applied load cycles for AE Specimen #2